

# Majorana fermions in magnetically ordered superconducting heterostructures

Zur Erlangung des akademischen Grades eines  
DOKTORS DER NATURWISSENSCHAFTEN  
von der Fakultät für Physik des  
Karlsruher Instituts für Technologie (KIT)

genehmigte  
DISSERTATION  
von

Dipl.-Phys. Daniel Philipp Mendler

aus Stuttgart

Datum der mündlichen Prüfung: 14. Juli 2017  
Referent: Prof. Dr. Gerd Schön  
Korreferent: Prof. Dr. Alexander Mirlin

---

This work is licensed under a Creative Commons  
“Attribution-ShareAlike 4.0 International” license. The  
license does not apply to reprinted figures.



# Contents

<b>Preface</b>	<b>4</b>
<b>1 Introduction to topological phases of matter</b>	<b>15</b>
1.1 Topological insulators and superconductors . . . . .	16
1.2 Phase transitions and symmetries . . . . .	23
1.3 Topological classification of Hamiltonians . . . . .	30
<b>2 Fundamentals of Majorana fermions</b>	<b>37</b>
2.1 Majorana zero modes: Definition and general properties . . . . .	38
2.2 Topological quantum computation . . . . .	40
2.3 Theoretical proposals for realization of Majorana fermions . . . . .	45
2.4 Majorana fermion signatures . . . . .	53
<b>3 Majorana bound states in magnetic adatom chains</b>	<b>57</b>
3.1 Status of magnetic adatom chain experiments . . . . .	58
3.2 Theoretical description of Yu-Shiba-Rusinov chains . . . . .	60
3.3 Majorana bound states and Majorana tunnel couplings . . . . .	64
3.4 Tunneling conductance signatures of Majorana spin character . . . . .	68
3.5 Summary and conclusion . . . . .	85
<b>4 Magnetic order on warped topological insulator surfaces</b>	<b>87</b>
4.1 Three-dimensional topological insulator . . . . .	88
4.2 Surface states and warping effects . . . . .	89
4.3 Magnetic instability . . . . .	93
4.4 Control and fingerprints of the magnetic phases . . . . .	108
4.5 Summary and conclusion . . . . .	110
<b>5 Topological superconductivity in magnetic skyrmion lattice and superconductor-based heterostructure</b>	<b>113</b>
5.1 Hamiltonian of a magnetic skyrmion lattice . . . . .	114
5.2 Feedback effects between superconductor and magnetic texture . . . . .	116

5.3	Analysis of a $\text{Bi}_2\text{Te}_3$ -superconductor heterostructure . . . . .	122
5.4	Topological superconductivity and Majorana flat bands . . . . .	129
5.5	Summary and conclusion . . . . .	134
<b>6</b>	<b>Conclusion and outlook</b>	<b>135</b>
<b>A</b>	<b>Appendices</b>	<b>139</b>
A.1	Tunneling conductance for two coupled magnetic adatom chains . . .	139
A.2	Magnetic order parameter classification of warped topological insulators	140
A.3	Magnetic susceptibility of warped topological insulators . . . . .	142
A.4	Free energy coefficients of warped topological insulators . . . . .	144
	<b>Bibliography</b>	<b>157</b>

# Preface

The research work covered by this thesis was carried out between May 2013 and June 2017 at the Institute for Theoretical Solid State Physics and the Institute of Nanotechnology at the Karlsruhe Institute of Technology in collaboration with Prof. Gerd Schön and Dr. Panagiotis Kotetes.

One of the main motivations of this thesis is the study of Majorana fermions in solid state systems. While Majorana fermions are discussed in high-energy physics as possible elementary particles for example in the context of neutrino physics, zero-energy excitations with similar characteristics can appear in solid state systems. There are various proposals predicting the appearance of Majorana zero modes. Some of those proposals are under experimental investigation right now with promising results [5, 6]. In transport experiments even the characteristic quantization of the tunneling conductance of  $2e^2/h$  through Majorana zero modes was recently reported [7].

Zero-energy Majorana modes living on a two-dimensional surface are non-abelian anyons. This means their exchange statistics are different from bosons and fermions. In contrast to those, moving localized Majorana particles around each other adiabatically, while keeping ‘safe’ distance between the particles, results in a modified wavefunction. In the case of abelian anyons the wavefunction acquires a complex phase factor, while for non-abelian anyons, like Majorana fermions, the components of the wavefunctions are rotated. This movement of the localized particles on a surface is called braiding, as the worldlines of the particles are threaded like strands. Braiding operations can be used for quantum information processing. The quantum information, represented as quantum bits or ‘qubits’ is encoded in the ground state degeneracy spanned by the Majorana zero modes. The dimension plays a crucial role for braiding, which can be seen as follows: If a particle is moved around another one on a closed path in two dimensions, this path cannot be contracted to a point. In three dimensions however, any closed path of one of the particles can be reduced to a point without interfering with the other particle. This difference arises from the topology of the parameter space describing the location of the two particles. Manipulation of qubits encoded in Majorana fermions is therefore referred to as topological quantum computation.

Topology is the mathematical discipline of classifying spaces in terms of topological invariants, e.g., integer numbers, which do not change their value under smooth deformations of the space. Staying with the example of the paths of the particles in two dimensions – the winding number of a path is a topological invariant and counts how often one particle moves around the other particle. The winding number is integral and does not change if the path is deformed slightly. This fact hints at an interesting stability property of systems characterized by topological invariants. It turns out that manipulating Majorana based qubits via braiding acts in a parity subspace of the Hilbert space. As long as perturbations leave this subspace intact the quantum information is ‘topologically protected’. Furthermore the Majorana zero modes are usually non-local, i.e., spatially separated with an energy splitting exponentially suppressed by their distance. Hence local perturbations cannot couple and destroy the modes. While the extent of the topological protection is still unclear and as of now experimentally untested, the idea of protecting quantum information from environmental noise in this way is certainly interesting. Even if ultimately Majorana based qubits disqualify as practical qubit building blocks, it would be a huge achievement to show their non-abelian exchange statistics via braiding in experiment.

More general, a physical system in a topological phase can be characterized by a topological invariant, which can be a measurable quantity, if this quantity will not change in the presence of small perturbations. For example the topological invariant associated to a band structure will not change as long as no gap closings happen under perturbation. A probably familiar topological invariant, the genus  $g$  of a manifold, behaves similarly. The genus counts the number of handles of the geometric object, for example a sphere has  $g = 0$ , a torus  $g = 1$  and a pretzel  $g = 3$ . Even if the pretzel is deformed it is still a pretzel with  $g = 3$  as long as none of the holes is closed.

The presence of Majorana modes on the boundary of a solid state system is closely connected to a topological invariant of the system. In fact there is a topological invariant arising from the bulk band structure counting the number of Majorana modes. For a three-dimensional bulk system, in particular topological superconductors engineered from topological insulators, the modes live on the two-dimensional surface. Often systems of lower dimension are considered too, e.g., two dimensional thin films or one-dimensional nanowires. This bulk invariant is non-zero if the band structure is ‘twisted’ in a non-trivial way. This connection between modes on the boundary and bulk properties is commonly called the ‘bulk boundary correspondence’. The correspondence in the general case is conjectured and has not been rigorously proven. However for specific physical systems, e.g., a nanowire with Majorana bound states localized at the

ends of the chain, both the number of bound states and the invariant of the bulk band structure can be calculated explicitly, confirming the correspondence in this case.

The second ingredient of this work are interaction effects leading to ordering, in particular magnetic ordering. Interactions can induce correlations and can lead to a phase transition and stabilization of order, e.g., the ordering of adatom spins on a superconducting surface or the stabilization of a magnetic skyrmion texture. In particular we focus on heterostructures, which are composed of elementary subsystems, where magnetic order is induced by interactions. For example one of the heterostructures considered consists of a superconducting substrate, e.g., Pb, on which a chain of magnetic Fe adatoms is placed.

A phase transition might be associated with the breaking of symmetries, e.g., magnetic ordering breaks rotational symmetry. Symmetries are associated with conservation laws, but also play an important role as a tool in the phenomenological description of physical systems – often the knowledge of symmetries suffice to write useful low energy theories, e.g., Landau theories. Additionally to that, symmetries allow classifying Hamiltonian operators and restrict the geometric structure of the operator space. This geometric structure can then be analyzed using methods from topology. In this work we study the relationship between interactions, the resulting phase transitions, symmetries, and the topological structure for certain concrete models with connection to experiment.

In the following we outline the contents of the chapters of this thesis. The first two chapters lay the foundational basis. The succeeding three chapters are based on the main results of this PhD work. We study solid state systems which act as platforms for Majorana bound states and illuminate different aspects. While the systems considered don't look much alike at first sight, they share the property of intrinsic ordering induced by interactions. Furthermore the mathematical description of the low energy physics of such Majorana platforms is often identical and can be reduced to that of a prototypical model, a spinless p-wave superconductor in one dimension as introduced by Kitaev [8].

Chapter 1 introduces topological phases in condensed matter systems. We discuss the class of quantum Hall effects systems, which are topological insulators. In particular we describe the integer quantum Hall effect (IQHE), the quantum anomalous Hall effect (QAHE) and the quantum spin Hall effect (QSHE). The IQHE was the first effect understood in terms of a topological invariant, the TKNN number, named after Thouless, Kohmoto, Nightingale and de Nijs [9, 10]. Topological insulators are generally characterized by fermionic conducting surface modes, while the bulk is gapped and insulating. Similarly the bulk of topological superconductors is characterized by a superconducting gap, while the surface hosts Majorana modes. The occurrence of

topological phases relies on specific symmetries of the system. Phase transitions in the Landau sense often involve spontaneous breaking of symmetry. To shed light on the relation of phase transitions in the Landau sense and in the topological sense we compare the two mechanisms. Furthermore this chapter summarizes fundamentals about symmetries and the classification of topological phases in terms of symmetries and topological invariants. In particular we discuss the periodic table of topological insulators based on the Altland-Zirnbauer classification of random matrices [11, 12]. This classification by antiunitary symmetries is exhaustive and covers all kinds of non-interacting solid state systems. The table assigns to each symmetry class and dimension a label 0 for trivial classes and  $\mathbb{Z}$  and  $\mathbb{Z}_2$  for classes with possible non-trivial topological phases.

Chapter 2 gives an overview over Majorana fermions which appear as zero energy modes on the boundary of topological superconductors, e.g., at the ends of a 1D p-wave superconducting chain. We motivate their application in the area of topological quantum computing based on braiding operations. Majorana zero modes are created by field operators with the reality condition  $\gamma = \gamma^\dagger$ . To satisfy this condition, the Majorana operator  $\gamma$  is decomposed as  $\gamma = (c + c^\dagger)/2$  with a fermionic operator  $c$ . This implies that a Majorana zero mode in an electronic system is composed of an electron and a hole.

Chapter 3 is based on our publications Ref. [2, 3]. We consider magnetic adatom chains on top of a superconducting substrate. At the end of the chain Majorana bound states will occur. We study first the magnetic ordering of the spins of the adatoms due to an exchange interaction of the spins mediated by the superconducting substrate. Due to the presence of spin-orbit coupling this interaction can be effectively described by a Ruderman-Kittel-Kasuya-Yosida (RKKY) superexchange interaction. This type of interaction can lead to a spiral ordering. However in the presence of weak symmetry breaking due to crystal field effects, the interaction leads to ferromagnetic or antiferromagnetic ordering. In both ferromagnetic and antiferromagnetic chains, the low energy behavior is dominated by Yu-Shiba-Rusinov (YSR) states. The low energy YSR chain can show topological phases hosting one or two Majorana bound states per end of the chain, which possess a spin-content. This chapter focuses mostly on the transport signatures of the Majorana bound states in various setups. In particular we studied coupled Majorana states in multiple wires. Transport signatures of Majorana bound states are one of the main proposals to demonstrate the existence of Majorana bound states. In our work we explore the richer set of signatures due to

spin polarization if a spin-polarized scanning tunneling microscope tip is used for the transport measurements.

Chapter 4 is based on Ref. [1] and focuses on warped topological insulators and the formation of magnetic order on the surface of such an insulator. Usual 3D topological insulators host surface modes described by a rotationally symmetric Dirac dispersion. However due to crystal effects the dispersion can be modified by additional warping terms breaking the rotational symmetry to a discrete symmetry. In the case of  $\text{Bi}_2\text{Te}_3$ , the topological insulator considered mainly in this work, the symmetry is reduced to a  $C_{3v}$  point group symmetry. Time reversal and point group symmetry lead to a Fermi surface of hexagonal shape. Depending on the chemical potential  $\mu$ , which can be adjusted by doping the material, the curvature of the Fermi surface can be controlled. Around a certain chemical potential  $\mu_{\text{hex}}$  the Fermi surface takes approximately hexagonal shape with flat sides. In this scenario three nesting vectors  $\mathbf{Q}_{1,2,3}$  connect the sides of the Fermi surface resulting in a tendency of magnetic ordering. For this system, we showed that a skyrmion magnetic texture can be stabilized in the presence of a sufficiently strong repulsive Hubbard interaction.

Chapter 5 extends the previous chapter, by considering a heterostructure of a surface with a magnetic texture, e.g., the previously discussed skyrmion lattice, and a superconductor. We discuss feedback effects in both directions. The superconducting gap  $\Delta$  induced in the magnetic system by the superconducting proximity effect competes with the magnetic ordering and as such leads to a suppression of the magnetic gap. In the other direction supercurrent correlations and staggered superconducting order parameters are induced. The heterostructure forms a topological superconductor supporting chiral Majorana modes propagating along the one-dimensional boundary. Additionally, we show that up to three degenerate Majorana modes appear along a domain wall where  $B - \Delta$  changes sign. Here  $B$  is the intrinsic effective magnetic field of the magnetic layer in a proper normalization. The Majorana modes can propagate along the wall and form a flat band which is susceptible to remnant interaction effects. A related system is an anisotropic p-wave superconductor, which is a prototype for the study of flat bands in interacting systems.

Chapter 6 concludes and points out further directions of our research.



## List of publications

This thesis is based on the following publications:

- [1] Mendler, D., Kotetes, P. & Schön, G. Magnetic order on a topological insulator surface with warping and proximity-induced superconductivity. *Phys. Rev. B* **91**, 155405 (2015)
- [2] Heimes, A., Mendler, D. & Kotetes, P. Interplay of topological phases in magnetic adatom-chains on top of a Rashba superconducting surface. *New J. Phys.* **17**, 023051 (2015)
- [3] Kotetes, P., Mendler, D., Heimes, A. & Schön, G. Majorana fermion fingerprints in spin-polarised scanning tunnelling microscopy. *Physica E* **74**, 614 (2015)

Furthermore the thesis includes content from unpublished works. Some of the introductory content is based on my diploma thesis [4]. The figures published in Ref. [2] are open-access and licensed under Creative Commons Attribution 3.0 Unported (CC-BY) which allows reprint in this thesis. The figures from Ref. [1] with Copyright 2015 American Physical Society are reprinted with permission from the American Physical Society. The figures from Ref. [3] with Copyright 2015 Elsevier are reprinted with permission from Elsevier.



## Acknowledgments

I want to thank Professor Gerd Schön for the support and the opportunity to work on my PhD thesis at the Institute for Theoretical Solid State Physics and the Institute of Nanotechnology. I also want to thank Professor Alexander Mirlin for being the second referee of my thesis.

Then I want to thank Panagiotis Kotetes for the guidance and support during my diploma and PhD. Much of the work presented in this thesis is a result of the collaboration with him. I enjoyed our discussions and the time we worked together very much!

The atmosphere at the institute was pleasant and supportive. I want to thank the members of the TFP, in particular the other PhD students Iris Schwenk, Andreas Heimes, Thomas Hellmuth, Christian Karlewski, Jan Reiner, and Sebastian Zanker. I also enjoyed our activities very much, amongst other things, playing Basketball and Billard. Thanks go to Dmitri Golubev, Lingzhen Guo, Michael Marthaler and Andreas Poenicke. I also want to thank Kumar Ghosh, Elio König, Yang Lu, Pascal Nagel and Mathias Scheurer for our interdisciplinary seminar on topological phenomena in physics.

But most importantly, I want to thank all my friends and my family. Their support is invaluable. My parents Eva and Peter, my sister Lea and brother Julian are always there in case. Many thanks go to Kathi who supported me in many ways while I was writing the thesis.



# 1

## Chapter 1

---

# Introduction to topological phases of matter

In this chapter we introduce topological phases, which are a recent topic in physics and in particular in condensed matter physics, where effects like the quantum Hall effect and related experimentally accessible phenomena are mathematically described by using methods from topology. The field of topology studies geometric properties of spaces. Spaces can be classified by associated invariants which do not change under smooth deformations. In this chapter, we start first with examples of topological phases in condensed matter physics, i.e., topological insulators and topological superconductors, that can be described by topological invariants. Both insulators and superconductors commonly are gapped systems, i.e., the bulk band structure exhibits an energy gap  $\Delta$  in the spectrum and the Fermi energy  $E_F$  lies within this gap.

Topological insulators have the peculiar property of hosting conducting fermionic surface modes while still being insulating in the bulk due to the energy gap. As examples of topological insulators we describe the integer quantum Hall effect and the related effects with spin-dependence, the quantum anomalous Hall effect and quantum spin Hall effect. In contrast to topological insulators, topological superconductors host Majorana surface modes. They are described in a mathematically similar fashion, however involving particle-hole degrees of freedom.

After introducing topological phases, we compare them to phases according the Landau paradigm of phases and transitions. Instead of considering topological invariants, such phase transitions are characterized by the presence of order parameters. Often phase transitions involve the breaking of symmetries, such that after the phase transition the system exhibits fewer symmetries.

We proceed with the discussion of the classification of topological phases relying on the presence of antiunitary symmetries. In particular we are interested in the topology of the space of Hamiltonian operators defined on a Brillouin zone  $\widehat{\mathcal{H}}(\mathbf{k})$ .

## 1.1 Topological insulators and superconductors

In this section we introduce topological insulators, which are materials, that are insulating in the bulk while hosting conducting fermionic surface modes. Similarly there are topological superconductors which also exhibit a bulk gap and as such can be treated and classified in a similar manner as the topological insulators. Since there exist multiple extensive and accessible reviews for topological insulators [13, 14] and topological superconductors [14, 15] we only shortly review the most important topological phases in a pedagogical manner. Topological systems exist in multiple dimensions. At first we discuss the two-dimensional quantum Hall systems.

### 1.1.1 Quantum Hall effect

The integer quantum Hall effect (IQHE) was discovered by von Klitzing in 1980 [16]. In contrast to the classical Hall effect with Hall resistance linear in the field strength, for small temperatures and strong magnetic fields the Hall conductivity shows exactly quantized plateaus, i.e.,

$$\sigma_{xy} = \frac{e^2}{h} \nu, \quad (1.1)$$

where  $\nu$  is an integer as shown in Fig. 1.1. Shortly thereafter scenarios were discovered where  $\nu$  takes specific rational values, e.g.,  $\nu = 1/3$ , giving rise to the fractional quantum Hall effect [17]. This effect can be understood by assuming that the relevant excitations are fractionalized by interaction effects.

The experimental setup of the IQHE consists of a small 2D sample in the  $xy$ -plane with a perpendicular magnetic field  $B_z$  restricting the electrons effectively to the  $xy$ -plane. Furthermore there is an electric field  $\mathbf{E}$  in  $x$ -direction leading to an electron flow with constant current  $I$ . The Hall effect manifests itself in a Hall voltage  $V_H$  induced in  $y$ -direction between the two sides of the sample.

Classically, the electrons flowing are deflected due to the Lorentz force, following a Drude equation of motion in equilibrium

$$0 = m\dot{\mathbf{v}} = e\mathbf{E} + e\mathbf{v} \times \mathbf{B} - \frac{m\mathbf{v}}{\tau} \quad (1.2)$$

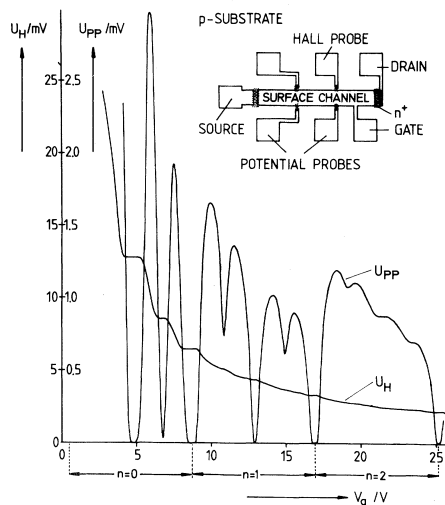


Figure 1.1: Original measurements of the Hall voltage  $U_H$  and voltage drop between potential probes  $U_{pp}$  over the gate voltage  $V_g$ . Temperature  $T = 1.5$  K, source drain current  $I = 1 \mu\text{A}$ , magnetic field  $B = 18$  T. Reprinted from Ref. [16] with permission by the American Physical Society, copyright 1980.

with electron charge  $e$ , velocity  $\mathbf{v}$  and scattering time  $\tau$ . Introducing the current density  $\mathbf{J} = ne\mathbf{v}$  yields Ohm's law  $\mathbf{J} = \sigma\mathbf{E}$  where  $\sigma$  is a  $2 \times 2$  conductivity tensor<sup>1</sup>. The transverse resistance  $R_{xy} = V_y/I_x = \rho_{xy} = B/(ne)$  is independent of the sample size and linear in the field strength  $B$ . The dependence on  $B$  contradicts the experimental result in the quantum regime, where the quantization of the energy levels of the electrons in the magnetic field must be considered. The minimally coupled Hamiltonian  $H_0 = (\mathbf{p} + e\mathbf{A})^2/(2m)$  with magnetic field  $\mathbf{B} = \nabla \times \mathbf{A}$ , no electric field  $\mathbf{E} = 0$  and vector potential in the Landau gauge  $\mathbf{A} = xB_z\hat{\mathbf{e}}_y$  reduces to the Hamiltonian of the harmonic oscillator with the Landau energy levels  $E_n = \hbar\omega_C(n + 1/2)$  and cyclotron frequency  $\omega_C = eB/m$ . The number of filled Landau levels below the Fermi level  $E_F$  is then observable in experiment for sufficiently low temperature  $k_B T \ll \hbar\omega_C$ . Since  $[p_y, H] = 0$  the Landau levels are highly degenerate. This degeneracy is lifted by an electric field, which leads to a drift of the states in  $y$ -direction.

The Hall conductivity is derived within linear response theory [18]. The unperturbed Hamiltonian  $H_0$  with the states  $|n\rangle$  given by  $H_0|n\rangle = E_n|n\rangle$  is extended with a term  $\delta H = -\mathbf{J} \cdot \mathbf{A}$  with  $\mathbf{E} = -\partial_t \mathbf{A}$ . One proceeds by calculating the expectation value  $\langle \mathbf{J}(t) \rangle$  of the current operator for an AC field  $\mathbf{E}(t) = \mathbf{E}e^{-i\omega t}$ . The expectation value is

<sup>1</sup>In experiment resistances  $R_{ij} \propto \rho_{ij}$  are measured, where  $\rho = \sigma^{-1}$  is the resistivity tensor.

given by

$$\langle J_i(t) \rangle = \frac{1}{\hbar\omega} \int_0^\infty dt' e^{i\omega t'} \langle 0 | [J_j(0), J_i(t')] | 0 \rangle E_j e^{-i\omega t}, \quad (1.3)$$

which shows linear response behavior, i.e., the current oscillates with the same frequency  $\omega$  as the applied electric field [18]. From there one obtains the Kubo formula for the Hall conductivity

$$\sigma_{xy}(\omega) = \frac{1}{\hbar\omega} \int_0^\infty dt e^{i\omega t} \langle 0 | [J_y(0), J_x(t)] | 0 \rangle. \quad (1.4)$$

Taking the DC limit  $\omega \rightarrow 0$  yields

$$\sigma_{xy} = \frac{i}{\hbar} \sum_{E_n < E_F < E_m} \frac{\langle n | J_y | m \rangle \langle m | J_x | n \rangle - \langle n | J_x | m \rangle \langle m | J_y | n \rangle}{(E_n - E_m)^2}. \quad (1.5)$$

Here it is non-obvious that the conductivity is an integer. Rewriting the current operators as  $J_i = ev_i$  and the velocities in terms of derivatives of the Hamiltonian, as in the seminal work by Thouless, Kohmoto, Nightingale and de Nijs [9, 10], allows to express the Hall conductivity in terms of a topological invariant, the first Chern number, which is an integer. We will discuss the topological invariant later in Section 1.3.3. The quantum Hall effect goes hand in hand with the appearance of chiral edge currents, which are intuitively understood by skipping orbits. In modern terminology the appearance of edge currents is seen as a realization of the bulk-boundary correspondence, discussed in Section 1.3.4.

### 1.1.2 Quantum anomalous Hall effect

In contrast to the integer quantum Hall effect, the quantum anomalous Hall effect (QAHE) does not rely on the presence of a magnetic field. The Hall conductivity  $\sigma = \nu e^2/h$  is still quantized with an integer  $\nu$ , which appears due to the intrinsic topological structure of the band structure of the material, instead of the topological structure created in an IQHE experiment by the magnetic field and the resulting Landau levels. Like the IQHE, the QAHE corresponds to the presence of chiral edge channels, implying that time reversal symmetry is broken. The first model showing a QAHE was the Haldane model on the honeycomb lattice [19]. However the essential physics is already captured by a simple two band model in two dimensions of the form  $\hat{\mathcal{H}}(\mathbf{k}) = \mathbf{g}(\mathbf{k}) \cdot \boldsymbol{\sigma}$  where  $\mathbf{g}$  is the configuration vector of the Hamiltonian defined on the two-dimensional Brillouin zone and  $\boldsymbol{\sigma} = (\sigma_x, \sigma_y, \sigma_z)$  are the Pauli matrices. The

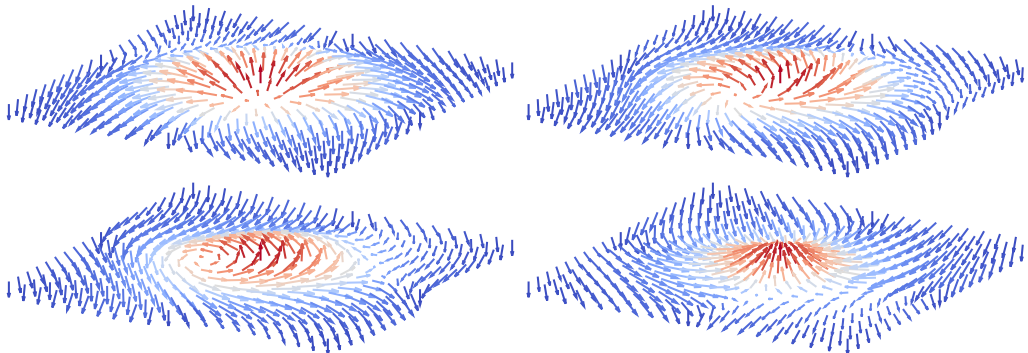


Figure 1.2: Skyrmion configuration  $\mathbf{g}(\mathbf{k}) = (\sin k_x, \sin k_y, \cos k_x + \cos k_y - 1)^\top$  defined on the torus  $\mathbb{T}^2 = [-\pi, \pi]^2$  with topological invariant  $C_1 = 1$ . We show different rotations  $0, \pi/4, \pi/2$  and  $\pi$  of the normalized vectors  $\hat{\mathbf{g}}(\mathbf{k})$  around the  $z$ -axis, since the Hamiltonian has a rotational gauge symmetry. Opposite sides of the plots are identified due to the torus topology.

configuration vector is given by

$$\mathbf{g}(\mathbf{k}) = (A \sin k_x, A \sin k_y, B(\cos k_x + \cos k_y - M))^\top \quad (1.6)$$

where  $A, B$  and  $M$  are material parameters. For a realistic system a full band structure could be obtained by density functional theory. The effective model is usually obtained from there by projecting to the lowest two bands. For this system the zero temperature Kubo formula of the Hall conductivity reduces to

$$\sigma_H = \frac{e^2}{h} \frac{1}{4\pi} \int d\mathbf{k} \hat{\mathbf{g}} \cdot (\partial_{k_x} \hat{\mathbf{g}} \times \partial_{k_y} \hat{\mathbf{g}}) \quad (1.7)$$

with the unit configuration vector  $\hat{\mathbf{g}} = \mathbf{g}/|\mathbf{g}|$ . This integral equation is the first Chern number (see Section 1.3.3), which counts the number of windings of the vector  $\hat{\mathbf{g}}$  on the Brillouin zone. In particular the conductivity does not change under smooth deformations of  $\mathbf{g}$ , as long as no gap closing happens. For example a gap closing at  $\mathbf{k} = 0$  occurs for  $M = 2$ . Furthermore the conductivity is independent of the length of the configuration vector  $|\mathbf{g}(\mathbf{k})|$ , corresponding to the energy scale.

For a non-zero value of  $\sigma_H$  the configuration vector forms a skyrmion. Skyrmions were proposed first by T. Skyrme in high energy physics as a unified theory for strongly interacting particles [20]. We display a trivial and non-trivial configuration of the configurations vectors in Fig. 1.2. The transition between the non-trivial skyrmion phase and the trivial phase is a topological phase transition which coincides with a gap closing in the band structure. The  $k$ -points with possible gap closings correspond to

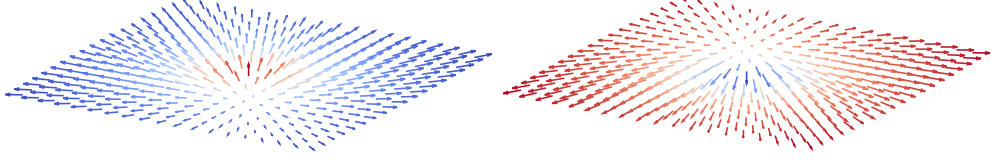


Figure 1.3: Meron  $\mathbf{g}_+$  and anti meron  $\mathbf{g}_-$  configurations for the linear model  $\mathbf{g}_\pm(\mathbf{k}) = (k_x, k_y, \pm 1)$  with topological charge  $C_1 = \pm 1/2$ . The plots show the normalized vectors  $\hat{\mathbf{g}}_\pm(\mathbf{k})$ .

the critical low-energy points of the systems. They suffice to determine the parameter values at which topological phase transitions occur. In the above Hamiltonian gap closings  $\mathbf{g}(\mathbf{k}) = 0$  occur for  $M = 0, \pm 2$ . For  $M = -2$  the critical point is  $\Gamma = (0, 0)$ , for  $M = 0$  one finds  $X = (\pi, 0)$  and  $Y = (0, \pi)$  and for  $M = 2$  a gap closing can occur at  $Z = (\pi, \pi)$ . Interestingly the low energy behavior around these points also determines the topological invariant of the full system. This can be seen by considering the linearized Hamiltonians around the critical points

$$\mathbf{g}_\Gamma(\mathbf{k}) = (Ak_x, Ak_y, B(2 - M))^\top, \quad (1.8)$$

$$\mathbf{g}_X(\mathbf{k}) = (-Ak_x, Ak_y, -BM)^\top, \quad (1.9)$$

$$\mathbf{g}_Y(\mathbf{k}) = (Ak_x, -Ak_y, -BM)^\top, \quad (1.10)$$

$$\mathbf{g}_Z(\mathbf{k}) = (-Ak_x, -Ak_y, -B(2 + M))^\top. \quad (1.11)$$

Integrating the Chern integral for each of the points  $p = \Gamma, X, Y, Z$  on the whole real plane yields a value  $C_{1,p} = \pm 1/2$ , corresponding to half a skyrmion or a so-called meron. Summing up the local half-integer invariants yields the invariant of the full system  $C_1 = \sum_{p=\Gamma, X, Y, Z} C_{1,p}$ . We illustrate the merons in Fig. 1.3.

### 1.1.3 Quantum spin Hall effect

In contrast to the QAHE, the quantum spin Hall effect (QSHE) shows helical edge channels, leading to a spin current. There exists one channel per spin with the electrons of the two channels flowing in opposite direction, i.e., the channels show spin momentum locking. Hence the QSHE can essentially be described as two copies of the QAHE. While a single conducting chiral channel breaks time-reversal symmetry, two chiral channels forming helical channels preserve time reversal symmetry. We illustrate the distinction in Fig. 1.4.

The QSHE was first proposed for graphene [22, 23], but was not observed due to weak spin orbit coupling. Later the QSHE was proposed for HgTe quantum wells [24, 25] and

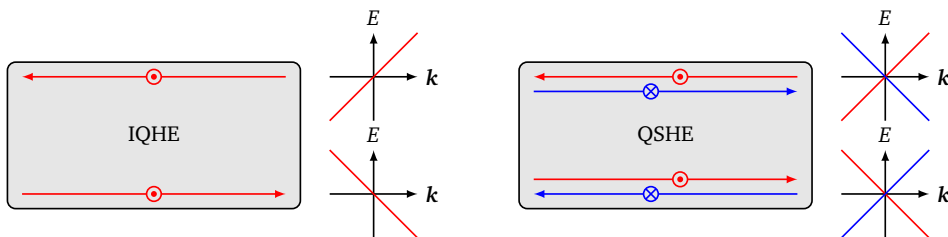


Figure 1.4: Integer quantum Hall effect and quantum spin Hall effect in comparison (adapted from Ref. [21]). The integer quantum Hall effect shows chiral edge modes, while the quantum spin Hall effect shows helical edge modes made up from two chiral edge modes each.

discovered [26]. The experimental setup consists of a HgTe well of thickness  $d$  which is sandwiched between two CdTe layers. As long as  $d > d_C$  with some critical thickness  $d_C$ , the QSHE is observable. The two materials HgTe and CdTe are both described by effective models with six bands. At the interface between the two materials there is a band inversion of two bands which leads to non-trivial behavior. Essentially the band structure of the whole setup acquires a non-trivial topological winding<sup>2</sup>. The projected model with four bands takes the form

$$\hat{\mathcal{H}}(\mathbf{k}) = \begin{pmatrix} \hat{h}_\uparrow(\mathbf{k}) & 0 \\ 0 & \hat{h}_\downarrow(\mathbf{k}) \end{pmatrix}, \quad (1.12)$$

$$\hat{h}_\sigma(\mathbf{k}) = \epsilon(\mathbf{k}) + \mathbf{g}_\sigma(\mathbf{k}) \cdot \boldsymbol{\rho}, \quad (1.13)$$

where  $\boldsymbol{\rho}$  are Pauli matrices. Symmetry analysis determines the configuration vector and dispersion at lowest order in terms of the harmonics

$$\epsilon(\mathbf{k}) = C + D(\cos k_x + \cos k_y), \quad (1.14)$$

$$\mathbf{g}_\sigma(\mathbf{k}) = (\sigma A \sin k_x, A \sin k_y, B(\cos k_x + \cos k_y - M))^T. \quad (1.15)$$

The configuration vector per spin is equivalent to the QAHE model, showing that indeed the QSHE consists of two copies of the QAHE. The parameters  $A$ ,  $B$ ,  $C$ ,  $D$  and  $M$  are given by the materials and the setup. For example  $M$  corresponds the thickness  $d$  of the quantum well. The block diagonal form of the Hamiltonian ensures that time

<sup>2</sup>See also Fig. 2.5 for an illustration of the winding of a band structure in the context of the Kitaev chain

reversal symmetry is preserved. The first Chern number per block is defined by

$$C_1^\sigma = \frac{1}{4\pi} \int_{\text{BZ}} dk_x dk_y \hat{\mathbf{g}}_\sigma \cdot \left( \partial_{k_x} \hat{\mathbf{g}}_\sigma \times \partial_{k_y} \hat{\mathbf{g}}_\sigma \right), \quad (1.16)$$

which is proportional to the conductivity  $\sigma_{xy}^\sigma$  per spin. Due the block diagonal form of the Hamiltonian  $\hat{\mathcal{H}}(\mathbf{k})$  the charge conductivity  $\sigma_{xy}^C = \sigma_{xy}^\uparrow + \sigma_{xy}^\downarrow = 0$  vanishes. However the difference of the conductivities  $\sigma_{xy}^S = \sigma_{xy}^\uparrow - \sigma_{xy}^\downarrow = 2\sigma_{xy}^\uparrow$  can be non-zero. This sum does not yet capture the topological phase of the QSH system since an even number of helical edge modes hybridizes by scattering at non-magnetic impurities, corresponding to additional off-block diagonal Hamiltonian terms. Only the case of an odd number of edge channels the system is topologically non-trivial. Therefore the topological phase of the system is described by a  $\mathbb{Z}_2$  invariant, i.e.,  $C_1^\uparrow = 0, 1 \pmod{2}$ .

#### 1.1.4 Topological superconductors

After discussing examples of topological insulators, we proceed with topological superconductors, which similarly exhibit a bulk gap. Furthermore the bands of the superconductor must allow the definition of a non-zero topological invariant, requiring non-trivial winding in the band structure. As in the case of topological insulators there are in-gap states localized at the boundary, which determine the low-energy physics. However in contrast to the topological insulators with fermionic boundary states, the boundary states of topological superconductors can be Majorana states due to the particle-hole degree of freedom in the system. We discuss zero-energy Majorana states in Chapter 2 in detail. Here we shortly connect topological insulators and superconductors to put them into context.

There are multiple classes of topological superfluids distinguishable by their symmetry properties. The first topological superfluid, discussed by Volovik, was He-3B [27]. The class of chiral p-wave superconductors with  $p_x + ip_y$  pairing in two dimensions supports chiral edge modes which propagate at an edge in one direction. Essentially one considers the model of the QAHE discussed before with the configuration vector

$$\mathbf{g}(\mathbf{k}) = (A \sin k_x, A \sin k_y, B(\cos k_x + \cos k_y - M))^T \quad (1.17)$$

and Hamiltonian  $\hat{\mathcal{H}}(\mathbf{k}) = \mathbf{g}(\mathbf{k}) \cdot \boldsymbol{\tau}$  defined in particle-hole space  $\boldsymbol{\tau}$ . The observable difference is that the edge modes in topological superconductors have Majorana character, which correspond to Majorana operators with the property  $\gamma_{\mathbf{k}} = \gamma_{-\mathbf{k}}$ . In solid state physics, the existence of intrinsic p-wave superconductivity is discussed for the ruthen-

ates [28]. However there are possibilities to artificially engineer p-wave superconductors from trivial superconductors, which will be discussed in Section 2.3.

Similar to  $p_x + ip_y$  superconductors with angular momentum  $l = 1$  there exist system with other types of unconventional superconductivity, for example the class of chiral d-wave superconductors with  $d_{x^2-y^2} \pm id_{xy}$  pairing with higher angular momentum  $l = 2$  but similar topological properties.

Dimensionally reducing the  $p_x + ip_y$  superconductor by one dimension yields a 1D spinless p-wave superconductor. We discuss this important model, called the Kitaev chain in Section 2.3.1. There are multiple systems which behave according to the Kitaev chain, namely 1D organic superconductors and polymers. Again there are ways to artificially realize 1D or quasi-1D p-wave models from well-understood building blocks (See Section 2.3).

After introducing topological phases we proceed with a discussion of phase transitions and symmetries which play a crucial role for the topological classification of solid state systems.

## 1.2 Phase transitions and symmetries

Symmetries play a crucial role for the characterization of physical systems. In this thesis we rely on symmetry analysis at many places such that a short review of some important symmetries is appropriate. In particular the classification of topological systems relies on the presence of certain symmetries as discussed in Section 1.3. There are certain ways to categorize symmetries, e.g., continuous or discrete symmetries. On the other hand one can consider internal symmetries of a system or space-time symmetries. Continuous symmetries are intimately related to conservation laws according to Noether's theorem.

A class of symmetries with a significant role in modern physics are gauge symmetries which are redundancies in the mathematical description. However the word redundancy is downplaying the significance since local gauge invariance gives rise to gauge fields and in the quantized version to gauge bosons. One of the best known examples is the gauge symmetry of Maxwell's equation where the equations stay invariant under a gauge transformation of the vector potential  $\mathbf{A} \rightarrow \mathbf{A} + \nabla f$  and the scalar potential  $\phi \rightarrow \phi - \partial_t f$  with a function  $f(\mathbf{r}, t)$ . An example in condensed matter physics is the U(1) gauge symmetry of a superconductor, which is broken in the superconducting phase.

In particular, in condensed matter discrete symmetries are omnipresent. The repetitive structure of crystals leads to discrete translational and rotational symmetries,

which break the continuous symmetries of the vacuum. However in contrast to fully disordered matter, the symmetries are not fully broken, but discrete symmetries are retained. The schema of allowed symmetries leads to a classification of all possible crystal structures, the so-called Bravais lattices. These lattices in two (three) dimensions are connected to their respective wallpaper (space) groups. We will describe point groups and other the spatial symmetries and their action on Hamiltonians in the Bogoliubov-de Gennes formalism in Section 1.2.2. Furthermore there are discrete symmetries with only one generator, e.g., inversion symmetry  $\mathcal{I}$ , time reversal symmetry  $\mathcal{T}$  or charge conjugation symmetry  $\mathcal{C}$ .

In the next section we relate symmetries to their role in classical phase transitions according to the Landau paradigm.

### 1.2.1 The Landau paradigm of phase transitions

Second order phase transitions are connected to the breaking of symmetries and the presence of an order parameter which changes continuously. There are also first order phase transitions where an order parameter of the system does not change continuously but changes abruptly and non-continuously. First order transitions are not necessarily connected to spontaneous symmetry breaking as for example the liquid-gas phase transition. Nonetheless, symmetries play a crucial role for the description of phases. The classification of topological phases also relies on symmetries – this means that spontaneous symmetry breaking can change the topological class of a system.

Interactions are crucial to derive phase transitions within a Landau theory picture. The starting point is a model Hamiltonian  $\mathcal{H}_0$  extended with interactions terms. In a tight-binding model the interactions commonly considered include on-site Hubbard repulsion  $\mathcal{H}_U = U \sum_i n_{i\uparrow} n_{i\downarrow}$  due to Coulomb interaction, or more general density-density interaction  $\mathcal{H}_V = \sum_{i \neq j} V_{ij} n_i n_j$  and spin-spin interaction  $\mathcal{H}_J = \sum_{ij} J_{ij} \mathbf{S}_i \cdot \mathbf{S}_j$ . The operators  $n_\sigma = c_{i\sigma}^\dagger c_{i\sigma}$  are number operators and  $S_i$  is a spin operator. In this thesis we rely on a spin-spin exchange interaction leading to an RKKY interaction between spins in Chapter 3 and on on-site Hubbard repulsion in Chapter 4. In both cases the interactions lead to magnetic ordering.

The ordering is described by an order parameter which arises due to mean-field decoupling. In this approximation the quartic interaction terms are expressed as product of an order parameter and two field operators. For example the effective interaction of a spinless p-wave superconductor in one dimension  $-V \sum_{k,k'} \sin k \sin k' \psi_k^\dagger \psi_{-k}^\dagger \psi_{-k'} \psi_{k'}$  can be written in the approximate form  $\Delta \sum_k \sin k \psi_k^\dagger \psi_{-k}^\dagger$ . The order parameter

$\Delta$  for the superconducting gap is introduced by the self-consistency equation  $\Delta = -V \sum_k \sin k \langle \psi_{-k} \psi_k \rangle$ . Products of fluctuations  $\psi_k^\dagger \psi_{-k}^\dagger - \langle \psi_k^\dagger \psi_{-k}^\dagger \rangle$  have been neglected.

Note that there are multiple ways to decouple an interaction by reordering the field operators using commutator relations. In this example the effective interaction was already written to obtain the p-wave order parameter directly. This way mean field theory can give rise to a plethora of different order parameters corresponding to many different phases. To determine the possible ground state of system one proceeds by deriving a Landau theory by expanding the free energy of the system as a polynomial in the order parameters. The minimum of the free energy determines then the physical ground state. In this state some of the order parameters can be non-zero. The coefficients of the polynomial can be derived microscopically as for example in Chapter 4. However in many cases it is also possible to propose a Landau theory purely by symmetry considerations. The Landau theory has to preserve the symmetries of the given Hamiltonian. However the ground state can have reduced symmetry, the effect of spontaneous symmetry breaking. A ferromagnet for example breaks rotational symmetry after choosing a specifically oriented ground state.

Spontaneous symmetry breaking is a fundamental principle in modern physics and strongly connected to the Landau picture of phase transitions. Recently the discovery of the Higgs boson at CERN got lots of attention, which is connected to the spontaneous symmetry breaking of the electroweak gauge symmetry  $SU(2)_L \otimes U(1)_Y$  to the lower electromagnetic gauge symmetry  $U(1)_Q$ . According to the Goldstone theorem the spontaneous breaking of a continuous symmetry results in massless Goldstone bosons. The occurrence of Goldstone bosons can for example be seen when a system becomes magnetic. In Chapter 4 we consider a system developing a skyrmion texture as a linear combination of three helical spin density waves. The skyrmion texture breaks the continuous translational symmetry to a discrete translational symmetry. Two phase degrees of freedom, so called phasons, remain as massless Goldstone bosons. However in the case of a broken gauge symmetry the Goldstone degrees of freedom are ‘eaten’ by the gauge bosons as predicted by Anderson for superconductors and by Higgs for the electroweak theory, giving rise to massive Higgs bosons.

### 1.2.2 Spatial symmetries: Inversion, translation, rotation and point group symmetries

Spatial symmetries play a crucial role in the study of solid state systems since essentially the ‘background’ is determined by the crystalline structure of the material under

Table 1.1: Crystallographic point groups in Schoenflies notation.  $C_n$  are the cyclic groups.  $C_{nh}$  contains  $C_n$  and adds a reflection plane perpendicular to the rotation axis.  $C_{nv}$  contains  $C_n$  and adds reflection planes parallel to the rotation axis.  $D_n$  are the dihedral groups.  $S_{2n}$  contain only a  $2n$ -fold rotation-reflection axis. Missing in the table are the tetrahedral and octohedral groups  $T$ ,  $T_d$ ,  $T_h$ ,  $O$  and  $O_h$ . Counting all the groups yields 32 crystallographic point groups in total.

n	1	2	3	4	6
$C_n$	$C_1$	$C_2$	$C_3$	$C_4$	$C_6$
$C_{nv}$	$C_{1v} = C_{1h}$	$C_{2v}$	$C_{3v}$	$C_{4v}$	$C_{6v}$
$C_{nh}$	$C_{1h}$	$C_{2h}$	$C_{3h}$	$C_{4h}$	$C_{6h}$
$D_n$	$D_1 = C_2$	$D_2$	$D_3$	$D_4$	$D_6$
$D_{nh}$	$D_{1h} = C_{2v}$	$D_{2h}$	$D_{3h}$	$D_{4h}$	$D_{6h}$
$D_{nd}$	$D_{1d} = C_{2h}$	$D_{2d}$	$D_{3d}$	$D_{4d}$	$D_{6d}$
$S_{2n}$	$S_2$	$S_4$	$S_6$	$S_8$	$S_{12}$

consideration. For simplicity, we exclude quasicrystals [29, 30] and amorphous materials with fewer symmetries from the discussion.

The crystal structures are classified in different classes by the Bravais lattices. The real space periodicity gives rise to Brillouin zones according to Bloch. Additional to the translation symmetries there are symmetries given by the a point group. Point groups are generated by rotation and reflection operations. The rotation operations are defined for fixed rotation axes and discrete angles. In particular for 2D coverings only 2-, 3-, 4- or 6-fold rotations are allowed. The combined rotation and translation symmetry groups yield the full space group.

As first spatial symmetry operation we discuss the inversion operation  $\mathcal{I}$ , which is often part of point groups.  $\mathcal{I}$  inverts spatial coordinates  $\mathbf{r} \mapsto -\mathbf{r}$ . In contrast to inversion parity operations are defined via  $\det \mathcal{P} = -1$ . In odd dimensions inversion is a parity operation but not in even dimensions. The actions of inversion symmetry on quantum mechanical operators for position  $\hat{\mathbf{r}}$ , momentum  $\hat{\mathbf{p}}$  and spin operator  $\hat{\mathbf{S}}$  are given by

$$\mathcal{I}^\dagger \hat{\mathbf{r}} \mathcal{I} = -\hat{\mathbf{r}}, \quad \mathcal{I}^\dagger \hat{\mathbf{p}} \mathcal{I} = -\hat{\mathbf{p}}, \quad \mathcal{I}^\dagger \hat{\mathbf{r}} \times \hat{\mathbf{p}} \mathcal{I} = +\hat{\mathbf{r}} \times \hat{\mathbf{p}}, \quad \mathcal{I}^\dagger \hat{\mathbf{S}} \mathcal{I} = +\hat{\mathbf{S}}. \quad (1.18)$$

Given a single-particle state  $|\mathbf{k}, \sigma, \nu\rangle$  with wavevector  $\mathbf{k}$ , spin  $\sigma$  which is an eigenvalue of  $\hat{S}_z$  and orbital quantum number  $\nu$ , the inversion symmetry acts as  $\mathcal{I}|\mathbf{k}, \sigma, \nu\rangle = \eta_\nu |-\mathbf{k}, \sigma, \nu\rangle$ . Here  $\eta_\nu = \langle \mathbf{k}, \sigma, \nu | \mathcal{I} | \mathbf{k}, \sigma, \nu \rangle$  is the intrinsic parity of the orbital which is  $\eta_\nu = 1$  in even dimension and can be either even  $\eta_\nu = +1$  or odd  $\eta_\nu = -1$  in odd

dimension since  $\mathcal{I}^2 = 1$ . A Hamiltonian transforms under inversion as

$$\widehat{\mathcal{H}}(\mathbf{k})' = \mathcal{I}^\dagger \widehat{\mathcal{H}}(\mathbf{k}) \mathcal{I} = \hat{\eta} \widehat{\mathcal{H}}(-\mathbf{k}) \hat{\eta}. \quad (1.19)$$

In this work we consider Bogoliubov-de Gennes (BdG) Hamiltonians, which act in particle-hole space in order to represent superconducting terms. By convention, the  $\boldsymbol{\tau} = (\tau_x, \tau_y, \tau_z)$  Pauli matrices span particle-hole space. Given the inherent particle-hole symmetry (and inversion of momenta) of a BdG Hamiltonian, inversion can also be represented as

$$\widehat{\mathcal{H}}(\mathbf{k})' = \mathcal{I}^\dagger \widehat{\mathcal{H}}(\mathbf{k}) \mathcal{I} = -\tau_x \widehat{\mathcal{H}}^\Gamma(\mathbf{k}) \tau_x. \quad (1.20)$$

If additionally to inversion, more spatial symmetry operations like reflections and rotations are considered, the set of symmetries can be combined in a finite group, the point group.

We show a subset of the most important point groups in Table 1.1, where the groups are labeled according the Schoenflies notation. As noted before the point group is a subgroup of the space group which includes translations. In tight binding models, where continuous translational symmetry is broken, the discrete translational symmetry of the space group is significant. However in the case of bulk models the point group by itself can provide important insights.

In the case of a BdG Hamiltonian point group operations act on both the momentum vector and the spinor components in the presence of strong spin orbit coupling

$$\widehat{\mathcal{H}}(\mathbf{k})' = \mathcal{G}_i^\dagger \widehat{\mathcal{H}}(\mathbf{k}) \mathcal{G}_i = \widehat{D}^\dagger(\mathcal{G}_i) \widehat{\mathcal{H}}(\mathcal{G}_i \mathbf{k}) \widehat{D}(\mathcal{G}_i). \quad (1.21)$$

The vector  $\mathbf{k}$  is rotated or reflected and the representations  $\widehat{D}(\mathcal{G}_i)$  transform the spinor space. The representation  $\widehat{D}(\mathcal{G}_i)$  is trivial if the system does not have orbital or spin degrees of freedom. This is the case for a low energy model in the presence of a strong Zeeman field fixing the spin direction.

A representation  $\widehat{D}_i$  is a mapping from the group elements to invertible matrices of some dimension, i.e., the representation of a group element  $\mathcal{G}_n$  is a matrix  $\widehat{D}_i(\mathcal{G}_n)$ . A representation is defined as a group homomorphism, i.e.,  $\widehat{D}_i(\mathcal{G}_n \cdot \mathcal{G}_m) = \widehat{D}_i(\mathcal{G}_n) \cdot \widehat{D}_i(\mathcal{G}_m)$ . The significance of representations lies in the fact that they can be built up from irreducible representations (IRs) with the one-dimensional representations being the most basic representations. Two irreducible representations can be combined as a direct sum to form a higher dimensional reducible representation  $\widehat{D} = \widehat{D}_1 \oplus \widehat{D}_2$ .

Table 1.2: Character table of the dihedral point group  $D_{4h}$  which consists of rotations and reflections. See Fig. 1.5 for a visualization.

I.R.	$E$	$2C_4$	$C_2$	$2C'_2$	$2C''_2$	$\mathcal{I}$	$2S_4$	$\sigma_h$	$2\sigma_v$	$2\sigma_d$	Linear	Higher
$A_{1g}$	+1	+1	+1	+1	+1	+1	+1	+1	+1	+1	$R_z$	$x^2 + y^2, z^2$
$A_{2g}$	+1	+1	+1	-1	-1	+1	+1	+1	-1	-1		$xy(x^2 - y^2)$
$B_{1g}$	+1	-1	+1	+1	-1	+1	-1	+1	+1	-1		$x^2 - y^2$
$B_{2g}$	+1	-1	+1	-1	+1	+1	-1	+1	-1	+1		$xy$
$E_g$	+2	0	-2	0	0	+2	0	-2	0	0		$(R_x, R_y)$
$A_{1u}$	+1	+1	+1	+1	+1	-1	-1	-1	-1	-1	$z$	$xyz(x^2 - y^2)$
$A_{2u}$	+1	+1	+1	-1	-1	-1	-1	-1	+1	+1		
$B_{1u}$	+1	-1	+1	+1	-1	-1	+1	-1	-1	+1		$xyz$
$B_{2u}$	+1	-1	+1	-1	+1	-1	+1	-1	+1	-1		$z(x^2 - y^2)$
$E_u$	+2	0	-2	0	0	-2	0	+2	0	0		$(x, y)$

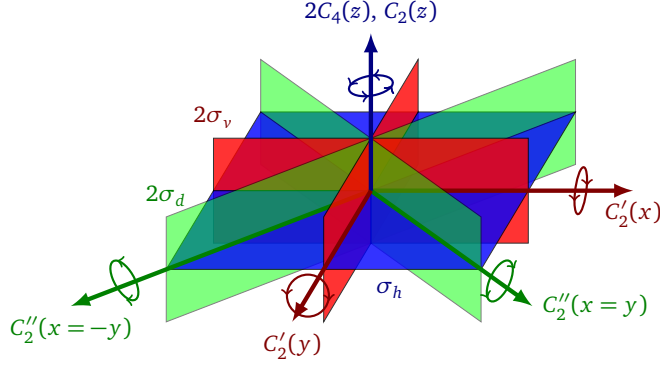
Given a representation one can define characters by tracing  $\chi_i(\mathcal{G}_n) = \text{tr } \hat{D}_i(\mathcal{G}_n)$ . The characters of group generators are summarized in a character table. Generators are the elements which span the group, e.g., for  $C_{3v}$ , the  $C_3$  rotation generates the  $C_3^2$  rotation. The construction of character tables relies on the great orthogonality theorem [4, 31].

To illustrate, we will consider the character table of the point group  $D_{4h}$ . The table is presented in Table 1.2, and the corresponding operations are illustrated in Fig. 1.5. The first column is the name of the IR. In the Mullikan nomenclature,  $A$  and  $B$  are used for one-dimensional representations and  $E$  is used for two-dimensional representations. The subscript  $g$  or  $u$  means ‘gerade’ or ‘ungerade’ which characterize the behavior under inversion  $\mathcal{I}$ . The last two columns list basis functions transforming under the given transformation. The row  $A_{1g}$  contains the trivial representation with  $D_{A_{1g}}(\mathcal{G}_i) = \chi_{A_{1g}}(\mathcal{G}_i) = 1$ . The function  $x^2 + y^2$  belongs to the trivial representation since it is invariant under the group operations. Rotations  $R_{x,y,z}$  which are pseudovectors are included in the column of the linear basis functions.

### 1.2.3 Antiunitary symmetries: Time reversal and charge conjugation

We review two important antiunitary symmetries, which are defined as a product of complex conjugation  $\mathcal{K}$  and a unitary operator  $U$ . Complex conjugation acts on complex numbers  $\mathcal{K}^\dagger z \mathcal{K} = z^*$  but also reverses momenta since the momentum operator is imaginary. Complex conjugation acts as follows on position, momentum and spin operators

$$\mathcal{K}^\dagger \hat{r} \mathcal{K} = +\hat{r}, \quad \mathcal{K}^\dagger \hat{p} \mathcal{K} = -\hat{p}, \quad \mathcal{K}^\dagger \hat{S}_{x,z} \mathcal{K} = +\hat{S}_{x,z}, \quad \mathcal{K}^\dagger \hat{S}_y \mathcal{K} = -\hat{S}_y, \quad (1.22)$$


 Figure 1.5: Mirror planes and rotation axes of the point group  $D_{4h}$ 

assuming that the spin operators are given in the usual representation with  $\hat{S}_y$  imaginary, which is the case for the Pauli matrices  $\hat{\mathbf{S}} = \boldsymbol{\sigma}$ . Time reversal symmetry  $\mathcal{T} = U_{\mathcal{T}}\mathcal{K}$  is the first example of an antiunitary symmetry. The action of time reversal symmetry is given as

$$\mathcal{T}^\dagger \hat{\mathbf{r}} \mathcal{T} = +\hat{\mathbf{r}}, \quad \mathcal{T}^\dagger \hat{\mathbf{p}} \mathcal{T} = -\hat{\mathbf{p}}, \quad \mathcal{T}^\dagger \hat{\mathbf{r}} \times \hat{\mathbf{p}} \mathcal{T} = -\hat{\mathbf{r}} \times \hat{\mathbf{p}}, \quad \mathcal{T}^\dagger \hat{\mathbf{S}} \mathcal{T} = -\hat{\mathbf{S}}. \quad (1.23)$$

These transformations fix the action of the unitary part of time reversal symmetry  $U_{\mathcal{T}}$ . In particular  $U_{\mathcal{T}} = e^{-i\pi\hat{S}_y/\hbar}$  satisfies the given relations. For a half-spin system with  $\hat{S}_y = \hbar\sigma_y/2$  one finds  $\mathcal{T} = -i\sigma_y\mathcal{K}$ . If a system has additional orbital degrees of freedom, i.e., states  $|\mathbf{k}, \sigma, \nu\rangle$  with orbital  $\nu$ , the orbital degree of freedom will also enter the time reversal operator  $\mathcal{T} = e^{-i\pi\hat{J}_y/\hbar}\mathcal{K}$ . The total angular momentum operator  $\hat{J}_y = \hat{L}_y + \hat{S}_y$  contains an angular momentum operator  $\hat{L}_y$ . Given a Hamiltonian  $\hat{\mathcal{H}}(\mathbf{k})$  defined in the state space spanned by orbital degrees of freedom time reversal symmetry acts as

$$\hat{\mathcal{H}}(\mathbf{k})' = \mathcal{T}^\dagger \hat{\mathcal{H}}(\mathbf{k}) \mathcal{T} = e^{+i\pi\hat{J}_y/\hbar} \hat{\mathcal{H}}^*(-\mathbf{k}) e^{-i\pi\hat{J}_y/\hbar}. \quad (1.24)$$

For a BdG Hamiltonian there is an intrinsic symmetry operation, namely charge conjugation  $\mathcal{C}$ . A BdG Hamiltonian has an intrinsic charge conjugation symmetry  $-\hat{\mathcal{H}}(\mathbf{k}) = \tau_x \hat{\mathcal{H}}^\dagger(-\mathbf{k}) \tau_x$  with the charge conjugation operator  $\mathcal{C} = \tau_x \mathcal{K}$ . Charge conjugation is antiunitary here<sup>3</sup>. This can be seen by

$$\hat{\mathcal{H}}(\mathbf{k})' = \mathcal{C}^\dagger \hat{\mathcal{H}}(\mathbf{k}) \mathcal{C} = \tau_x \hat{\mathcal{H}}^\dagger(-\mathbf{k}) \tau_x = -H(\mathbf{k}). \quad (1.25)$$

<sup>3</sup>The representation of charge conjugation is unfixed in non-relativistic theories and can be chosen to be unitary. In relativistic quantum theory charge conjugation is necessarily antiunitary due to the  $\mathcal{CPT}$  theorem, which requires  $\mathcal{CPT} = 1$ , where  $\mathcal{P}$  is the parity operation.

Using the charge conjugation symmetry of a BdG Hamiltonian  $\widehat{\mathcal{H}}(\mathbf{k})$  time reversal symmetry can be rewritten using the  $\tau_x$  Pauli matrices representing the complex conjugation of the Hamiltonian

$$\widehat{\mathcal{H}}(\mathbf{k})' = \mathcal{T}^\dagger \widehat{\mathcal{H}}(\mathbf{k}) \mathcal{T} = -\tau_x e^{+i\pi \widehat{J}_y / \hbar} \widehat{\mathcal{H}}(\mathbf{k}) \tau_x e^{-i\pi \widehat{J}_y / \hbar}. \quad (1.26)$$

In the next section we focus on the topological aspect of symmetries which give rise to the topological classification of Hamiltonians.

### 1.3 Topological classification of Hamiltonians

Hamiltonians can be classified in terms of symmetries. For random Hamiltonians with all unitary symmetries broken, a classification can be performed in terms of antiunitary symmetries. Altland and Zirnbauer (AZ) classified random matrices using the antiunitary symmetries time reversal symmetry  $\mathcal{T}$ , charge conjugation symmetry  $\mathcal{C}$  and chiral symmetry  $\mathcal{S}$  [11]. The AZ classification extends the Wigner-Dyson classification [32, 33] which relies solely on time reversal symmetry. The random matrices can describe disordered systems. For non-random systems it is necessary to check for additional space group symmetries [34]. Given the three antiunitary symmetries the matrices fall in ten different symmetry classes which are summarized in the periodic table of topological insulators and superconductors [12].

The periodic table associates a  $\mathbb{Z}$  or  $\mathbb{Z}_2$  invariant with each symmetry class and dimension. In certain cases the topological invariants are connected to measurable physical quantities, e.g., the Hall conductivity  $\sigma_{xy}$  in the quantum Hall effect [16] corresponds to the first Chern number [9, 10] as discussed in Section 1.1.1.

#### 1.3.1 Random matrix theory and symmetries

Random matrix theory considers random matrices of a given size where all unitary symmetries are broken. This classification of random matrices is connected to symmetric spaces and topology [12]. We assume that a Hamiltonian  $\widehat{\mathcal{H}}$  is Hermitian and that no unitary operators exist, which commute with the Hamiltonian, except for trivial scalar operators. In our work we focus particularly on many body Hamiltonians in  $\mathbf{k}$ -space  $\widehat{\mathcal{H}}(\mathbf{k})$ . For such Hamiltonians one has to ensure that no additional symmetries exist due to the  $\mathbf{k}$ -dependence [34], which would require diagonalizing the Hamiltonian using this additional symmetry.

The classification proceeds then using three remaining symmetries: Time reversal symmetry  $\mathcal{T}$ , charge conjugation symmetry  $\mathcal{C}$  and chiral or sublattice symmetry  $\mathcal{S}$ . However note that the physical names are not of importance here.  $\mathcal{T}$  and  $\mathcal{C}$  are antiunitary symmetries, which can be written as a product of a unitary operator  $U$  and the complex conjugation operator  $\mathcal{K}$ . For time reversal symmetry we write  $\mathcal{T} = \mathcal{K}U_{\mathcal{T}} = U_{\mathcal{T}}^*\mathcal{K}$ . Chiral symmetry  $\mathcal{S}$  is not an antiunitary symmetry, but a unitary operator, which anticommutes with the Hamiltonian.

The Altland and Zirnbauer (AZ) classification [11] defines that for a Hamiltonian operator  $\hat{\mathcal{H}}(\mathbf{k})$ , time reversal symmetry  $\mathcal{T}$ , charge conjugation symmetry  $\mathcal{C}$  or chiral symmetry  $\mathcal{S}$  are present if the respective relation holds

$$\mathcal{T}: \quad \mathcal{T}^\dagger \hat{\mathcal{H}}(\mathbf{k}) \mathcal{T} = U_{\mathcal{T}}^\dagger \hat{\mathcal{H}}^*(-\mathbf{k}) U_{\mathcal{T}} = + \hat{\mathcal{H}}(\mathbf{k}), \quad (1.27)$$

$$\mathcal{C}: \quad \mathcal{C}^\dagger \hat{\mathcal{H}}(\mathbf{k}) \mathcal{C} = U_{\mathcal{C}}^\dagger \hat{\mathcal{H}}^*(-\mathbf{k}) U_{\mathcal{C}} = - \hat{\mathcal{H}}(\mathbf{k}), \quad (1.28)$$

$$\mathcal{S}: \quad \mathcal{S}^\dagger \hat{\mathcal{H}}(\mathbf{k}) \mathcal{S} = U_{\mathcal{S}}^\dagger \hat{\mathcal{H}}(\mathbf{k}) U_{\mathcal{S}} = - \hat{\mathcal{H}}(\mathbf{k}), \quad (1.29)$$

where  $U_{\mathcal{T}}$ ,  $U_{\mathcal{C}}$  and  $U_{\mathcal{S}}$  are unitary matrices. Note that there are no possibilities for further symmetries. Chiral symmetry  $\mathcal{S}$  is defined as the product of time reversal and charge conjugation symmetry, which means that the presence of the latter implies the presence of chiral symmetry. However if neither time reversal nor charge conjugation symmetry is present, chiral symmetry can still be present.

To classify the matrices one writes  $\mathcal{T} = 0$  ( $\mathcal{C} = 0$ ) if time reversal symmetry  $\mathcal{T}$  (charge conjugation symmetry  $\mathcal{C}$ ) is absent. The presence of a symmetry is denoted by  $\mathcal{T} \equiv \pm 1$  or  $\mathcal{C} \equiv \pm 1$  respectively depending on the square of the corresponding symmetry, e.g.,  $\mathcal{T}^2 = \pm 1$ . Note that the symmetries can only square to  $\pm 1$  [4]. Physically a symmetry which squares to  $-1$  involves half-integer spin. There are 9 different classes with  $\mathcal{T} = 0, \pm 1$  and  $\mathcal{C} = 0, \pm 1$ . Additionally chiral symmetry  $\mathcal{S}$  distinguishes the two cases  $\mathcal{S} = 0$  and  $\mathcal{S} = 1$  for  $\mathcal{T} = \mathcal{C} = 0$ .

Since both time reversal  $\mathcal{T}$  and charge conjugation  $\mathcal{C}$  involve complex conjugation, their absence signals that the Hamiltonian is complex. The other eight classes are real. In the next section we discuss the classes and their associated topological properties.

### 1.3.2 Classification in the periodic table

Time reversal symmetry  $\mathcal{T}$ , charge conjugation symmetry  $\mathcal{C}$  and chiral symmetry  $\mathcal{S}$  allow to distinguish ten different classes of Hamiltonians. These classes correspond to symmetric spaces defined by Élie Cartan. However Cartan's exhaustive classification contains more than ten classes, including exceptional classes with fixed matrix size.

Table 1.3: Periodic table of topological insulators and superconductors. The symmetries  $\mathcal{T}$ ,  $\mathcal{C}$  and  $\mathcal{S}$  distinguish ten classes. The classes with  $\mathcal{S} = 1$  are chiral. The first two complex classes have a Bott periodicity of two in the dimension, the other eight real classes have a periodicity of eight.

Symmetry		$\mathcal{T}$ $\mathcal{C}$ $\mathcal{S}$			Dimension							
					1	2	3	4	5	6	7	8
A	unitary	0	0	0	0	$\mathbb{Z}$	0	$\mathbb{Z}$	0	$\mathbb{Z}$	0	$\mathbb{Z}$
AIII	chiral unitary	0	0	1	$\mathbb{Z}$	0	$\mathbb{Z}$	0	$\mathbb{Z}$	0	$\mathbb{Z}$	0
AI	orthogonal	1	0	0	0	0	0	$\mathbb{Z}$	0	$\mathbb{Z}_2$	$\mathbb{Z}_2$	$\mathbb{Z}$
BDI	chiral orthogonal	1	1	1	$\mathbb{Z}$	0	0	0	$\mathbb{Z}$	0	$\mathbb{Z}_2$	$\mathbb{Z}_2$
D	BdG	0	1	0	$\mathbb{Z}_2$	$\mathbb{Z}$	0	0	0	$\mathbb{Z}$	0	$\mathbb{Z}_2$
DIII	chiral BdG	-1	1	1	$\mathbb{Z}_2$	$\mathbb{Z}_2$	$\mathbb{Z}$	0	0	0	$\mathbb{Z}$	0
AII	symplectic	-1	0	0	0	$\mathbb{Z}_2$	$\mathbb{Z}_2$	$\mathbb{Z}$	0	0	0	$\mathbb{Z}$
CII	chiral symplectic	-1	-1	1	$\mathbb{Z}$	0	$\mathbb{Z}_2$	$\mathbb{Z}_2$	$\mathbb{Z}$	0	0	0
C	BdG	0	-1	0	0	$\mathbb{Z}$	0	$\mathbb{Z}_2$	$\mathbb{Z}_2$	$\mathbb{Z}$	0	0
CI	chiral BdG	1	-1	1	0	0	$\mathbb{Z}$	0	$\mathbb{Z}_2$	$\mathbb{Z}_2$	$\mathbb{Z}$	0

These exceptional classes correspond to exceptional Lie groups. The periodic table of topological insulators and superconductors only covers the spaces with variable matrix size  $N$  since these allow the description of physical systems of arbitrary size. The classes termed ‘BdG’ (Bogoliubov-de Gennes) contain physical systems exhibiting particle-hole symmetry. We present the periodic table [12] in Table 1.3. The table includes dimension up to eight since the associated topological invariants repeat with a periodicity. The first two complex classes A and AIII have a Bott periodicity of two, the other eight real classes have a periodicity of eight. The phenomenon of Bott periodicity is known from real and complex K-theory [35].

Each class and space dimension has an associated  $\mathbb{Z}$  or  $\mathbb{Z}_2$  label, which describes possible topological invariants of Hamiltonians defined in the particular class. More precisely, the  $\mathbb{Z}$  and  $\mathbb{Z}_2$  labels denote the stable homotopy groups  $\pi_d(M(N))$  of a symmetric space  $M(N)$  spanned by matrices of dimension  $N \times N$ . The homotopy groups of the symmetric spaces depend on matrix size  $N$ , but stabilize for large matrix sizes, i.e., they do not change anymore for even larger matrices. A homotopy group is a group which classifies topological spaces like a symmetric space. For completeness we shortly review the definition. Choose a base point  $a \in S^d$  in the  $d$ -sphere and a base point  $b \in M$ . The group  $\pi_d(M)$  is defined as the set of equivalence classes of maps  $f : S^d \rightarrow M$  with  $f(a) = b$ , i.e.,

$$\pi_d(M) = \left\{ f : S^d \rightarrow M \mid f(a) = b \right\}_{\sim} . \quad (1.30)$$

Maps are equivalent if they can be continuously transformed into each other, i.e., if they are homotopic. For  $d = 0$  the homotopy group  $\pi_0(M)$  is the set of connected components of  $M$ . For  $d \geq 1$  the homotopy group or fundamental group forms a group by path composition. For example for  $d = 1$  two paths  $f$  and  $g$  defined on  $t \in [0, 1]$  (with  $0 = 1$  identified since  $S^1$  is a circle) can be composed to  $h = f * g$  such that  $h(t) = f(2t)$  for  $t \leq 1/2$  and  $h(t) = g(2t - 1)$  for  $t \geq 1/2$ . For higher dimensional homotopy groups the definition relies on the wedge sum of the domain spheres. The wedge sum of two spheres  $S^d$  is defined as the disjoint union, with the two base points of the two spheres identified. Composition of the two maps  $h = f + g$  is defined by taking  $h = f$  on the first sphere and  $h = g$  on the second sphere of the wedge sum [36].

### 1.3.3 Topological invariants

In this section we discuss topological invariants which are means to classify topological phases by integer numbers. Slight perturbations to the system parameters do not change the value of the topological invariants. Perhaps the best known invariant is the genus which counts the number of handles of a geometric space. The genus  $g(S)$  of a compact surface without boundary  $S$  is calculated using the Gauss-Bonnet formula

$$\int_S K \, ds = 2\pi\chi(S) = 2\pi(2 - 2g(S)), \quad (1.31)$$

with  $K$  the curvature of the manifold at a point and  $\chi(S) = 2 - 2g(S)$  the Euler characteristic. Interestingly, a far reaching generalization of the Gauss-Bonnet theorem, the Atiyah-Singer index theorem, is connected to the bulk-boundary correspondence, which plays an important role in the topological systems discussed in this thesis. In the following we highlight invariants appearing in condensed matter systems, starting from a band structure picture.

#### Berry phase of a band structure

Band structures in condensed matter arise due to the periodicity of a lattice in real space. The Bloch equation  $H(\mathbf{k}) |u_n(\mathbf{k})\rangle = E_n(\mathbf{k}) |u_n(\mathbf{k})\rangle$  for a band  $n$  determines the Bloch eigenfunctions  $|u_n(\mathbf{k})\rangle$  giving rise to periodic wavefunctions  $|\psi_n\rangle = e^{i\mathbf{k}\cdot\mathbf{r}} |u_n(\mathbf{k})\rangle$ . The Berry phase is a geometric phase acquired by the Bloch wavefunction while moving along a path. The Berry connection (or Berry potential) is defined as  $\mathcal{A}_n(\mathbf{k}) = i \langle u_n(\mathbf{k}) | \nabla_{\mathbf{k}} |u_n(\mathbf{k})\rangle$ . Integrating the (non-gauge invariant) Berry connection along a

closed curve  $C$  yields the Berry phase

$$\gamma_n = \oint_C d\mathbf{k} \cdot \mathcal{A}_n(\mathbf{k}), \quad (1.32)$$

which is a gauge invariant quantity modulo  $2\pi$ . A gauge transformation  $|u_n(\mathbf{k})\rangle \mapsto e^{i\phi_n(\mathbf{k})} |u_n(\mathbf{k})\rangle$  yields  $\gamma_n \mapsto \gamma_n + 2\pi m$  with  $m \in \mathbb{Z}$ . Furthermore, similar to a gauge potential, the Berry connection  $\mathcal{A}_n(\mathbf{k})$  allows the definition of another gauge invariant quantity, the Berry curvature (or Berry flux)  $\mathcal{F}_n(\mathbf{k}) = \nabla_{\mathbf{k}} \times \mathcal{A}_n(\mathbf{k})$ .

Calculating the Berry phase via Stokes' theorem yields

$$\gamma_n = \oint_C d\mathbf{k} \cdot \mathcal{A}_n(\mathbf{k}) = \int_S d\mathbf{k} \hat{\mathbf{n}} \cdot [\nabla_{\mathbf{k}} \times \mathcal{A}_n(\mathbf{k})] = \int_S d\mathbf{k} \hat{\mathbf{n}} \cdot \mathcal{F}_n(\mathbf{k}). \quad (1.33)$$

If integration is performed over the full 2D Brillouin zone  $S = \text{BZ}$ , which forms a  $\mathbb{T}^2$  torus, the boundary term vanishes and the surface term yields a value of  $2\pi m$ . This means the Berry phase over the whole Brillouin zone is a quantized topological invariant, the so called first Chern number.

### Chern number and winding number

We rewrite the Chern number in a more direct form, expressed in terms of the Bloch wavefunctions

$$C_1^n = \frac{\gamma_n}{2\pi} = i \int dk_x dk_y \left[ \partial_{k_x} \langle u_n(\mathbf{k}) | \partial_{k_y} u_n(\mathbf{k}) \rangle - \partial_{k_y} \langle u_n(\mathbf{k}) | \partial_{k_x} u_n(\mathbf{k}) \rangle \right]. \quad (1.34)$$

In the case of simple two-band Hamiltonians  $\hat{\mathcal{H}}(\mathbf{k}) = \mathbf{g}(\mathbf{k}) \cdot \boldsymbol{\sigma}$  the equation simplifies even further. The Chern number reduces to the familiar form

$$C_1 = \frac{1}{4\pi} \int dk_x dk_y \hat{\mathbf{g}} \cdot \left( \partial_{k_x} \hat{\mathbf{g}} \times \partial_{k_y} \hat{\mathbf{g}} \right), \quad (1.35)$$

which also appeared in the equation of the Hall conductivity in Section 1.1.2.

This number counts how often the unit configuration vector  $\hat{\mathbf{g}}(\mathbf{k})$  winds if integrated over the whole Brillouin zone. Essentially the number determines the skyrmionic charge of the configuration vector. Choosing the  $S^2$  base manifold we can for example consider the configuration  $\hat{\mathbf{g}}(\theta, \phi) = (\cos A\phi \sin \theta, \sin A\phi \sin \theta, \cos \theta)^\top$ . For  $A = 1$  the vector  $\hat{\mathbf{g}}(\mathbf{k})$  parametrizes the sphere and one obtains  $C_1 = 1$ . For  $A > 1$  the vector winds multiple times resulting in a higher Chern number  $C_1 = A > 1$ .

Reducing the system by one dimension yields the topological invariant

$$n = \frac{1}{2\pi} \int dk (\hat{\mathbf{g}} \times \partial_k \hat{\mathbf{g}})_z . \quad (1.36)$$

This integral can be rewritten as a winding number in the complex plane

$$n = \frac{1}{2\pi i} \int_C \frac{dz}{z} = \frac{1}{2\pi i} \int_C dk \frac{\partial_k z(k)}{z(k)} \quad (1.37)$$

with  $z(k) = g_x(k) + i g_y(k)$ , which counts the number of times the closed curve  $C$  parametrized by  $z(k)$  winds around the singularity  $1/z$  at  $z = 0$ . The Kitaev chain is a physical system, described by a winding number, which will be discussed in Section 2.3.1. The winding number determines the number of Majorana bound states per end of the chain via the bulk boundary correspondence.

### $\mathbb{Z}_2$ topological invariants

Up to now we discussed integer topological invariants  $n \in \mathbb{Z}$ . Now we consider the classes in the periodic table of topological insulators, which are characterized by a  $\mathbb{Z}_2$  invariant. The systems in those classes exhibit two possible different topological phases labeled by  $0, 1 \in \mathbb{Z}_2$  or equivalently by  $\pm 1 \in \mathbb{Z}_2$ .

In particular, time-reversal invariant topological insulators exhibit Kramers pairs  $|u_n^I(k)\rangle$  and  $|u_n^{II}(k)\rangle$  which are two degenerate energy eigenstates. For a 1D (2D) system this has the consequence that the winding (Chern) number vanishes. However for each of the states  $I$  and  $II$  of the pair a separate Chern  $C^{I/II}$  can be defined, where  $C^I = -C^{II}$ . Taking the parity  $(-1)^{C^I}$  yields a  $\mathbb{Z}_2$  invariant. This definition of the topological invariant corresponds to the invariant defined in terms of the Pfaffian [22, 23]. As part of our work in Chapter 4, we discuss the  $\text{Bi}_2\text{Te}_3$  topological insulator, which can be classified according to a  $\mathbb{Z}_2$  invariant.

#### 1.3.4 Bulk-boundary correspondence

The bulk boundary correspondence connects the bulk topology, i.e., the topology of the band structure, with the number of localized states at the boundary of a corresponding finite system. This correspondence can be approached in an intuitive manner. Introducing a boundary or creating an interface to another material necessarily changes the band structure near the boundary. In the simplest case assume an interface of two different materials  $A$  and  $B$  with two bands  $A_{1,2}$  and  $B_{2,1}$  respectively. Furthermore we assume band inversion of corresponding bands  $A_i = B_i$ , i.e., the

energies satisfy  $E(A_1) > E(A_2)$ ,  $E(B_2) > E(B_1)$ . If the band inversion happens smoothly, the bands must necessarily go through zero energy corresponding to the existence of a zero energy bound state. This scenario is realized in the case of HgTe quantum wells which were used to demonstrate the quantum spin Hall effect (see Section 1.1.3).

The exact form of the bulk boundary correspondence depends on the system under consideration and is non-obvious in the general case. For a given model like the Kitaev chain it is possible to show the correspondence explicitly.

The concept of bulk-boundary correspondence in general is related to index theorems of Dirac operators, in particular the Atiyah-Patodi-Singer index theorem, which is a generalization of the Atiyah-Singer index theorem for manifolds with boundaries [37, 38]. The theorem can be stated as the equation

$$\text{ind } D = \int_X \text{AS} - \frac{1}{2}\eta(D_0) \tag{1.38}$$

for a Dirac operator  $D$  where the right hand side of the equation captures the analytical properties of the operator and the left hand side the topological nature. The index of the Dirac operator  $\text{ind } D = \dim \ker D - \dim \ker D^\dagger$  counts the number of zero modes of the operator. The right hand side involves an integral of the Atiyah-Singer integrand AS over the manifold  $X$ , defined via the Chern character and genus, and the additional boundary term according to Atiyah-Patodi-Singer for the boundary operator  $D_0$ . Interestingly the left hand side yields an integer value, which is non-obvious for the right hand side. This already hints on to the deep implications of this theorem.

# 2

## Chapter 2

# Fundamentals of Majorana fermions

In this chapter we focus on Majorana fermions in solid state systems. They are named after Ettore Majorana who discovered that the Dirac equation supports purely real solutions. These solutions describe particles which are their own antiparticles. The Dirac equation describe a relativistic fermion  $\psi$  and can be written in non-Lorentz invariant form as

$$i\frac{\hbar}{c}\partial_t\psi(\mathbf{r},t) = [-i\hbar\boldsymbol{\alpha}\cdot\boldsymbol{\partial}_r + \beta mc]\psi(\mathbf{r},t), \quad (2.1)$$

where  $m$  is the fermion mass and  $\boldsymbol{\alpha}$  and  $\beta$  are  $4 \times 4$  matrices, which obey the anti-commutation relations  $\{\alpha_i, \alpha_j\} = 2\delta_{i,j}$ ,  $\{\alpha_i, \beta\} = 0$  and  $\beta^2 = \mathbb{1}$ . There are multiple possible choices for  $\boldsymbol{\alpha}$  and  $\beta$  satisfying the algebra. In particular, if a basis with  $\boldsymbol{\alpha}^* = \boldsymbol{\alpha}$  and  $\beta^* = -\beta$  is chosen, the complex conjugated Dirac equation describing the antifermion  $\psi^*$  is of identical form as the original equation. In this case the reality condition  $\psi = \psi^*$  can be imposed.

In high energy physics it is discussed whether neutrinos are Majorana fermions [39]. Experimental confirmation however is very difficult since neutrinos interact very weakly and usually appear in decays as ‘missing’ energy. In fact, the missing energy was the reason for Fermi to propose the existence of neutrinos. Furthermore there are hypothetical particles, expected to be of Majorana character, e.g., superpartners of real gauge fields. However in condensed matter physics the situation is different: Majorana fermions appear as excitations and not as elementary particles. To qualify as Majorana particles, the corresponding Majorana operators must fulfill the Majorana condition  $\gamma_E = \gamma_{-E}^\dagger$  with energy  $E$ . In particular for zero energy modes with  $E = 0$ , the condition  $\gamma_0 = \gamma_0^\dagger$  holds. We will discuss the occurrence of such zero modes in various systems in Section 2.3. But first, we give an overview over the general properties

of the Majorana zero modes and proceed with their possible application as constituents for quantum bits to perform topological quantum computation. In the following we will use the term Majorana fermion to subsume elementary Majorana particles and Majorana zero modes in condensed matter systems.

## 2.1 Majorana zero modes: Definition and general properties

We follow Ref. [40] for this section. Majorana zero modes are created by a fermionic operator  $\gamma$  with  $\gamma^2 = 1/2$ . It is also possible to use a different normalization where the Majorana operators square to another constant. Due to the squaring condition,  $\gamma = \gamma^\dagger$  necessarily holds, which means that the Majorana operators are real. Furthermore  $\gamma$  corresponds to a zero energy state, as such the operator has to commute with the Hamiltonian of the system  $[H, \gamma] = 0$ . In condensed matter systems multiple zero modes  $\gamma_i$  ( $i = 1, \dots, 2n$ ) can appear as localized excitations which are separated by a certain distance  $l$ . Given the length it is more realistic that  $[H, \gamma] = e^{-l/\xi}$ , where  $\xi$  is a characteristic correlation length associated with the Hamiltonian, e.g., superconducting coherence length.

The zero modes appear only in pairs since they arise as fractionalization of ordinary electrons, i.e., each Majorana mode corresponds to half of an electron. For the given normalization, multiple Majorana operators satisfy the anticommutation relation  $\{\gamma_i, \gamma_j\} = \delta_{ij}$ . Since each of the Majorana operators commute with the Hamiltonian, a series of operators  $\nu\gamma_1\gamma_2, \nu\gamma_3\gamma_4, \dots, \nu\gamma_{2n-1}\gamma_{2n}$  can be defined, which all commute with the Hamiltonian and span an eigenspace of dimension  $2^n$ . This eigenspace forms the degenerate ground state of the system. In the physically realistic scenario this ground state is only approximate with an energy exponentially suppressed with  $l$ . It is the goal to exploit this ground state degeneracy for quantum information purposes, which we will discuss in Section 2.2.

### 2.1.1 Non-abelian anyons

A crucial aspect of Majorana zero modes are their non-abelian statistics. Let us first consider the case of *abelian* anyons. For two particles in three dimensions at positions  $\mathbf{r}_1$  and  $\mathbf{r}_2$  we require that the particles always keep a safe distance  $|\mathbf{r}_1 - \mathbf{r}_2| > l$ . The wavefunction of the two particles  $\psi(\mathbf{r}_1, \mathbf{r}_2)$  can generally acquire a phase  $\theta$  when the particles are moved on paths such that they are exchanged, i.e.  $\psi(\mathbf{r}_1, \mathbf{r}_2) \mapsto e^{i\theta}\psi(\mathbf{r}_2, \mathbf{r}_1)$ . However the modulus of the wavefunction cannot change, i.e.  $|\psi| = \text{const}$ . After one exchange, the particles are exchanged a second time  $e^{i\theta}\psi(\mathbf{r}_2, \mathbf{r}_1) \mapsto e^{2i\theta}\psi(\mathbf{r}_1, \mathbf{r}_2)$ . Since

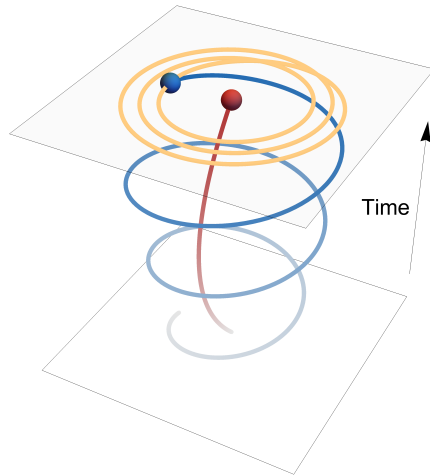


Figure 2.1: Anyons are moved adiabatically around each other, constituting an elementary braiding operation. The blue particle is moved three times around the red particle. The blue and red lines illustrate the worldlines through time and space. The closed yellow path shows the movement in space, characterized by the winding number  $n = 3$ .

the two exchanges are equivalent to no exchange at all it must hold  $e^{2i\theta} = 1$  which implies  $e^{i\theta} = \pm 1$  and  $\theta = 0, \pi$ . This means that under exchange the wavefunction can only acquire a sign giving rise to fermions or does not change in the case of bosons. Again - the crucial argument is that two exchanges are equivalent to no exchange at all. However for this argument to hold the topology of the paths must be considered. In three dimensions the paths involved in the exchange are contractible to a point such that no exchange can be seen as a limit of performing an exchange.

In contrast to three dimensions, the argument does not work in two dimensions! The paths involved in the exchange cannot be contracted to single points. Therefore no condition on the phase  $e^{in\theta}$  for  $n$  exchanges exists. The phase can possibly take *any* value and the particles are anyons with anyonic exchange statistics  $\psi_i\psi_j = e^{i\theta}\psi_j\psi_i$ . In second quantization  $\psi_{i,j}$  correspond to the field operators creating the anyonic excitations.

Now let us repeat the crucial argument in more mathematical terms by considering the first homotopy group of the configuration space of the system [41]. The distance vector  $\delta\mathbf{r} = \mathbf{r}_1 - \mathbf{r}_2$  with  $\delta r_x > 0$  is an element of  $(\mathbb{R}^3 \setminus \{0\})/\mathbb{Z}_2$ . The origin  $\{0\}$  is removed since the two particles must maintain their distance. Furthermore the division by  $\mathbb{Z}_2$  ensures that the identical particles are not distinct. By definition, this space coincides with the projective real plane  $\mathbb{RP}^2$  with the first homotopy group

$\pi_1((\mathbb{R}^3 \setminus \{0\})/\mathbb{Z}_2) = \pi_1(\mathbb{RP}^2) = \mathbb{Z}_2$ . The  $\mathbb{Z}_2$  group shows that there are only two distinguishable paths, namely paths which exchange and paths which do nothing. In two dimension one obtains

$$\pi_1((\mathbb{R}^2 \setminus \{0\})/\mathbb{Z}_2) = \pi_1(\mathbb{RP}^1) = \mathbb{Z}, \quad (2.2)$$

only that  $\mathbb{Z}$  different possible paths exist, corresponding to the numbers of times the first particle encircles the other one. Such exchange operations can be used to implement braiding which is the basis for topological quantum information. We illustrate the movement of the two particles in Fig. 2.1.

Now we focus on *non-abelian* anyons where the wavefunction acquires more than a phase factor under exchange. Two Majorana zero modes can be combined to form a fermion  $c = \gamma_1 + \nu\gamma_2$ . The number operator  $c^\dagger c = 0, 1$  yields the fermion parity of the degenerate state. Since fermion parity is conserved, exchanging  $\gamma_1$  and  $\gamma_2$  in two dimensions requires that

$$\begin{pmatrix} \gamma_1 \\ \gamma_2 \end{pmatrix} \mapsto U \begin{pmatrix} \gamma_1 \\ \gamma_2 \end{pmatrix} = \begin{pmatrix} \pm\gamma_2 \\ \gamma_1 \end{pmatrix}, \quad (2.3)$$

where the overall sign can be changed by a gauge transformation. Since only the sign changes in the first component, Majorana zero modes are of Ising type. The exchange operations are generated by *non-abelian* unitary braiding operators  $U = e^{i\theta} e^{\frac{\pi}{4}\gamma_1\gamma_2}$ . Therefore Majorana zero modes are non-abelian Ising anyons. In the next section we focus on the use of braiding operations for topological quantum computation.

## 2.2 Topological quantum computation

The key assumption of topological quantum computation is that qubits encoded in the ground state degeneracy spanned by Majorana zero modes are topologically protected against local fluctuations in contrast to classical qubits like the superconducting flux and charge qubits or alternative qubit implementations. The assumption is justified by the delocalized nature of the topological qubit implemented by spatially-separated Majorana zero modes. To exploit Majorana zero modes for quantum computation, artificial delocalized fermions composed out of two Majorana operators are considered, e.g.,  $c = \gamma_1 + \nu\gamma_2$ . The occupation numbers of these fermions for  $2n$  Majorana zero modes span a ground state space of dimension  $2^{n-1}$  for fixed fermion parity. In the following we first discuss the problem of fault tolerance in quantum computation and

proceed with a discussion of braiding operations. Furthermore we give an outlook to universal topological quantum computation.

### 2.2.1 Fault tolerance and topological protection

The main obstacle for quantum computation is decoherence due to coupling of the qubit to other system degrees of freedom. Usually the full system is modeled as two level systems describing the qubits, coupled to a bosonic bath, representing the additional degrees of freedom. The stability of qubits is quantified by two coherence times, the longitudinal  $T_1$  and the traversal coherence time  $T_2$ , where usually  $T_1 \gg T_2$ . The qubit decays exponentially  $\propto e^{-t/T_i}$ . The  $T_1$  time measures the loss of energy of the system, while  $T_2$  measures the time span for which the system stays coherent. Essentially, after time  $T_2$  the system loses its quantum behavior and acts classically.

The important question is how to reduce the possible sources of noise. Due to the non-local nature of Majorana qubits, they can only couple to non-local noise which makes them presumably stable. Considering a one-dimensional wire with Majorana bound states located at the ends far apart, electric charge noise on one side of the chain cannot couple directly to the Majorana state which is only half an electron. This feature of Majorana qubits is called topological protection.

However Majorana qubits rely on fermion parity conservation. As long as only Cooper pairs enter or leave the superconductor as fluctuations, fermion parity is preserved and the encoded qubits remain safe. If single electrons are allowed to enter the system from the environment, fermion parity is violated and the systems leaves the topologically protected subspace. Unfortunately there is a source of single electrons which comes directly from the superconductor, in form of quasiparticle poisoning. The density of (electronic) quasiparticles does not vanish for small temperatures as would be expected from standard BCS-theory, where at  $T = 0$  all electrons should be condensed in Cooper pairs. Therefore quasiparticles remain a problem even at very low temperatures [42]. We note that at the current experimental status it is hard to tell if Majorana based qubits would offer an advantage over conventional qubit designs due to quasiparticle poisoning, since no experiments managed yet to successfully demonstrate such qubits.

### 2.2.2 Braiding

For the following discussion we again follow Ref. [40]. Braiding operations exchange Majorana zero modes by moving them around each other adiabatically with a safe distance [43]. Through the exchange certain qubit rotations are possible, since the

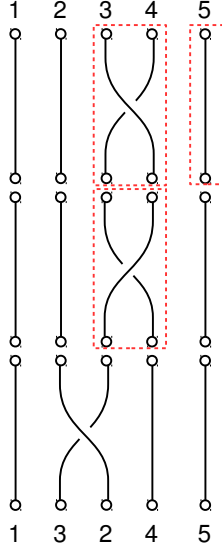


Figure 2.2: Braid group element. We show five strands on which the braid group acts. The red boxes highlight an elementary exchange, its inverse and a neutral operation. The tensor product of one elementary exchange with neutral operations on the other strands yields the braid group generators.

Majorana zero modes enjoy non-abelian exchange statistics as described before. Unfortunately braiding operations alone do not suffice to build a complete set of quantum gates. We will discuss this shortcoming in the following section and discuss certain possibilities to achieve universality.

Braiding operations are elements of the braid group  $B_n$  which describes how  $n$  strands can be ‘knotted’. The generators of the group are exchanges of two strands. Two group elements are composed by connecting the corresponding strands of the group. We show an exemplary braid group element in Fig. 2.2. In a physical system the braided zero modes are located on a two-dimensional surface, for example trapped in vortices which are then moved around. More realistically however might be a setup of nanowires and T-junctions also supporting exchange operations [43] as illustrated in Fig. 2.3.

There are multiple possibilities to encode qubits in Majorana zero modes. In particular the dense encoding allows to encode  $n$  qubits in  $2n + 2$  Majorana zero modes. There the eigenvalues  $\nu\gamma_{2k-1}\gamma_{2k} = \pm 1$  correspond to the  $\sigma_z$  eigenvalues of the  $k$ -th qubit. However it can be useful to use a sparse encoding with more redundancy, where four Majorana zero modes form one qubit. The  $k$ -th qubit  $k$  is encoded in  $\gamma_{4k-3}, \gamma_{4k-2}, \gamma_{4k-1}$  and  $\gamma_{4k}$  such that  $\gamma_{4k-3}\gamma_{4k-2}\gamma_{4k-1} = -1$ . This fixes an even fermion parity in the

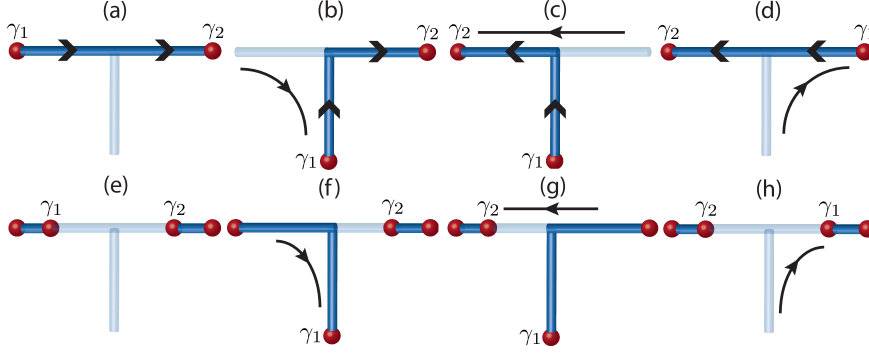


Figure 2.3: Adiabatic exchange of two Majorana fermions living on one-dimensional wires. The two Majoranas are either bridged by a topological region (dark blue line) as in (a-d) or by a non-topological region (light blue line) as in (e-h). Reprinted from Ref. [43] with permission by the Nature Publishing Group.

subspace of these four Majorana zero modes. The qubit operator  $\sigma_z$  is defined as  $\sigma_z \equiv \nu\gamma_{4k-3}\gamma_{4k-2}$ .

For (approximate) universal quantum computation the Hadamard gate  $H$ , the  $\pi/8$  phase gate  $T$  and the controlled  $Z$  gate  $C(Z)$  are needed:

$$H = \frac{1}{\sqrt{2}} \begin{pmatrix} 1 & 1 \\ 1 & -1 \end{pmatrix}, \quad T = \begin{pmatrix} 1 & 0 \\ 0 & e^{i\pi/4} \end{pmatrix}, \quad Z = \begin{pmatrix} 1 & 0 \\ 0 & -1 \end{pmatrix}. \quad (2.4)$$

Using these qubit operations the full set of qubit operations can be approximated according to the Solovay-Kitaev theorem [44]. To perform the Hadamard gate on the  $k$ -th qubit,  $\gamma_{4k-2}$  and  $\gamma_{4k-1}$  are exchanged counterclockwise. To apply the gate  $C(Z)$  one switches first from the sparse to the dense representation and afterwards back by measuring a subset of the involved Majorana operators. For details on the operation see Ref. [40].

However it is not possible to implement the  $\pi/8$  phase gate using topologically protected braiding operations. To perform universal quantum computations that safe place must be left unfortunately – at least in the case of Ising anyons.

### 2.2.3 Roads to universal quantum computation

Unfortunately the braiding operations yield only certain rotations on the Bloch sphere. However for universal quantum computation it is necessary to cover the whole sphere. If only Majorana zero modes are used as building blocks of the qubits, universality cannot be achieved while maintaining topological protection.

However if topological protection is violated it is possible to implement the aforementioned  $\pi/8$  phase gate by moving Majorana zero modes close to each other such that the wavefunctions overlap with a splitting energy  $\Delta E$ . Letting the qubit evolve for a certain time  $t$  leads to a gate operation

$$U(t) = \begin{pmatrix} 1 & 0 \\ 0 & e^{i\Delta Et} \end{pmatrix}. \quad (2.5)$$

After some time the Majorana zero modes are moved again apart. If the parameters of the system can be controlled to sufficient precision such that  $t = \frac{\pi}{4\Delta E}$  the necessary phase gate  $T = U(t)$  is obtained.

Another scenario involves coupling Majorana qubits to conventional universal qubits, e.g., qubits implemented based on superconducting circuits. Coupling the conventional and the topological system could happen momentarily such that the Majorana part of the setup still enjoys topological protection while being uncoupled from the unprotected qubits. Topologically protected non-universal qubits could be used as quantum memory in such a hybrid setup.

Another more intriguing possibility to achieve universal quantum computation is to rely on ‘more capable’ excitations, e.g., Fibonacci anyons, which follow richer algebraic relations Ref. [45]. The basic idea is that, in contrast to Majorana zero modes which combine to fermions, combining two Fibonacci anyons possibly yields a new anyon. The fusion operation  $\otimes$  follows a set of fusion rules, forming a fusion algebra.

At first we shortly review the fusion rules for Ising anyons, which include the previously discussed Majorana zero modes, in order to highlight the additional capabilities of Fibonacci anyons. The algebra for Majorana zero modes acts on the trivial particle  $\mathbb{1}$ , a fermion  $\psi$  and the Majorana zero mode  $\sigma$ . The algebra includes trivial fusion rules  $\mathbb{1} \otimes \mathbb{1} = \mathbb{1}$ ,  $\mathbb{1} \otimes \sigma = \sigma \otimes \mathbb{1} = \sigma$  and  $\mathbb{1} \otimes \psi = \psi \otimes \mathbb{1} = \psi$ . The rules describing the fusion of fermions and Majorana zero modes are given by

$$(I) \quad \sigma \otimes \sigma = \mathbb{1} \oplus \psi \quad (2.6)$$

$$(II) \quad \psi \otimes \sigma = \sigma \quad (2.7)$$

$$(III) \quad \psi \otimes \psi = \mathbb{1} \quad (2.8)$$

Rule (I) encodes that two Majorana zero modes  $\sigma$  can be combined, resulting in either a trivial particle  $\mathbb{1}$  (unoccupied fermionic state) or a fermion  $\psi$ . Rule (II) means that the anyon  $\sigma$  will persist if it fuses with a fermion  $\psi$  and the rule (III) states that two fermions combine resulting in a trivial particle. Physically, these rules encode that the

Majorana zero modes are stable as long as they are not allowed to fuse and maintain their safe distance.

For Fibonacci anyons  $\tau$  the fusion rules are given by

$$\mathbb{1} \otimes \mathbb{1} = \mathbb{1} \tag{2.9}$$

$$\mathbb{1} \otimes \tau = \tau \otimes \mathbb{1} = \tau \tag{2.10}$$

$$\tau \otimes \tau = \mathbb{1} \oplus \tau \tag{2.11}$$

which is even simpler than the set of rules for the Ising anyons. The crucial ingredient is the fusion rule  $\tau \otimes \tau = \mathbb{1} \oplus \tau$ . In contrast to the Ising anyons, combining Fibonacci anyons yields further Fibonacci anyons. This aspect allows to build up fusion trees. It is possible to build universal qubit gates acting on a state space spanned by the anyons. For more details see Ref. [45]. In a physical system, Fibonacci anyons can be realized from coupled parafermions [46].

## 2.3 Theoretical proposals for realization of Majorana fermions

In this section we focus on the main theoretical proposals for realization of Majorana fermions in condensed matter systems. The starting point was the discovery by Kitaev that one-dimensional spinless p-wave superconductors show a topological phase transition and host isolated zero energy Majorana bound states in the topological regime. We dedicate the next paragraph to a discussion of that proposal. Since a one-dimensional p-wave superconductor is mostly a theoretical construct, we discuss engineered physical setups afterwards. These setups are effectively described as a p-wave superconductor in the low energy regime. In Chapter 3, we present our work on adatom chains, which is an engineered system, hosting Majorana bound states.

In two dimensions it is possible for vortices of a topological superconductor to host point-like Majorana zero modes. Topological superconductors can be engineered from topological insulators, which exists in nature, and conventional superconductors. In our work we study a setup of this type, as presented in Chapter 5.

### 2.3.1 Edge states of 1D p-wave superconductor

The spinless 1D p-wave superconductor, or Kitaev chain, is the prototypical example of a topological superconductor, which was first described by Kitaev [8]. We consider a finite chain of length  $N$  with p-wave superconducting pairing  $\Delta$ , nearest neighbor hopping amplitude  $t$  and chemical potential  $\mu$ .

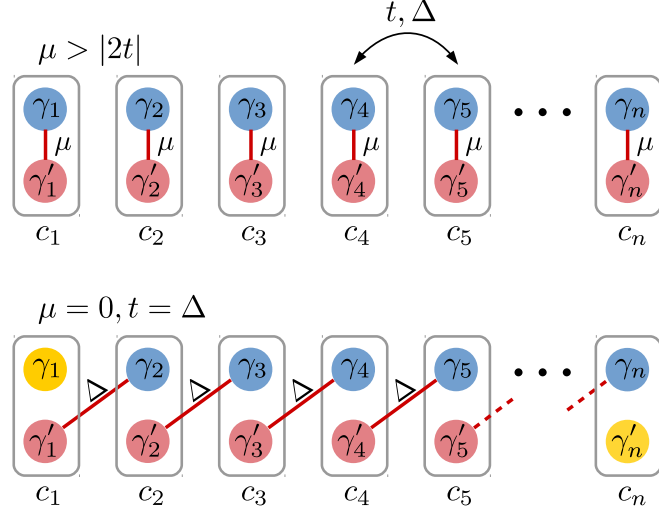


Figure 2.4: Illustration of a Kitaev chain in the trivial phase and in the topological phase, where two Majorana operators remain uncoupled at the ends of the chain.

The Hamiltonian has the form

$$\mathcal{H} = -\mu \sum_{i=1}^N c_i^\dagger c_i + \sum_{i=1}^{N-1} [tc_i^\dagger c_{i+1} + \Delta c_i c_{i+1} + \text{H.c.}]. \quad (2.12)$$

Note that the fermionic operators  $c_i$  are spinless and fulfill the usual fermionic commutation relation  $\{c_i, c_j^\dagger\} = \delta_{ij}$ . Because of Pauli's exclusion principle no s-wave superconducting pairing term could be written. The p-wave pairing must have triplet character. The spinless character of the fermions can be achieved by applying a strong polarizing magnetic field which pushes one of the spin components to significantly higher energies. We will discuss realizations of the model later, in particular how p-wave pairing can be achieved.

Varying the parameters allows to tune the system into different phases, which can be understood in terms of topology. According to the bulk-boundary correspondence there are two approaches to understand the topology of the system, (a) the occurrence of states on the boundary and (b) the bulk topology. We focus first on approach (a), the occurrence of bound states. For this purpose we introduce Majorana operators

$$\gamma_i = \frac{c_i + c_i^\dagger}{\sqrt{2}} \quad \text{and} \quad \gamma'_i = \frac{c_i - c_i^\dagger}{i\sqrt{2}}, \quad (2.13)$$

satisfying the commutator relations  $\{\gamma_i, \gamma_j\} = \delta_{ij}$ ,  $\{\gamma'_i, \gamma'_j\} = \delta_{ij}$  and  $\{\gamma_i, \gamma'_j\} = 0$ .

Expressing the Hamiltonian in Majorana operators yields

$$\mathcal{H} = -\mu \sum_{i=1}^N \left( \frac{1}{2} - v\gamma'_i \gamma_i \right) - v \sum_{i=1}^{N-1} \left[ (\Delta + t)\gamma_{i+1}\gamma'_i + (\Delta - t)\gamma'_{i+1}\gamma_i \right]. \quad (2.14)$$

The form of the Hamiltonian suggests that we consider the cases with  $\Delta = t$ . In particular: (i)  $\Delta = t = 0$ ,  $\mu > 0$ . The Hamiltonian reduces to the trivial form

$$\mathcal{H} = -\mu \sum_{i=1}^N \left( \frac{1}{2} - v\gamma'_i \gamma_i \right) = -\mu \sum_{i=1}^N c_i^\dagger c_i. \quad (2.15)$$

In this scenario the system is in a topologically trivial metallic state, since no special states are found. Each site  $i$  can be either occupied by an electronic state with energy  $-\mu$  or unoccupied.

(ii)  $\Delta = t \neq 0$ ,  $\mu = 0$ . In this case the Hamiltonian takes the form

$$\mathcal{H} = -2v\Delta \sum_{i=1}^{N-1} \gamma_{i+1}\gamma'_i. \quad (2.16)$$

Now something special happened: The operators  $\gamma_1$  and  $\gamma'_N$  do not appear in the Hamiltonian. Hence the states generated by these operators stay at zero energy. These two unpaired states are located precisely at the ends of the chain. The appearance of the end states signals that the system is topologically non-trivial. The scenario is illustrated in Fig. 2.4.

If one departs slightly from the limit discussed here with  $\Delta = t = 0$ , these highly localized states start to leak into the bulk of the chain. The wavefunctions decay exponentially such that the overlap of the two wavefunctions is exponentially suppressed with the length of the chain. Adjusting the model parameters slightly does not remove them. This behavior of the states is characteristic for their topological origin. For an illustration of a Majorana wavefunction in a realistic setup see Fig. 3.8.

Now we turn our focus on approach (b), the bulk picture. The Fourier transformed Hamiltonian is given by

$$\mathcal{H} = \frac{1}{2} \sum_k \psi_k^\dagger \widehat{\mathcal{H}}(k) \psi_k \quad \text{with} \quad \widehat{\mathcal{H}}(k) = (2t \cos k - \mu)\tau_z - 2\Delta \sin k \tau_y. \quad (2.17)$$

The Hamiltonian  $\widehat{\mathcal{H}}(k)$  acts in particle-hole space spanned by the spinor  $\psi_k^\dagger = (c_k^\dagger, c_{-k})$ . In this form of the Hamiltonian the p-wave character of the superconducting pairing becomes obvious, since the superconducting term is odd under inversion.

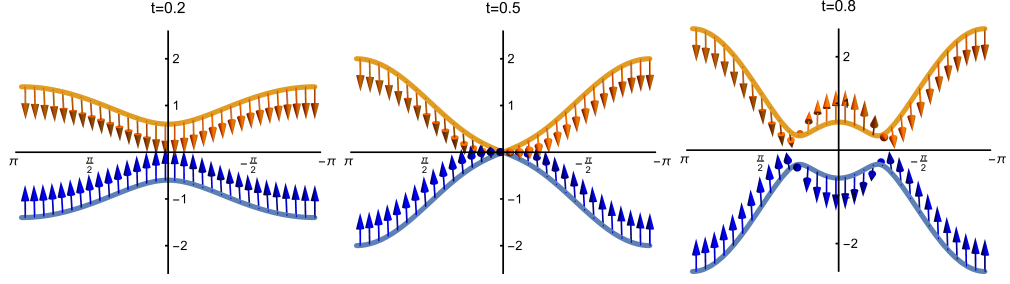


Figure 2.5: Bulk band structure of the Kitaev chain for  $\Delta = 0.2$ ,  $\mu = 1$ ,  $t = 0.2, 0.5, 0.8$ . The topological phase transition happens at  $t = 0.5$ . The vectors show the orientation of  $\hat{\mathbf{g}}(k)$  or equivalently the orientation of the eigenstates in particle-hole space. For  $t = 0.8$  the system is in the topological regime. The non-trivial topology is reflected in the winding of the eigenstates. The topological phase transition can also be interpreted as a band inversion in vicinity of the  $k = 0$  point.

The dispersion is given by

$$E_k = \pm \sqrt{(2t \cos k - \mu)^2 - 4\Delta^2 \sin^2 k} \quad (2.18)$$

and shows a gap closing at  $k = 0, \pi$  for  $|\mu| = 2t$ . This gap closing has the crucial role of signaling a topological phase transition. The nodes at the gap closing points are the topologically relevant bulk nodes. We illustrate the bulk band structure in Fig. 2.5.

The topological invariant corresponding to the number of Majorana bound states at the ends of the chain can be calculated as a winding number  $n$  of a complex curve  $z(k) = a(k) + ib(k)$  as follows

$$a(k) = 2t \cos k - \mu, \quad b(k) = 2\Delta \sin k, \quad (2.19)$$

$$n = \frac{1}{2\pi i} \oint \frac{dz}{z} = \frac{1}{2\pi i} \int_{-\pi}^{\pi} \frac{dk}{z(k)} \frac{\partial z(k)}{\partial k} = \theta(2t - |\mu|). \quad (2.20)$$

This winding number  $n$  counts how often the curve  $z(k)$  circles around the singularity of  $1/z$  at  $z = 0$ . Deforming the curve by modifying the parameters  $t$  and  $\Delta$  slightly does not change the number of times the curve circles around the singularity.

### 2.3.2 Quasi-1D p-wave superconductors and Majorana flat bands

Instead of the Kitaev chain, we can consider a variant of the model, which is extended anisotropically in the  $xy$ -plane. Furthermore we additionally consider the spin degree

of freedom. The Hamiltonian is given by

$$\widehat{\mathcal{H}}(\mathbf{k}) = [2t_z \cos k_z + 2t_\perp (\cos k_x + \cos k_y) - \mu] \tau_z - 2\Delta \sin k_z \tau_y, \quad (2.21)$$

with anisotropic hopping  $t_z \gg t_\perp > 0$  and  $p_z$ -superconducting gap  $\Delta > 0$ . The Hamiltonian acts in the spinor space  $\Psi_{\mathbf{k}}^\dagger = (\psi_{\mathbf{k}\uparrow}^\dagger, \psi_{\mathbf{k}\downarrow}^\dagger, \psi_{-\mathbf{k}\uparrow}, \psi_{-\mathbf{k}\downarrow})$ . For  $t_\perp = 0$  and neglecting the spin degree of freedom, one recovers the Kitaev chain in  $z$ -direction.

We assume that spin-spin inter-site interactions of the form  $\mathcal{H}_J = -\sum_{ab} \sum_{ij} J_{ij}^{ab} S_i^a S_j^b$  are present. Here  $S_i^a = \sum_z \psi_i^\dagger(z) \sigma^a \psi_i(z)$  is the spin operator at site  $i$ . We can especially concentrate on an anisotropic interaction, such that the interaction drives the  $p_z$ -superconducting order in the bulk. The possible interactions for the spin component in  $z$ -direction and the spin components in the  $xy$ -plane are given by

$$\mathcal{H}_{J^z} = -\sum_{ij} J_{ij}^z S_i^z S_j^z \quad \text{and} \quad \mathcal{H}_{J^\perp} = -\sum_{ij} J_{ij}^\perp \mathbf{S}_i^\perp \cdot \mathbf{S}_j^\perp. \quad (2.22)$$

Now we consider the possible Majorana modes, which can appear at a surface in the  $xy$ -plane. The two spin blocks of the bulk Hamiltonian belong to the symmetry class BDI with time-reversal symmetry  $\Theta = \mathcal{K}$ , charge conjugation symmetry  $\Xi = \tau_x \mathcal{K}$  and chiral symmetry  $\Pi = \tau_x$ , thus these surface modes are only weakly protected by the presence of translational symmetry in the  $xy$ -plane.

One Majorana bound state appears per spin block at each  $\mathbf{k}_\perp = (k_x, k_y)^\top$  point on the surface if the 1D subsystem along the  $k_z$ -axis is in the topologically non-trivial phase. This is the case if the criterion  $2t_z > |2t_\perp (\cos k_x + \cos k_y) - \mu|$  is satisfied. The in-plane hopping term  $\propto t_\perp$  modifies the chemical potential and enters the topological criterion and the topological invariant. From that viewpoint the 3D system is seen as a bundle of Kitaev chains in  $z$ -direction which all end on the surface at  $z = 0$ . The bulk extends to  $z \rightarrow \infty$ .

Since at each  $\mathbf{k}_\perp$  point one Majorana bound state is present per spin, these states form two zero energy Majorana flat bands. Since the topological criterion depends on the  $\mathbf{k}_\perp$ -coordinates, only certain regions of the  $\mathbf{k}_\perp$  Brillouin zone might be topological and contribute to the flat bands. The topological regions are given by the regions where a Fermi surface is present for  $\Delta = 0$ . Previously Majorana flat bands (MFB) have been discussed in  $p$ -wave SCs [47, 48],  $d$ -wave SCs [47], lattice models [49], gapless TSCs [50–53], nodal  $d$ -wave SCs [54], noncentrosymmetric SCs [55–60], hybrid structures [61, 62] and in relation to ferromagnetism [63].

In the case when the whole  $\mathbf{k}_\perp$ -plane is in the topologically non-trivial phase, the Majorana solutions at site  $i$  on the surface are given by

$$\gamma_{i\uparrow} = \sum_z \phi(z) \frac{\psi_{i\uparrow}(z) + \psi_{i\uparrow}^\dagger(z)}{\sqrt{2}} \quad \text{and} \quad \gamma_{i\downarrow} = \sum_z \phi(z) \frac{\psi_{i\downarrow}(z) - \psi_{i\downarrow}^\dagger(z)}{i\sqrt{2}}, \quad (2.23)$$

where  $\phi$  decays exponentially in  $z$ -direction. The Majorana operators satisfy  $\{\gamma_{is}, \gamma_{js'}\} = \delta_{ij} \delta_{ss'}$ .

Since the flat bands are highly degenerate the bulk interaction effects on them must be considered. To take interactions into account, we project the electronic degrees of freedom onto the Majorana solutions, which are eigenstates to  $\tau_x \sigma_z = 1$ . This yields the projected spin operator  $S_i^a = \Phi(\gamma_{i\uparrow}, -i\gamma_{i\downarrow}) \sigma^a (\gamma_{i\uparrow}, i\gamma_{i\downarrow})^\top$  with form factor  $\Phi = \sum_z \phi^2(z)$ . The projected fermionic operators are given by  $\psi_{i\uparrow}(z) \approx \phi(z) \gamma_{i\uparrow} / \sqrt{2}$  and  $\psi_{i\downarrow}(z) \approx i\phi(z) \gamma_{i\downarrow} / \sqrt{2}$ . With these operators the interaction  $\mathcal{H}_{Jz}$  becomes constant for the Majorana operators but the interaction of the in-plane spin components acts on the Majorana bands as

$$\mathcal{H}_{J\perp} = -\Phi^2 \sum_{ij} J_{ij}^\perp (i\gamma_{i\uparrow} \gamma_{i\downarrow}) (i\gamma_{j\uparrow} \gamma_{j\downarrow}). \quad (2.24)$$

This interaction acts on the flat Majorana bands and can possibly lead to a chiral dispersion. We will discuss a system where flat bands occur in Chapter 5. However the study of systems with flat bands and interactions is an interesting research topic on its own.

### 2.3.3 Majorana bound states in vortices of $p + ip$ -superconductors

Majorana bound states can be obtained at domain walls and in vortices of topological superconductors, which was first recognized by Read and Green [64]. We shortly review how such Majorana zero modes come about using standard BCS theory. At first one considers the effective quasiparticle Hamiltonian with  $p$ -wave pairing  $\Delta_{\mathbf{k}} \approx \Delta(k_x + ik_y)$  in the form

$$\mathcal{H} = \sum_{\mathbf{k}} \left[ \xi_{\mathbf{k}} c_{\mathbf{k}}^\dagger c_{\mathbf{k}} + \frac{1}{2} \left( \Delta_{\mathbf{k}}^* c_{-\mathbf{k}} c_{\mathbf{k}} + \text{H.c.} \right) \right]. \quad (2.25)$$

Using the Bogoliubov transformation  $\alpha_{\mathbf{k}} = u_{\mathbf{k}} c_{\mathbf{k}} - v_{\mathbf{k}} c_{-\mathbf{k}}^\dagger$  and  $\alpha_{\mathbf{k}}^\dagger = u_{\mathbf{k}}^* c_{\mathbf{k}}^\dagger - v_{\mathbf{k}}^* c_{-\mathbf{k}}$  one obtains the Hamiltonian  $H_{\text{eff}} = \sum_{\mathbf{k}} E_{\mathbf{k}} \alpha_{\mathbf{k}}^\dagger \alpha_{\mathbf{k}} + \text{const}$  and the Bogoliubov-de Gennes equations  $E_{\mathbf{k}} u_{\mathbf{k}} = \xi_{\mathbf{k}} u_{\mathbf{k}} - \Delta_{\mathbf{k}}^* v_{\mathbf{k}}$ ,  $E_{\mathbf{k}} v_{\mathbf{k}} = -\xi_{\mathbf{k}} v_{\mathbf{k}} - \Delta_{\mathbf{k}} u_{\mathbf{k}}$  with  $E_{\mathbf{k}} = \sqrt{\xi_{\mathbf{k}}^2 + |\Delta_{\mathbf{k}}|^2}$ ,

$|u_{\mathbf{k}}|^2 = (1 + \xi_{\mathbf{k}}/E_{\mathbf{k}})/2$  and  $|v_{\mathbf{k}}|^2 = (1 - \xi_{\mathbf{k}}/E_{\mathbf{k}})/2$ . From these equations it is necessary to distinguish two limiting cases for  $\mathbf{k} \rightarrow 0$ : (i)  $\xi_{\mathbf{k}} > 0$  such that  $|u_{\mathbf{k}}| \rightarrow 1, |v_{\mathbf{k}}| \rightarrow 0$  which is the strong-pairing BEC or trivial phase and (ii)  $\xi_{\mathbf{k}} < 0$  such that  $|u_{\mathbf{k}}| \rightarrow 0, |v_{\mathbf{k}}| \rightarrow 1$  which is the weak-pairing BCS or non-trivial phase. In the low energy regime for small  $\mathbf{k}$  and chemical potential  $\mu$  where  $\xi_{\mathbf{k}} \approx -\mu$ , the chemical potential determines the transition between weak and strong pairing at  $\xi_{\mathbf{k}} = 0$ . Within linear approximation the BdG equations become in real space

$$i\partial_t u = -\mu u + i\Delta^*(\partial_x + i\partial_y)v \quad \text{and} \quad i\partial_t v = \mu v + i\Delta(\partial_x - i\partial_y)u, \quad (2.26)$$

which resembles the Dirac equation for a spinor  $(u, v)$ . For  $u^* = v$  the two equations are equivalent. Therefore there exists a zero-energy real solution, which is its own antiparticle, a Majorana bound state.

Introducing a domain wall  $\mu(x) = |\mu| \text{sign } x$  and solving the Schrödinger equation yields Jackiw-Rebbi-type solutions bound at the wall. These solutions have the form  $u(x) \propto e^{-i\pi/4} e^{-|\mu|x/\Delta}$  and  $v = iu$ . The solutions with non-zero energy propagate along the wall in only one direction, i.e., are chiral Majorana modes.

Vortices can be treated in a similar manner, where a small circular domain wall on the superconductor surface with  $\mu < 0$  is considered, which encloses a region with  $\mu > 0$ . Then one exponentially decaying zero energy bound state will be trapped within this vortex. Since p-wave superconductors are problematic to obtain in nature, engineered systems with effective p-wave pairing are considered. The prototype is due to Fu and Kane [65], which a heterostructure composed of a conventional s-wave superconductor in proximity to a topological insulator surface. Our work in Chapter 5 pursues this direction. In the next section we discuss a proposal, which engineers topological superconductors from even more elementary subsystems, not relying on topological insulators.

### 2.3.4 Proximity induced superconductivity and engineered topological superconductors

There are materials, like the ruthenates, which are discussed to show p-wave correlations and if true would act as a natural topological superconductor [28]. However it seems to be more feasible to consider engineered topological superconductors, composed of easily experimentally accessible and well-understood conventional components. In this section we discuss such an engineered setup.

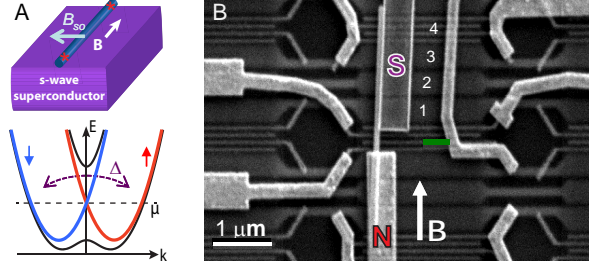


Figure 2.6: Experimental nanowire setup reprinted from Ref. [5] with permission from AAAS. (a) Theoretical proposal. Top: Device layout with a semiconducting nanowire in proximity to an s-wave superconductor with external  $B$ -field. The Rashba spin-orbit coupling is indicated as an effective magnetic field  $B_{so}$ . Red stars indicate Majorana bound states. Bottom: Energy  $E$  versus momentum  $k$ . The spin-orbit coupling shifts the spin-down band (blue) to the left and spin-up band (red) to the right. Blue and red parabolas are for  $B = 0$ . Black curves for  $B \neq 0$  illustrate the formation of a gap near  $k = 0$  of size  $g\mu_B B$ . ( $\mu$  is the Fermi energy with  $\mu = 0$  defined at crossing of parabolas at  $k = 0$ ). The superconductor induces a gap  $\Delta$ . (b) Scanning electron microscope image of the implemented device with normal (N) and superconducting (S) contacts. The S-contact only covers the right part of the nanowire. The underlying gates 1 to 4 are covered by a dielectric.

To achieve engineered topological superconductors three essential building blocks are necessary: 1. Conventional s-wave superconductivity, 2. Rashba spin orbit coupling and 3. magnetic field or intrinsic magnetism. The proposals rely on the superconducting proximity effect. Cooper pairs of the superconductor tunnel into the other material, inducing a superconducting gap  $\Delta$  within the other material near the interface.

One of the first models proposed was the nanowire model [66, 67]. The Hamiltonian acts in particle-hole space  $\tau$  and spin space  $\sigma$  and has the form

$$\hat{\mathcal{H}}(k) = \left( \frac{k^2}{2m} - \mu \right) \tau_z + \alpha k \sigma_z - B \tau_z \sigma_x - \Delta \tau_y \sigma_y, \quad (2.27)$$

with Rashba spin orbit coupling  $\alpha$ , magnetic Zeeman field  $B$  and a proximity-induced conventional s-wave superconducting gap  $\Delta$ . A sufficiently strong magnetic field will polarize the excitations in such a way that only one of the spin-direction is relevant. Effectively the system is then described by a two band model of the low energy bands, which is obtained by projection  $\tilde{\mathcal{H}}(k) = (\tilde{\epsilon}_k - \tilde{\mu}) \tau_z - 2\tilde{\Delta} k \tau_y$ , where  $\tilde{\epsilon}_k$  is quadratic in  $k$ . From this continuum model the tight-binding model of the Kitaev chain is regained by compactification (see Section 2.3.1). The first experiment realizing the nanowire

model [5] is shown in Fig. 2.6. In this experiment a zero-bias peak was observed in a tunneling conductance measurement as shown in Fig. 2.7.

There are other proposals not relying on semiconductors. In particular in our work we considered magnetic adatoms placed on a superconducting substrate [68]. The external magnetic field is replaced by intrinsic magnetism of the adatoms. We will discuss this model in detail in Chapter 3. Furthermore there are similar models relying on nanomagnets [69], special rare-earth superconductors which combine magnetism with superconductivity [70] and systems relying on magnetic random impurities [71].

## 2.4 Majorana fermion signatures

There are multiple proposed experimental signatures for Majorana states. At first we discuss the signature in tunneling experiments, the zero bias anomaly. These experiments try to measure the tunneling through the Majorana bound states, retrieving a tunneling spectrum by varying the bias voltage  $V$ . In Chapter 3 we focus exclusively on such transport signatures in the extended case with spin polarized tip and richer signatures.

The second signature is the  $4\pi$ -Josephson effect. The Josephson effect leads to a supercurrent through a weak link between superconductors with a phase difference. The  $4\pi$ -Josephson effect is related to the suppression of Shapiro steps.

However the ultimate smoking gun experiment would involve a measurement of the non-abelian exchange statistics of the Majorana states by performing braiding operations as discussed in Section 2.2.2. To perform such an experiment, a setup was proposed, which consists of multiple p-wave chains organized such that T-junctions are formed. By gating the chains it is possible to braid the bound states [43]. Such braiding experiments would open the door towards topological quantum computation as discussed in Section 2.2.

### 2.4.1 Tunneling conductance: Zero bias anomaly

The most well known experimental signatures of Majorana zero modes is a zero bias peak in the tunneling spectrum. Chapter 3 focuses on our work on signatures in different Majorana adatom chain setups. Here we summarize the most important aspects of the zero bias peak following Ref. [72]. A finite 1D system in  $x$ -direction is assumed. The Majorana operator  $\gamma_i$  corresponding to a Majorana zero mode can be

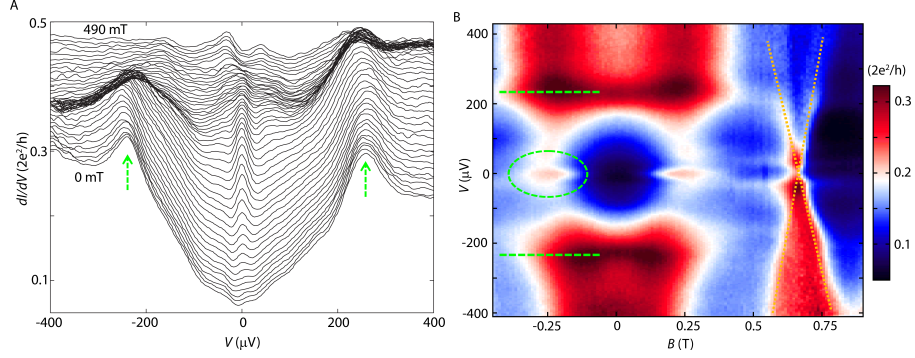


Figure 2.7: Experimental results of magnetic field dependent spectroscopy reprinted from Ref. [5] with permission from AAAS. (a)  $dI/dV$  over  $V$  at  $T = 70$  mK at different  $B$ -fields from 0 to 490 mT in 10 mT steps. (b) Full color scale plot of  $dI/dV$  over  $V$  and  $B$ . The zero-bias peak is highlighted by a dashed oval. The dashed lines indicate the gap edges. At 0.6 T a non-Majorana state is crossing zero bias, which is indicated by tilted dotted lines.

written in the general form

$$\gamma_i = \sum_{\sigma} \int dx \left[ f_{\sigma,i}(x) \psi_{\sigma}(x) + f_{\sigma,i}^*(x) \psi_{\sigma}^{\dagger}(x) \right]. \quad (2.28)$$

The spectral weight of the coefficient function  $f_{\sigma,i}(x)$  is localized at the ends of the chain. In experiment the region of high spectral weight is approached with a tunneling tip, such that a tunneling current depending on a bias voltage can be measured. The tunneling is modeled with a Hamiltonian

$$H_T = \sum_{k\sigma} \int dx \left[ t_k^*(x) c_{k\sigma}^{\dagger} \psi_{\sigma}(x) + \text{H.c.} \right], \quad (2.29)$$

which couples the electrons of the lead electrons  $c_{k\sigma}$  of the tip to the superconducting electrons  $\psi_{\sigma}(x)$ . The current flowing through the tip is then given by the current operator

$$I = -e\dot{N} = -e \frac{d}{dt} \sum_{k\sigma} c_{k\sigma}^{\dagger} c_{k\sigma}. \quad (2.30)$$

For zero-temperature the differential conductance is given by

$$\frac{dI}{dV} = \frac{2e^2}{h} \frac{4\Gamma^2}{(eV)^2 + 4\Gamma^2} \quad (2.31)$$

with an approximately energy-independent linewidth  $\Gamma$ . For  $V = 0$  this Lorentzian curve shows a quantized peak of  $2e^2/h$ . In the nanowire experiment a zero-bias peak was observed as shown in Fig. 2.7 [5]. In recent experiments even the quantization of the tunneling conductance was reported [7].

### 2.4.2 $4\pi$ -Josephson effect and Shapiro steps

The  $4\pi$ -Josephson effect should be measurable in topological Josephson junctions between topological superconductors [73]. There are Majorana bound states located at each side of the Josephson junction. The tunnel coupling through the junction hybridizes the Majorana bound states, forming Andreev bound states with finite energy  $\epsilon(\delta\phi)$  depending on the phase difference  $\delta\phi$ . This finite energy is  $4\pi$  periodic in the phase difference  $\delta\phi$ , i.e.,  $\epsilon(\delta\phi) \propto \cos(\delta\phi/2)$ . This leads to a current phase relation  $I(\delta\phi) \propto \sin(\delta\phi/2)$ .

Furthermore this  $4\pi$  periodicity appears in the coupling  $M$  of the two bound states on both sides of the junction. This coupling enters the  $dI/dV$  function, which allows the direct observation of the periodicity if the phase difference  $\delta\phi$  over the junction is changed between tunneling conductance measurements. Controlling the phase difference is achieved by applying magnetic flux in a setup with SQUID-like geometry.

Another signature of the Andreev bound states due to Majorana modes are missing odd Shapiro steps. Shapiro steps are observed if an AC voltage  $V_{AC} \sin(\omega t)$  and a DC voltage  $V_{DC}$  are applied to the junction. The Josephson current

$$I = I_J \sin \left[ \phi_0 + \frac{2eV_{DC}t}{\hbar} - \frac{2eV_{AC} \cos(\omega t)}{\hbar\omega} \right] \quad (2.32)$$

shows Shapiro steps in the  $dI/dV_{DC}$  measurements for  $2eV_{DC}/\hbar = 2n\omega$ . However the odd Shapiro steps are missing, which might act as a signature of Majorana bound states [73].



# 3

## Chapter 3

---

# Majorana bound states in magnetic adatom chains

This chapter is based on our publications Ref. [2] and Ref. [3]. We present our work on one of the most prominent theoretical proposals for the realization of Majorana bound states which is currently also under experimental investigation [6]. We consider hybrid superconducting devices consisting of a superconducting substrate with Rashba spin-orbit coupling and magnetic adatoms placed on top of it. The adatoms form a chain with magnetic ordering and lead to in-gap Yu-Shiba-Rusinov (YSR) states in the superconductor.

If the system is tuned to the topological regime, which depends on the material parameters, one or more Majorana bound states are expected to appear at the ends of the chain as illustrated in Fig. 3.1. In tunneling conductance measurements, the tip of a scanning tunneling microscope (STM) couples to the Majorana states leading to the appearance of a zero bias conductance peak in the tunneling spectrum.

In the next section we review the current experimental situation of such adatom setups. Then we introduce the theoretical model describing adatom chains. We discuss the possible classical magnetic ground states of the adatom chains. After that we focus on the form of the Majorana bound states which can appear in a chain with ferromagnetic ordering. Interestingly the Majorana wavefunctions have a distinctive spinful character, which can be probed. For that purpose, we introduce possible tunnel couplings between Majorana states and the electrons of a spin-polarized superconducting tip. Furthermore we discuss couplings of multiple Majorana states located in a single adatom chain and between states located in multiple chains separated by Josephson junctions.

Using the couplings we derive the specific signatures which are expected in tunneling experiments. For an isolated YSR chain with one Majorana bound state we show that the tunneling conductance depends on the polarization direction of the tip, even such that the tunneling conductance vanishes completely in certain directions. In the case with multiple bound states we also show a strong dependence on the polarization direction. This behavior could provide an explanation for the value of the conductance measured in first tunneling experiments, which is lower than the quantized conductance unit  $2e/h^2$ .

### 3.1 Status of magnetic adatom chain experiments

There have been multiple experiments recently on hybrid superconducting devices with the goal of detecting Majorana bound states [5–7, 74]. A detection would open the door for further experiments analyzing the exotic non-abelian statistics with possible application in topological quantum computation.

The first experiments have been performed in semiconducting nanowires with spin-orbit coupling [5] which was predicted before [66, 67]. In these systems Majorana bound states are expected to appear at the ends of the nanowire, leading to a zero bias peak in the tunneling conductance [72, 75]. In particular the zero bias peak is quantized with height  $2e^2/h$ . In recent experiments this quantization was reported [7]. However the appearance of zero bias peaks is not unique to Majorana bound states [76, 77].

The debate on the Majorana signatures motivated new ideas which do not involve semiconductors. Instead conventional superconductors are used in the presence of a magnetic texture. It was shown that a magnetic chain with randomly ordered spins on top of a superconductor can harbor Majorana bound states [71]. Not even spin-orbit coupling and other external fields are necessary if a helical magnetic texture is present [34, 70, 78, 79].

It was realized that in magnetic chains spin-polarized tunneling microscopy can allow spatial visualization and thus provide a better method for detecting Majorana bound states and their properties [6]. The advantage of detecting spin-polarized Majorana bound states has motivated further proposals involving helical magnetism [61, 68]. If spin-orbit coupling is present, a ferromagnetic [2, 80–86] or an antiferromagnetic [2, 82] chain suffices to achieve a topological superconductor. Such a situation setup appears to have been recently realized experimentally [6], as shown in Fig. 3.2. However more

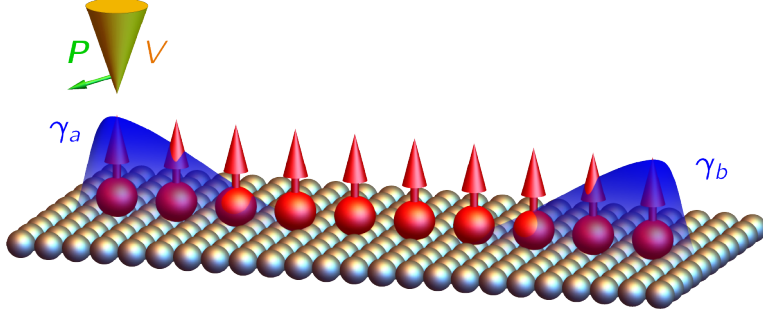


Figure 3.1: Ferromagnetic chain of adatoms on top of a superconducting substrate. The Majorana bound states  $\gamma_{a,b}$  are probed using a spin-polarized STM tip with bias voltage  $V$  and polarization  $P$ .

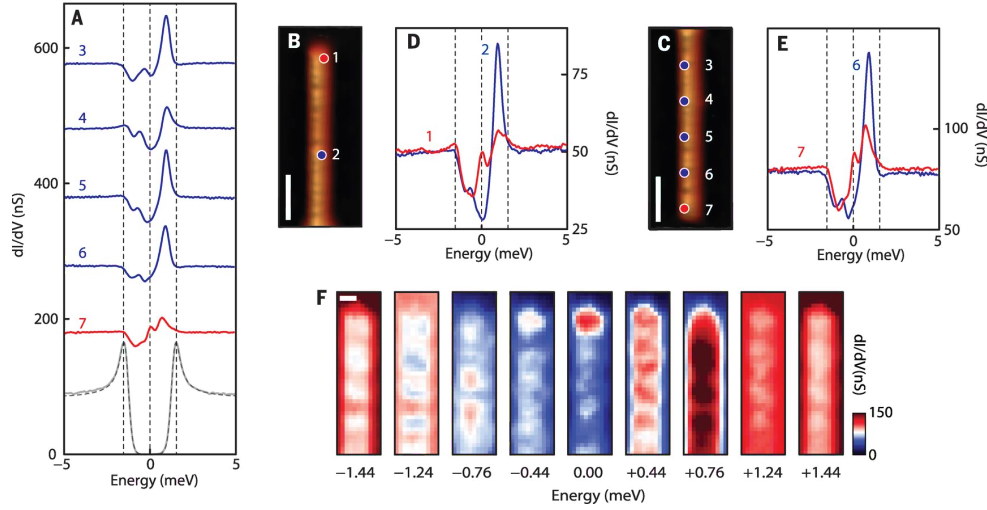


Figure 3.2: Spectroscopic mapping of atomic chains and ZBPs reprinted from Ref. [6] with permission by AAAS. (A) STM spectra measured at locations indicated in (B) and (C). The spectra are offset by 100 nS. The red spectrum shows the ZBP at one end of the chain. The gray trace was measured on Pb substrate and corresponds to the BCS gap. (B, C) Zoom-in topography of the upper (B) and lower end (C) of the chain and locations for spectra marked (1-7). (D, E) Spectra measured at marked locations. (F) Spatial and energy-resolved conductance maps of another Fe atomic chain close to its end with similar features as in (A).

experiments at lower temperature and with better resolution are required to confirm the results.

In this work we explore experimental fingerprints of Majorana bound states, some of which can be directly tested in the existing devices [6]. Crucial element is the magnetic spin-polarization of the tip. Previous studies focused on a non-magnetic tip in the normal [83, 84] or superconducting phase [83]. For nanowire based devices, spin-selective Andreev processes due to Majorana bound states have been previously studied [87].

### 3.2 Theoretical description of Yu-Shiba-Rusinov chains

In this section we discuss the derivation of the theoretical model for Yu-Shiba-Rusinov (YSR) adatom chains as in Ref. [2]. For simplicity the magnetic ordering of the adatom spins is first derived considering a metallic substrate with Rashba spin orbit coupling. The Hamiltonian of the surface electrons is given by

$$\mathcal{H}_{\text{metal}} = \sum_{\mathbf{k}} \psi_{\mathbf{k}}^{\dagger} \left[ \xi_{\mathbf{k}} + \alpha(\mathbf{k} \times \hat{z}) \cdot \boldsymbol{\sigma} \right] \psi_{\mathbf{k}} \quad (3.1)$$

with the Pauli matrices  $\boldsymbol{\sigma}$  and the spinor  $\psi^{\dagger} = (\psi_{\mathbf{k}\uparrow}^{\dagger}, \psi_{\mathbf{k}\downarrow}^{\dagger})$ . Here  $\xi_{\mathbf{k}}$  is the energy dispersion of free electrons and  $\alpha$  denotes the spin-orbit coupling strength. The adatoms are modeled as classical spins  $\mathbf{S}_j$  with  $|\mathbf{S}_j| = S$  located at positions  $\mathbf{R}_j = ja\hat{x}$ . The spins are coupled via an exchange interaction mediated by the substrate electrons

$$\mathcal{H}_J = J \sum_{j=1}^N \sum_{s,s'} \int \frac{d\mathbf{k} d\mathbf{k}'}{(2\pi)^2} e^{-i(\mathbf{k}-\mathbf{k}') \cdot \mathbf{R}_j} \psi_{\mathbf{k}s}^{\dagger} (\mathbf{S}_j \cdot \boldsymbol{\sigma})_{ss'} \psi_{\mathbf{k}'s'}. \quad (3.2)$$

For small  $J$  and unmodified substrate electron spectrum one can derive the Ruderman-Kittel-Kasuya-Yosida (RKKY) superexchange interaction acting between the spins

$$\mathcal{H}_{\text{RKKY}} = -m \left( \frac{Jk_F}{\pi} \right)^2 \sum_{ij} \frac{\sin(2k_F|\mathbf{R}_i - \mathbf{R}_j|)}{(2k_F|\mathbf{R}_i - \mathbf{R}_j|)^2} \mathbf{S}_i \cdot \mathbf{S}_j(\theta_{ij}) \quad (3.3)$$

with  $\mathbf{S}_j$  rotated by tilting angles  $\theta_{ij}$  [2]. Furthermore we consider an additional symmetry breaking term due to the crystal field

$$\mathcal{H}_{\text{CF}} = -\frac{D}{2} \sum_j (S_j^z)^2 \quad (3.4)$$

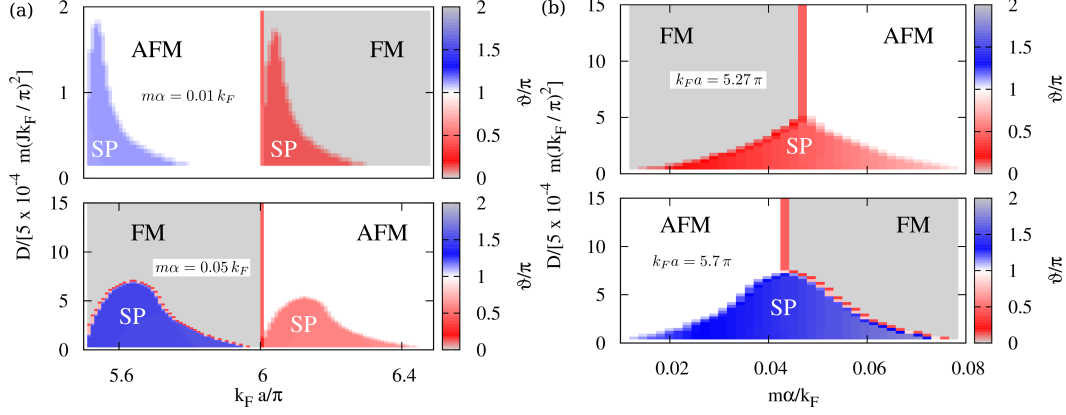


Figure 3.3: Phase diagrams for the classical magnetic ground state [2]. (a) The parameter plane is defined by the adatom spacing  $a$ , and the rescaled strength  $D$  of the crystal field anisotropy. The plots were calculated for two values of the Rashba SOC strength  $\alpha$ . Large  $\alpha$  coupling favors the spiral configuration, whereas increasing the Ising anisotropy strength  $D$  promotes the FM and AFM phases. (b) Parameter plane defined by the rescaled SOC strength  $\alpha$ , and the rescaled Ising anisotropy strength  $D$ . The plots were calculated for two values of the adatom spacing  $a$ . The FM or AFM phases stabilize for increasing anisotropy. Tuning the SOC strength allows switching between the FM and AFM phases.

with Ising anisotropy strength  $D$ . We classically minimize the Hamiltonian to determine the classical ground state and the orientation of the adatom spins. It is possible that the chains exhibit either a ferromagnetic, antiferromagnetic or spiral magnetic order. The stability of the ground state in the presence of thermal and quantum fluctuations was investigated in Ref. [2]. It was found that ferromagnetic and antiferromagnetic are stable for large regions of the parameter space as shown in Fig. 3.3.

Extending the model of adatoms on a metallic substrate to a superconducting model with bulk superconducting gap  $\Delta$  yields the Hamiltonian

$$\mathcal{H}_{\text{SC}} = \frac{1}{2} \sum_{\mathbf{k}} \Psi_{\mathbf{k}}^{\dagger} [\xi_{\mathbf{k}} \tau_z + \alpha \tau_z (\mathbf{k} \times \hat{\mathbf{z}}) \cdot \tilde{\boldsymbol{\sigma}} - \Delta \tau_y \sigma_y] \Psi_{\mathbf{k}}, \quad (3.5)$$

with the Pauli matrices  $\boldsymbol{\sigma}$  and  $\boldsymbol{\tau}$  defined in spin and particle-hole space respectively. The extended spin Pauli matrices are defined as  $\tilde{\boldsymbol{\sigma}} = (\tau_z \sigma_x, \sigma_y, \tau_z \sigma_z)$ . The Hamiltonian acts on spinors  $\Psi_{\mathbf{k}}^{\dagger} = (\psi_{\mathbf{k}\uparrow}^{\dagger}, \psi_{\mathbf{k}\downarrow}^{\dagger}, \psi_{-\mathbf{k}\uparrow}, \psi_{-\mathbf{k}\downarrow})$ , where  $\psi_{\mathbf{k},\sigma}^{\dagger}$  is the creation operator for electrons of momentum  $\mathbf{k}$  with spin  $\sigma$ . The Cooper pair breaking effect of the magnetic adatoms on the superconducting substrate leads to YSR states, with low energy  $\varepsilon \ll \Delta$ . The states are localized at the positions of the magnetic adatoms.

The RKKY interaction acquires an additional contribution due to YSR states. It was discussed that this contribution can dominate, such that an antiferromagnetic ordering is favored [88]. However in the case considered in our work with short adatom distances of  $\sim 1$  nm and superconducting coherence length of 80 nm the YSR contribution is negligible [2]. Therefore it is unnecessary to consider the YSR states to determine the magnetic order of the adatom chains.

We assume that the magnetic ordering is already fixed by the effective RKKY interaction of the adatom spins  $\mathbf{S}_j$ , leading to an effective Hamiltonian of the form

$$\mathcal{H}_J = \frac{1}{2} \sum_{j=1}^N \int \frac{d\mathbf{k} d\mathbf{k}'}{(2\pi)^2} e^{-i(\mathbf{k}-\mathbf{k}') \cdot \mathbf{R}_j} \psi_{\mathbf{k}}^\dagger M_j \tau_z \sigma_z \psi_{\mathbf{k}'}, \quad (3.6)$$

with  $M_j = JS(\pm 1)^j$  where  $+1$  ( $-1$ ) corresponds to ferromagnetic (antiferromagnetic) ordering.

As shown in Ref. [2], the Bogoliubov-de Gennes (BdG) equation of the system can be reduced to a Schrödinger equation for the YSR midgap states  $\sum_j \hat{\mathcal{H}}_{ij} \phi_j = \varepsilon \phi_i$  with wavefunction  $\phi_i^\dagger = (u_{i,\uparrow}^*, u_{i,\downarrow}^*, v_{i,\uparrow}, v_{i,\downarrow})$  and the Hamiltonian

$$\begin{aligned} \hat{\mathcal{H}}_{ij} = & \frac{\Delta}{\pi\nu_F M^2} \left[ \left( \pi\nu_F M^2 \tau_y \sigma_y - M \tau_z \sigma_z \right) \delta_{ij} \right. \\ & \left. + M^2 \left( G_{ij}^s \tau_z - G_{ij}^a \tau_z \sigma_y + F_{ij}^s \tau_y \sigma_y - F_{ij}^a \tau_y \right) \right], \end{aligned} \quad (3.7)$$

at sites  $i$  and  $j$ . The coefficients are given by

$$\frac{G^s(r)}{\pi\nu_F} = \cos(k_F \alpha r / v_F) \sin(k_F |r| - \frac{\pi}{4}) e^{-\frac{|r|}{\xi_0}} \sqrt{\frac{2}{\pi k_F |r|}}, \quad (3.8)$$

$$\frac{F^s(r)}{\pi\nu_F} = \cos(k_F \alpha r / v_F) \cos(k_F |r| - \frac{\pi}{4}) e^{-\frac{|r|}{\xi_0}} \sqrt{\frac{2}{\pi k_F |r|}}, \quad (3.9)$$

$$\frac{G^a(r)}{v\pi\nu_F} = \sin(k_F \alpha r / v_F) \sin(k_F |r| - \frac{\pi}{4}) e^{-\frac{|r|}{\xi_0}} \sqrt{\frac{2}{\pi k_F |r|}}, \quad (3.10)$$

$$\frac{F^a(r)}{v\pi\nu_F} = \sin(k_F \alpha r / v_F) \cos(k_F |r| - \frac{\pi}{4}) e^{-\frac{|r|}{\xi_0}} \sqrt{\frac{2}{\pi k_F |r|}}, \quad (3.11)$$

with the superconducting coherence length  $\xi_0$ , Fermi wavevector  $k_F$ , Fermi velocity  $v_F$  and  $r = (i - j)a$  with adatom spacing  $a$ . The super scripts of the functions denote if the function is symmetric ( $s$ ) or antisymmetric ( $a$ ). In the following we use  $k_F$  in units of  $\pi/a$ ,  $\alpha$  in units of  $v_F$ ,  $M$  in units of  $1/(\pi\nu_F)$  and  $\xi_0$  in units of  $a$ .

We transfer the given Hamiltonian from real space to  $k$ -space and obtain the BdG Hamiltonian

$$\widehat{\mathcal{H}}_k = t_k \tau_z - v_k \tau_z \sigma_y + (\Delta + \mathcal{D}_k) \tau_y \sigma_y - d_k \tau_y - \mathcal{B} \tau_z \sigma_z, \quad (3.12)$$

where we introduced the coefficients  $\mathcal{B} = \Delta / (\pi \nu_F J S)$  and

$$t_k = \sum_{\delta=1}^{\infty} t_{\delta} \cos(\delta k a) \quad \text{with} \quad t_{\delta} = \frac{2\Delta}{\pi \nu_F} G_{\delta}^s, \quad (3.13)$$

$$v_k = \sum_{\delta=1}^{\infty} v_{\delta} \sin(\delta k a) \quad \text{with} \quad v_{\delta} = \frac{2\Delta}{i\pi \nu_F} G_{\delta}^a, \quad (3.14)$$

$$\mathcal{D}_k = \sum_{\delta=1}^{\infty} \mathcal{D}_{\delta} \cos(\delta k a) \quad \text{with} \quad \mathcal{D}_{\delta} = \frac{2\Delta}{\pi \nu_F} F_{\delta}^s, \quad (3.15)$$

$$d_k = \sum_{\delta=1}^{\infty} d_{\delta} \sin(\delta k a) \quad \text{with} \quad d_{\delta} = \frac{2\Delta}{i\pi \nu_F} F_{\delta}^a. \quad (3.16)$$

The BdG Hamiltonian lives in class BDI [89] since it has time-reversal symmetry  $\Theta = \mathcal{K}$ , chiral symmetry  $\Pi = \tau_x$  and charge-conjugation symmetry  $\Xi = \tau_x \mathcal{K}$ . Class BDI in one dimension supports a  $\mathbb{Z}$  invariant and therefore a  $\mathbb{Z}$  number of Majorana bound states per end of the chain. Chiral symmetry  $\hat{\Pi} = \tau_x$  allows to block off-diagonalize the Hamiltonian [89, 90] via a rotation about the  $\tau_y$ -axis

$$\widehat{\mathcal{H}}'_k = \begin{pmatrix} 0 & A_k \\ A_k^{\dagger} & 0 \end{pmatrix} \quad \text{with} \quad A_k = t_k - i d_k - \mathcal{B} \sigma_z - [v_k - i(\Delta + \mathcal{D}_k)] \sigma_y. \quad (3.17)$$

The determinant  $z(k) = \det A_k$  is a complex number parametrized by  $k \in [-\pi/a, \pi/a]$  and describes a curve in the complex plane around the origin. The number of times this curve encircles the origin is given by the winding number  $\mathcal{N}$  as described in Section 1.3.3. The winding number  $\mathcal{N}$  is an integer value and can take the values zero, one or two in our case. Respectively the system supports zero, one or two Majorana bound states per end depending on the parameters of the system as shown in the topological phase diagram Fig. 3.4. The detailed diagram has been extracted in Ref. [2] and for similar systems in Ref. [81, 84]. In two-dimensional systems multiple Majorana modes have also been found [91].

The multiple Majorana solutions are not particularly stable since external perturbations, violating chiral symmetry  $\Pi$  or time-reversal symmetry  $\Theta$ , will move the system to class D which only allows a  $\mathbb{Z}_2$  invariant and a single Majorana bound state per end of the chain. A small perturbation  $m$  will therefore split the two Majorana bound

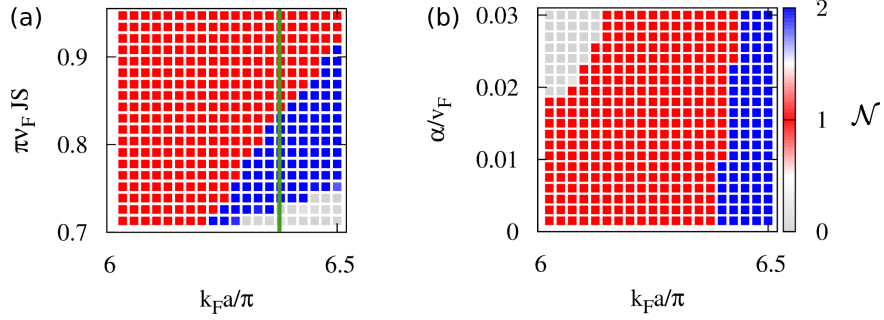


Figure 3.4:  $\mathbb{Z}$  topological invariant (winding number) for varying adatom spacing  $a$  and (a) magnetic exchange energy  $JS$  ( $\alpha = 0.01 v_F$ ) or (b) normalized SOC strength  $\alpha$  ( $\pi \nu_F JS = 0.85$ ) [2]. The topological phases harbor one or two MFs per chain end. In (a) tuning the magnetic exchange energy allows to switch between one and two MF phases. Close to the phase boundary the switching could be achieved by a weak perpendicular Zeeman field. In (b) for an infinitesimal small SOC strength both one and two MF phases are accessible. For the single MF phase where  $\alpha$  does not enter the topological criterion this is expected, but remarkably, the same happens in the two MF situation. Electrical tuning of  $\alpha$  can be used to achieve topological quantum phase transitions.

states to finite energy bound states with energy proportional to  $m$ . In contrast, the phase with one Majorana bound state per end is not affected by weak perturbations. The small perturbation  $m$  which breaks chiral symmetry could originate from a Zeeman field in  $y$  direction. Magnetic fields in  $x$  and  $z$  direction will not violate chiral symmetry. Such a chiral symmetry violating  $B_y$  field splits the two Majorana bound states at the end independent on if it is applied globally or as a local perturbation, e.g., due to the polarization of a spin polarized tip. In the case of two Majorana bound states, it should in principle be possible to observe a double unit of conductance  $4e^2/h$  in a transport experiment, which reduces to a single unit of conductance  $2e^2/h$  as soon as chiral symmetry is violated. Such interesting behavior is the main motivation for the following transport calculations.

### 3.3 Majorana bound states and Majorana tunnel couplings

In this section we look into the structure of the Majorana solutions and their possible couplings at lowest order. We consider that Majorana wavefunctions, which are harbored in a single chain, can overlap and couple to each other. Then we consider Majorana bound states in different chains separated by a Josephson junction which

couple through tunneling. Finally we focus on the Hamiltonian description of a spin-polarized tip which can couple to Majorana bound states and can be used to conduct tunneling conductance measurements. For each case, specific Majorana signatures will appear in the tunneling conductance spectrum.

### 3.3.1 Majorana wavefunctions and coupling between Majorana states

We solve the Schrödinger equation of a finite chain and retrieve the Majorana wavefunctions which have the form  $\Phi_{i,n}^\dagger = (u_{i,\uparrow,n}^*, u_{i,\downarrow,n}^*, u_{i,\uparrow,n}, u_{i,\downarrow,n})$ , where  $i$  is the site and  $n$  the index of the solution. The wavefunction satisfies the normalization condition  $\sum_{i,\sigma} |u_{i,\sigma,n}|^2 = 1/2$ . This condition implies that the Majorana operators fulfill the usual Majorana anticommutation relation  $\{\gamma_n, \gamma_m\} = \delta_{n,m}$ . Since we are interested in the physics of the Majorana states at low energy, we can focus only on the sector of these solutions and neglect BdG quasiparticles as long as their energy is higher than the bulk superconducting gap. This means we are only considering the physics of the in-gap states. Therefore we can approximate the electronic YSR states by their projection on the Majorana degrees of freedom and write them in the form  $\psi_{i,\sigma} \approx \sum_n u_{i,\sigma,n} \gamma_n$ .

Ideally the Majorana states remain unpaired [8] and located strictly at the ends of the chains and fixed at zero energy. This happens for infinitely long chains, for shorter chains coupling remains, which is exponentially suppressed with the length of the chain. The coupling between the distant Majorana states is given by the overlap of the Majorana wavefunctions and yields quasiparticles with finite energy splitting  $\delta\epsilon$ .

If there are multiple Majorana states per end in a chain, these states remain uncoupled in the presence of chiral symmetry. However the states couple if the symmetry is broken weakly by an additional term of strength  $m$ . Furthermore there is the possibility to couple Majorana states of different chains by tunneling through a junction between the chains.

The general Hamiltonian describing the coupled Majorana fermions is given by

$$\mathcal{H}_{\text{MF}} = \frac{i}{2} \sum_{n,m} \mathcal{M}_{nm} \gamma_n \gamma_m, \quad (3.18)$$

which is a sufficient description of the low energy physics as long as the couplings stay well below the superconducting bulk gap. Of the possible terms we note that the weakly chiral symmetry breaking term  $m$  is introduced on a phenomenological level and could correspond to appropriate external fields in an experimental setup. For the tunnel coupling between the chains we consider a particular model.

### 3.3.2 Hamiltonian for the tunnel coupling between the chains

For the tunneling between the chains we consider the electronic degrees of freedom of the superconductors. The assumption is that the chains are located on superconductors which are separated by an insulating thin film such that the result is a Josephson junction with a superconducting phase difference  $\delta\varphi$ . The phase difference can be imposed by inducing supercurrents through the junction or conceptually by gluing together the left and right sides of the superconducting substrate such that a certain flux can be enclosed by the loop.

We assume that the electrons of the superconductors are coupled via a Hamiltonian of the general form

$$\mathcal{H}_T = \sum_{i,j} \left[ \psi_{i,\sigma}^\dagger T_{i,j} e^{i(\varphi_i - \varphi_j)/2} \psi_{j,\sigma} + \text{H.c.} \right]. \quad (3.19)$$

For simplicity we consider an exponentially decaying profile for the tunneling coefficients, i.e.,

$$T_{i,j} = t \frac{1 - \text{sign}(ij)}{2} \exp \left[ -\frac{|ai - bj| - (a + b)}{l} \right]. \quad (3.20)$$

The specific form is chosen such that one of the chains is located on positive sites  $i, j > 0$  and the other on negative sites. The first term  $[1 - \text{sign}(ij)]/2$  ensures that tunneling happens only between the chains and not within one chain. The decay is controlled by the characteristic decay length  $l$  and  $a$  and  $b$  are the adatom spacings of the left and right chain. Furthermore the phases per site are given by  $\varphi_i = \text{sign}(i)\delta\varphi/2$ . Finally the coupling of the Majorana bound states between the chains takes the form

$$\mathcal{M}_{nm} = 4 \text{Im} \sum_{i,j,\sigma} u_{i,\sigma,n}^* T_{i,j} e^{i(\varphi_i - \varphi_j)/2} u_{j,\sigma,m}. \quad (3.21)$$

In the next section we consider the Hamiltonian of an spin-polarized STM tip and subsequently the coupling of the Majorana bound states to the tip.

### 3.3.3 Hamiltonian for spin-polarized STM tip

We first write the model for a spin-polarized STM tip. We assume that the electrons of the tip behave as electrons under the influence of a spin-splitting field  $\mathbf{P}$ . Since the goal is to couple the tip to the adatom chain, we index the tip with the site  $i$ , above which the tip is located. By keeping the index  $i$  we allow to address the case of a spin polarized tunneling microscope with multiple tips. In the most general case  $\mathbf{P}$  should

also be indexed by  $i$ . The electrons of the tip are created by the operator  $c_{\mathbf{k},\alpha,i}^\dagger$ . The tip electrons carry momentum  $\mathbf{k}$  and spin  $\alpha$ . Additional to the splitting field the tip feels a bias voltage  $V_i$ . This bias voltage drives the system out of equilibrium and leads to a tunneling current. In previous works non-magnetic tips in the normal [83, 84] and superconducting phase [83] were considered.

The Hamiltonian for the tip electrons has the form

$$\mathcal{H}_{\text{Tip},i} = \sum_{\mathbf{k},\alpha,\beta} [(\epsilon_{\mathbf{k}} - eV_i)\delta_{\alpha\beta} - \mathbf{P} \cdot \boldsymbol{\sigma}_{\alpha\beta}] c_{\mathbf{k},\alpha,i}^\dagger c_{\mathbf{k},\beta,i}. \quad (3.22)$$

The spin polarization can be parametrized by polar coordinates

$$\mathbf{P} = P(\cos \vartheta \sin \eta, \sin \vartheta \sin \eta, \cos \eta)^\top. \quad (3.23)$$

In the presence of a spin-polarization, the density of states  $\rho_\sigma(E)$  of the spin up and down electrons at an energy  $E$  is modified. The full density of states is given by the sum  $\rho(E) = \rho_\uparrow(E) + \rho_\downarrow(E)$ .

The difference is proportional to the polarization  $P \propto \rho_\uparrow(E) - \rho_\downarrow(E)$ . Furthermore we introduce a normalized density of states per spin  $\nu_\sigma = \rho_\sigma(E)/\rho(E)$  and a normalized polarization degree  $P_s = \nu_\uparrow - \nu_\downarrow \in [-1, +1]$ . The extreme values of  $P_s$  occur for fully spin-polarized tips. The polarization degree depends strongly on the material of the tip. It is possible to achieve full polarization by using a half-metal. For such a material one of the spin-bands does not cross the Fermi level and as such does not contribute to the polarization [92].

To simplify the further analysis we perform a rotation and diagonalize the Hamiltonian in spin-space. The term  $\mathbf{P} \cdot \boldsymbol{\sigma}$  can be diagonalized as follows

$$\hat{R} \mathbf{P} \cdot \boldsymbol{\sigma} \hat{R}^\dagger = P\sigma_z \quad \text{with} \quad \hat{R} = \exp(i\eta\sigma_y/2) \exp(i\vartheta\sigma_z/2). \quad (3.24)$$

Plugging in the rotated polarization yields the Hamiltonian

$$\mathcal{H}_{\text{Tip},i} = \sum_{\mathbf{k},\sigma=\pm} (\epsilon_{\mathbf{k},\sigma} - eV_i) \tilde{c}_{\mathbf{k},\sigma,i}^\dagger \tilde{c}_{\mathbf{k},\sigma,i}, \quad (3.25)$$

where  $\sigma = \pm$  labels the two eigenstates of  $\sigma_z$  and  $\epsilon_{\mathbf{k},\sigma} = \epsilon_{\mathbf{k}} - \sigma P$ . In the next section we discuss how the tip electrons couple to the Majorana states if we assume a certain tunneling from the tip electrons to the electronic degrees of freedom of the substrate.

### 3.3.4 Coupling between Majorana bound states and the tip

The spin polarized tip couples to the electronic degrees of freedom of the superconductor at site  $i$ . We write a phenomenological tunneling Hamiltonian of the form

$$\mathcal{H}_{\text{Tip-MF},i} = \sum_{\mathbf{k},\sigma} T_{\mathbf{k},i} c_{\mathbf{k},\sigma,i}^\dagger \psi_{i,\sigma} + \text{H.c.} . \quad (3.26)$$

The tunneling coefficient  $T_{\mathbf{k},i}$  is momentum dependent. However we assume that the tunneling does not depend on spin, such that spin is preserved. By expressing the YSR state operators  $\psi_{i,\sigma} \approx \sum_n u_{i,\sigma,n} \gamma_n$  approximately in terms of the Majorana operators we obtain the desired form which directly describes the coupling between tip electrons and Majorana states. After diagonalization in spin space the Hamiltonian takes the form

$$\mathcal{H}_{\text{Tip-MF},i} = \sum_{\mathbf{k},\sigma,n} \left( \mathcal{V}_{\mathbf{k},\sigma,i,n} \tilde{c}_{\mathbf{k},\sigma,i}^\dagger - \mathcal{V}_{\mathbf{k},\sigma,i,n}^* \tilde{c}_{\mathbf{k},\sigma,i} \right) \gamma_n . \quad (3.27)$$

The matrix elements which describe the coupling between the tip electrons and the Majorana states are given by

$$\mathcal{V}_{\mathbf{k},\sigma,i,n} = \sum_{\sigma'} T_{\mathbf{k},i} R_{\sigma,\sigma'} u_{i,\sigma',n} . \quad (3.28)$$

Using the tunneling Hamiltonian we can proceed to calculate the tunneling conductance  $dI_i/dV_i$  through the Majorana states. We are particularly interested in the tunneling conductance at  $V_i = 0$  and show the occurrence of a zero bias peak. Furthermore the goal is to study how this zero bias peak changes for different scenarios, e.g., overlapping Majorana states in a short chain or multiple coupled Majorana states in multiple chains.

## 3.4 Tunneling conductance signatures of Majorana spin character

In this section we discuss signatures of the Majorana bound states in tunneling conductance measurements. At first we review the method to compute the tunneling conductance within the Keldysh formalism and proceed with the signatures in different setups. In particular we discuss the consequences of using a spin polarized tip in the scanning tunneling microscope. The polarization allows to unveil additional features of the Majorana bound states.

### 3.4.1 Calculation of the tunneling conductance

In this section we proceed with the calculation of the differential tunneling conductance  $dI_i/dV_i$ . At first we derive the Heisenberg operator for the current through the tip at site  $i$ . The current is given by the time derivative of the electron number operator times the electron charge  $e$

$$\hat{I}_i(t) = -e\dot{N}_{\text{Tip}}(t) = -e \sum_{\mathbf{k},\sigma} \frac{d}{dt} \left( \tilde{c}_{\mathbf{k},\sigma,i}^\dagger(t) \tilde{c}_{\mathbf{k},\sigma,i}(t) \right). \quad (3.29)$$

Via the Heisenberg equation and by neglecting fluctuations in the electron number of the tip the current operator in the Heisenberg picture takes the form

$$\hat{I}_i(t) = -\frac{e\imath}{\hbar} \sum_{\mathbf{k},\sigma} \left[ \mathcal{H}_{\text{Tip-MF},i}, \tilde{c}_{\mathbf{k},\sigma,i}^\dagger \tilde{c}_{\mathbf{k},\sigma,i} \right] (t). \quad (3.30)$$

Transforming from the Heisenberg to the Schrödinger picture yields

$$\hat{I}_i = \frac{e\imath}{\hbar} \sum_{\mathbf{k},\sigma,n} \left( \mathcal{V}_{\mathbf{k},\sigma,i,n} \tilde{c}_{\mathbf{k},\sigma,i}^\dagger + \mathcal{V}_{\mathbf{k},\sigma,i,n}^* \tilde{c}_{\mathbf{k},\sigma,i} \right) \gamma_n. \quad (3.31)$$

The current is given by the expectation value of the current operator  $I_i(t) \equiv \langle \hat{I}_i(t) \rangle$ , which takes the form

$$I_i(t) = \frac{2e}{\hbar} \sum_{\mathbf{k},\sigma,n} \text{Im} \left[ \mathcal{V}_{\mathbf{k},\sigma,i,n}^* \langle \gamma_n(t) \tilde{c}_{\mathbf{k},\sigma,i}(t) \rangle \right] = -\frac{2e}{\hbar} \sum_{\mathbf{k},\sigma,n} \text{Re} \left[ \mathcal{V}_{\mathbf{k},\sigma,i,n}^* G_{\mathbf{k},\sigma,i,n}^<(t,t) \right]. \quad (3.32)$$

Here we introduced the lesser mixed Green's function  $G_{\mathbf{k},\sigma,i,n}^<(t,t') \equiv \imath \langle \gamma_n(t') \tilde{c}_{\mathbf{k},\sigma,i}(t) \rangle$ , which involves both the Majorana and the electronic operator.

To calculate this expectation value we employ the Keldysh formalism following the method of Ref. [72]. At first we introduce the retarded and advanced Majorana Green's functions

$$\mathcal{G}_{nm}^R(t,t') \equiv -\imath \Theta(t-t') \langle \gamma_n(t) \gamma_m(t') \rangle, \quad (3.33)$$

$$\mathcal{G}_{nm}^A(t,t') \equiv \imath \Theta(t'-t) \langle \gamma_n(t) \gamma_m(t') \rangle. \quad (3.34)$$

We obtain the result

$$I_i = \frac{e}{\hbar} \int_{-\infty}^{+\infty} d\omega \mathcal{T}_i(\omega) [n_F(\omega - eV_i) - n_F(-\omega + eV_i)], \quad (3.35)$$

with the Fermi-Dirac distribution  $n_F(\omega)$  at energy  $\omega$  and a transmission coefficient  $\mathcal{T}_i(\omega)$ , as in the Landauer-Büttiker formalism. The transmission coefficient

$$\mathcal{T}_i(\omega) \equiv \text{tr} \left[ \widehat{\mathcal{G}}^R(\omega) \widehat{\Gamma}^{i*}(-\omega) \widehat{\mathcal{G}}^A(\omega) \widehat{\Gamma}^i(\omega) \right] \quad (3.36)$$

involves the Green's functions and linewidth matrices  $\widehat{\Gamma}^i(\omega)$ . However compared to the usual Landauer formula for ballistic transport, in this equation the second Fermi-Dirac distribution corresponds to holes. This modification of the formula is a consequence of the transport through Majorana states which are formed by an equal superposition of electrons and holes

The matrix elements of the linewidth matrices are given by

$$\Gamma_{nm}^i(\omega) = 2\pi \sum_{\mathbf{k}, \sigma} \mathcal{V}_{\mathbf{k}, \sigma, i, n}^* \mathcal{V}_{\mathbf{k}, \sigma, i, m} \delta(\omega - \epsilon_{\mathbf{k}, \sigma}). \quad (3.37)$$

We adopt the wideband approximation, where the linewidth matrix elements are energy independent, i.e.,  $\Gamma_{nm}^i(\omega) \equiv \Gamma_{nm}^i$ .

Furthermore we assume that the tunneling coefficient  $\mathbb{T}_{\mathbf{k}, i} = \mathbb{T}$  is  $\mathbf{k}$  independent and set the DOS of the tip to approximately  $\rho_\sigma(E_F)$  which corresponds to the most relevant contribution. Using these approximations we obtain

$$\Gamma_{nm}^i = \Gamma \mathbf{u}_{i, n}^\dagger \frac{\mathbb{1} + P_s \hat{\mathbf{P}} \cdot \boldsymbol{\sigma}}{2} \mathbf{u}_{i, m}, \quad (3.38)$$

with normalization constant  $\Gamma = 2\pi\rho(E_F)|\mathbb{T}|^2$ ,  $\mathbf{u}_{i, n}^\dagger = (u_{i, \uparrow, n}^*, u_{i, \downarrow, n}^*)$  and the polarization direction  $\hat{\mathbf{P}} = \mathbf{P}/P$ .

To obtain the transmission coefficient we calculate the retarded and advanced Majorana matrix Green's functions given by

$$\widehat{\mathcal{G}}^R(\omega) = \left( \omega \mathbb{1} - i\widehat{\mathcal{M}} + i \text{Re} \widehat{\Gamma}^i \right)^{-1}, \quad (3.39)$$

and  $\widehat{\mathcal{G}}^A(\omega) = [\widehat{\mathcal{G}}^R(\omega)]^\dagger$ . Here  $\widehat{\mathcal{M}}$  couples the different Majorana states. Furthermore we assumed that the self-energies of the Majorana Green's functions only contain the linewidth. In our further analysis of different setups we focus on the zero temperature tunneling conductance given by

$$\frac{dI_i}{dV_i} = \frac{2e^2}{h} \mathcal{T}_i(eV). \quad (3.40)$$

We perform numerical calculations and usually set  $\Gamma = 1$  for convenience.

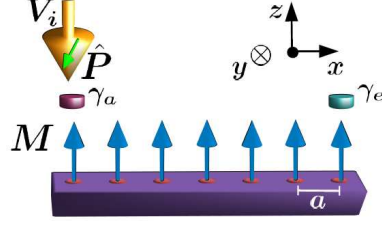


Figure 3.5: Ferromagnetic adatom chain probed by a spin-polarized STM tip, which couples locally to the electronic density below it. Given a long chain only the  $\gamma_a$  Majorana bound state contributes to the tunneling conductance. For short chains both Majorana bound states contribute.

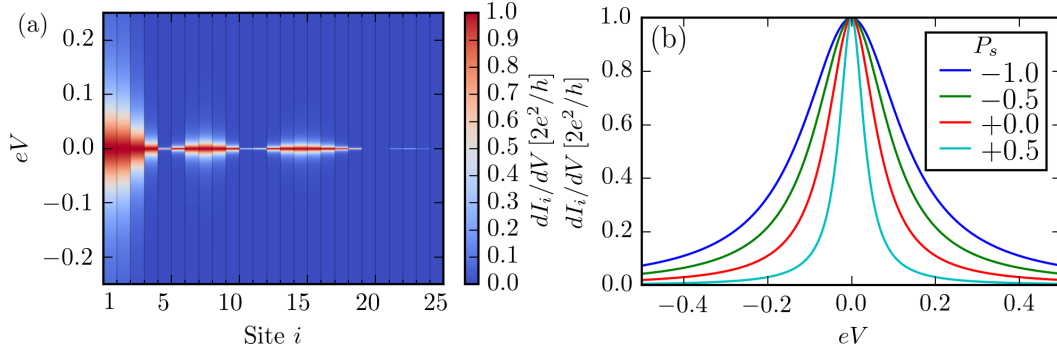


Figure 3.6: Tunneling conductance for a tip coupled to a single Majorana bound state at the end of a chain with  $N = 100$  sites. (a) Spatial profile of the conductance for an unpolarized tip ( $P_s = 0$ ). (b) Conductance at site  $i = 1$  for a tip polarized in  $x$ -direction. The polarization degree  $P_s$  modifies the broadening of the zero bias peak.

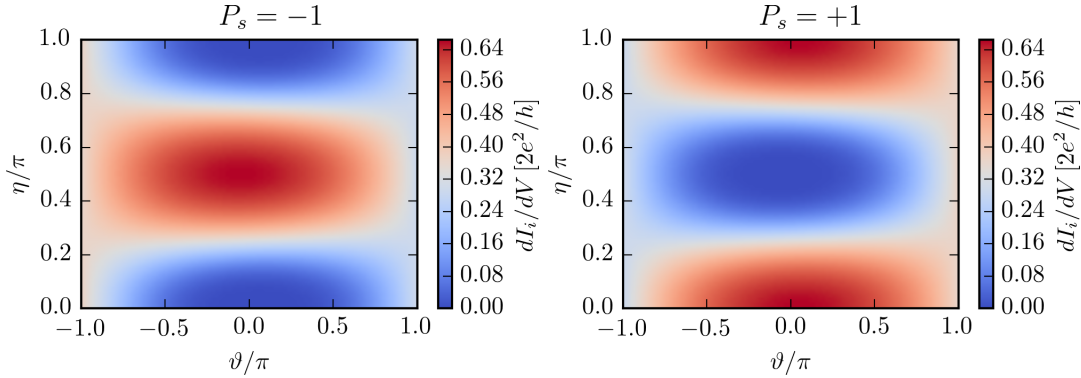


Figure 3.7: Tunneling conductance as a function of the polarization angles ( $\vartheta, \eta$ ) for a fully polarized tip  $P_s = \pm 1$ . The tip is coupled to a single Majorana bound state at the  $i = 1$  site in a chain with  $N = 100$  sites. The strong anisotropy is one of the characteristic signatures of bound states with spin character, like  $\gamma_a$ . Parameters:  $\xi_0 = 80$ ,  $k_F = 6.0$ ,  $\alpha = 0.01$  and  $M = 0.85$ .

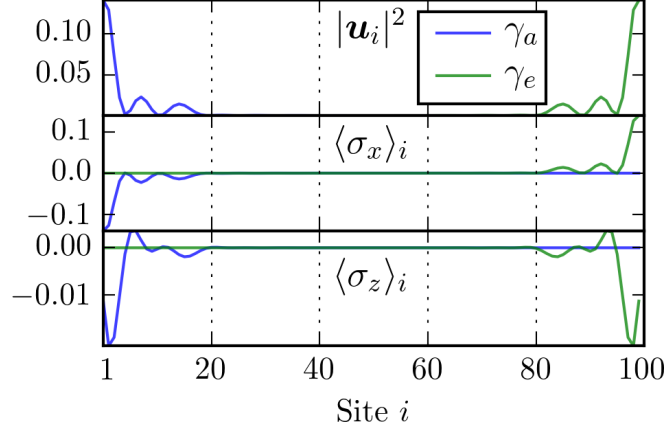


Figure 3.8: Majorana wavefunctions in a chain with  $N = 100$  sites. There is a single Majorana bound state per end of the chain. The plot shows the local spectral weight  $|\mathbf{u}_i|^2$  and electronic spin polarization  $\langle \sigma \rangle_i$  at site  $i$ . The spin polarization in  $y$  direction is omitted since it vanishes exactly due to time reversal symmetry  $\Theta = \mathcal{K}$ .

### 3.4.2 Single adatom chain with a single Majorana state per end

Now we discuss the simplest scenario of an isolated adatom chain with a single Majorana per end as shown in Fig. 3.5. In this case one finds a single Lorentzian peak in the conductance curve. Similar to the result in Ref. [72] we obtain

$$\frac{dI_i}{dV} = \frac{2e^2}{h} \frac{(\Gamma_{aa}^i)^2}{(eV)^2 + (\Gamma_{aa}^i)^2}. \quad (3.41)$$

In the equation and in the rest of this chapter we set  $V_i \equiv V$  for convenience. The peak appears at  $V = 0$ , hence called zero bias peak. We plot the curve in Fig. 3.6. The broadening of the peak is given by

$$\Gamma_{aa}^i = \Gamma_{\mathbf{u}_{i,a}}^\dagger \frac{\mathbb{1} + P_s \hat{\mathbf{P}} \cdot \boldsymbol{\sigma}}{2} \mathbf{u}_{i,a}. \quad (3.42)$$

The difference in our analysis is the inclusion of the polarization of the tip, which modifies the Majorana signature and opens new possibilities to pinpoint the presence of a Majorana bound state.

From the above equation one observes that if  $\hat{\mathbf{P}} \cdot \boldsymbol{\sigma} \mathbf{u}_{i,a} = -\mathbf{u}_{i,a}$  the linewidth term reduces to  $\Gamma_{aa}^i = \nu_\downarrow \Gamma_{\mathbf{u}_{i,a}}^\dagger \mathbf{u}_{i,a}$ . In this case the tunneling conductance will vanish for a fully spin polarized tip with  $\nu_\downarrow = 0$ . For these special conditions, the spin-polarization of the tip electrons is antiparallel to the polarization of the electrons at the end of the

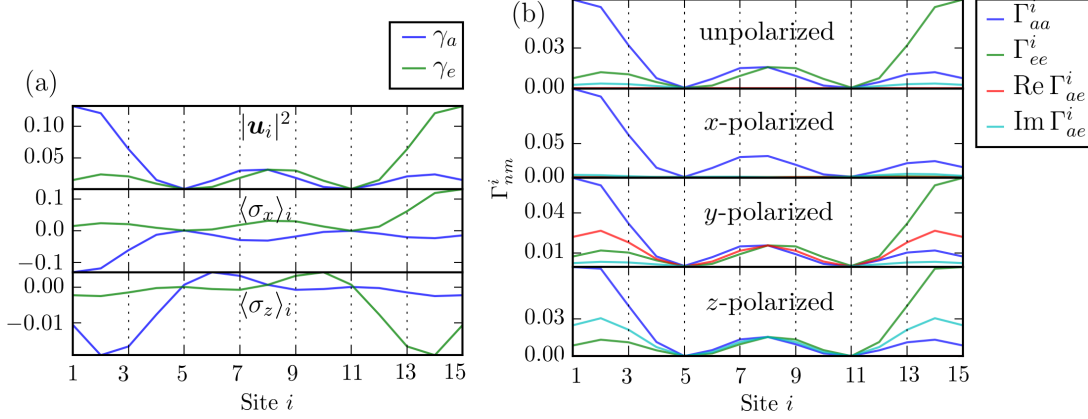


Figure 3.9: (a) Majorana wavefunctions in a short chain with  $N = 15$  sites. The plots show the local spectral weight and the electronic spin-polarization of the wavefunctions. Because of the short chain the two Majorana bound states hybridize and form finite energy quasiparticle excitations. However the spin signature coincides mostly with the signatures of bound states in a longer chain. (b) Non-zero matrix elements of the linewidth matrix  $\hat{\Gamma}^i$  for a short chain with  $N = 15$ . We consider a full polarized tip  $P_s = 1$  in different directions. Parameters for both plots:  $\xi_0 = 80$ ,  $k_F = 6.0$ ,  $\alpha = 0.01$  and  $M = 0.85$ .

adatom chain  $\langle \boldsymbol{\sigma} \rangle_i = \mathbf{u}_{i,a}^\dagger \boldsymbol{\sigma} \mathbf{u}_{i,a}$ , which is induced by the Majorana bound state. Since the tunneling is spin conserving the coupling of tip and Majorana bound states must necessarily drop to zero. We plot the polarization dependence in Fig. 3.7.

In Fig. 3.8 we plot the spin-polarization of the Majorana bound states. One observes that the polarization is confined to the  $xz$ -plane, which is a result of time reversal symmetry  $\Theta = \mathcal{K}$ . This symmetry enforces that the spin-part of the wavefunction is real. We note that a similar result for the spin polarization profile was previously obtained for nanowire based topological superconductors in Ref. [93]. The characteristic anisotropic dependence of the tunneling conductance on the polarization angles  $\vartheta$  and  $\eta$  was pointed out before in Ref. [87], which studies spin selective Andreev reflections due to Majorana fermions. They conclude that Majorana fermions can therefore be used to create fully spin-polarized currents in paramagnetic leads.

Now we take the possibility into account, that the Majorana bound states living at the two ends of the chain couple. The coupling is proportional to the overlap of the wavefunctions which is exponentially suppressed with the length of the chain. Since in experiments the chains are relatively short this scenario is relevant [6]. The overlap of the Majorana wave functions will generate a coupling of the form  $i\delta\epsilon\gamma_a\gamma_e$ , where  $\gamma_a$  corresponds to the Majorana below the tip and  $\gamma_e$  is the Majorana on other side of the

chain. The coupling will lead to finite energy excitations and will move the Majorana bound states away from zero energy. We consider a chain with 15 sites and plot the Majorana wavefunctions in Fig. 3.9( a).

The couplings give rise to the coupling matrices of the form

$$\widehat{\mathcal{M}} = \begin{pmatrix} 0 & \delta\epsilon \\ -\delta\epsilon & 0 \end{pmatrix} \quad \text{and} \quad \widehat{\Gamma}^i = \begin{pmatrix} \Gamma_{aa}^i & \Gamma_{ae}^i \\ (\Gamma_{ae}^i)^* & \Gamma_{ee}^i \end{pmatrix}. \quad (3.43)$$

In particular the tip also couples weakly to the Majorana  $\gamma_e$  on the other side of the chain. The matrix elements of the  $\widehat{\Gamma}$  are shown in Fig. 3.9(b).

We obtain the tunneling conductance formula

$$\begin{aligned} \frac{dI_i}{dV} &= \frac{2e^2}{h} \left\{ 2 \left[ \det(\text{Re } \widehat{\Gamma}^i) + \delta\epsilon^2 \right] \det \widehat{\Gamma}^i \right. \\ &\quad \left. + (eV)^2 \left[ \left( \Gamma_{aa}^i \right)^2 + \left( \Gamma_{ee}^i \right)^2 + 2 \left( \text{Re}^2 \Gamma_{ae}^i - \text{Im}^2 \Gamma_{ae}^i \right) \right] \right\} \\ &\quad \times \left\{ \left[ (eV)^2 - \delta\epsilon^2 - \det(\text{Re } \widehat{\Gamma}^i) \right]^2 + (eV)^2 \left( \Gamma_{aa}^i + \Gamma_{ee}^i \right)^2 \right\}^{-1}. \end{aligned} \quad (3.44)$$

For  $V = 0$  this equation simplifies to

$$\left. \frac{dI_i}{dV} \right|_{V=0} = 2 \cdot \frac{2e^2}{h} \frac{\Gamma_{aa}^i \Gamma_{ee}^i - |\Gamma_{ae}^i|^2}{\Gamma_{aa}^i \Gamma_{ee}^i - \text{Re}^2 \Gamma_{ae}^i + \delta\epsilon^2}, \quad (3.45)$$

which is the height of the residual zero bias conductance. We note that the zero bias tunneling conductance persists even though the tip accesses both Majorana bound states. However the spectral weight at  $V = 0$  is heavily reduced compared to the case with only one Majorana involved in the tunneling. The residual spectral weight disappears for  $\Gamma_{ee}^i = \Gamma_{ae}^i = 0$  as can be seen from the equation. This means that the residual weight at  $V = 0$  is due to the coupling of the tip to the  $\gamma_e$  Majorana, which is away from the tip.

More significant than the residual weight at  $V = 0$  are two finite bias peaks appearing at  $eV = \pm \sqrt{\delta\epsilon^2 + \det(\text{Re } \widehat{\Gamma}^i)}$ . The peaks are split away from zero by the overlap energy  $\delta\epsilon$  and the correction from the determinant of  $\widehat{\Gamma}^i$ . The height of these finite bias peaks is given by

$$\left. \frac{dI_i}{dV} \right|_{\text{FBPs}} = \frac{2e^2}{h} \frac{(\Gamma_{aa}^i + \Gamma_{ee}^i)^2 - 4 \text{Im}^2 \Gamma_{ae}^i}{(\Gamma_{aa}^i + \Gamma_{ee}^i)^2}. \quad (3.46)$$

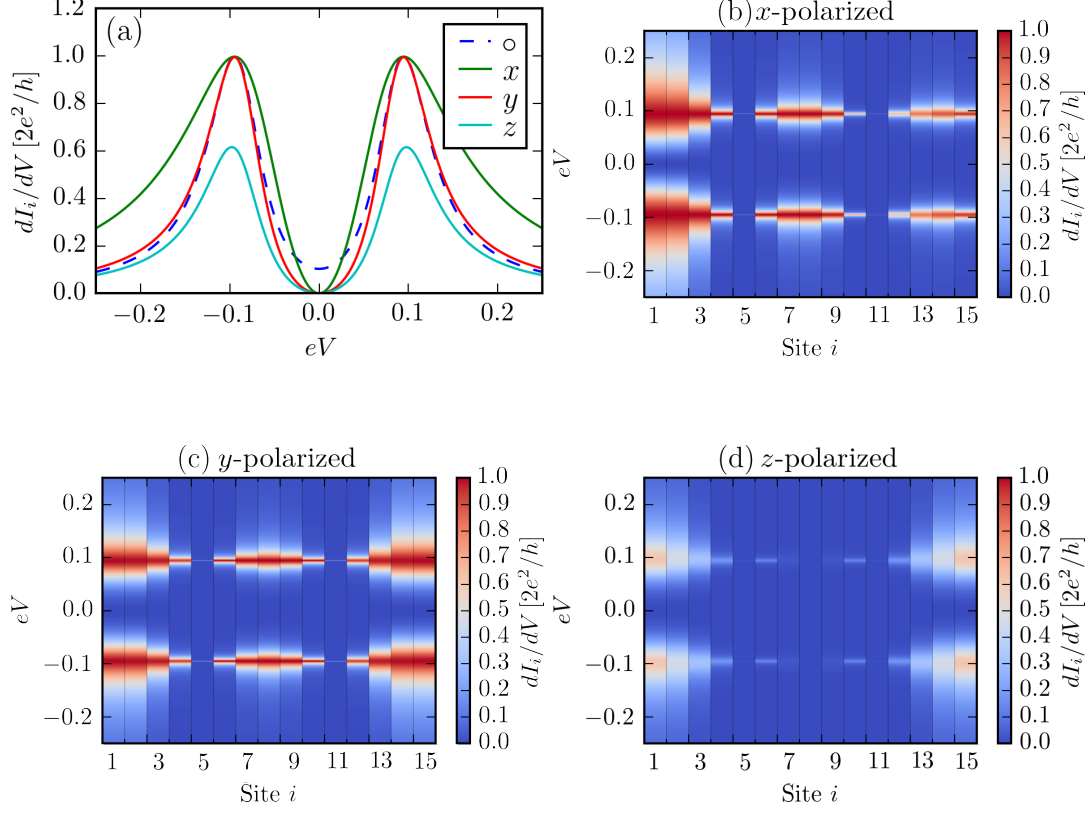


Figure 3.10: Tunneling conductance for a short chain with  $N = 15$  sites. Each end of the chain hosts one Majorana bound state. (a) Conductance profile at site  $i = 1$  for spin unpolarized ( $\circ$ ) and fully polarized tip in  $x, y, z$  direction. The zero bias peak splits into two finite bias peaks. For an unpolarized tip residual spectral weight remains at  $V = 0$ . The spin anisotropy due to the Majorana bound states results in different heights of the finite bias peaks for polarization in  $z$ -direction. However for a polarization in  $xy$ -plane or an unpolarized tip, the conductance remains equal to  $2e^2/h$ . We show the spatial profile in (b-d) for fully polarized tips in  $x, y, z$  direction. In particular note the asymmetry in (b). Parameters:  $\xi_0 = 80$ ,  $k_F = 6.0$ ,  $\alpha = 0.01$  and  $M = 0.85$ .

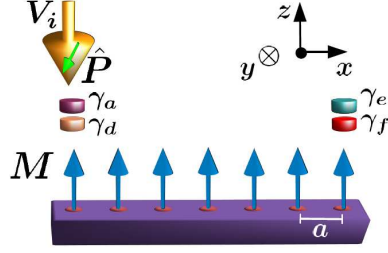


Figure 3.11: Single adatom chain with two Majorana bound states per end, which are protected by chiral symmetry. Only the Majorana bound states below the tip contribute to the tunneling conductance for sufficiently long chains. Tip polarization in  $y$  direction can locally break chiral symmetry even in the absence of additional symmetry breaking fields.

We note that the finite peaks assume the ideal height  $2e^2/h$  only if  $\text{Im} \Gamma_{ae}^i = 0$ . We plot the resulting conductance curve in Fig. 3.10. From the plot, one can observe that the height stays in almost all cases equal to the ideal value. The only special case occurs if the magnetic tip is polarized in  $z$  direction, where we find a much smaller tunneling conductance. In a recent experiment exactly that configuration was used [6], and our model could possibly explain the highly reduced signal. However a significant reduction of the peak height is due to broadening because of finite temperature.

In our model a tip polarization in  $x$  or  $y$  direction will lead to a tunneling conductance almost equal to the idealized value. Interestingly the zero bias peaks appear for short chains of  $N = 15$  sites. From this we conclude that spin polarized measurements are a powerful method to detect and analyze Majorana bound states in adatom chains.

Now we also consider the simpler case where the tip does not couple to the Majorana  $\gamma_e$  which is away from the tip. We obtain the result from Ref. [72], i.e.,

$$\frac{dI_i}{dV} = \frac{2e^2}{h} \frac{(eV)^2 (\Gamma_{aa}^i)^2}{[(eV)^2 - \delta\epsilon^2]^2 + (eV)^2 (\Gamma_{aa}^i)^2}. \quad (3.47)$$

where no residual spectral weight is left at  $V = 0$ . Here the zero bias peak splits completely in two finite peaks which appear at the splitting energies  $eV = \pm\delta\epsilon$ .

### 3.4.3 Single adatom chain with two Majorana states per end

Now we proceed with the case of a single chain and two Majorana bound states per end. The tip can possibly probe both of those Majorana bound states. The scenario is illustrated in Fig. 3.11. The necessary condition for the presence of two Majorana states is that chiral symmetry is preserved. Experimentally this situation is difficult to

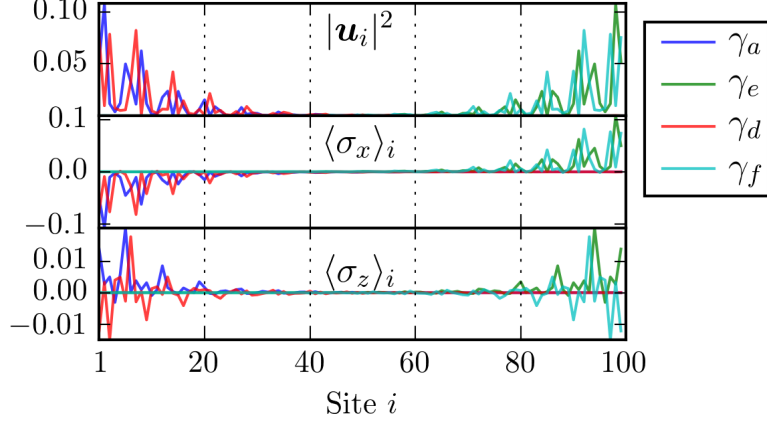


Figure 3.12: Spectral weight  $|\mathbf{u}_i|^2$  and spin-polarization of Majorana wavefunctions in chain with  $N = 100$  sites. The  $y$  component of the spin polarization vanishes. Parameters:  $N = 100$ ,  $\xi_0 = 80$ ,  $k_F = 6.0$ ,  $\alpha = 0.01$  and  $M = 0.85$ .

achieve and up to now there have not been experiments claiming the detection of two states. However the phase should be accessible in principle, based on the fact that it can be engineered starting from the phase with one Majorana bound state per end as for example in a recent experiment [6]. To achieve the phase with two Majorana bound states a topological phase transition has to take place which is triggered by varying the parameters of the setup, in particular the spacing of the adatoms, the strength of the magnetic field or the strength of the spin orbit coupling as described in Ref. [2].

Now we analyze the tunneling conductance in the presence of two Majorana bound states. For simplicity we focus on the case where the chain is long such that a restriction to the Majorana states below the tip is justified. This means that neither the coupling of the tip and the bound states far away nor the overlap between the bound states themselves play a role. Thus there are two Majorana operators  $\gamma_a$  and  $\gamma_d$  which are relevant and couple to the tip.

Additionally they can couple to each other by a matrix element  $m$  which corresponds to weakly broken chiral symmetry. Such a chiral symmetry breaking can be induced by a tip with a polarization component in  $y$  direction or an external field. The coupling matrices for the setup under consideration are given by

$$\widehat{\mathcal{M}} = \begin{pmatrix} 0 & m \\ -m & 0 \end{pmatrix} \quad \text{and} \quad \widehat{\Gamma}^i = \begin{pmatrix} \Gamma_{aa}^i & \Gamma_{ad}^i \\ (\Gamma_{ad}^i)^* & \Gamma_{dd}^i \end{pmatrix}. \quad (3.48)$$

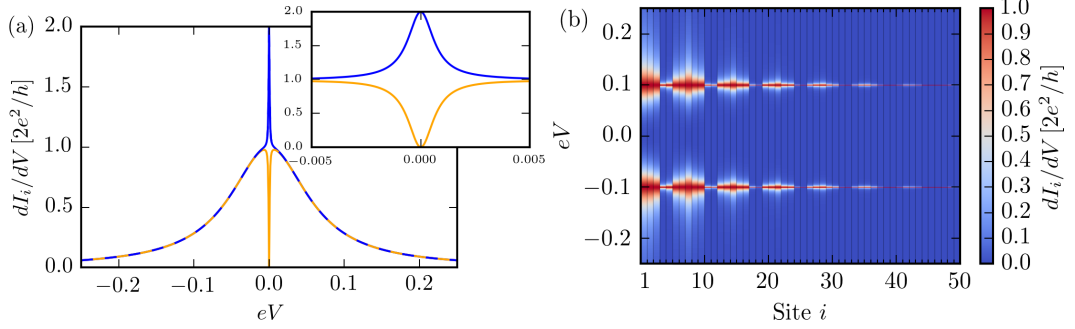


Figure 3.13: (a) Conductance profile at site  $i = 1$  and zero bias peak when chiral symmetry is preserved. At a small crossover voltage the spike-like profile switches to a broad hump. The curve arises due to the combination of the two peaks of  $\gamma_a$  and  $\gamma_d$  with much different widths. The blue curve is the full conductance while the orange curve corresponds only to the second summand in Eq. (3.50). The inset zooms in around  $V = 0$ . (b) Spatial conductance profile for broken chiral symmetry  $m = 0.1$  and unpolarized tip. Parameters:  $N = 100$ ,  $\xi_0 = 80$ ,  $k_F = 6.0$ ,  $\alpha = 0.01$  and  $M = 0.85$ .

We note that these matrices are identical to Eq. (3.43) for the replacements  $\delta\epsilon \mapsto m$  and  $e \mapsto d$ . Correspondingly the tunneling conductance can be obtained from Eq. (3.44). For example in the case of  $V = 0$  one obtains

$$\left. \frac{dI_i}{dV} \right|_{V=0} = 2 \cdot \frac{2e^2}{h} \frac{\Gamma_{aa}^i \Gamma_{dd}^i - |\Gamma_{ad}^i|^2}{\Gamma_{aa}^i \Gamma_{dd}^i - \text{Re}^2 \Gamma_{ad}^i + m^2}. \quad (3.49)$$

It is important to note that the off-diagonal linewidth elements  $\Gamma_{ad}^i$  cannot be neglected since the two Majorana bound states, which are protected by chiral symmetry are located at the same sites of the chain. In the previously discussed case in Section 3.4.2 and in Ref. [72] the off-diagonal elements are not as crucial as here.

As in the case for single Majorana bound states the zero bias peak persists and the value depends on the strength of the chiral symmetry breaking  $m$  and  $\text{Im} \Gamma_{ad}^i$ . The spin-polarization of the Majorana wavefunctions is confined to the  $xz$ -plane as shown in Fig. 3.12. Additionally both wavefunctions are real, which has the consequence that a tip polarization in  $y$ -direction leads to finite values of both  $m$  and  $\text{Im} \Gamma_{ad}^i$ . On the other hand for a spin-polarization in the  $xz$ -plane or a tip without polarization we find  $m = \text{Im} \Gamma_{ad}^i = 0$ . This corresponds to a zero bias peak with the double quantum  $4e^2/h$ . This means that the Majorana bound states act as if they were unpaired [8, 72].

The tunneling spectrum in this case with  $m = \text{Im} \Gamma_{ad}^i = 0$  has the form

$$\frac{dI_i}{dV} = \frac{2e^2}{h} \frac{2 \det^2(\hat{\Gamma}^i) + (eV)^2 \left[ (\Gamma_{aa}^i)^2 + (\Gamma_{dd}^i)^2 + 2(\Gamma_{ad}^i)^2 \right]}{\left[ (eV)^2 - \det \hat{\Gamma}^i \right]^2 + (eV)^2 (\Gamma_{aa}^i + \Gamma_{dd}^i)^2}. \quad (3.50)$$

The first summand leads to the aforementioned double quantum of the zero bias conductance. This can be seen in Fig. 3.13 which shows a sharp peak at  $V = 0$ . The second term is relevant for  $eV > \min\{\Gamma_{aa}^i, \Gamma_{dd}^i\}$ , where the curve switches from the sharp peak to a broader bell-like curve. This behavior happens even for uncoupled bound states with  $\Gamma_{ad}^i = 0$  and  $\Gamma_{aa}^i > \Gamma_{dd}^i$ . In particular the equation can be rewritten as

$$\frac{dI_i}{dV} = \frac{2e^2}{h} \left( \frac{(\Gamma_{aa}^i)^2}{(\Gamma_{aa}^i)^2 + (eV)^2} + \frac{(\Gamma_{dd}^i)^2}{(\Gamma_{dd}^i)^2 + (eV)^2} + \mathcal{O} \left[ (\Gamma_{ad}^i)^2 \right] \right). \quad (3.51)$$

We observe that the double conductance arises due to the coupling of the tip to the separate Majorana bound states. Each of the bound states provides a separate peak. Since  $\Gamma_{aa}^i > \Gamma_{dd}^i$  the peak corresponding to  $\gamma_a$  is much broader than the peak corresponding to  $\gamma_d$ .

Interestingly in the situation with two Majorana bound states there is a special case where the conductance peak looks identical to the case with one Majorana bound state. Therefore the presence of two bound states in such a case could be misinterpreted in the experiment. This happens when chiral symmetry is preserved  $m = 0$  and when the special condition  $\Gamma_{aa}^i \Gamma_{dd}^i = (\Gamma_{ad}^i)^2 = \text{Re}^2 \Gamma_{ad}^i$  holds. Then the conduction formula reduces to

$$\frac{dI_i}{dV} = \frac{2e^2}{h} \frac{(\Gamma_{aa}^i + \Gamma_{dd}^i)^2}{(eV)^2 + (\Gamma_{aa}^i + \Gamma_{dd}^i)^2}, \quad (3.52)$$

which is the same result as for a single Majorana per end, where  $\Gamma_{aa}^i + \Gamma_{dd}^i$  plays the role of an effective broadening.

#### 3.4.4 Two coupled adatom chains, both with one Majorana state per end

Now we consider two chains where the Majorana bound states of the chains couple via tunneling through a junction. We illustrate the situation in Fig. 3.14. This kind of scenario is interesting since it allows to probe the  $4\pi$ -periodic Josephson effect. For simplicity we assume that the chains are long enough, such that the Majorana bound states away from the junction do not contribute. Therefore only two Majorana bound

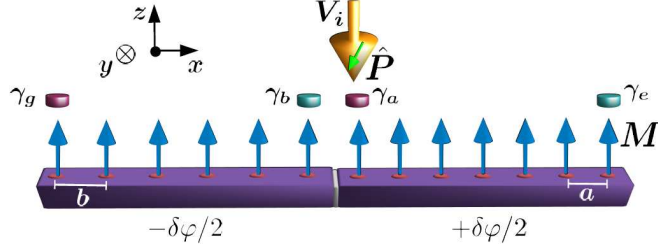


Figure 3.14: Two adatom chains coupled via a Josephson junction with one Majorana bound state per chain end. Only the Majorana bound states near the junction contribute for sufficiently long chains. Only  $\gamma_a$  couples directly to the tip. The Josephson coupling of the two Majorana bound states  $\gamma_a$  and  $\gamma_b$  is  $4\pi$ -periodic.

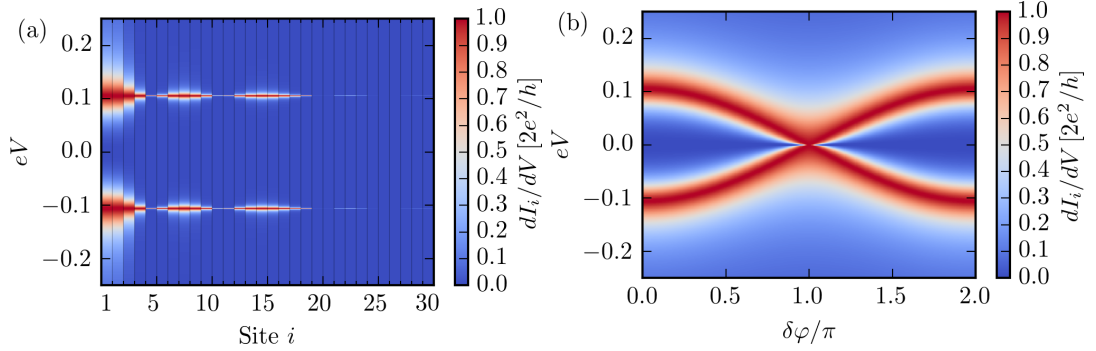


Figure 3.15: (a) Spatial profile of the tunneling conductance for  $\delta\varphi = 0$ . There are two finite bias peaks at  $eV = \pm M(\delta\varphi)$ . (b) The tunneling conductance at site  $i = 1$  is  $2\pi$ -periodic over  $\delta\varphi$ . For  $\delta\varphi = \pi$  one obtains a zero bias peak. Parameters: Tunneling constant  $t = 0.1$ , decay length  $l = 10$  in units of  $a = b = 1$ .

states are involved in the tunneling processes. The Josephson coupling of the Majorana bound states due to tunneling through the junction can be written in the form

$$M = 4 \operatorname{Im} \sum_{i,j,\sigma} u_{i,\sigma,a}^* T_{i,j} e^{i(\varphi_i - \varphi_j)/2} u_{j,\sigma,b} \quad (3.53)$$

with tunneling coefficients  $T_{i,j}$ . In particular, the Josephson coupling is  $4\pi$ -periodic in the phase difference. The matrices describing the coupling between the Majorana bound states and between Majorana bound states and tip are given by

$$\widehat{\mathcal{M}} = \begin{pmatrix} 0 & M \\ -M & 0 \end{pmatrix} \quad \text{and} \quad \widehat{\Gamma}^i = \begin{pmatrix} \Gamma_{aa}^i & 0 \\ 0 & 0 \end{pmatrix}. \quad (3.54)$$

Using these coupling matrices we obtain the tunneling conductance

$$\frac{dI_i}{dV} = \frac{2e^2}{h} \frac{(eV)^2 (\Gamma_{aa}^i)^2}{[(eV)^2 - M^2]^2 + (eV)^2 (\Gamma_{aa}^i)^2} \quad (3.55)$$

which again results in two finite bias peaks. If a phase difference  $\delta\varphi = \phi_i - \phi_j$  between the superconductors below the chains is imposed,  $M$  modifies the location of the peaks. In particular the tunneling conductance at a fixed location is  $2\pi$  periodic due to the  $4\pi$ -periodic coupling  $\propto \cos(\delta\varphi/2)$  between the Majorana bound states  $\gamma_a$  and  $\gamma_b$ . We plot our results in Fig. 3.15.

### 3.4.5 Two coupled adatom chains: One Majorana state below the tip and two in the other chain

Now we consider the scenario where two chains are in different topological states with one and two Majorana bound states respectively. The two chains are connected by a junction and we focus on the bound states near the junction and neglect the Majorana bound states which live far away in the chains. We assume that the tip is located above the single Majorana  $\gamma_a$  and couples only to this Majorana. The setup is illustrated in Fig. 3.16. Then the coupling matrices of our model are given by

$$\widehat{\mathcal{M}} = \begin{pmatrix} 0 & M_{ab} & M_{ac} \\ -M_{ab} & 0 & m_{bc} \\ -M_{ac} & -m_{bc} & 0 \end{pmatrix} \quad \text{and} \quad \widehat{\Gamma}^i = \begin{pmatrix} \Gamma_{aa}^i & 0 & 0 \\ 0 & 0 & 0 \\ 0 & 0 & 0 \end{pmatrix}. \quad (3.56)$$

Here the Majorana couplings  $M_{ab}$  and  $M_{ac}$  arise from the interchain tunneling through the junction as before. In contrast  $m_{bc}$  arises due to breaking of chiral symmetry within the left or even in both chains. We note that violation of chiral symmetry does not modify the wavefunction of  $\gamma_a$  and leaves the coupling matrices unchanged. We find the following equation for the tunneling conductance

$$\frac{dI_i}{dV} = \frac{2e^2}{h} \frac{[(eV)^2 - m_{bc}^2]^2 (\Gamma_{aa}^i)^2}{(eV)^2 [(eV)^2 - \mathcal{M}^2]^2 + (\Gamma_{aa}^i)^2 [(eV)^2 - m_{bc}^2]^2}, \quad (3.57)$$

with  $\mathcal{M} = \sqrt{M_{ab}^2 + M_{ca}^2 + m_{bc}^2}$ . For  $V = 0$  this equation yields a zero bias peak. This is consistent with the rule derived in Ref. [72], which states that an odd number of coupled Majorana bound states leads to the emergence of a zero bias peak.

Additionally to the zero bias peak there are two finite bias peaks of conductance  $2e^2/h$  at  $eV = \pm\mathcal{M}$ . Now we discuss the case with preserved chiral symmetry, i.e.,

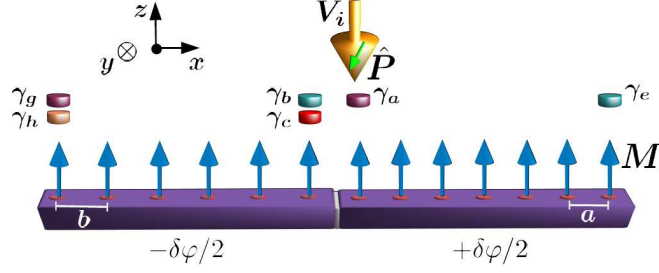


Figure 3.16: Two adatom chains coupled via a Josephson junction, where the two chains host one and two Majorana bound states per end respectively. The Majorana bound states far away from the junction are not taken into account. Only  $\gamma_a$  couples to the tip. Chiral symmetry breaking leads to a hybridization of  $\gamma_b$  and  $\gamma_c$ .

$m_{bc} = 0$ . In this case the conductance equation simplifies to

$$\frac{dI_i}{dV} = \frac{2e^2}{h} \frac{(eV)^2 (\Gamma_{aa}^i)^2}{[(eV)^2 - M^2]^2 + (eV)^2 (\Gamma_{aa}^i)^2}, \quad (3.58)$$

where we introduced an effective coupling  $M = \sqrt{M_{ab}^2 + M_{ac}^2}$ . For preserved chiral symmetry the system behaves the same as the system where both chains have one Majorana per end with coupling  $M$ . This correspondence can be seen directly by expressing the coupling as

$$i\gamma_a(M_{ab}\gamma_b + M_{ac}\gamma_c) = iM\gamma_a \left( \frac{M_{ab}}{M}\gamma_b + \frac{M_{ac}}{M}\gamma_c \right) = iM\gamma_a\tilde{\gamma}_{bc}. \quad (3.59)$$

The orthogonal linear combination  $M_{ac}\gamma_b - M_{ab}\gamma_c$  does not couple to  $\gamma_a$  [8] and cannot be seen by the spin polarized tip. Since it could be experimentally feasible to selectively switch chiral symmetry breaking fields on and off, one can assume that this provides a valuable experimental knob to pinpoint the presence of Majorana bound states in such a setup. Combining chiral symmetry breaking with the possibility to modify the phase difference between the superconductors  $\delta\varphi$  yields a rich set of options for experiments.

### 3.4.6 Two coupled adatom chains: Two Majorana states below the tip and one in the other chain

Now we consider the opposite situation where the tip is located instead above the end of the chain where two Majorana bound states live. We depict the setup in Fig. 3.17.

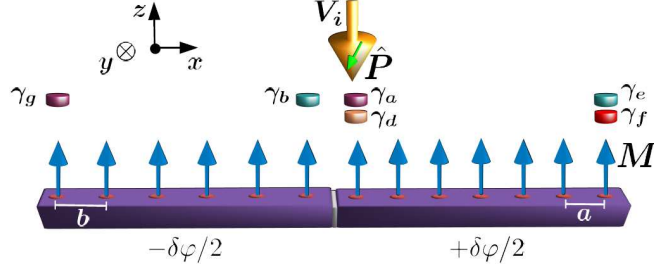


Figure 3.17: Two adatom chains coupled via a Josephson junction, where the two chains host one and two Majorana bound states per end respectively. The Majorana bound states far away from the junction are not taken into account. Only  $\gamma_a$  and  $\gamma_d$  couple to the tip. Chiral symmetry breaking leads to a hybridization of  $\gamma_a$  and  $\gamma_d$ .

Here the coupling matrices take the form

$$\widehat{\mathcal{M}} = \begin{pmatrix} 0 & m_{ad} & M_{ab} \\ -m_{ad} & 0 & M_{db} \\ -M_{ab} & -M_{db} & 0 \end{pmatrix} \quad \text{and} \quad \widehat{\Gamma}^i = \begin{pmatrix} \Gamma_{aa}^i & \Gamma_{ad}^i & 0 \\ (\Gamma_{ad}^i)^* & \Gamma_{dd}^i & 0 \\ 0 & 0 & 0 \end{pmatrix}. \quad (3.60)$$

As before the matrix elements  $M_{ab}$  and  $M_{db}$  describe the interchain tunneling and  $m_{ad}$  is induced by chiral symmetry breaking. Again weakly breaking the chiral symmetry does not affect the wavefunction of the single Majorana.

The expression for the conductance is quite long in this case and available in Appendix A.1. From the setup we can directly infer that the zero bias peak will persist according to the odd number rule [72]. Since all Majorana bound states are coupled by the tip, this rule applies in the presence or absence of chiral symmetry. However if the coupling to the single Majorana  $\gamma_b$  of the left chain vanishes, chiral symmetry matters and the system reduces to the case of a single chain with two Majorana bound states at the end as discussed in Section 3.4.3.

### 3.4.7 Two coupled adatom chains, both with two Majorana states

The final case considers two chains which both host two Majorana bound states per end. As usual the two chains are coupled via a junction and we assume sufficiently long chains such that it is possible to neglect the Majorana bound states at the far ends of

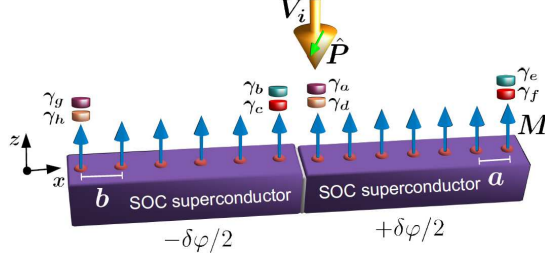


Figure 3.18: Two adatom chains coupled via a Josephson junction, where the two chains both host two Majorana bound states per end. The Majorana bound states far away from the junction are not taken into account. Only  $\gamma_a$  and  $\gamma_d$  couple to the tip.

the chains. The setup is shown in Fig. 3.18. The coupling matrices have the form

$$\widehat{\mathcal{M}} = \begin{pmatrix} 0 & m_{ad} & M_{ac} & M_{ab} \\ -m_{ad} & 0 & M_{dc} & M_{db} \\ -M_{ac} & -M_{dc} & 0 & m_{cb} \\ -M_{ab} & -M_{db} & -m_{cb} & 0 \end{pmatrix} \quad \text{and} \quad \widehat{\Gamma}^i = \begin{pmatrix} \Gamma_{aa}^i & \Gamma_{ad}^i & 0 & 0 \\ (\Gamma_{ad}^i)^* & \Gamma_{dd}^i & 0 & 0 \\ 0 & 0 & 0 & 0 \\ 0 & 0 & 0 & 0 \end{pmatrix}. \quad (3.61)$$

Here we omit the long expression for the tunneling conductance and focus instead on the value at zero bias. We find for  $V = 0$

$$\left. \frac{dI_i}{dV} \right|_{V=0} = \frac{2e^2}{h} \frac{2m_{cb}^2 \det \widehat{\Gamma}^i}{(\det \widehat{\mathcal{M}} - m_{ad}m_{cb})^2 + m_{cb}^2 \det(\text{Re} \widehat{\Gamma}^i)}, \quad (3.62)$$

where we introduced the tunneling coupling matrix

$$\widehat{M} = \begin{pmatrix} M_{ac} & M_{ab} \\ M_{dc} & M_{db} \end{pmatrix}. \quad (3.63)$$

From the equation we can infer that a zero bias conductance exist. However it does not take the ideal quantized value of  $\frac{2e^2}{h}$ . Since  $m_{cb}$  appears in the numerator, the zero bias conductance vanishes for  $m_{cb} = 0$ , which means that chiral symmetry is restored in the left chain, which does not couple to the tip. In contrast to that, if chiral symmetry is present in the chain below the tip, i.e.,  $m_{ad} = 0$  and  $P_y = 0$ , some modified value of the zero bias conductance remains. The conductance is still not quantized. The special case with  $m_{ad} = 0$  and additionally  $\det \widehat{M} = 0$  however yields a quantized peak with the doubled quantum  $\frac{4e^2}{h}$ . In this case the system acts as if there are two unpaired Majorana bound states which contribute to the tunneling. Finally, there is also the

case where  $\det \widehat{M} = 0$ , but  $m_{ad} \neq 0$ , which corresponds to effectively uncoupled chains. Then the system reduces to the case of a single chain with two Majorana bound states as discussed in Section 3.4.3.

### 3.5 Summary and conclusion

This chapter discussed magnetic adatom chains on top of a superconducting substrate, so called YSR chains, named after the in-gap states in the superconductor due to the magnetic adatoms. After describing the current experimental status we developed the theoretical model. In particular the spins of the magnetic adatoms were treated as classical spins coupled via an exchange interaction mediated by the substrate electrons. This interaction could be reduced to an RKKY interaction. In the topological treatment of the chain we assumed a ferromagnetic ordering as supported by a study of the magnetic phase diagram. Given a ferromagnetic chain we found the possibility for one or two Majorana bound states per end of the chain. The topological phase with two Majorana states is protected by the presence of a chiral symmetry. Note that the Majorana bound states have a spin character, which was a motivation for the next steps discussed in this chapter.

We focused on the transport signatures of the Majorana bound states, in particular considering the spin structure by applying a spin polarized tip. For that purpose we analyzed three types of tunnel Hamiltonians, (i) coupling of Majorana bound states to a tip, (ii) coupling of two Majorana bound states within one short chain, (iii) coupling of two Majorana bound states within two chains separated by a Josephson junction.

Within a Keldysh approach we obtained the tunneling signatures of multiple setups, the simplest one being the single Majorana bound state at the end of a chain coupled to a tip. In this case the tunneling conductance depends on the polarization direction of the tip. In particular for a fully spin-polarized tip and specific angles of the polarization the tunneling conductance vanishes. Similarly, in the case of short chains, where the Majorana bound states of both ends of the chain contribute, the signal can be very weak in one direction while staying nearly quantized in other directions.

Furthermore we showed that for a single chain with two chiral symmetry protected bound states per end, the polarized tip or an additional Zeeman field in  $y$ -direction can break chiral symmetry. This allows to controllably modify the tunneling spectrum.

Then we discussed setups of increasing complexity with two coupled chains. There the tunneling conductance can be used as a probe of the  $4\pi$ -Josephson effect. The emerging finite bias peaks can be moved by modifying the  $4\pi$ -Josephson coupling.

Furthermore for two chains with different number of bound states per end, tunable chiral symmetry violation and restoration can be used to switch a zero bias peak on and off. While current experiments based on self-assembled magnetic chains as in Ref. [6] do not support junctions yet, Josephson effects could possibly be accessed by either inducing a supercurrent flow along a chain [68, 94] or by employing a chain in ring geometry with threaded magnetic flux. These two configurations both lead to coupled Majorana bound states on the left and right ends, which feel different superconducting phases.

To conclude, the signatures described in this work rely on Majorana spin polarization which was extracted from a realistic model for YSR chains. These signatures present new possibilities for experiments to detect Majorana bound states in the future and study the spin character of the states.

# 4

## Chapter 4

---

# Magnetic order on warped topological insulator surfaces

This chapter is based on our publication Ref. [1]. We focus on magnetic topological insulator surfaces originating from three-dimensional bulk topological insulators. Topological insulators have been predicted [25, 95, 96] and discovered [26, 97–102]. They rely on the presence of topologically protected surface states [13, 14, 22, 23, 103–106]. These electronic surface states are characterized by spin-momentum locking, leading in the simplest form to a helical Dirac cone energy dispersion.

After describing  $\mathbb{Z}_2$  topological insulators with Dirac cones we focus on a more complex variation of such a system. In particular we consider a topological insulator with warping effects, which are observable in the Fermi surface of the surface electrons. The modifications arise due to the crystal structure and reflect the point group symmetry of the material. For Bi-based topological insulators the Fermi surface exhibits a  $C_{3v}$  symmetric warping [107–112]. Some of the consequences of warping on magnetic [107, 113–115] and transport [116–118] have been discussed in the literature before, including the possibility of a skyrmion lattice [115]. In particular, the warping leads to enhanced Fermi surface nesting due to parallel flat lines appearing in the Fermi surface and thus to the possibility of magnetic phases. However the question of the magnetic ground state has not been resolved before.

We investigate the spin susceptibility and derive a Landau theory to compare the different magnetic ground states which are possible. The possible ground states include a magnetic texture involving a single wavevector  $\mathbf{Q}$  and textures involving three  $\mathbf{Q}$  wavevectors including the possibility of a skyrmion lattice. We show that for a nearly hexagonal Fermi surface a sufficiently strong interaction yields a magnetic texture formed by a skyrmion lattice. This lattice can be viewed as the superposition of three

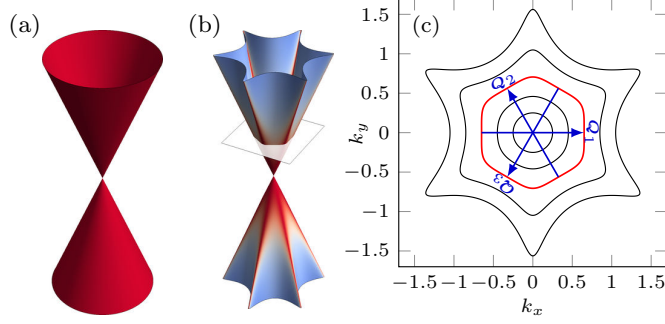


Figure 4.1: (a) Dirac cone energy dispersion of the surface states of a 3D topological insulator without warping ( $\gamma = 0$ ). (b) Warped Dirac cone ( $\gamma > 0$ ). The color shows the direction-resolved density of states. (c) Warped Fermi surfaces at different chemical potentials. For  $\mu = \mu_{\text{hex}}$  the Fermi surface is nearly hexagonal. In this case the three nesting vectors  $\mathbf{Q}_{1,2,3}$  connect the flat sides of the Fermi surface. The white plane in (b) corresponds to  $E = \mu_{\text{hex}}$ .

helical spin density waves such that  $C_3$  symmetry is preserved. The skyrmions are topological objects, which carry non-zero topological charge. This chapter concludes with a classification of the means to control the magnetic ground state using external fields or imposed currents.

## 4.1 Three-dimensional topological insulator

This chapter focuses on the surface states of a 3D topological insulator. The class of 3D topological insulators include time reversal invariant systems with a bulk gap and are classified by a  $\mathbb{Z}_2$  topological invariant, reflecting the number of Dirac cones. The surfaces can either exhibit one cone in the non-trivial phase or zero cones.

The surface Hamiltonian arises from the bulk by projection of the Hamiltonian expanded around the  $\Gamma$  point. The surface electrons form a Dirac cone or relativistic (linear) spectrum with constant density of states (DOS) as shown in Fig. 4.1(a). At lowest order the surface Hamiltonian with Rashba spin orbit coupling with Dirac velocity  $v$  is given by

$$\hat{\mathcal{H}}(\mathbf{k}) = v(k_x\sigma_y - k_y\sigma_x), \quad (4.1)$$

with the Pauli matrices  $\boldsymbol{\sigma}$  acting in an effective spin space. We work in natural units by setting  $\hbar = 1$  in this chapter. The structure of the spin-orbit coupling has the consequence of locking the spin to the momentum, which means if the spin expectation

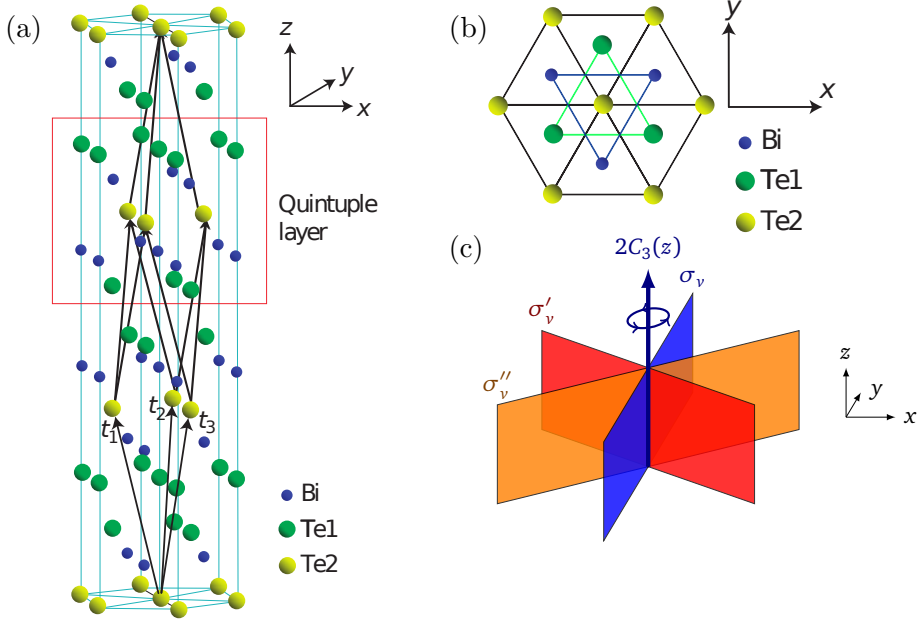


Figure 4.2: (a,b) Crystal structure of  $\text{Bi}_2\text{Te}_3$  reprinted from Ref. [96] with permission by the Nature Publishing Group. (a) Side view. The quintuple layer repeats itself along the  $z$ -axis. The  $[111]$  plane is perpendicular to  $1 \cdot \mathbf{t}_1 + 1 \cdot \mathbf{t}_2 + 1 \cdot \mathbf{t}_3$  where  $\mathbf{t}_{1,2,3}$  are the basis vectors. (b) Top view at the  $[111]$  surface. The structure shows a threefold rotation symmetry. (c) Point group symmetry  $C_{3v}$ .  $x$ -axis goes from  $\Gamma$  to  $K$  point. Mirror planes and rotation axes of the point group  $C_{3v}$

value of the eigenstates are computed, a spin direction pointing tangentially around the cone is obtained. The Hamiltonian has a  $U(1)$  rotational symmetry around the  $z$ -axis. Furthermore it is invariant under mirror operations.

## 4.2 Surface states and warping effects

Now we consider more realistic systems with additional terms modifying the dispersion. For example one can include second order kinetic terms  $\epsilon_0(\mathbf{k})$  and terms which break the rotational symmetry to a lower discrete symmetry according to the point group of the crystal. In this section we focus on a system where the surface states are hexagonally warped due to a threefold  $C_{3v}$  symmetry of the material. Of particular interest are Bi-based topological insulators, e.g.,  $\text{Bi}_2\text{Te}_3$ , as shown in Fig. 4.2. At first we determine the eigenvalues and eigenstates. Later we consider the consequences of the warping for different values of the chemical potential, namely possible nesting and magnetization effects.

### 4.2.1 Hamiltonian of a warped topological insulator

The Hamiltonian describing the warped topological insulators follow from a Dirac Hamiltonian with an additional term which breaks rotational symmetry [107]. The 2D surface lies in the  $xy$ -plane and the Hamiltonian has the form

$$\hat{\mathcal{H}}_0(\mathbf{k}) = v(k_x\sigma_y - k_y\sigma_x) + \gamma k_x(k_x^2 - 3k_y^2)\sigma_z + \epsilon_0(\mathbf{k}). \quad (4.2)$$

As before the Pauli matrices  $\boldsymbol{\sigma}$  act in an effective spin space. More precisely the space is spanned by the eigenstates  $|\uparrow\rangle, |\downarrow\rangle$  of the  $z$ -component of the total angular momentum operators. In the case of the materials described here, the total angular momentum operator almost coincides with the spin operator  $\mathbf{S}$  [119, 120].

Now we take a closer look at the second term of the Hamiltonian

$$\gamma k_x(k_x^2 - 3k_y^2)\sigma_z = \frac{\gamma}{2}(k_+^3 + k_-^3)\sigma_z, \quad (4.3)$$

which can be rewritten in terms of the complex momenta  $k_{\pm} = k_x \pm ik_y = ke^{\pm i\theta_{\mathbf{k}}}$ , such that the threefold symmetry becomes evident. The strength of the warping is controlled by the parameter  $\gamma$ . The term reduces the continuous rotational symmetry to a discrete  $C_3$  subgroup. The generators of the group are a  $2\pi/3$  counterclockwise rotation ( $C_3$ ) of the system about the  $z$ -axis. Additional to the rotation, the system is invariant under and a mirror operation at the  $yz$ -plane  $\sigma_v: x \mapsto -x$ . This yields the  $C_{3v}$  as full point group symmetry. The point group is specified by the character table Table 4.1. Additional to the point group symmetry the Hamiltonian respects time reversal  $\mathcal{T}$  symmetry which leads to a Kramers pairs and a hexagonal Fermi surface.

In the Hamiltonian, the third term  $\epsilon_0(\mathbf{k})$  is a kinetic energy term which is assumed to be invariant under the symmetry operations. The term includes chemical potential  $\mu$ , quadratic kinetic energy  $\propto \mathbf{k}^2$ . In the material under consideration the quadratic term is not relevant, so we assume that only the chemical potential is present, i.e., we set  $\epsilon_0(\mathbf{k}) = -\mu$ . This chemical potential can be controlled by doping the topological insulator. This has been shown experimentally in angular resolved photoemission spectroscopy (ARPES) measurements [99, 121] as presented in Fig. 4.3.

In the rest of this chapter we rely on a dimensionless rescaling of the Hamiltonian for convenience, such that only the rescaled chemical potential appears as free parameter. The momenta are scaled by  $k_s = \sqrt{v/\gamma}$  and the energies by  $E_s = vk_s$  respectively. The parameters  $v$  and  $\gamma$  can be determined by ARPES. See for instance Ref. [113]. In our work we consider mostly  $\text{Bi}_2\text{Te}_3$  which has strong warping effects. The parameters for

Table 4.1: Character table of point group  $C_{3v}$ . The table shows linear and higher order quantities transforming according to an irreducible representation.

IR	$\mathbb{1}$	$2C_3$	$3\sigma_v$	Linear	Higher order
$A_1$	1	1	1	$z$	$x^2 + y^2, z^2, z^3, y(y^2 - 3x^2)$
$A_2$	1	1	-1	$S_z$	$x(x^2 - 3y^2)$
$E$	2	-1	0	$(x, y), (S_x, S_y)$	$(2xy, x^2 - y^2), (xz, yz)$

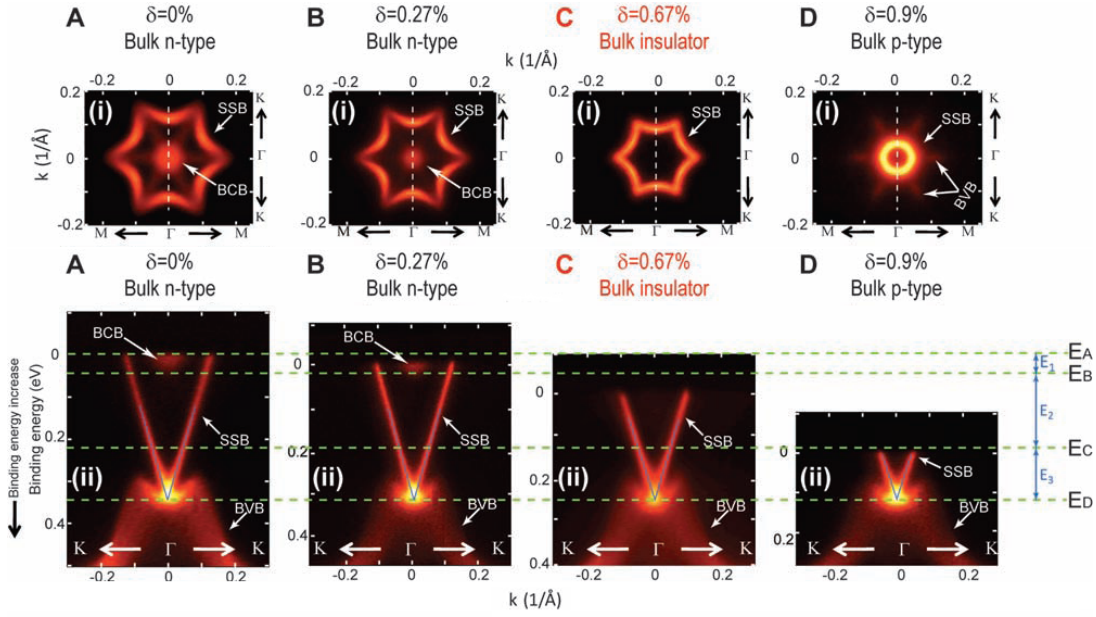


Figure 4.3: ARPES measurement of the  $\text{Bi}_2\text{Te}_3$  surface reprinted from Ref. [99] with permission by AAAS. Columns A to D show Fermi surfaces and band dispersions for 0, 0.27, 0.67 and 0.9% doping. We are interested in the bulk insulating phase (around doping 0.67%) where the Fermi surface forms a hexagon. First row: Fermi surface symmetrized according to hexagonal symmetry. The pocket formed by the surface state band (SSB) is observed for all dopings. The pocket from the bulk conduction band (BCB) shrinks upon doping and vanishes in columns C and D. In column D pockets formed by the bulk valence band (BVB) emerge outside the SSB pockets. The K-G-K direction is indicated by white dashed lines. Second row: Band dispersions along K-G-K direction. The  $E_F$  positions of the four doping samples are at 0.34, 0.325, 0.25, and 0.12 eV above the Dirac point, respectively.  $E_A$  is the Fermi energy for undoped BiTe,  $E_B$  is the bottom of the BCB,  $E_C$  is the top of the BVB and  $E_D$  is the position of the Dirac point.

Bi<sub>2</sub>Te<sub>3</sub> are  $k_s = 0.1 \text{ \AA}^{-1}$  and  $E_s = 0.26 \text{ eV}$ . The dimensionless Hamiltonian takes the form  $\widehat{\mathcal{H}}_0(\mathbf{k}) = \mathbf{g}(\mathbf{k}) \cdot \boldsymbol{\sigma} - \mu$ , where we introduced the configuration vector

$$\mathbf{g}(\mathbf{k}) = \begin{pmatrix} -k_y \\ k_x \\ k_x(k_x^2 - 3k_y^2) \end{pmatrix} = |\mathbf{g}(\mathbf{k})| \begin{pmatrix} \sin \vartheta_{\mathbf{k}} \cos \varphi_{\mathbf{k}} \\ \sin \vartheta_{\mathbf{k}} \sin \varphi_{\mathbf{k}} \\ \cos \vartheta_{\mathbf{k}} \end{pmatrix} \quad (4.4)$$

with the polar angles  $\cot \vartheta_{\mathbf{k}} = \sin \varphi_{\mathbf{k}}(k_x^2 - 3k_y^2)$ ,  $\tan \varphi_{\mathbf{k}} = -k_x/k_y$  and  $\varphi_{\mathbf{k}} = \theta_{\mathbf{k}} + \pi/2$ . The formulation using the polar angles is especially useful to write the eigenstates compactly. In the next section we take a closer look at the spectrum and the eigenstates.

### 4.2.2 Spectrum and eigenstates

The spectrum of the given Hamiltonian has the form  $\epsilon_{\mathbf{k},\pm} = \pm |\mathbf{g}(k, \theta_{\mathbf{k}})| - \mu$ . In our case we write the energy depending on angle and the modulus of the momentum  $\epsilon_{\mathbf{k},\pm} = \pm k \sqrt{1 + k^4 \cos^2(3\theta_{\mathbf{k}})} - \mu$ . The Fermi surface for different values of the chemical potentials  $\mu$  is depicted in Fig. 4.1(b). In the spin basis, the eigenstates take the form

$$|\mathbf{k}, +\rangle = \begin{pmatrix} e^{-\frac{i\varphi_{\mathbf{k}}}{2}} \cos \frac{\vartheta_{\mathbf{k}}}{2} \\ e^{+\frac{i\varphi_{\mathbf{k}}}{2}} \sin \frac{\vartheta_{\mathbf{k}}}{2} \end{pmatrix} \quad \text{and} \quad |\mathbf{k}, -\rangle = \begin{pmatrix} -e^{-\frac{i\varphi_{\mathbf{k}}}{2}} \sin \frac{\vartheta_{\mathbf{k}}}{2} \\ e^{+\frac{i\varphi_{\mathbf{k}}}{2}} \cos \frac{\vartheta_{\mathbf{k}}}{2} \end{pmatrix}. \quad (4.5)$$

In the following, we call these states  $\pm$ -helicity eigenstates.

For completeness we describe the transformation properties of the relevant operators and states under the point group generators  $C_3$  and  $\sigma_v$  of the group  $C_{3v}$ . We distinguish between the group elements  $\mathcal{G}$  and the representation of the group elements  $\widehat{D}_{\mathcal{G}}^+$  ( $\widehat{D}_{\mathcal{G}}^-$ ) acting on vectors (pseudovectors). The representations  $\widehat{D}_{C_3}^+ = \widehat{D}_{C_3}^-$  of the rotation  $C_3$  coincide and are given by the rotation matrix about the  $z$ -axis by  $2\pi/3$ . For example the rotation acts on the momentum vector as  $C_3 \mathbf{k} = \widehat{D}_{C_3}^+ \mathbf{k}$  and on the spin operators as  $C_3 \boldsymbol{\sigma} = \widehat{D}_{C_3}^- \boldsymbol{\sigma}$ . The mirror operation acts as  $\sigma_v \mathbf{k} = \widehat{D}_{\sigma_v}^+ \mathbf{k} = \text{diag}(-1, 1, 1) \mathbf{k}$  on vectors and as  $\sigma_v \boldsymbol{\sigma} = \text{diag}(1, -1, -1) \boldsymbol{\sigma} = \widehat{D}_{\sigma_v}^- \boldsymbol{\sigma} = -\widehat{D}_{\sigma_v}^+ \boldsymbol{\sigma}$  on pseudovectors. The Hamiltonian is invariant under the group operations  $\mathcal{G} \in C_{3v}$ . Therefore one obtains the transformation of the configuration vector

$$\mathbf{g}(\mathcal{G}\mathbf{k}) \cdot \mathcal{G}\boldsymbol{\sigma} = \mathbf{g}(\mathbf{k}) \cdot \boldsymbol{\sigma} \Rightarrow \mathbf{g}(\mathcal{G}\mathbf{k}) = \widehat{D}_{\mathcal{G}}^- \mathbf{g}(\mathbf{k}). \quad (4.6)$$

The transformation properties of the helicity eigenstates are given by

$$|C_3 \mathbf{k}, \pm\rangle = e^{-i\pi\sigma_z/3} |\mathbf{k}, \pm\rangle \quad \text{and} \quad |\sigma_v \mathbf{k}, \pm\rangle = i\sigma_x |\mathbf{k}, \pm\rangle. \quad (4.7)$$

In the next section we consider the geometric structure of the Fermi surface and show how this structure enhances nesting for certain values of the chemical potential  $\mu$ .

### 4.2.3 Nesting in the warped Fermi surface

We depict in Fig. 4.1(c) the Fermi surface for different chemical potentials  $\mu$ . For low energies  $\mu \lesssim 0.5$  the Fermi surface is roughly circular and evolves to a more hexagonal and finally to a snowflake-like form for  $\mu \gtrsim 1$ . The Fermi surface is defined by the cubic equation  $|\mathbf{g}(k, \theta_{\mathbf{k}})| = \mu$ . Solving this equation for  $\cos(3\theta) = 0$  yields the value  $k(\theta, \mu) = \mu$ . In general we obtain the solution

$$k(\theta, \mu) = \sqrt{t(\theta, \mu) - \frac{1}{3 \cos^2(3\theta)t(\theta, \mu)}} \quad \text{with}$$

$$t(\theta, \mu) = \sqrt[3]{\frac{\mu^2}{2 \cos^2(3\theta)} + \sqrt{\frac{\mu^4}{4 \cos^4(3\theta)} + \frac{1}{27 \cos^6(3\theta)}}}. \quad (4.8)$$

Since we want to study the susceptibility of the material towards the formation of magnetic order we focus on the situation where the Fermi surface becomes nearly hexagonal with strong nesting. This kind of hexagonal form occurs for approximately  $\mu = \mu_{\text{hex}} = 0.725$ .

Nesting means that there exist dominant wavevectors connecting the sides of the Fermi surface. We find six of those nesting vectors  $\pm \mathbf{Q}_{1,2,3}$ , which are given in  $xy$ -coordinates by

$$\begin{aligned} \mathbf{Q}_1 &\equiv 2k_0(1, 0), \\ \mathbf{Q}_2 &\equiv C_3 \mathbf{Q}_1 = 2k_0(-1/2, +\sqrt{3}/2), \\ \mathbf{Q}_3 &\equiv C_3 \mathbf{Q}_2 = 2k_0(-1/2, -\sqrt{3}/2). \end{aligned} \quad (4.9)$$

The wavevectors have the length of the Fermi wavevector  $k_0$ . At the Fermi surface it holds  $\epsilon_{k_0,+} = 0$ , which implies the relation  $\mu = |\mathbf{g}(k_0, 0)| = k_0 \sqrt{1 + k_0^4}$  for the chemical potential.

## 4.3 Magnetic instability

As discussed before, the Fermi surface can take a hexagonal shape which leads to the nesting vectors  $\pm \mathbf{Q}_{1,2,3}$  connecting the sides of the Fermi surface. Systems with nesting can support spontaneous symmetry breaking and the formation of a magnetic

grounds state, since certain scattering processes are enhanced if large regions of the Fermi surface or regions with high density of states are connected by wavevectors.

In Section 4.3.1 we discuss the form of the magnetic order parameter which can develop in the presence of a repulsive Hubbard interaction at the mean-field level. In the following section we derive the Landau theory up to sixth order. At second order it is only possible to determine the susceptibility of the system to become magnetized. We find possible order parameters  $\mathbf{M}_{\mathbf{Q}_{1,2,3}}$  corresponding to the  $\mathbf{Q}_{1,2,3}$  vectors.

At fourth and sixth order of the free energy expansion more information can be extracted. At fourth order it is possible to infer if a magnetic phase with only one  $\mathbf{M}_{\mathbf{Q}_i}$  dominates, which will lead to a magnetic stripe pattern. The other possibility is a triple- $\mathbf{Q}$  phase, which leads to a lattice-like pattern. At fourth order the complex phases of the order parameters are still undetermined. The sixth order is required to completely determine the structure of the order parameters. However two phase degrees of freedom corresponding to Goldstone modes remain free at any order of the Landau theory.

### 4.3.1 Magnetic interaction and order parameter

For the stabilization of the magnetic order an interaction is necessary, additional to the nesting. Here we assume the presence of a repulsive Hubbard interaction with  $U > 0$ . The Hubbard interaction is on-site and can be written in the form

$$\mathcal{H}_U = U \int d\mathbf{r} n_{\uparrow}(\mathbf{r}) n_{\downarrow}(\mathbf{r}) = U \int d\mathbf{r} \left[ \frac{\rho^2(\mathbf{r})}{4} - \frac{\mathbf{S}^2(\mathbf{r})}{3} \right]. \quad (4.10)$$

We decompose the product of the particle number density operators  $n_{\uparrow}(\mathbf{r})$  and  $n_{\downarrow}(\mathbf{r})$  in particle and spin density operators  $\rho(\mathbf{r}) = \psi^{\dagger}(\mathbf{r})\mathbb{1}\psi(\mathbf{r})$  and  $\mathbf{S}(\mathbf{r}) = \psi^{\dagger}(\mathbf{r})(\boldsymbol{\sigma}/2)\psi(\mathbf{r})$ . For the given repulsive interaction charge density-wave instabilities are not expected, hence we neglect the non-magnetic term in the following analysis. However the spin part is relevant.

We perform the mean-field decoupling and introduce the order parameter  $\mathbf{M}(\mathbf{r}) = -U \langle \mathbf{S}(\mathbf{r}) \rangle$ . The remaining interaction can then be written in the decoupled form

$$\mathcal{H}_{\text{mag}} = \int d\mathbf{r} \frac{\mathbf{M}^2(\mathbf{r})}{U} + \int d\mathbf{r} \psi^{\dagger}(\mathbf{r}) \mathbf{M}(\mathbf{r}) \cdot \boldsymbol{\sigma} \psi(\mathbf{r}). \quad (4.11)$$

Then we introduce the Fourier-transformed order parameters  $\mathbf{M}_{\mathbf{q}}$ , which depend on wavevectors  $\mathbf{q}$ ,

$$\mathbf{M}(\mathbf{r}) = \int \frac{d\mathbf{q}}{(2\pi)^2} e^{i\mathbf{q}\cdot\mathbf{r}} \mathbf{M}_{\mathbf{q}}. \quad (4.12)$$

The Hamiltonian takes the form

$$\mathcal{H}_{\text{mag}} = \int \frac{d\mathbf{q}}{(2\pi)^2} \left[ \frac{|\mathbf{M}_{\mathbf{q}}|^2}{U} + \int \frac{d\mathbf{k}}{(2\pi)^2} \psi_{\mathbf{k}+\mathbf{q}/2}^\dagger \mathbf{M}_{\mathbf{q}} \cdot \boldsymbol{\sigma} \psi_{\mathbf{k}-\mathbf{q}/2} \right] \quad (4.13)$$

in Fourier space. Similarly the self-consistency relation of the order parameter reads

$$\mathbf{M}_{\mathbf{q}} = -U \int d\mathbf{r} e^{-i\mathbf{q}\cdot\mathbf{r}} \langle \mathbf{S}(\mathbf{r}) \rangle = -\frac{U}{2} \int \frac{d\mathbf{k}}{(2\pi)^2} \langle \psi_{\mathbf{k}-\mathbf{q}/2}^\dagger \boldsymbol{\sigma} \psi_{\mathbf{k}+\mathbf{q}/2} \rangle. \quad (4.14)$$

These order parameters fulfill the relation  $\mathbf{M}_{-\mathbf{q}} = \mathbf{M}_{\mathbf{q}}^*$ . They transform under a group operation  $\mathcal{G}$  of the point group  $C_{3v}$  as  $\mathcal{G}\mathbf{M}_{\mathbf{q}} \equiv \widehat{D}_{\mathcal{G}} \mathbf{M}_{\mathcal{G}^{-1}\mathbf{q}}$ . In Appendix A.2, we present a complete classification of the possible magnetic order parameters with wavevectors  $\mathbf{q}$ ,  $C_3\mathbf{q}$  and  $C_3^2\mathbf{q}$  under the point group  $C_{3v}$ .

This classification of the order parameters according to the point group will turn out useful later when we discuss the structure of the dominant magnetic order, which will be either a non-trivial skyrmion lattice or a trivial lattice transforming according to  $A_1$  and  $A_2$  representations respectively. In the next section we discuss the free energy expansion in powers of the magnetic order parameters.

### 4.3.2 Free energy expansion

The free energy expansion allows to obtain information about the dominant magnetic instability and preferred wavevectors. Note that due to geometry we already expect that  $\mathbf{Q}_{1,2,3}$  dominate. The numerical analysis that we performed in the course of this section confirms the analytic expectations.

At first we integrate out the electronic degrees of freedom in the path-integral formalism in terms of Grassman fields. The free energy  $\mathcal{F} = -\ln \mathcal{Z}/\beta$  is given by the logarithm of the partition function

$$\mathcal{Z} = \int D[\bar{\psi}, \psi] e^{-\mathcal{S}[\bar{\psi}, \psi]}. \quad (4.15)$$

The action is given by the bare Hamiltonian and the magnetic order parameter and takes the form

$$\begin{aligned}
 \mathcal{S}[\bar{\psi}, \psi] &= \sum_{k,q} \bar{\psi}_{k+q} \left\{ - \left[ ik_n - \widehat{\mathcal{H}}_0(k) \right] \delta_{q,0} + \mathbf{M}_q \cdot \boldsymbol{\sigma} \right\} \psi_k \\
 &\equiv \sum_{k,q} \bar{\psi}_{k+q} \left[ -\widehat{G}_0^{-1}(k) \delta_{q,0} + \widehat{\mathcal{V}}(k+q, k) \right] \psi_k \\
 &\equiv \bar{\psi} \left( -\widehat{G}_0^{-1} + \widehat{\mathcal{V}} \right) \psi.
 \end{aligned} \tag{4.16}$$

We introduced the fermionic and bosonic (2+1)-vectors  $k = (\mathbf{k}, k_n)$  and  $q = (\mathbf{q}, \omega_n)$ , where the fermionic Matsubara frequencies  $k_n = (2n+1)\pi/\beta$  and bosonic Matsubara frequencies  $\omega_n = 2n\pi/\beta$  enter. For the integration over the (2+1)-vectors we introduced the shorthand summation notation  $\sum_k \equiv \sum_{k_n} \int d\mathbf{k} / (2\pi)^2$  and the shorthand Kronecker delta  $\delta_{q,q'} = (2\pi)^2 \delta(\mathbf{q} - \mathbf{q}') \delta_{\omega_n, \omega'_n}$ .

The non-interacting Green's function is given by  $\widehat{G}_0(k) = [ik_n - \widehat{\mathcal{H}}_0(k)]^{-1}$ . We can write the action in a basis independent form

$$\mathcal{S}[\bar{\psi}, \psi] \equiv \bar{\psi} \left( -\widehat{G}_0^{-1} + \widehat{\mathcal{V}} \right) \psi, \tag{4.17}$$

with the operators  $\widehat{G}_0$  and  $\widehat{\mathcal{V}}$  defined by the matrix elements  $\widehat{G}_0(k) \equiv \langle k | \widehat{G}_0 | k \rangle$  and  $\widehat{\mathcal{V}}(k+q, k) \equiv \langle k+q | \widehat{\mathcal{V}} | k \rangle$ . Since we are only interested in the static magnetization we concentrate on the zero-frequency component  $\mathbf{M}_{q,0}$  and the static magnetic potential  $\widehat{\mathcal{V}}(k+q, k) \equiv \widehat{\mathcal{V}}(\mathbf{q}) \delta_{\omega_n, 0}$ . Integrating the Grassmann variables results in the fermionic determinant which yields the partition function

$$\mathcal{Z} = \det \beta \left( -\widehat{G}_0^{-1} + \widehat{\mathcal{V}} \right) = e^{\text{trln}[\beta(-\widehat{G}_0^{-1} + \widehat{\mathcal{V}})]}. \tag{4.18}$$

Plugging the partition function into the free energy yields

$$\mathcal{F} = -\frac{1}{\beta} \ln \mathcal{Z} = \mathcal{F}_0 - \frac{1}{\beta} \text{trln} \left( \mathbf{1} - \widehat{G}_0 \widehat{\mathcal{V}} \right), \tag{4.19}$$

which can in turn be expanded.

We perform the series expansion of the logarithm in powers of the magnetic potential. The expansion complemented by the quadratic term due the mean-field decoupling is then given by

$$\mathcal{F}_{\text{mag}} = \frac{1}{\beta} \sum_{\nu=1}^{\infty} \frac{\text{tr} \left( \widehat{G}_0 \widehat{\mathcal{V}} \right)^{\nu}}{\nu} + \int \frac{d\mathbf{q}}{(2\pi)^2} \frac{|\mathbf{M}_q|^2}{U}. \tag{4.20}$$

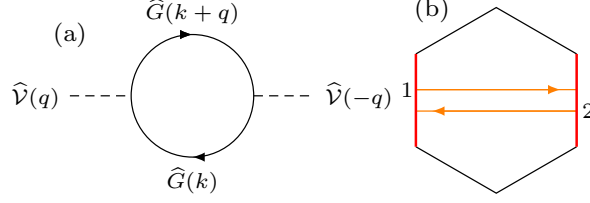


Figure 4.4: (a) Loop diagram for the magnetic susceptibility corresponding to the quadratic term of the Landau expansion. Solid lines correspond to fermionic propagators. (b) Dominant scattering process between nested sides of the Fermi surface.

The Green's function can be given explicitly in terms of projectors  $P_{\pm}(\mathbf{k}) = [1 \pm \hat{\mathbf{g}}(\mathbf{k}) \cdot \boldsymbol{\sigma}] / 2$  with unit vector  $\hat{\mathbf{g}}(\mathbf{k}) \equiv \mathbf{g}(\mathbf{k}) / |\mathbf{g}(\mathbf{k})|$  as follows

$$\hat{G}_0(\mathbf{k}) = \frac{ik_n + \mu + \mathbf{g}(\mathbf{k}) \cdot \boldsymbol{\sigma}}{(ik_n + \mu)^2 - |\mathbf{g}(\mathbf{k})|^2} = \sum_{s=\pm} \frac{P_s(\mathbf{k})}{ik_n - \epsilon_{\mathbf{k},s}}. \quad (4.21)$$

For our numerical analysis we used this form of the Green's function, since the poles in the integration and the resulting residues can be controlled. In Appendix A.4 we present the details of the calculation of the coefficients of the free energy expansion.

### 4.3.3 Landau theory at second order: Magnetic susceptibility

To obtain the leading instability the lowest order term of the free energy expansion must be analyzed. The quadratic term has the form

$$\mathcal{F}^{(2)} = \frac{1}{2} \int \frac{d\mathbf{q}}{(2\pi)^2} M_{-\mathbf{q}}^a \left( \frac{2}{U} \delta^{ab} - \chi_{\mathbf{q}}^{ab} \right) M_{\mathbf{q}}^b, \quad (4.22)$$

which depends on the spin susceptibility  $\chi_{\mathbf{q}}^{ab} = \sum_{s,s'=\pm} \chi_{\mathbf{q},s,s'}^{ab}$ . Here we imply a summation over repeated indices  $a, b = x, y, z$ . In Fig. 4.4(a) we depict the loop diagram corresponding to the susceptibility and the dominant scattering process at second order between nested sides of the Fermi surface. The spin susceptibility can be decomposed in contributions involving upper and lower helicity bands,  $s, s' = \pm$ ,

$$\chi_{\mathbf{q},s,s'}^{ab} = - \int \frac{d\mathbf{k}}{(2\pi)^2} \frac{n_F(\epsilon_{\mathbf{k},s}) - n_F(\epsilon_{\mathbf{k}+\mathbf{q},s'})}{\epsilon_{\mathbf{k},s} - \epsilon_{\mathbf{k}+\mathbf{q},s'}} \langle \mathbf{k}, s | \sigma^a | \mathbf{k} + \mathbf{q}, s' \rangle \langle \mathbf{k} + \mathbf{q}, s' | \sigma^b | \mathbf{k}, s \rangle. \quad (4.23)$$

To illustrate the different scattering processes contributing to the spin susceptibility, we present the band structure in Fig. 4.5. For chemical potential  $\mu > 0$  and  $T = 0$  the lower helicity band  $|\mathbf{k}, -\rangle$  is located deep below the Fermi level and therefore fully

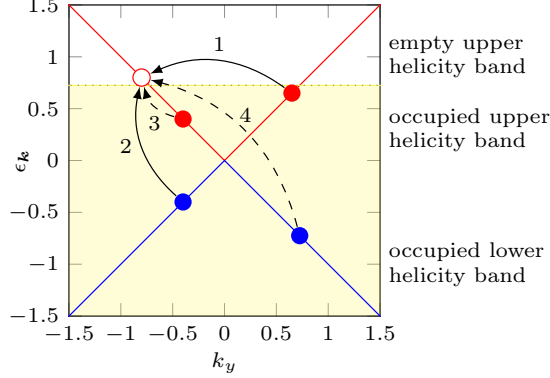


Figure 4.5: Energy dispersion  $E(k_y)$  for  $k_x = 0$ . We show scattering processes from occupied states with  $E < \mu$  to empty states with  $E > \mu$ . Given a Fermi surface with good nesting, process 1 dominates the susceptibility of the upper helicity band. Process 2 is most relevant to the interband susceptibility. At low temperatures, the processes 3 and 4 are suppressed.

occupied, i.e., we assume  $n_F(\epsilon_{\mathbf{k},-}) = 1$ . Therefore, intraband scattering in the lower band is completely suppressed. The only relevant processes involve the upper helicity band  $|\mathbf{k}, +\rangle$ .

We see that processes of type 1 of Fig. 4.5, i.e., intraband scattering in the upper helicity band with large wavevector transfer are the most dominant ones. The interband processes 2 and 4 enter the susceptibility suppressed by a small factor  $\sim 1/(\epsilon_{\mathbf{k},-} - \epsilon_{\mathbf{k},+}) < 1/\mu$ . Furthermore processes of type 3, i.e., intraband scattering in the upper helicity band with small wavevector transfer, can be neglected since the occupation of the two states remains nearly unchanged.

If we consider the case of an almost hexagonal Fermi surface the dominant scattering process contributing to the susceptibility for  $\mathcal{Q}_1$  involves nested parts of the Fermi surface as shown in Fig. 4.4(b). We point out that in the present problem the susceptibility for the nested wavevectors is strongly enhanced. In contrast to that, in 1D systems [122] with perfect nesting, the susceptibility might diverge, which would result in the onset of a magnetic instability. In the present problem a sufficiently strong interaction is necessary to lead to the development of the magnetic instability.

Now if the spin susceptibility matrix for each wavevector  $\mathbf{q}$  is diagonalized, three eigenvalues and corresponding unit eigenvectors,  $\hat{\chi}_{\mathbf{q}} \widehat{\mathbf{M}}_{\mathbf{q}}^i = \chi_{\mathbf{q}}^i \widehat{\mathbf{M}}_{\mathbf{q}}^i$  are obtained. The leading magnetic instability corresponds to the largest eigenvalue. Since all instabilities are triggered by the same interaction potential  $U$ , there are no other competing instabilities and we can focus on the dominant instability only. The critical interaction for the onset of the instability is given by the Stoner criterion  $\det[(2/U_{\text{crit}})\mathbb{1} - \hat{\chi}_{\mathbf{q}}] = 0$ .

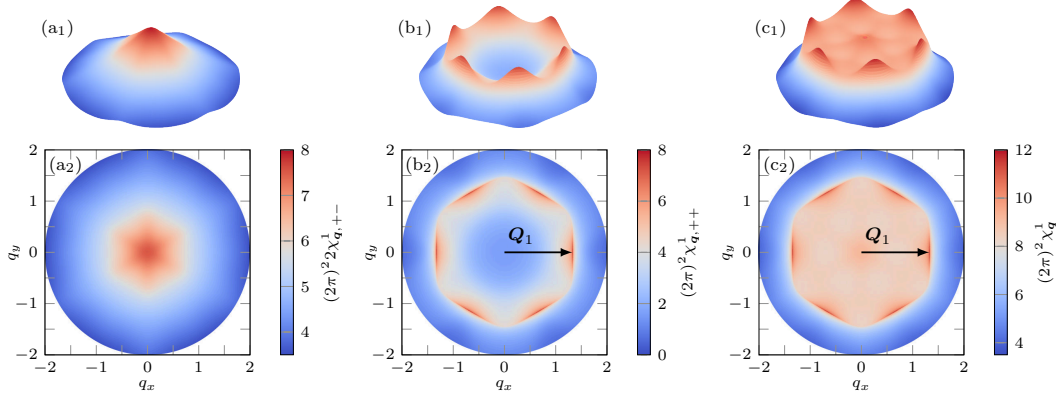


Figure 4.6: Largest eigenvalue of the spin-susceptibility over the wavevector  $\mathbf{q} = (q_x, q_y)$  in 3D view [(a<sub>1</sub>), (b<sub>1</sub>), (c<sub>1</sub>)] and top view [(a<sub>2</sub>), (b<sub>2</sub>), (c<sub>2</sub>)]. We used  $\mu = \mu_{\text{hex}} = 0.725$  for all plots. The temperature is  $T = 0.01$  in (a<sub>1</sub>), (b<sub>1</sub>), (c<sub>1</sub>) and  $T = 0$  in (a<sub>2</sub>), (b<sub>2</sub>), (c<sub>2</sub>). Plot (a) shows the interband contribution. Plot (b) shows the intraband contribution from the upper helicity band. Plot (c) shows the total susceptibility, i.e., sum of (a) and (b). The nesting vector  $\mathbf{Q}_1$  connects two sides of the Fermi surface. The other nesting vectors  $\mathbf{Q}_{2,3}$  are given by  $C_3$  rotations of  $\mathbf{Q}_1$ .

We perform a numerical calculation of the susceptibility and plot in Fig. 4.6 the largest eigenvalue of the spin susceptibility  $\chi_{\mathbf{q}}^1$  for different wavevectors  $\mathbf{q} = (q_x, q_y)$ . We focus on zero temperature and on the most perfectly hexagonally warped Fermi surface, which is the case for  $\mu = \mu_{\text{hex}}$ . In the plot, we show the decomposition of the susceptibility into the inter- and intraband contributions.

The major contribution of the interband scattering shown in Fig. 4.6(a), comes from  $\mathbf{q} \approx \mathbf{0}$  with only a weak signature of the hexagonal warping. A large value of  $\chi_{\mathbf{0}}^1$  would then indicate a tendency to a ferromagnetic ground state. The upper helicity intraband contribution, plotted in Fig. 4.6(b), peaks for the nesting wavevectors  $\pm \mathbf{Q}_{1,2,3}$ .

For  $T = 0$  the intraband contribution of the lower helicity band vanishes. In Fig. 4.6(c) we depict the total susceptibility, i.e., the sum of both the interband and upper helicity intraband contributions. The picture persists qualitatively unchanged as long as temperature is low, i.e.,  $T \lesssim 0.05$ .

From the plots we can read of the largest eigenvalue of the susceptibility, i.e.,  $\chi_{\mathbf{Q}_1}^1 \approx 12/(2\pi)^2$ . The Stoner criterion implies that a magnetic instability arises when the interaction is stronger than a critical value, which at  $T = 0$  is  $U_{\text{crit}} = 2/\chi_{\mathbf{Q}_1}^1 \approx 6.58$ . Given the material parameters of  $\text{Bi}_2\text{Te}_3$ , this corresponds to an interaction strength of  $U \approx 1.71$  eV. If only the upper helicity band contribution is taken into account a

higher value of  $U \approx 2.57 \text{ eV}$  is necessary. In the following qualitative discussions we will concentrate on the contribution from the upper helicity band only.

Once the leading instability corresponding to the largest eigenvalue is established, the remaining two instabilities corresponding to the other two eigenvalues  $\chi_q^{2,3}$  are suppressed. This follows from the fact that most of the Fermi surface is already gapped by the leading instability. Hence we can consider only the emergence of the leading magnetic instability. This simplification is justified for all temperatures and is confirmed by our numerical results where the eigenvalues of the remaining instabilities are very small. The results of our work are in agreement with previous studies [113, 115].

Now we proceed to analyze the structure of the leading order parameter, which is determined by the unit eigenvector  $\widehat{\mathbf{M}}_q^1$  of the spin susceptibility  $\chi_q^1$ . Since we only consider the dominant eigenvector and eigenvalue we omit the index 1 from here on for convenience. The complex unit eigenvector  $\widehat{\mathbf{M}}_{Q_1}$  can be parametrized by spherical coordinates with the angles  $\zeta$  and  $v$

$$\widehat{\mathbf{M}}_{Q_1}(\zeta, v) = \begin{pmatrix} \cos \zeta \\ i \sin \zeta \sin v \\ i \sin \zeta \cos v \end{pmatrix}. \quad (4.24)$$

We observe that the  $x$  component of the eigenvector is real, while the  $y$  and  $z$  components are imaginary. This  $\pi/2$  phase shift is a consequence of the spin-momentum locking of the surface states. The leading instability corresponds to a helical magnetic phase.

The orientation of the magnetic order can be understood on purely geometric arguments directly from the structure of the Hamiltonian. Considering only the upper helicity band, as we justified above, we can project the magnetic term of the Hamiltonian to the upper helicity band obtaining

$$\mathcal{H}_{\text{mag}}^+ = \int \frac{d\mathbf{q}}{(2\pi)^2} \left[ \frac{|\mathbf{M}_q|^2}{U} + \int \frac{d\mathbf{k}}{(2\pi)^2} \psi_{\mathbf{k}+\mathbf{q}/2,+}^\dagger \mathbf{M}_q \cdot \boldsymbol{\sigma}_q^+(\mathbf{k}) \psi_{\mathbf{k}-\mathbf{q}/2,+} \right]. \quad (4.25)$$

For this purpose we introduced the projected matrix element, which is related to the effective magnetic moment of the upper helicity band,

$$\begin{aligned}
 \sigma_q^+(\mathbf{k}) &\equiv \langle \mathbf{k} + \mathbf{q}/2, + | \sigma | \mathbf{k} - \mathbf{q}/2, + \rangle \\
 &= \left( \sin \frac{\vartheta_{\mathbf{k}+\mathbf{q}/2}}{2} \cos \frac{\vartheta_{\mathbf{k}-\mathbf{q}/2}}{2} \exp[-i\delta_{\mathbf{k},\mathbf{q},+}] + \cos \frac{\vartheta_{\mathbf{k}+\mathbf{q}/2}}{2} \sin \frac{\vartheta_{\mathbf{k}-\mathbf{q}/2}}{2} \exp[i\delta_{\mathbf{k},\mathbf{q},+}] , \right. \\
 &\quad i \sin \frac{\vartheta_{\mathbf{k}+\mathbf{q}/2}}{2} \cos \frac{\vartheta_{\mathbf{k}-\mathbf{q}/2}}{2} \exp[-i\delta_{\mathbf{k},\mathbf{q},+}] - i \cos \frac{\vartheta_{\mathbf{k}+\mathbf{q}/2}}{2} \sin \frac{\vartheta_{\mathbf{k}-\mathbf{q}/2}}{2} \exp[i\delta_{\mathbf{k},\mathbf{q},+}] , \\
 &\quad \left. \cos \frac{\vartheta_{\mathbf{k}+\mathbf{q}/2}}{2} \cos \frac{\vartheta_{\mathbf{k}-\mathbf{q}/2}}{2} \exp[i\delta_{\mathbf{k},\mathbf{q},-}] - \sin \frac{\vartheta_{\mathbf{k}+\mathbf{q}/2}}{2} \sin \frac{\vartheta_{\mathbf{k}-\mathbf{q}/2}}{2} \exp[-i\delta_{\mathbf{k},\mathbf{q},-}] \right),
 \end{aligned} \tag{4.26}$$

with  $\delta_{\mathbf{k},\mathbf{q},\pm} = (\varphi_{\mathbf{k}+\mathbf{q}/2} \pm \varphi_{\mathbf{k}-\mathbf{q}/2})/2$ . Note that for  $\mathbf{k} \approx \mathbf{0}$  the projected matrix element  $\sigma_q^+(\mathbf{0})$  reduces to

$$\sigma_q^+(\mathbf{0}) = \begin{pmatrix} \cos \vartheta_{q/2} \cos \varphi_{q/2} + i \sin \varphi_{q/2} \\ \cos \vartheta_{q/2} \sin \varphi_{q/2} - i \cos \varphi_{q/2} \\ -\sin \vartheta_{q/2} \end{pmatrix}. \tag{4.27}$$

Specifically for  $\mathbf{q} = \mathbf{Q}_1$  it holds  $\sigma_{\mathbf{Q}_1}^+(\mathbf{0}) = (i, k_0^3/\mu_{\text{hex}}, -k_0/\mu_{\text{hex}})^\top$ . The maximum magnetic gap at the hexagonal Fermi surface is achieved when  $|\mathbf{M}_{\mathbf{Q}_i} \cdot \sigma_{\mathbf{Q}_i}^+(\mathbf{k})|$  for  $i = 1, 2, 3$  become maximized. In the case of a flat Fermi surface nested by the wavevectors  $\mathbf{q} = \mathbf{Q}_{1,2,3}$ , this happens when  $\widehat{\mathbf{M}}_{\mathbf{Q}_{1,2,3}}$  is parallel to  $\sigma_{\mathbf{Q}_{1,2,3}}^+(\mathbf{0})$  respectively. For  $\mathbf{Q}_1$  one finds the magnetization direction

$$\widehat{\mathbf{M}}_{\mathbf{Q}_1} \approx \frac{1}{\sqrt{2}} \begin{pmatrix} 1 \\ ik_0^3/\mu_{\text{hex}} \\ -ik_0/\mu_{\text{hex}} \end{pmatrix}. \tag{4.28}$$

Note that the phases are not fixed and chosen by convention. Numerically we found  $\zeta \approx \pi/4$  and  $v \approx 0.9\pi$ , which is in good agreement with the approximate Eq. (4.28) determined using the geometric argument. Approximately it holds  $\sin(\zeta) \approx \cos(\zeta) \approx 1/\sqrt{2}$ ,  $\sin(v) \approx k_0^3/\mu_{\text{hex}}$ , and  $\cos(v) \approx -k_0/\mu_{\text{hex}}$ . There are small discrepancies between the numerical and approximate result due to additional contributions in the numerical results from other parts of the Fermi surface with poor nesting, such as for instance the round corners.

The other eigenvectors  $\widehat{\mathbf{M}}_{\pm\mathbf{Q}_{2,3}}$  can be obtained from the transformation properties of the susceptibility matrix under the point group operations  $\mathcal{G} \in C_{3v}$ , i.e.,  $\hat{\chi}_{\mathcal{G}\mathbf{q}} = \widehat{D}_{\mathcal{G}}^- \hat{\chi}_{\mathbf{q}} (\widehat{D}_{\mathcal{G}}^-)^\top$ . This implies  $\widehat{\mathbf{M}}_{\mathcal{G}\mathbf{q}} = \widehat{D}_{\mathcal{G}}^- \widehat{\mathbf{M}}_{\mathbf{q}}$ .

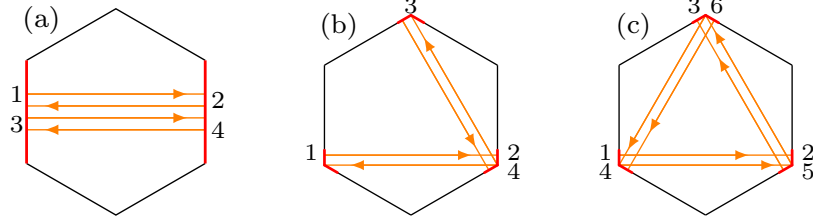


Figure 4.7: Scattering processes at fourth and sixth order in the hexagonal Fermi surface. The scattering vectors connect regions of high density of state in the Fermi surface. The process shown in (a) determines  $\beta_1$ , the process shown in (b) determines  $\beta_2$ . There are similar sixth order processes. However there is one distinct process at sixth order, which is shown in (c). This triangle scattering process determines  $\eta$ . The scattering phase space is shown in red. Due to momentum conservation the scattering phase space for  $\beta_2$  and  $\eta$  is significantly smaller than the space for  $\alpha$  and  $\beta_1$ .

This discussion shows, that the magnetic order parameter opens a gap at the well-nested parts of the Fermi surface, however, there is no guarantee for a gap opening at the remaining parts of the Fermi surface. This behavior is typical for two-dimensional systems with imperfect nesting [123].

#### 4.3.4 Landau theory at quartic order: Single- versus triple- $\mathbf{Q}$ phase

In this section we focus on the fourth order of the free energy expansion. Previous works on hexagonally warped surface states focused on the spin susceptibility or equivalently on the quadratic part of a Landau expansion. However at this level it is not possible to discriminate between single- $\mathbf{Q}$  or triple- $\mathbf{Q}$  magnetic phases [107]. A checkerboard phase with two  $\mathbf{Q}$  order parameters cannot appear since such a configuration never minimizes the free energy.

To determine which of the, at second order degenerate, ground states is the real ground state, we go to higher order in the Landau theory. As it turns out even the sixth-order coefficients of the Landau expansion are necessary. Here in this section we show that the quartic order decides in favor of a triple- $\mathbf{Q}$  order parameter.

As our analysis in the previous showed, we can focus on the dominant nesting vectors  $\pm\mathbf{Q}_i$  and the corresponding magnetic order parameters  $\mathbf{M}_{\mathbf{Q}_i}$ . At first we split the favored magnetization vectors  $\mathbf{M}_{\mathbf{Q}_i} = M_i \widehat{\mathbf{M}}_i$  into a complex amplitude  $M_i = e^{i\phi_i} |M_i|$  and a unit vector  $\widehat{\mathbf{M}}_i = \widehat{\mathbf{M}}_{\mathbf{Q}_i}$ . Under complex conjugation the order parameters behave as  $\mathbf{M}_{-\mathbf{Q}_i} = M_i^* \widehat{\mathbf{M}}_{-\mathbf{Q}_i}$ .

From the previous section the orientation of the magnetic order parameters is fixed. There remain six degrees of freedom from the moduli  $M_i$  and the phases  $\Phi_i$ . The free energy expansion at fourth order involving only the moduli  $M_i$  can then be written as

$$\mathcal{F}^{(4)} = \alpha \sum_{i=1}^3 |M_i|^2 + \frac{\beta_1}{2} \sum_{i=1}^3 |M_i|^4 + \beta_2 \sum_{i < j} |M_i|^2 |M_j|^2. \quad (4.29)$$

The first coefficient  $\alpha = 2/U - \chi_{\mathbf{Q}_1}^1$  vanishes when the Stoner criterion is fulfilled and the instability sets in. The higher coefficients  $\beta_1$  and  $\beta_2$  originate from the scattering processes shown in Fig. 4.7(a) and (b), respectively. The values of the coefficients can be obtained from four-leg loop diagrams. The second-order term in the Landau expansion exhibits a U(3) symmetry [107]. This means that we can express the three complex scalar order parameters as a vector with angles  $\omega$  and  $\rho$

$$\begin{pmatrix} M_1 \\ M_2 \\ M_3 \end{pmatrix} = |M| \begin{pmatrix} e^{i\Phi_1} \sin \omega \cos \rho \\ e^{i\Phi_2} \sin \omega \sin \rho \\ e^{i\Phi_3} \cos \omega \end{pmatrix}. \quad (4.30)$$

Furthermore the symmetry can be shown explicitly by splitting the fourth-order terms into a U(3)-symmetric term with coefficient  $\beta_S = \beta_2/2$  and an anisotropic term with coefficient  $\beta_A = (\beta_1 - \beta_2)/2$  as follows

$$\mathcal{F}^{(4)} = \alpha \sum_{i=1}^3 |M_i|^2 + \beta_S \left( \sum_{i=1}^3 |M_i|^2 \right)^2 + \beta_A \sum_{i=1}^3 |M_i|^4. \quad (4.31)$$

The U(3) symmetry can be broken by higher order terms.

Minimizing the free energy determines which of the magnetic order parameters appear in the ground state. It would be possible that the order parameters coexist or compete. For that it is necessary to analyze the relation between  $\beta_1$  and  $\beta_2$  (or equivalently between  $\beta_S$  and  $\beta_A$ ). At first we consider the case  $\beta_S > 0$ . Then it is sufficient to minimize the anisotropic term

$$\beta_A |M|^4 \left[ \sin^4 \omega (\cos^4 \rho + \sin^4 \rho) + \cos^4 \omega \right]. \quad (4.32)$$

In this case for  $\beta_A < 0$  the minima are located at  $\omega = 0$  (independent of  $\rho$ ) and at  $\omega = \pm\pi/2$  with  $\rho = 0, \pm\pi/2$ . These minima correspond to a magnetization with a single wavevector  $\mathbf{Q}_i$ . On the other hand, for  $\beta_A > 0$  the minimum at  $\rho = \pm\pi/4$  with  $\omega = \arctan \sqrt{2}$  implies that  $|M_{1,2,3}|$  appear equally together.

Now in the second case  $\beta_S < 0$  the favored value for the modulus  $|M|$  is obtained by minimizing the Landau functional up to quartic order. It reduces to the three equations

$$|M_i| \left( \alpha + \beta_1 |M_i|^2 + \beta_2 \sum_{j \neq i} |M_j|^2 \right) = 0. \quad (4.33)$$

This system of equations has three solutions:

- (i) Nonmagnetic phase with  $|M_i| = 0$ .
- (ii) Single- $\mathbf{Q}$  phase. Here we have, e.g.,  $|M_1| \neq 0$  and  $|M_{2,3}| = 0$  and obtain  $|M_1|^2 = |\alpha|/\beta_1$ . The free energy takes the value  $\mathcal{F} = -\alpha^2/(2\beta_1)$ .
- (iii) Triple- $\mathbf{Q}$  phase. We obtain  $|M_i|^2 = |\alpha|/(\beta_1 + 2\beta_2)$  for  $i = 1, 2, 3$  and the free energy  $\mathcal{F} = -3\alpha^2/[2(\beta_1 + 2\beta_2)]$ .

Comparing the single and triple phases, we find that the triple- $\mathbf{Q}$  phase is stabilized when  $\beta_1 > \beta_2$  or  $\beta_1 > -2\beta_2$ . We note again that a double- $\mathbf{Q}$  phase cannot appear, since whenever two order parameters would appear together, due to the  $\beta_2$  coupling, these order parameters would act as sources for the remaining third-order parameter which would then lead to a triple- $\mathbf{Q}$  phase.

According to this analysis, the magnitude of the order parameters is fixed at the quartic order of the Landau theory. However there are still three phase degrees of freedom yet to be determined. Two of the phase degrees of freedom,  $\Phi_x = 2\Phi_1 - \Phi_2 - \Phi_3$  and  $\Phi_y = \sqrt{3}(\Phi_2 - \Phi_3)$  form Goldstone modes, i.e., phasons which are related to the broken translational symmetry in the two-dimensional coordinate space. They correspond to translations of the magnetic texture in the plane. The two phases  $\Phi_{x,y}$  transform according to the two-dimensional irreducible representation E of  $C_{3v}$ . There is another ‘center of mass’ phase  $\Phi_z = \Phi_1 + \Phi_2 + \Phi_3$ , which transforms according to the  $A_2$  irreducible representation of  $C_{3v}$ . We will see that this center of mass phase is fixed at the sixth order of the Landau expansion in the next section.

The coefficients  $\beta_{1,2}$  are obtained by evaluating four-leg loop diagrams, where we present our numerical results in Fig. 4.8. We find that  $\beta_1 \gg 2|\beta_2|$  for the whole temperature regime which is relevant for our scenario. This implies that the triple- $\mathbf{Q}$  phase with equal values of  $|M_i|$  for  $i = 1, 2, 3$  is favored over the stripe phase if the system is tuned to a hexagonally warped Fermi surface by setting  $\mu = \mu_{\text{hex}}$  at low temperature. The stabilization of this triple- $\mathbf{Q}$  magnetic phase renders the system  $C_3$ -symmetric. Although the stripe phase is disfavored within our analysis, it can still become relevant in cases where external fields or structural defects break the  $C_3$  symmetry.

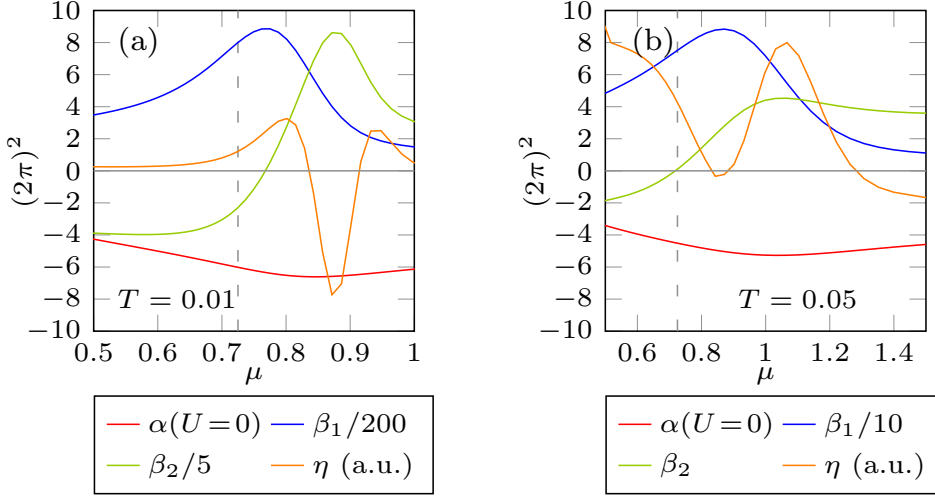


Figure 4.8: (a,b) Second, fourth and sixth order coefficients of the Landau expansion for  $T = 0.01$  and  $T = 0.05$ . The temperatures correspond to  $T = 30$  K and  $T = 150$  K for  $\text{Bi}_2\text{Te}_3$ . The dashed lines show the chemical potential  $\mu = \mu_{\text{hex}}$  of hexagonal warping. For  $\mu = \mu_{\text{hex}}$  the relation between the coefficients  $\alpha$ ,  $\beta_{1,2}$ , and  $\eta$  favors the triple- $\mathbf{Q}$  magnetic phases, including the skyrmion texture. We plot  $\eta$  in arbitrary units since only the sign matters for the selection of the phase. In the numeric calculation we considered only the upper helicity band.

### 4.3.5 Sixth order Landau theory: Phase locking

In this section we go to the sixth order of the Landau theory and show that at this level one additional phase of the order parameters is locked. At sixth order there are terms of the form  $|M_i|^6$ ,  $|M_i|^2|M_j|^4$  with  $i \neq j$  and  $|M_1M_2M_3|^2$ . These terms yield only quantitative corrections since they consist of factors already appearing at lower order. Therefore they cannot provide any information about the phases.

However there appears an additional unique term which contains the ‘‘center of mass’’ phase  $\Phi_z$

$$\mathcal{F}_{\Phi_z}^{(6)} = \eta(M_1M_2M_3)^2 + \eta(M_1^*M_2^*M_3^*)^2 = 2\eta|M_1M_2M_3|^2 \cos(2\Phi_z). \quad (4.34)$$

This term is allowed due to the relation of the momenta  $\mathbf{Q}_1 + \mathbf{Q}_2 + \mathbf{Q}_3 = \mathbf{0}$ . Minimization of this term will lead to a locking of the phase  $\Phi_z$ . We show the most relevant scattering process connecting regions of high density of states in Fig. 4.7(c). There the particle scatters twice around the triangular path.

For  $\eta < 0$  ( $\eta > 0$ ) the free energy is minimized if  $\Phi_z = 0, \pi$  ( $\Phi_z = \pm\pi/2$ ). We determine the sign of  $\eta$  using numerical calculations (see figure Fig. 4.8) and observe that the results depend on the shape of the Fermi surface which in turn depends on the chemical potential  $\mu$ . In the plot there are points, where  $\eta$  vanishes, which leads to a degeneracy and unlocked  $\Phi_z$ . In such a scenario  $\Phi_z$  stays a Goldstone mode. However in the hexagonal regime, which we are most interested in, with  $\mu = \mu_{\text{hex}} = 0.725$ , it holds  $\eta > 0$ . This leads to a specific magnetic texture, a skyrmion lattice, which we describe in the next section.

### 4.3.6 Magnetic texture and skyrmion lattices

Since  $\Phi_z = \pm\pi/2$  is locked, we can examine the real-space structure of the magnetic texture  $\mathbf{M}(\mathbf{r}) = \sum_{i=1}^3 \mathbf{M}_{\mathbf{Q}_i} e^{i\mathbf{Q}_i \cdot \mathbf{r}} + \text{c.c.}$ , which is given by its Fourier components. We show the resulting magnetization profiles in Fig. 4.9 for the different cases. In the following we call the two possible phases either  $A_1$  or  $A_2$  (Skyrmion) phase. This terminology is justified by looking at the transformation behavior of the magnetic texture under the point group operations. For this purpose we fix the Goldstone phases, which correspond to translations in the  $xy$ -plane such that the  $M_{\mathbf{Q}_1, x}$  component of the order parameter is real and the  $M_{\mathbf{Q}_1, y/z}$  components are purely imaginary. This is the same convention used in Section 4.3.3. Looking at the plot of the magnetization profiles we can directly identify the irreducible representation. In the case  $\Phi_z = 0, \pi$  we find the  $A_1$  representation, since the  $M_x(\mathbf{r})$  component is even under mirror symmetry  $x \mapsto -x$ , while the  $M_{y,z}(\mathbf{r})$  components change sign. The alternative situation is given in the  $A_2$  or skyrmion case, with  $\Phi_z = \pm\pi/2$  where only the  $C_3$  symmetry is preserved. For more details on the different representations of the magnetic order see Appendix A.2.

The skyrmion phase has an associated topological invariant in real space per skyrmion of the lattice. As shown in Fig. 4.9(b,c) the periodicity allows to introduce a unit cell in real space (enclosed by green lines), which is spanned by the unit vectors

$$\mathbf{a}_1 = \frac{2\pi}{\sqrt{3}k_0} \begin{pmatrix} \frac{\sqrt{3}}{2} & 1 \\ 2 & 2 \end{pmatrix} \quad \text{and} \quad \mathbf{a}_2 = \frac{2\pi}{\sqrt{3}k_0} (0, 1). \quad (4.35)$$

In the figure we show a hexagon with  $|\mathbf{r} \cdot \mathbf{Q}_i| \leq 2\pi$ , which consists of three unit cells to highlight the unbroken  $C_3$  symmetry. The periodicity of the magnetization in real space yields a Brillouin zone in  $\mathbf{k}$  space with  $|\mathbf{k} \cdot \hat{\mathbf{Q}}_i| \leq k_0$ . The magnetization direction at opposite edges of the unit cell is the same which allows compactification of the unit cell. This means that the opposite edges can be glued together to obtain a manifold homeomorphic to the flat 2-torus  $\mathbb{T}^2$ . The magnetization vectors  $\widehat{\mathbf{M}}(\mathbf{r})$  which live on

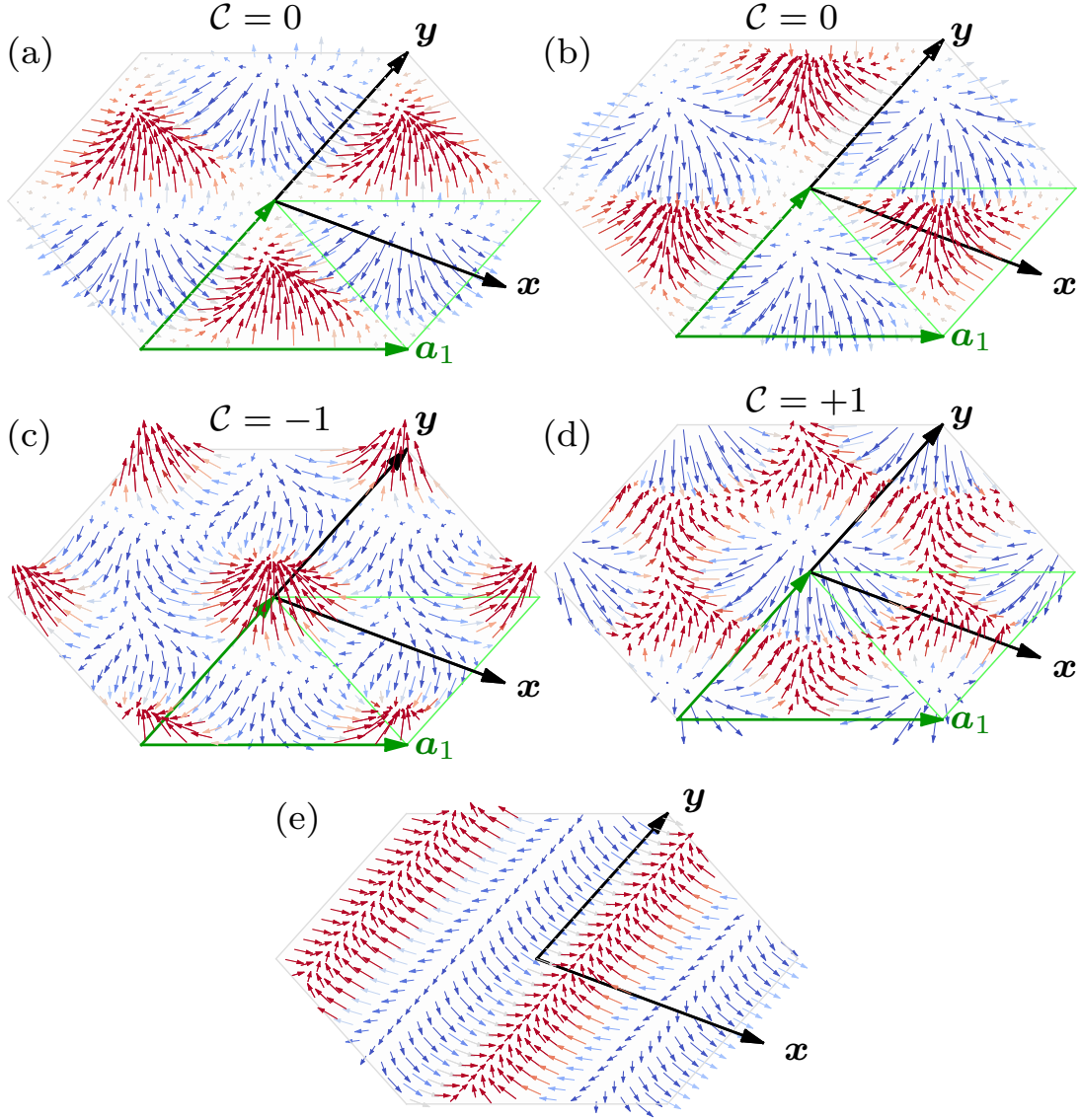


Figure 4.9: Magnetic texture on the surface of a warped topological insulating for  $|\mathbf{r} \cdot \hat{\mathbf{Q}}_i| \leq 2\pi$ . The unit cell is shown as a green parallelogram. Figures (a,b) show triple- $\mathbf{Q}$  phases which belong to the  $A_1$  representation of the group  $C_{3v}$  with trivial skyrmion charge  $\mathcal{C} = 0$ . (a)  $\Phi_z = \Phi_{1,2,3} = 0$  and (b)  $\Phi_z = \Phi_{1,2,3} = \pi$ . Figures (c,d) show triple- $\mathbf{Q}$  phases belonging to the  $A_2$  representation of the group  $C_{3v}$  with non-trivial skyrmion charge  $\mathcal{C} = \pm 1$ . (c)  $\Phi_z = -\pi/2$ ,  $\Phi_{1,2,3} = \pi/2$  and (d)  $\Phi_z = \pi/2$ ,  $\Phi_{1,2,3} = -\pi/2$ . Figure (e) shows the excluded single- $\mathbf{Q}$  phase (strip phase) with order parameter breaking the  $C_3$  symmetry. The vector normalization in (e) is different from (a) to (d) to improve the presentation.

Table 4.2: Symmetry classification of the phase degrees of freedom  $\Phi$ , electric field  $\mathbf{E}$ , magnetic field  $\mathbf{B}$  and current  $\mathbf{J}$ , according to the irreducible representations of the point group  $C_{3v}$  and the behavior under time reversal  $\mathcal{T}$ .

IR	$\mathbb{1}$	$2C_3$	$3\sigma_v$	$\mathcal{T} = +1$	$\mathcal{T} = -1$
$A_1$	1	1	1	$E_z$	$J_z$
$A_2$	1	1	-1	$\Phi_z$	$B_z$
$E$	2	-1	0	$(\Phi_x, \Phi_y), (E_x, E_y)$	$(B_x, B_y), (J_x, J_y)$

this manifold take on values on the 2-sphere  $S^2$ . Now a topological invariant can be assigned to the mapping  $\mathbb{T}^2 \rightarrow S^2$ . The relevant topological invariant is the first Chern number, which takes only integer values and is defined as

$$\mathcal{C} = \frac{1}{4\pi} \int_{\text{UC}} d\mathbf{r} \widehat{\mathbf{M}}(\mathbf{r}) \cdot \left( \partial_x \widehat{\mathbf{M}}(\mathbf{r}) \times \partial_y \widehat{\mathbf{M}}(\mathbf{r}) \right). \quad (4.36)$$

Interestingly this topological invariant also appears in the quantum Hall effect to describe the number of Landau levels as discussed in Section 1.1.1. For the two phases, we find  $\mathcal{C} = \text{sign}(\Phi_z)$ , thus  $\mathcal{C} = 0$  for the  $A_1$  phases with  $\varphi = 0$  and  $\mathcal{C} = \pm 1$  for the  $A_2$  phase with  $\Phi_z = \pm\pi/2$ . The  $A_1$  phase is therefore a trivial phase, and  $A_2$  a topologically non-trivial phase. The possibility of a non-trivial magnetic ground state has been discussed earlier in Ref. [115]. Our detailed analysis confirms that indeed the skyrmion lattice is the true ground state of such a system with hexagonal Fermi surface and repulsive Hubbard interaction.

## 4.4 Control and fingerprints of the magnetic phases

In this section we study how the magnetic phases can be controlled by applying external magnetic fields or imposing currents. We focus on the  $C_3$  symmetric phases, which are favored compared to the single- $\mathbf{Q}$  phases. The single- $\mathbf{Q}$  phases can only be favored if appropriate symmetry breaking fields are introduced.

Within the  $C_3$ -symmetric phases, particularly interesting is the possibility to couple a magnetic field in  $z$ -direction to the skyrmion charge of the magnetic texture. This way it is possible to select the  $\mathcal{C} = \pm 1$  phases and to stabilize the texture.

We classify external electric  $\mathbf{E}(\mathbf{r})$  and magnetic fields  $\mathbf{B}(\mathbf{r})$  according to the  $C_{3v}$  point group symmetry. In Table 4.2 all the components of the electric and magnetic fields are classified according to their respective irreducible representations and to their transformation behavior under time reversal symmetry  $\mathcal{T}$ . In the table we included the current vector  $\mathbf{J}(\mathbf{r})$  too. This is particularly relevant when the topological insulator

Table 4.3: Combinations of magnetic field  $\mathbf{B}$  and current  $\mathbf{J}$  which couple to the third order terms  $|M_1 M_2 M_3| \cos \Phi_z$  or  $|M_1 M_2 M_3| \sin \Phi_z$ . The presence of such terms can select the triple- $\mathbf{Q}$  magnetic ground state. The  $\cos \Phi_z$  ( $\sin \Phi_z$ ) establishes the  $\Phi_z = 0, \pi$  ( $\Phi_z = \pm\pi/2$ ) magnetic ground state. In particular,  $\sin \Phi_z$  stabilizes the skyrmion lattice.

$ M_1 M_2 M_3  \cos \Phi_z$	$ M_1 M_2 M_3  \sin \Phi_z$
$B_x(B_x^2 - 3B_y^2)$	$B_z, B_z^3, B_z(B_x^2 + B_y^2)$
$J_y(J_y^2 - 3J_x^2)$	$B_y(B_y^2 - 3B_x^2), J_x(J_x^2 - 3J_y^2)$
$2J_x J_y B_y - (J_x^2 - J_y^2)B_x$	$2J_x J_y B_x + (J_x^2 - J_y^2)B_y$
$2B_x B_y J_x + (B_x^2 - B_y^2)J_y$	$2B_x B_y J_y - (B_x^2 - B_y^2)J_x$

surface is in proximity to a bulk superconductor with superconducting order parameter  $\Delta(\mathbf{r}) = \Delta e^{i\phi(\mathbf{r})}$  and  $\mathbf{J}(\mathbf{r}) \propto \nabla\phi(\mathbf{r})$ .

Homogeneous and spatially static fields can only modify the magnetic phase diagram by coupling to the phases of the order parameters. Constant  $\mathbf{B}$  and  $\mathbf{J}$  fields can only couple to  $\Phi_z$ . Accordingly an electric field  $\mathbf{E}$  can lead to terms of the form  $\Phi_x E_x + \Phi_y E_y$ . Coupling to  $\Phi_z$  allows to determine the favored triple- $\mathbf{Q}$  phase.  $\Phi_z$  appears in the Landau expansion only in terms of order three of the form  $(M_1 M_2 M_3)^n = |M_1 M_2 M_3| e^{in\Phi_z}$  and  $(M_1^* M_2^* M_3^*)^n = |M_1 M_2 M_3| e^{-in\Phi_z}$  with  $n \in \mathbb{N}$ . Since the system respects time reversal symmetry  $\mathcal{T}$ , the lowest allowed term is of sixth order with the form  $2\eta |M_1 M_2 M_3|^2 \cos(2\Phi_z)$ . More general, only even  $n$  is allowed.

At sixth order coupling to external  $\mathcal{T}$ -symmetric fields allows switching between possible triple- $\mathbf{Q}$  phases. This allows to control the skyrmion charge  $\mathcal{C} = \pm 1$ . However effects at lower order are probably more interesting. For example applying  $\mathcal{T}$ -violating external fields as given in Table 4.3 can already act at third order and can influence the phase diagram. The higher order terms, in particular the sixth order terms and the value of  $\eta$  are then rendered irrelevant near the boundaries of the magnetic phase where the order parameters are small.

The relevant terms at third-order are  $|M_1 M_2 M_3| \cos \Phi_z$  and  $|M_1 M_2 M_3| \sin \Phi_z$ , which belong to the  $A_1$  and  $A_2$  representations respectively. These two terms can couple to external fields which break  $\mathcal{T}$  symmetry. Coupling to  $\cos \Phi_z$  ( $\sin \Phi_z$ ) will lead to a stabilization of the triple- $\mathbf{Q}$  phases with  $\Phi_z = 0, \pi$  ( $\Phi_z = \pm\pi/2$ ).

The magnetic field in  $B_z$  only couples to the  $A_2$  term and yields  $|M_1 M_2 M_3| \sin \Phi_z B_z$ . For the extremal values of  $\sin \Phi_z$  this term takes the form  $\mathcal{C} B_z$  with  $\mathcal{C} = \pm 1$ . This means that the field  $B_z$ , which is easily accessible in experiment, directly couples to the skyrmion charge and as such allows stabilization and manipulation of the skyrmion

phase. In contrast to  $B_z$ , in-plane fields  $B_{x,y}$  or currents  $J_{x,y}$  break the  $C_3$  point group symmetry and favor magnetic stripe phases.

Concerning the terms at third order in Table 4.3: The fields with non-vanishing moments  $B_x(B_x^2 - 3B_y^2)$  or  $J_x(J_x^2 - 3J_y^2)$  (and similarly for the other third-order combinations which are  $C_3$  symmetric but break  $\mathcal{T}$  symmetry) would stabilize the  $A_1$  or  $A_2$  phase with  $\mathcal{C} = 0$  or  $\mathcal{C} = \pm 1$  respectively. However these higher order terms do not have practical relevance since it would be difficult to generate third order moments without also creating linear  $C_3$  symmetry violating fields  $B_{x,y}$  or  $J_{x,y}$  which couple then at lower order. The required structure of the external fields restricts the potential use of them to manipulate the magnetic phase. However the other way round, these field distributions could play a role as a signature of the magnetic phase, since these are precisely the field distributions that are generated by the magnetic texture itself.

## 4.5 Summary and conclusion

In this chapter we discussed the electronic surface states of a 3D topological insulator with warping. We investigated the magnetic instabilities which can spontaneously develop in the surface states in the case of strong hexagonal warping of the Fermi surface. Due to imperfect nesting, the phase transition can only occur above a critical strength of a repulsive Hubbard interaction.

We microscopically derived and analyzed a Landau theory for varying values of the chemical potential and extended earlier work considering this problem. At fourth order the Landau theory showed that the phase with a single dominant wavevector  $\mathbf{Q}_i$  is not favored. This phase can be favored if the  $C_3$  symmetry of the system is broken by external effects, e.g., by an applied field. Instead a phase with three contributing wavevectors  $\mathbf{Q}_{1,2,3}$  is favored, which yields a magnetic lattice. There are three possible phases with  $\mathbf{Q}_{1,2,3}$  which differ by the skyrmion charge  $\mathcal{C}$ . Tuning the chemical potential allows to switch between the different phases with  $\mathcal{C} = 0, \pm 1$ . The phases with  $\mathcal{C} = \pm 1$  exhibit topologically non-trivial skyrmions in real space. In particular, we showed that the case with a nearly hexagonal Fermi surface favors a skyrmion phase with  $\mathcal{C} = \pm 1$ .

Furthermore we investigated the modification of the magnetic phase diagram when external fields are applied, e.g., a magnetic field in  $z$ -direction can induce a quantum phase transition between two topologically distinct magnetic phases, this way creating a skyrmion charge switch. However in this case the complete lattice switches, which is different from experimental platforms currently under investigation, where isolated skyrmion excitations are studied [92].

To conclude this chapter, we showed that warped topological insulators indeed support a skyrmion lattice if a sufficiently strong repulsive interaction is present. While the Fermi surface warping was discovered in experiment, there are ongoing efforts to study the magnetic behavior of such materials. The crucial question is whether there are materials providing a sufficiently strong interaction.

In the next chapter we will extend this work and combine the topological insulator with a conventional superconductor to engineer a topological superconductor which can act as a host for Majorana bound states.



# 5

## Chapter 5

---

# Topological superconductivity in magnetic skyrmion lattice and superconductor-based heterostructure

This chapter is partially based on our publication Ref. [1] and partially on unpublished works. Our goal is to engineer topological superconductors from topological insulators and conventional superconductors [34, 65, 124–127]. There are multiple experiments, which take steps towards the implementation of such systems [128–134]. We are particularly interested in interface effects and focus on materials with a magnetic texture, as discussed in Chapter 4.

First we discuss the general description of a system consisting of a magnetic surface with a superconducting layer on top. We introduce a tunneling coupling between the two components and derive the relevant free energy description. From there we investigate the feedback effects between superconductor and magnetic layer. In particular we discuss the suppression of the magnetic instability in the presence of the superconductor, leading to a reduction of the magnetic gap due to the superconductor. Vice versa there is an effect from the magnetic order on the superconductor, e.g., a multipolar supercurrent distribution is induced in the superconductor. Furthermore certain staggered superconducting correlations appear.

Then we focus on the particular example of a Bi-based topological insulator as discussed in Chapter 4, analyze this system in a self-consistent manner and verify the possibility to obtain a topological superconductor.

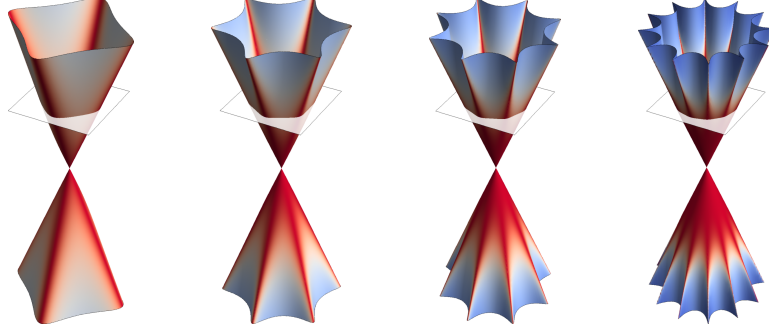


Figure 5.1: Warped Dirac cones for  $C_{nv}$  with  $n = 2, 3, 4$ . We plot the unitless dispersion with  $v = \gamma = 1$ . The  $C_{2v}$  case uses a stronger warping  $\gamma = 3$  for presentational purposes.  $C_{6v}$  uses  $\gamma = 0.2$ . Color coding shows the direction-resolved density of states.

Finally we discuss the properties of the topological superconductors, i.e., the possibility to host Majorana bound states. Majorana states occur at domain walls where the energy difference between the magnetic order parameter and a proximity-induced superconducting gap changes sign [65, 126, 135, 136]. In the systems at hand, chiral Majorana bands and additional Majorana flat bands can appear due to an anisotropy in the low energy description. The flat bands arise from degenerate Majorana solutions with a flat dispersion in one momentum direction. We discuss the effects of interactions on Majorana flat bands.

## 5.1 Hamiltonian of a magnetic skyrmion lattice

In the following we describe a heterostructure based on a magnetic skyrmion lattice in the  $xy$ -plane at  $z = 0$ . On top of the skyrmion lattice at  $z \in [0, L]$  is a superconducting layer with thickness  $L$ . Generalized from Chapter 4, a magnetic skyrmion lattice can be described by a Hamiltonian of the form

$$\mathcal{H}_{\text{mag}} = \int d\mathbf{r} \psi^\dagger(\mathbf{r}) \hat{\mathcal{H}}_{\text{mag}}^0(\hat{\mathbf{p}}) \psi(\mathbf{r}) + U \int d\mathbf{r} n_\uparrow(\mathbf{r}) n_\downarrow(\mathbf{r}). \quad (5.1)$$

The spinor  $\psi(\mathbf{r}) = (\psi_\uparrow(\mathbf{r}), \psi_\downarrow(\mathbf{r}))^\top$  is defined in spin-space and the integration is performed in the  $xy$ -plane with  $\mathbf{r} = (x, y, 0)$ . As a convention we write  $\mathbf{R} = (\mathbf{r}, z)$  for the coordinates in three dimensions, which include the superconducting layer. Here the magnetic layer is described as a purely two-dimensional film in the  $xy$ -plane at  $z = 0$ . In reality the layer has a finite thickness and the surface states decay into the bulk. However we exclude the influence of the underlying bulk, which is a reasonable

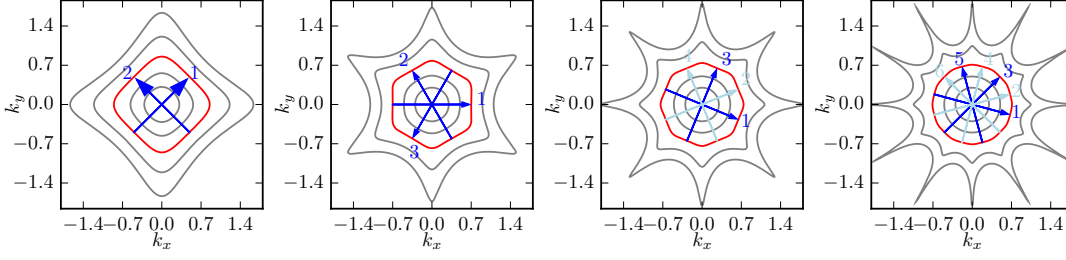


Figure 5.2: Fermi surface nesting for  $C_{nv}$ -symmetric FS depending on the chemical potential for  $n = 2, 3, 4, 6$ . We concentrate on the situation  $\mu = \mu_{\text{flat}}$  at which the FS becomes approximately flat (shown in red in the figures), thus leading to a good FS nesting. The nesting vectors  $\mathbf{Q}_l$  are shown in blue with the index  $l$ . All Fermi surfaces are plotted for  $\gamma = 1$  for different chemical potentials  $\mu$ .

approximation for topological insulators, where the surface physics is dominated by the surface modes. The phase transition to a magnetic texture is possible since the system is three-dimensional in fact. The non-interacting single-particle Hamiltonian  $\hat{\mathcal{H}}_{\text{mag}}^0(\hat{\mathbf{p}})$  with momentum dependence is supplemented by a repulsive Hubbard interaction with  $U > 0$ , which is necessary to drive the magnetic order. Note that, in general systems with other types of interactions could be studied in the given context. The presence of Hubbard interaction however is particularly suitable to drive magnetic ordering if the system exhibits nesting. The single-particle Hamiltonian takes the form

$$\hat{\mathcal{H}}_{\text{mag}}^0(\hat{\mathbf{p}}) = \delta_{\text{mag}}(\hat{\mathbf{p}}) + \mathbf{g}(\hat{\mathbf{p}}) \cdot \boldsymbol{\sigma} - \mu, \quad (5.2)$$

where we introduced a dispersion  $\delta_{\text{mag}}(\hat{\mathbf{p}}) = \delta_{\text{mag}}(-\hat{\mathbf{p}})$  and a spin-orbit coupling term  $\mathbf{g}(\hat{\mathbf{p}}) = -\mathbf{g}(-\hat{\mathbf{p}})$ . Similar to the coordinates  $\mathbf{r}$  and  $\mathbf{R}$ , we denote the momentum operators as  $\hat{\mathbf{p}} = (\hat{p}_x, \hat{p}_y, 0)^\top$  and  $\hat{\mathbf{P}} = (\hat{p}, \hat{p}_z)^\top$ . The chemical potential  $\mu$  can be tuned by doping of the material.

Given a stabilized magnetic texture we define the magnetic order parameter  $\mathbf{M}(\mathbf{r}) = -U/2 \langle \boldsymbol{\psi}^\dagger(\mathbf{r}) \boldsymbol{\sigma} \boldsymbol{\psi}(\mathbf{r}) \rangle$  on a mean-field level. Since we assume a magnetic texture in the form of a lattice, the magnetic order parameter can be written in Fourier representation with a small set of dominant wavevectors  $\mathbf{Q}_i = (\mathbf{q}_i, 0)$  with  $\mathbf{q}_i = (q_{i,x}, q_{i,y})$ . The form of the wavevectors depend on the point group symmetry of the system under consideration. In the case of  $\text{Bi}_2\text{Te}_3$  we obtained three wavevectors due to the point group  $C_{3v}$  as discussed in Chapter 4. The generalization includes systems with different point group symmetries and nesting vectors as shown in Fig. 5.1 and Fig. 5.2.

Given the magnetic order parameter, the mean-field decoupled Hamiltonian takes the form

$$\begin{aligned}\mathcal{H}_{\text{mag}} &= \int d\mathbf{r} \frac{\mathbf{M}^2(\mathbf{r})}{U} + \frac{1}{2} \int d\mathbf{r} \Psi^\dagger(\mathbf{r}) \hat{\mathcal{H}}_{\text{mag}}(\hat{\mathbf{p}}, \mathbf{r}) \Psi(\mathbf{r}), \\ \hat{\mathcal{H}}_{\text{mag}}(\hat{\mathbf{p}}, \mathbf{r}) &= \delta_{\text{mag}}(\hat{\mathbf{p}}) \tau_z + \mathbf{g}(\hat{\mathbf{p}}) \cdot \tau_z \tilde{\boldsymbol{\sigma}} - \mu \tau_z + \mathbf{M}(\mathbf{r}) \cdot \tilde{\boldsymbol{\sigma}}.\end{aligned}\quad (5.3)$$

Since we are interested in superconducting terms, we extended the Hamiltonian in particle-hole space spanned by the  $\boldsymbol{\tau}$  Pauli matrices. The Hamiltonian acts on the Nambu spinor  $\Psi^\dagger(\mathbf{r}) = (\psi_\uparrow^\dagger(\mathbf{r}), \psi_\downarrow^\dagger(\mathbf{r}), \psi_\uparrow(\mathbf{r}), \psi_\downarrow(\mathbf{r}))$ . Furthermore the spin matrices are replaced by  $\tilde{\boldsymbol{\sigma}} = (\tau_z \sigma_x, \sigma_y, \tau_z \sigma_z)$  here. Note the factor 1/2 which is necessary to avoid double counting the electronic degrees of freedom. In the next section we discuss the feedback effects between the magnetic and the superconducting layer.

## 5.2 Feedback effects between superconductor and magnetic texture

In order to discuss feedback effects we first introduce the Hamiltonian description of the superconductor and the coupling between the two subsystems. Then we derive a free energy description to identify the relevant feedback effects, which are expected at such an interface.

### 5.2.1 Coupling between superconductor and magnetic texture

We start from the Hamiltonian for the superconductor in coordinate space given in the form

$$\mathcal{H}_{\text{sc}} = \int d\mathbf{R} c^\dagger(\mathbf{R}) \epsilon(\hat{\mathbf{P}}) c(\mathbf{R}) - g \int d\mathbf{R} c_\uparrow^\dagger(\mathbf{R}) c_\downarrow^\dagger(\mathbf{R}) c_\downarrow(\mathbf{R}) c_\uparrow(\mathbf{R}) \quad (5.4)$$

with interaction strength  $g > 0$ . We assume a featureless dispersion given solely by the quadratic term  $\epsilon(\hat{\mathbf{P}}) = (\hat{\mathbf{P}}^2 - P_F^2)/(2m)$  with Fermi momentum  $P_F$  and electron mass  $m$ . The boundary conditions of the bulk superconductor are assumed to be periodic in all three directions such that plane waves with appropriately quantized wavevectors can be employed as a basis. Despite the featureless dispersion the superconducting order parameter  $\Delta(\mathbf{R})$  acquires a spatial dependence due to the coupling to the spatially inhomogeneous magnetic lattice. In particular we expect the Fourier components  $\Delta_{\mathbf{0}}(z)$  and  $\Delta_{\mathbf{q}_i}(z)$  to appear. The order parameter is determined by the self-consistency equation  $\Delta(\mathbf{R}) = -g \langle c_\downarrow(\mathbf{R}) c_\uparrow(\mathbf{R}) \rangle$ . Given the order parameter, the mean-field decoupled

Hamiltonian takes the form

$$\begin{aligned}\mathcal{H}_{\text{sc}} &= \int d\mathbf{R} \frac{|\Delta(\mathbf{R})|^2}{g} + \frac{1}{2} \int d\mathbf{R} C^\dagger(\mathbf{R}) \hat{\mathcal{H}}_{\text{sc}}(\hat{\mathbf{P}}, \mathbf{R}) C(\mathbf{R}), \\ \hat{\mathcal{H}}_{\text{sc}}(\hat{\mathbf{P}}, \mathbf{R}) &= \epsilon(\hat{\mathbf{P}}) \tau_z + \text{Re} \Delta(\mathbf{R}) \tau_y \sigma_y - \text{Im} \Delta(\mathbf{R}) \tau_x \sigma_y.\end{aligned}\quad (5.5)$$

The Hamiltonian is defined in particle-hole space with the Nambu spinor  $C^\dagger(\mathbf{R}) = (c_\uparrow^\dagger(\mathbf{R}), c_\downarrow^\dagger(\mathbf{R}), c_\uparrow(\mathbf{R}), c_\downarrow(\mathbf{R}))$ .

The coupling of the two subsystems is described by a tunneling Hamiltonian

$$\mathcal{H}_T = t \int d\mathbf{r} \psi^\dagger(\mathbf{r}) \mathbf{c}(\mathbf{r}) + \text{H.c.} = \frac{1}{2} \int d\mathbf{r} \Psi^\dagger(\mathbf{r}) \hat{T} C(\mathbf{r}) + \text{H.c.}, \quad (5.6)$$

where we introduced a tunneling constant  $t$  and a tunneling matrix  $\hat{T} = t\tau_z$ . The magnetic skyrmion lattice leads to non-zero currents in the superconductor. The currents are screened by the superconductor by building up a non-vanishing vector potential  $\mathbf{A}(\mathbf{R}) = (\mathbf{a}(\mathbf{R}), A_z(\mathbf{R}))^\top$  with  $\mathbf{a}(\mathbf{r}) = (a_x(\mathbf{r}), a_y(\mathbf{r}))^\top$ . Since the vector potential can modify  $\Delta(\mathbf{R})$  we include it in the following analysis. The vector potential follows the equation of motion  $\nabla^2 \mathbf{A}(\mathbf{R}) = -\mu \mathbf{J}(\mathbf{R})$  with magnetic permeability  $\mu$ . Since the superconductor is a non-magnetic material, we use  $\mu \approx \mu_0$  with the magnetic permeability  $\mu_0$  of the vacuum. For convenience we set  $\mu_0 = 1$  in the following. The fermionic current  $\mathbf{J}(\mathbf{R})$  is given by the functional derivative  $\mathbf{J}(\mathbf{R}) = -\delta \mathcal{F}_f / \delta \mathbf{A}(\mathbf{R})$ . Here  $\mathcal{F}_f$  is the free energy obtained by integrating out the fermionic degrees of freedom.

The vector potential couples via minimal coupling, i.e., by substituting  $\hat{\mathbf{p}} \rightarrow \hat{\mathbf{p}} + e\tau_z \mathbf{a}(\mathbf{r})$  and  $\hat{\mathbf{P}} \rightarrow \hat{\mathbf{P}} + e\tau_z \mathbf{A}(\mathbf{R})$ . In this work we will consider a perturbative coupling to the vector potential, given as  $\tilde{\mathcal{H}}_A = \mathcal{H}_A + \mathcal{H}_{A^2} + \dots$  and similar for the coupling between magnetic layer and vector potential  $\mathbf{a}$ . In particular, we keep the linear parametric terms  $\mathcal{H}_A$  and  $\mathcal{H}_a$  and the quadratic diamagnetic terms  $\mathcal{H}_{A^2}$  and  $\mathcal{H}_{a^2}$ . By the minimal coupling substitution one obtains the Hamiltonians

$$\mathcal{H}_A = \frac{1}{2} \int d\mathbf{R} C^\dagger(\mathbf{R}) \frac{e}{2m} (\hat{\mathbf{P}} \cdot \mathbf{A} + \mathbf{A} \cdot \hat{\mathbf{P}}) C(\mathbf{R}), \quad (5.7)$$

$$\mathcal{H}_{A^2} = \frac{1}{2} \int d\mathbf{R} C^\dagger(\mathbf{R}) \frac{e^2 \mathbf{A}^2}{2m} \tau_z C(\mathbf{R}), \quad (5.8)$$

for the coupling between vector potential and the electrons of the superconductor. After introducing the full Hamiltonian  $\mathcal{H}_{\text{mag}} + \mathcal{H}_{\text{sc}} + \mathcal{H}_T + \mathcal{H}_A + \mathcal{H}_{A^2} + \mathcal{H}_a + \mathcal{H}_{a^2}$  we proceed to derive the free energy description of the heterostructure.

### 5.2.2 Free energy description of the coupled subsystems

Now we derive the free energy description of the coupled systems within the Matsubara formalism. This approach is sufficient since we are interested in static phenomena. We transfer to the path integral formalism which is useful for the development of a perturbation theory and express the free energy functional in terms of Green's functions. The Matsubara action of the fermionic degrees is given by

$$\mathcal{S}_f = -\bar{\Psi}\hat{\mathcal{G}}_{\text{mag}}^{-1}\Psi - \bar{C}\hat{\mathcal{G}}_{\text{sc}}^{-1}C + \bar{\Psi}\hat{T}C + \bar{C}\hat{T}^\dagger\Psi. \quad (5.9)$$

The Green's function are given here in full matrix form as in Chapter 4. The action does not include the constant quadratic terms  $\Delta^2$  and  $M^2$  produced by the mean-field decoupling, since we can add them when needed. Introducing the shifted Grassmann variable  $C' = C - \hat{\mathcal{G}}_{\text{sc}}\hat{T}^\dagger\Psi$  and  $\bar{C}' = \bar{C} - \bar{\Psi}\hat{T}\hat{\mathcal{G}}_{\text{sc}}$  and  $\hat{\mathcal{G}}_{\text{mag,sc}}^{-1} = \hat{\mathcal{G}}_{\text{mag}}^{-1} - \hat{T}\hat{\mathcal{G}}_{\text{sc}}\hat{T}^\dagger$  yields the simplified action  $\mathcal{S}_f = -\bar{\Psi}\hat{\mathcal{G}}_{\text{mag,sc}}^{-1}\Psi - \bar{C}'\hat{\mathcal{G}}_{\text{sc}}^{-1}C'$ . We proceed with integrating out the fermionic degrees of freedom to obtain the free energy  $\mathcal{F}_f = \mathcal{F}_{\text{sc}} + \mathcal{F}_{\text{mag,sc}}$  with

$$\mathcal{F}_{\text{sc}} = \mathcal{F}_{\Delta^2} - \frac{1}{2\beta} \text{trln}(-\hat{\mathcal{G}}_{\text{sc}}^{-1}) \quad \text{and} \quad \mathcal{F}_{\text{mag,sc}} = \mathcal{F}_{M^2} - \frac{1}{2\beta} \text{trln}(-\hat{\mathcal{G}}_{\text{mag,sc}}^{-1}). \quad (5.10)$$

Note that the factors 1/2 are necessary to avoid double counting. The constants  $\mathcal{F}_{\Delta^2}$  and  $\mathcal{F}_{M^2}$  are the quadratic contributions to the free energy due to the mean-field decoupling. The Green's functions also include the coupling to the vector potential.

In the following we assume that the superconducting gap is only weakly influenced by the magnetic lattice and only near  $z = 0$ , i.e., is given as  $\Delta(\mathbf{R}) \approx \Delta_0 + \delta\Delta(\mathbf{R})$  with  $\Delta_0(z) \approx \Delta_0 = \Delta_0^*$ . As consequence the term  $\delta\Delta(\mathbf{R})$  contains only Fourier contributions related to  $\Delta_{\mathbf{Q}_i}(z)$ . Without these assumptions all superconducting order parameters for all Fourier components would require perturbative treatment. Furthermore we assume  $|\delta\Delta(\mathbf{R})| \ll \Delta_0$  which allows to expand the superconducting Green's function perturbatively. We obtain

$$\begin{aligned} -\hat{\mathcal{G}}_{\text{sc}}^{-1} &= -\hat{\mathcal{G}}_{\text{sc},0}^{-1} + \delta\hat{\Delta} + \hat{\mathcal{H}}_A + \hat{\mathcal{H}}_{A^2} \\ \Rightarrow \hat{\mathcal{G}}_{\text{sc}} &\approx \hat{\mathcal{G}}_{\text{sc},0} + \hat{\mathcal{G}}_{\text{sc},0} \left( \mathbf{1} + \delta\hat{\Delta} + \hat{\mathcal{H}}_A + \hat{\mathcal{H}}_{A^2} \right) \hat{\mathcal{G}}_{\text{sc},0}, \end{aligned} \quad (5.11)$$

$$\begin{aligned} -\hat{\mathcal{G}}_{\text{mag}}^{-1} &= -\hat{\mathcal{G}}_{\text{mag},0}^{-1} + \hat{\mathcal{H}}_a + \hat{\mathcal{H}}_{a^2} \\ \Rightarrow \hat{\mathcal{G}}_{\text{mag}} &\approx \hat{\mathcal{G}}_{\text{mag},0} + \hat{\mathcal{G}}_{\text{mag},0} \left( \mathbf{1} + \hat{\mathcal{H}}_a + \hat{\mathcal{H}}_{a^2} \right) \hat{\mathcal{G}}_{\text{mag},0}. \end{aligned} \quad (5.12)$$

We define  $\hat{\mathcal{G}}_{\text{mag,sc},0}^{-1} = \hat{\mathcal{G}}_{\text{mag},0}^{-1} - \hat{T}\hat{\mathcal{G}}_{\text{sc},0}\hat{T}^\dagger$  and obtain the free energy  $\mathcal{F}_f \approx \mathcal{F}_{\text{sc},0} + \mathcal{F}_{\text{mag,sc},0} + \mathcal{F}_{\text{fb}}$  via the approximated Green's functions. The first two terms of the free

energy are given by

$$\mathcal{F}_{\text{sc},0} = \mathcal{F}_{\Delta_0^2} - \frac{1}{2\beta} \text{trln}(-\widehat{\mathcal{G}}_{\text{sc},0}^{-1}) \quad \text{and} \quad \mathcal{F}_{\text{mag,sc},0} = \mathcal{F}_{M^2} - \frac{1}{2\beta} \text{trln}(-\widehat{\mathcal{G}}_{\text{mag,sc},0}^{-1}). \quad (5.13)$$

Of particular interest is the feedback term which arises from expanding the logarithm up to quadratic order

$$\begin{aligned} \mathcal{F}_{\text{fb}} = & \frac{1}{2\beta} \text{tr} \left\{ \widehat{\mathcal{G}}_{\text{mag,sc},0} \left[ \widehat{\mathcal{H}}_{\mathbf{a}} + \widehat{T} \widehat{\mathcal{G}}_{\text{sc},0} \left( \delta \tilde{\Delta} + \widehat{\mathcal{H}}_{\mathbf{A}} \right) \widehat{\mathcal{G}}_{\text{sc},0} \widehat{T}^\dagger + \widehat{\mathcal{H}}_{\mathbf{a}^2} + \widehat{T} \widehat{\mathcal{G}}_{\text{sc},0} \widehat{\mathcal{H}}_{\mathbf{A}^2} \widehat{\mathcal{G}}_{\text{sc},0} \widehat{T}^\dagger \right] \right\} \\ & + \frac{1}{2\beta} \text{tr} \left\{ \widehat{\mathcal{G}}_{\text{sc},0} \widehat{\mathcal{H}}_{\mathbf{A}^2} \right\} + \mathcal{F}_{\delta \Delta^2} + \frac{1}{4\beta} \text{tr} \left\{ \widehat{\mathcal{G}}_{\text{sc},0} \left( \delta \widehat{\Delta} + \widehat{\mathcal{H}}_{\mathbf{A}} \right) \right\}^2 \\ & + \frac{1}{4\beta} \text{tr} \left\{ \widehat{\mathcal{G}}_{\text{mag,sc},0} \left( \widehat{\mathcal{H}}_{\mathbf{a}} + \widehat{T} \widehat{\mathcal{G}}_{\text{sc},0} (\delta \widehat{\Delta} + \widehat{\mathcal{H}}_{\mathbf{A}}) \widehat{\mathcal{G}}_{\text{sc},0} \widehat{T}^\dagger \right) \right\}^2. \end{aligned} \quad (5.14)$$

The construction of the full free energy  $\mathcal{F}_f$  assumes that  $\Delta_0$  is determined first by minimizing only  $\mathcal{F}_{\text{sc},0}$ . Then the magnetic order  $\mathbf{M}(\mathbf{r})$  will be determined in the presence of the superconducting gap  $\Delta_0$  by minimizing  $\mathcal{F}_{\text{mag,sc},0}$ , which we will describe in the following Section 5.2.3. After that the feedback onto the superconductor  $\delta \Delta(\mathbf{r})$  and  $\mathbf{J}(\mathbf{R})$  will be determined by minimizing the feedback term  $\mathcal{F}_{\text{fb}}$ .

The feedback free energy can be decomposed in terms leading to different effects. Here we highlight the source terms due to the magnetic layer. In particular there are source terms for the vector potential  $\mathbf{A}$  and  $\mathbf{a}$  and staggered superconductivity  $\delta \Delta$ :

- (i) Paramagnetic source term for the vector potential  $\mathbf{a}$  due to the magnetic layer  $\frac{1}{2\beta} \text{tr} \left( \widehat{\mathcal{G}}_{\text{mag,sc},0} \widehat{\mathcal{H}}_{\mathbf{a}} \right)$ . We will analyze this term in Section 5.2.4 to obtain the induced current at the interface.

There are further diamagnetic coupling terms of vector potential and magnetic layer and a subdominant quadratic paramagnetic term. The diamagnetic coupling terms are irrelevant compared to the corresponding terms of the superconductor electrons, since the superconductor has much higher carrier density.

- (ii) Source terms for the vector potential  $\mathbf{A}$  due to tunnel coupling  $\widehat{T}$  of magnetic layer and superconductor  $\frac{1}{2\beta} \text{tr} \left\{ \widehat{\mathcal{G}}_{\text{mag,sc},0} \left( \widehat{T} \widehat{\mathcal{G}}_{\text{sc},0} \widehat{\mathcal{H}}_{\mathbf{A}} \widehat{\mathcal{G}}_{\text{sc},0} \widehat{T}^\dagger \right) \right\}$ .
- (iii) Source terms for staggered superconductivity  $\delta \Delta$  due to tunnel coupling  $\widehat{T}$  of the magnetic layer to the superconductor  $\frac{1}{2\beta} \text{tr} \left\{ \widehat{\mathcal{G}}_{\text{mag,sc},0} \left( \widehat{T} \widehat{\mathcal{G}}_{\text{sc},0} \delta \tilde{\Delta} \widehat{\mathcal{G}}_{\text{sc},0} \widehat{T}^\dagger \right) \right\}$ . This term is responsible for the appearance of staggered superconducting correlations  $\Delta_{Q_i}$ .

Furthermore there are contributions of the superconducting electrons to the effective action of the vector potential  $\mathbf{A}$  and to the effective action of staggered superconductivity  $\delta\Delta$  and the coupling between  $\mathbf{A}$  and  $\delta\Delta$ :

- (iv) Contribution to the vector potential  $\frac{1}{2\beta} \text{tr} \left( \widehat{\mathcal{G}}_{\text{sc},0} \widehat{\mathcal{H}}_{\mathbf{A}^2} \right) + \frac{1}{4\beta} \text{tr} \left( \widehat{\mathcal{G}}_{\text{sc},0} \widehat{\mathcal{H}}_{\mathbf{A}} \right)^2$ .
- (v) Contribution to staggered superconductivity  $\mathcal{F}_{\delta\Delta^2} + \frac{1}{4\beta} \text{tr} \left( \widehat{\mathcal{G}}_{\text{sc},0} \delta\widehat{\Delta} \right)^2$ .
- (vi) Contribution to the coupling of vector potential and staggered superconductivity  $\frac{1}{2\beta} \text{tr} \left( \widehat{\mathcal{G}}_{\text{sc},0} \delta\widehat{\Delta} \widehat{\mathcal{G}}_{\text{sc},0} \widehat{\mathcal{H}}_{\mathbf{A}} + \widehat{\mathcal{G}}_{\text{sc},0} \widehat{\mathcal{H}}_{\mathbf{A}} \widehat{\mathcal{G}}_{\text{sc},0} \delta\widehat{\Delta} \right)$ .

There are further quadratic terms which are subdominant to the linear terms and will not change the qualitative picture given by the aforementioned terms. In the following we will focus on the magnetic instability in the presence of the superconducting layer and the induced currents at the interface due to the texture of the magnetic layer.

### 5.2.3 Superconducting proximity effects on the magnetic instability

Now we determine the magnetic order from the term  $\mathcal{F}_{\text{mag,sc},0}$ . In the plane wave basis  $|\mathbf{k}\rangle$  for  $\mathbf{k} = (k_x, k_y)$  and  $\mathbf{K} = (\mathbf{k}, k_z)$  the Green's function  $\widehat{\mathcal{G}}_{\text{mag,sc},0}$  is given by

$$\widehat{\mathcal{G}}_{\text{mag,sc},0}^{-1}(E, \mathbf{k} + \mathbf{q}, \mathbf{k}) = \left\{ E - \tau_z [\delta_{\text{mag}}(\mathbf{k}) + \mathbf{g}(\mathbf{k}) \cdot \tilde{\boldsymbol{\sigma}} - \mu] - t^2 \tau_z \widehat{\mathcal{G}}_{\text{sc},0}(E, \mathbf{k}, z=0) \tau_z \right\} \delta(\mathbf{q}) - \mathbf{M}_{\mathbf{q}} \cdot \tilde{\boldsymbol{\sigma}} \quad (5.15)$$

with  $\mathbf{M}(\mathbf{r}) = \int \frac{d\mathbf{q}}{(2\pi)^2} e^{i\mathbf{q}\cdot\mathbf{r}} \mathbf{M}_{\mathbf{q}}$ . The Green's function of the superconductor for energies below the gap, i.e.,  $E < \Delta_0$  is given by

$$\begin{aligned} \widehat{\mathcal{G}}_{\text{sc},0}(E, \mathbf{k}, z=0) &= \int \frac{dk_z}{2\pi} \widehat{\mathcal{G}}_{\text{sc},0}(E, \mathbf{K}) = \int \frac{dk_z}{2\pi} \frac{E + \epsilon(\mathbf{K})\tau_z - \Delta_0\tau_y\sigma_y}{E^2 - \epsilon^2(\mathbf{K}) - \Delta_0^2} \\ &\approx \nu_F \int_{-\infty}^{\infty} \frac{d\epsilon}{2\pi} \frac{E + \epsilon\tau_z - \Delta_0\tau_y\sigma_y}{E^2 - \epsilon^2 - \Delta_0^2} = -\frac{\nu_F}{2} \frac{E + \Delta_0\tau_y\sigma_y}{\sqrt{\Delta_0^2 - E^2}} \end{aligned} \quad (5.16)$$

with the density of states at the Fermi level  $\nu_F$ . If we consider energies  $E \ll \Delta_0$  far below the superconducting gap we can introduce an effective gap  $\Delta = \nu_F t^2 / 2$ , which is induced in the magnetic lattice. With this effective gap  $\Delta$  the Green's function becomes

$$\widehat{\mathcal{G}}_{\text{mag,sc},0}^{-1}(E, \mathbf{k} + \mathbf{q}, \mathbf{k}) = \{ E - \tau_z [\delta_{\text{mag}}(\mathbf{k}) + \mathbf{g}(\mathbf{k}) \cdot \tilde{\boldsymbol{\sigma}} - \mu] - \Delta\tau_y\sigma_y \} \delta(\mathbf{q}) - \mathbf{M}_{\mathbf{q}} \cdot \tilde{\boldsymbol{\sigma}}.$$

In the next step it is necessary to determine the magnetic susceptibility. Furthermore the magnetic gap can be determined self-consistently in the presence of the induced gap  $\Delta$ . We will perform this analysis in the case of  $\text{Bi}_2\text{Te}_3$  in Section 5.3.3.

#### 5.2.4 Induced current in the magnetic layer

In this section we derive the induced current at the interface between magnetic layer and superconductor. We use  $\langle \mathbf{k} | \hat{\mathcal{H}}_a | \mathbf{k} + \mathbf{q} \rangle = -\mathbf{j}_{\mathbf{k}, \mathbf{k} + \mathbf{q}} \cdot \mathbf{a}_{-\mathbf{q}}$  with the single-particle current

$$\mathbf{q} \cdot \mathbf{j}_{\mathbf{k}, \mathbf{k} + \mathbf{q}} = -\frac{e}{\hbar} \left( \hat{\mathcal{H}}_{\text{mag}}^0(\mathbf{k} + \mathbf{q}) - \hat{\mathcal{H}}_{\text{mag}}^0(\mathbf{k}) \right). \quad (5.17)$$

The current is diagonal in particle-hole space which can be seen from the form of the magnetic Hamiltonian  $\hat{\mathcal{H}}_{\text{mag}}^0$ . However the current is non-diagonal in spin-space. This observation implies that the current is driven purely by magnetoelectric effects. It is useful to decompose the current into charge and spin parts  $\mathbf{j}_{\mathbf{k}, \mathbf{k} + \mathbf{q}} = \mathbf{j}_{\mathbf{k}, \mathbf{k} + \mathbf{q}}^c + \mathbf{j}_{\mathbf{k}, \mathbf{k} + \mathbf{q}}^s \cdot \tilde{\boldsymbol{\sigma}}$  with

$$\mathbf{q} \cdot \mathbf{j}_{\mathbf{k}, \mathbf{k} + \mathbf{q}}^c = -\frac{e}{\hbar} [\delta_{\text{mag}}(\mathbf{k} + \mathbf{q}) - \delta_{\text{mag}}(\mathbf{k})] \tau_z, \quad (5.18)$$

$$\mathbf{q} \cdot \mathbf{j}_{\mathbf{k}, \mathbf{k} + \mathbf{q}}^s = -\frac{e}{\hbar} [\mathbf{g}(\mathbf{k} + \mathbf{q}) - \mathbf{g}(\mathbf{k})] \cdot \tilde{\boldsymbol{\sigma}}. \quad (5.19)$$

As an example, we consider a Rashba Hamiltonian  $\mathbf{g}(\mathbf{k}) = \hbar\alpha\hat{\mathbf{z}} \times \mathbf{k}$  and  $\delta_{\text{mag}}(\mathbf{k}) = 0$ . We obtain for the current  $\mathbf{j}_{\mathbf{k}, \mathbf{k} + \mathbf{q}}^s = e\alpha\mathbf{q} \cdot (\hat{\mathbf{z}} \times \tilde{\boldsymbol{\sigma}})$ . The induced current is then determined by the paramagnetic coupling of the magnetic layer to the vector potential

$$\text{tr} \left( \hat{\mathcal{G}}_{\text{mag}, \text{sc}, 0} \hat{\mathcal{H}}_a \right) = - \int \frac{d\mathbf{k}}{(2\pi)^2} \frac{d\mathbf{q}}{(2\pi)^2} \mathbf{a}_{-\mathbf{q}} \cdot \sum_{ik_n} \text{tr} \left( \hat{\mathcal{G}}_{\text{mag}, \text{sc}, 0}(ik_n, \mathbf{k} + \mathbf{q}, \mathbf{k}) \mathbf{j}_{\mathbf{k}, \mathbf{k} + \mathbf{q}} \right). \quad (5.20)$$

The relevant contributions are given by the low energy behavior of the system near the Fermi points with good nesting, which all have the same  $\mathbf{M}_q$ . We write  $N_F$  for the number of relevant Fermi points. The free energy term reduces to

$$\frac{1}{2\beta} \text{tr} \left( \hat{\mathcal{G}}_{\text{mag}, \text{sc}, 0} \hat{\mathcal{H}}_a \right) = - \int \frac{d\mathbf{q}}{(2\pi)^2} e\mathbf{a}_{-\mathbf{q}} \cdot \mathbf{j}_q, \quad (5.21)$$

with the induced staggered current  $\mathbf{j}_q = (2e\alpha N_F)/U \hat{\mathbf{z}} \times \mathbf{M}_q$ . The staggered currents are then fully determined by the magnetic order. The proportionality  $\mathbf{j}_q \propto \hat{\mathbf{z}} \times \mathbf{M}_q$  for the supercurrent can be obtained by symmetry considerations, as we will describe in Section 5.3.4.

### 5.3 Analysis of a Bi<sub>2</sub>Te<sub>3</sub>-superconductor heterostructure

After the general discussion of a heterostructure consisting of a magnetic layer coupled via a tunnel coupling to a conventional superconductor, we consider now the more specific system based on the topological insulator Bi<sub>2</sub>Te<sub>3</sub>, which was discussed in Chapter 4. As shown in Section 5.2.3 we can assume that the superconductor proximity induces an effective superconducting gap  $\Delta$  on the topological insulator. Since the superconductor competes with the magnetic instability we expect that a higher interaction strength is necessary to drive the system to the magnetic phase.

Here we neglect the effects onto the superconductor and assume the superconducting gap to stay constant and unchanged by the magnetic texture. We analyze the magnetic susceptibility in the presence of such an effective superconducting gap and compute the gap in a self-consistent manner. Later we will consider superconducting correlations induced in the superconductor, which follow the structure of the magnetic texture. This analysis was published in Ref. [1].

#### 5.3.1 Magnetic susceptibility in the presence of a superconducting gap

We showed that the superconductor induces a superconducting gap  $\Delta$  onto the electrons of the topological insulator in Section 5.2.3. By symmetry the induced superconducting gap can couple to the magnetic order parameters at fourth order in the Landau expansion

$$\mathcal{F}_{\text{mag,sc}} = c|\Delta|^2 \sum_{i=1}^3 |M_i|^2. \quad (5.22)$$

The sign of  $c$  must be positive since the magnetic phase competes with the singlet superconducting gap, since the magnetic order parameters are  $\mathcal{T}$  symmetry violating in contrast to the superconducting order parameter. If we assume the free energy term Eq. (5.22), the coefficient  $\alpha$  of the bare free energy is modified as

$$\alpha(\Delta) = \frac{2}{U} - \chi_{Q_1}^1 + c|\Delta|^2. \quad (5.23)$$

This modification acts like a renormalization of the interaction  $U$ . We see that the effective interaction  $\tilde{U}(U) = \frac{U}{1+Uc|\Delta|^2/2} < U$  is reduced compared to the case with  $\Delta = 0$ . Therefore if a superconducting gap  $\Delta$  is present a stronger interaction  $U$  is necessary to allow the magnetic instability to develop.

Here we do not consider other higher order terms which could change either the superconductor or the structure of the magnetic texture. In particular, the conclusions concerning the structure of the magnetic texture and the dominance of the skyrmionic phase with three  $\mathbf{Q}$  wavevectors are unaffected. The assumption that the symmetric structure stays unchanged is justified if one considers that the above additional term  $\mathcal{F}_{\text{mag,sc}}$  to the free energy is sufficiently weak and does not break any symmetries.

The strength of the induced gap can be controlled experimentally in principle by the way the interface is grown and the superconducting material. In the following we perform a similar analysis of the susceptibility as before including the gap  $\Delta$  in the Bogoliubov-de Gennes Hamiltonian

$$\hat{\mathcal{H}}_{0,\text{sc}}(\mathbf{k}) = \mathbf{g}(\mathbf{k}) \cdot \tau_z \tilde{\boldsymbol{\sigma}} - \mu \tau_z - \Delta \tau_y \sigma_y. \quad (5.24)$$

The  $\boldsymbol{\tau}$  Pauli matrices act in particle-hole space. The Hamiltonian has a U(1) gauge symmetry corresponding to rotations around the  $\tau_z$ -axis. Here we chose the gauge such that  $\Delta$  is real and positive.

Additional to the bare Hamiltonian, the mean-field decoupled magnetic term

$$\mathcal{H}_{\text{mag}} = \int \frac{d\mathbf{q}}{(2\pi)^2} \left[ \frac{|\mathbf{M}_{\mathbf{q}}|^2}{U} + \frac{1}{2} \int \frac{d\mathbf{k}}{(2\pi)^2} \boldsymbol{\Psi}_{\mathbf{k}+\mathbf{q}/2}^\dagger \mathbf{M}_{\mathbf{q}} \cdot \tilde{\boldsymbol{\sigma}} \boldsymbol{\Psi}_{\mathbf{k}-\mathbf{q}/2} \right] \quad (5.25)$$

must be included. The Green's function of the modified Hamiltonian is given by

$$\begin{aligned} \hat{G}_{0,\text{sc}}(k) &= \frac{(ik_n)^2 - (|\mathbf{g}(\mathbf{k})|^2 + \mu^2 + \Delta^2) - 2\mu\mathbf{g}(\mathbf{k}) \cdot \tilde{\boldsymbol{\sigma}}}{(k_n^2 + \tilde{\epsilon}_{\mathbf{k},+}^2)(k_n^2 + \tilde{\epsilon}_{\mathbf{k},-}^2)} [ik_n + \hat{\mathcal{H}}_{0,\text{sc}}(\mathbf{k})] \\ &= \sum_{s=\pm} \frac{\tilde{P}_s(\mathbf{k}) [ik_n + \hat{\mathcal{H}}_{0,\text{sc}}(\mathbf{k})]}{(ik_n - \tilde{\epsilon}_{\mathbf{k},s})(ik_n + \tilde{\epsilon}_{\mathbf{k},s})}. \end{aligned} \quad (5.26)$$

The fermionic Matsubara frequencies are denoted by  $k_n$  and the eigenenergies are given by  $\tilde{\epsilon}_{\mathbf{k},\pm} = \sqrt{\epsilon_{\mathbf{k},\pm}^2 + \Delta^2}$ . As before we write the Green's function in terms of projectors  $\tilde{P}_\pm(\mathbf{k}) = [\mathbf{1} \pm \hat{\mathbf{g}}(\mathbf{k}) \cdot \tilde{\boldsymbol{\sigma}}] / 2$  and obtain

$$\hat{G}_{0,\text{sc}}(k) = \sum_{s=\pm} \frac{\tilde{P}_s(\mathbf{k}) [ik_n + \hat{\mathcal{H}}_{0,\text{sc}}(\mathbf{k})]}{(ik_n - \tilde{\epsilon}_{\mathbf{k},s})(ik_n + \tilde{\epsilon}_{\mathbf{k},s})}. \quad (5.27)$$

In the analysis in Chapter 4, the significant contributions to the susceptibility were due to intraband processes in the upper helicity band. For simplicity we only take into account this band to compute the modified spin-susceptibility in the presence of

$\Delta$ . The helicity basis of the Hamiltonian is spanned by  $|e, \mathbf{k}, s\rangle$  and  $|h, \mathbf{k}, s\rangle$  with the helicities  $s = \pm 1$  and  $e$  ( $h$ ) corresponding to electron (hole) space:

$$|e, \mathbf{k}, \pm\rangle = \begin{pmatrix} 1 \\ 0 \end{pmatrix} \otimes |\mathbf{k}, \pm\rangle \quad \text{and} \quad |h, \mathbf{k}, \pm\rangle = \Xi |e, \mathbf{k}, \pm\rangle = \begin{pmatrix} 0 \\ 1 \end{pmatrix} \otimes |-\mathbf{k}, \pm\rangle^*. \quad (5.28)$$

The charge conjugate partners of  $|e, \mathbf{k}, \pm\rangle$  are obtained by acting with the charge conjugation operator  $\Xi = \tau_x \mathcal{K}$ . For instance one obtains

$$|h, \mathbf{k}, +\rangle = \begin{pmatrix} 0 \\ 1 \end{pmatrix} \otimes \begin{pmatrix} -e^{+\frac{i\varphi_{\mathbf{k}}}{2}} \sin \frac{\vartheta_{\mathbf{k}}}{2} \\ e^{-\frac{i\varphi_{\mathbf{k}}}{2}} \cos \frac{\vartheta_{\mathbf{k}}}{2} \end{pmatrix} \quad (5.29)$$

for the upper helicity band using the relations  $\varphi_{-\mathbf{k}} = \varphi_{\mathbf{k}}$  and  $\vartheta_{-\mathbf{k}} = \vartheta_{\mathbf{k}} + \pi$ .

The projected Hamiltonian acting in the upper helicity space takes the form  $\hat{\mathcal{H}}_{0,\text{sc}}^+(\mathbf{k}) = \epsilon_{\mathbf{k},+} \tau_z + \Delta \tau_x$ . With the given choice of the helicity eigenstates the projected superconducting gap stays  $\mathbf{k}$ -independent. A different gauge could lead to an odd  $\mathbf{k}$ -dependence as discussed in Ref. [65].

Using the corresponding Green's function

$$\hat{G}_{0,\text{sc}}^+(k) = \frac{ik_n + \hat{\mathcal{H}}_{0,\text{sc}}^+(\mathbf{k})}{(ik_n - \tilde{\epsilon}_{\mathbf{k},+})(ik_n + \tilde{\epsilon}_{\mathbf{k},+})}, \quad (5.30)$$

we obtain the modified spin susceptibility

$$\begin{aligned} \tilde{\chi}_{\mathbf{q},++}^{ab} = & -\frac{1}{2} \sum_{\lambda, \lambda' = \pm} \int \frac{d\mathbf{k}}{(2\pi)^2} \frac{n_F(\lambda \tilde{\epsilon}_{\mathbf{k},+}) - n_F(\lambda' \tilde{\epsilon}_{\mathbf{k}+\mathbf{q},+})}{\lambda \tilde{\epsilon}_{\mathbf{k},+} - \lambda' \tilde{\epsilon}_{\mathbf{k}+\mathbf{q},+}} \\ & \times \frac{\tilde{\epsilon}_{\mathbf{k},+} \tilde{\epsilon}_{\mathbf{k}+\mathbf{q},+} + \lambda \lambda' (\epsilon_{\mathbf{k},+} \epsilon_{\mathbf{k}+\mathbf{q},+} + \Delta^2)}{2\tilde{\epsilon}_{\mathbf{k},+} \tilde{\epsilon}_{\mathbf{k}+\mathbf{q},+}} \langle \mathbf{k}, + | \sigma^a | \mathbf{k} + \mathbf{q}, + \rangle \langle \mathbf{k} + \mathbf{q}, + | \sigma^b | \mathbf{k}, + \rangle. \end{aligned} \quad (5.31)$$

We note that the formula is mainly changed by the modified eigenenergies  $\tilde{\epsilon}_{\mathbf{k},\pm} = \sqrt{\epsilon_{\mathbf{k},\pm}^2 + \Delta^2}$  and a form factor. In Fig. 5.3, we plot the spin susceptibility for  $T = 0$  as function of chemical potential  $\mu$  and  $\Delta$ . The plot shows the expected reduction of the susceptibility due to  $\Delta$ . For example, for  $\Delta = 1.93 \times 10^{-3}$  corresponding to 0.5 meV for  $\text{Bi}_2\text{Te}_3$ , we find a reduction of the spin susceptibility by approximately 10%.

### 5.3.2 Low energy model

In this section we derive the low energy model describing the surface electrons in the presence of the magnetic order parameters and proximity induced s-wave supercon-

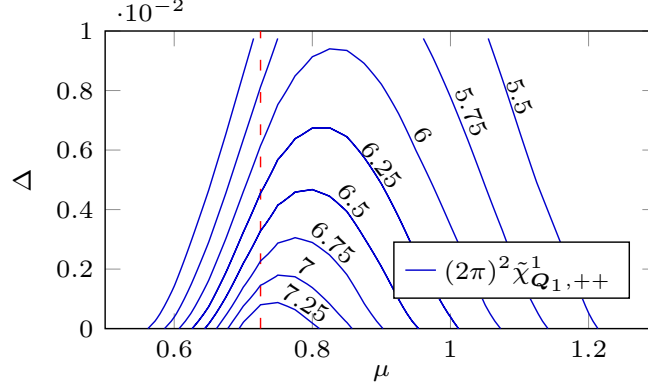


Figure 5.3: Contour plot of the largest susceptibility eigenvalue versus the proximity induced superconducting gap  $\Delta$  and chemical potential  $\mu$ . We only show the contribution of the upper helicity band. The dashed red line marks the chemical potential  $\mu = \mu_{\text{hex}}$ , for which the Fermi surface is approximately hexagonal.

ductivity. This model corresponds to a topological superconductor, which can host Majorana bound states if the system is in a topologically non-trivial phase.

The starting point is the Hamiltonian in the upper helicity basis with the magnetic term of Eq. (5.25). Again we focus on the most relevant nesting wavevectors  $\pm \mathbf{Q}_i$ , giving raise to the corresponding order parameters  $M_i$  for  $i = 1, 2, 3$ . We obtain the Bogoliubov-de Gennes Hamiltonian  $\hat{\mathcal{H}}_{\text{mag,sc}}(\mathbf{k})$  with three decoupled blocks  $\hat{h}_i(\mathbf{k})$  corresponding to the wavevectors  $\mathbf{Q}_i$ . Each of the Hamiltonian blocks acts in a basis with the momentum index  $i$ . The blocks have the form

$$\hat{h}_i(\mathbf{k}) = \delta_{i,\mathbf{k},+\tau_z} + \delta_{i,\mathbf{k},-\tau_z}\rho_z + \Delta\tau_x + M f_i^R(\mathbf{k})\rho_x - M f_i^I(\mathbf{k})\rho_y, \quad (5.32)$$

$$\delta_{i,\mathbf{k},\pm} = \frac{\epsilon_{\mathbf{k}+\mathbf{Q}_i/2,+} \pm \epsilon_{\mathbf{k}-\mathbf{Q}_i/2,+}}{2}, \quad (5.33)$$

where  $f_i(\mathbf{k}) \equiv \widehat{\mathbf{M}}_i \cdot \boldsymbol{\sigma}_i^+(\mathbf{k})$ . The projected matrix element  $\boldsymbol{\sigma}_i^+(\mathbf{k})$  was introduced before in Section 4.3.3. The Hamiltonian blocks act in the enlarged spinor space to account for the two vectors  $\mathbf{k} \pm \mathbf{Q}_i/2$ . The  $\boldsymbol{\rho}$  Pauli matrices act in this new  $2 \times 2$  subspace. The full spinor for each of the block is defined in  $\boldsymbol{\tau} \otimes \boldsymbol{\rho}$  space as

$$\Psi_{i,\mathbf{k}}^\dagger = (\psi_{\mathbf{k}+\mathbf{Q}_i/2,+}^\dagger, \psi_{\mathbf{k}-\mathbf{Q}_i/2,+}^\dagger, \psi_{-\mathbf{k}-\mathbf{Q}_i/2,+}, \psi_{-\mathbf{k}+\mathbf{Q}_i/2,+}). \quad (5.34)$$

The eigenenergies are given by  $\pm E_{i,\mathbf{k},s}$  with  $s = \pm 1$ ,

$$E_{i,\mathbf{k},s} = \sqrt{\delta_{i,\mathbf{k},+}^2 + \delta_{i,\mathbf{k},-}^2 + \Delta^2 + M^2|f_i(\mathbf{k})|^2 + s2T_i(\mathbf{k})}, \quad (5.35)$$

$$T_i(\mathbf{k}) = \sqrt{\delta_{i,\mathbf{k},+}^2 \delta_{i,\mathbf{k},-}^2 + M^2|f_i(\mathbf{k})|^2 (\delta_{i,\mathbf{k},+}^2 + \Delta^2)}. \quad (5.36)$$

When a gap in the dispersion closes for  $\mathbf{k} = \mathbf{0}$ , the system can become topologically non-trivial. To investigate that, we proceed with calculating the magnetic gap in the presence of superconductivity.

### 5.3.3 Self-consistent calculation of the magnetic gap

The dependence of the magnetic gap  $M$  on the superconducting gap  $\Delta$  is relevant to determine if the system can transit to the topologically non-trivial phase. Therefore we determine the dependence self-consistently at zero temperature, which is most relevant for Majorana physics. The free energy of the Hamiltonian blocks  $\hat{h}_i(\mathbf{k})$  is given by

$$\mathcal{F}_i = \frac{2M^2}{U} - \frac{1}{2} \sum_{s=\pm} \int \frac{d\mathbf{k}}{(2\pi)^2} E_{i,\mathbf{k},s}. \quad (5.37)$$

Minimization yields the self-consistency relation

$$M = U \sum_{s=\pm} \int \frac{d\mathbf{k}}{(2\pi)^2} \frac{M|f_i(\mathbf{k})|^2}{8E_{i,\mathbf{k},s}} \left[ 1 + \frac{\Delta^2 + \delta_{i,\mathbf{k},+}^2}{sT_i(\mathbf{k})} \right] \quad (5.38)$$

for the magnetic order parameter  $M$ . We solve this relation numerically in an iterative fashion for various values of the interaction  $U$  and the induced gap  $\Delta$ . The induced gap  $\Delta$  is assumed to be constant and just imposed on the system.

The resulting magnetic gap  $M(U, \Delta)$  is shown in Fig. 5.4. In the plot the magnetic gap does not appear for zero interaction strength, since the susceptibility does not diverge due to imperfect nesting. Our results for  $M$  are mostly independent of the chemical potential  $\mu$  if one stays within 5% detuning from the hexagonal scenario with  $\mu = \mu_{\text{hex}}$ . For larger values, the FS strongly differs from the hexagonal surface, and additional nesting vectors become important (see Appendix A.3).

The magnetic order parameter  $M$  shows a first order transition for increasing  $\Delta$ . A first order transition is expected due to the different behavior of  $\Delta$  and  $M$  under time reversal symmetry  $\mathcal{T}$ . In our analysis we did not analyze the values of the free energy at the transition point, but we think the overall qualitative picture is realistic. Similar phase transitions have been found before, e.g., in a system with spatially modulated superconducting pairing terms [137].

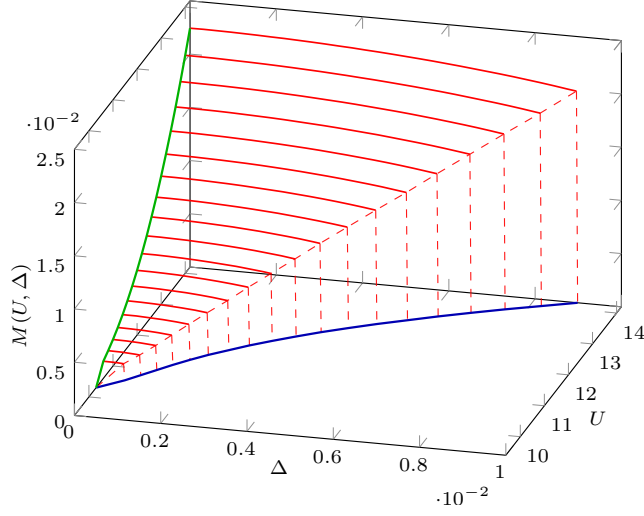


Figure 5.4: Magnetic gap  $M(U, \Delta)$  calculated self-consistently depending on interaction strength  $U$  and superconducting gap  $\Delta$ . We find a first-order transition for increasing  $\Delta$ . For  $\text{Bi}_2\text{Te}_3$  the value  $U = 13$  corresponds to  $U = 3.38 \text{ eV}$ ,  $\Delta = 0.0025$  to  $\Delta = 0.65 \text{ meV}$ , and  $M \approx 0.01$  to  $M = 2.6 \text{ meV}$ . The blue line marks the onset of the instability at  $U_{\text{crit}} = 2/\chi_{\mathbf{Q}_1, ++}^1$ . The green curve shows the increase of the magnetization  $M(U, \Delta = 0)$ . In the numerical calculations we only took the relevant upper helicity band into account.

For non-zero superconducting gap  $\Delta$  below a critical value, the spectrum is fully gapped. We display the reconstructed Fermi surface and band structure in Fig. 5.5 in the presence of only a non-vanishing magnetic gap  $M$ . Ungapped parts remain due to imperfect nesting and appear at the points of the Fermi surface which were not connected by the dominant nesting vectors and do not participate in the scattering processes leading the stabilization of the magnetic order. If the chemical potential  $\mu$  is tuned away from the optimal hexagonal scenario with  $\mu = \mu_{\text{hex}}$  the ungapped parts grow, since less and less points are well nested. We note that the nesting wavevector  $\mathbf{Q}_1(k_0)$  depends on the Fermi wavevector  $k_0$  and as such depends on  $\mu$ . The features of the partially gapped band structure in the absence of superconductivity could be observable in angular resolved photoemission spectroscopy.

### 5.3.4 Supercurrent signature of skyrmions

It is possible to couple supercurrent operators to the magnetic order parameters. This way it is possible to stabilize the magnetic phase. Vice versa the magnetic texture will induce multipolar patterns of supercurrents. These supercurrent patterns could serve as signatures of the magnetic phases.

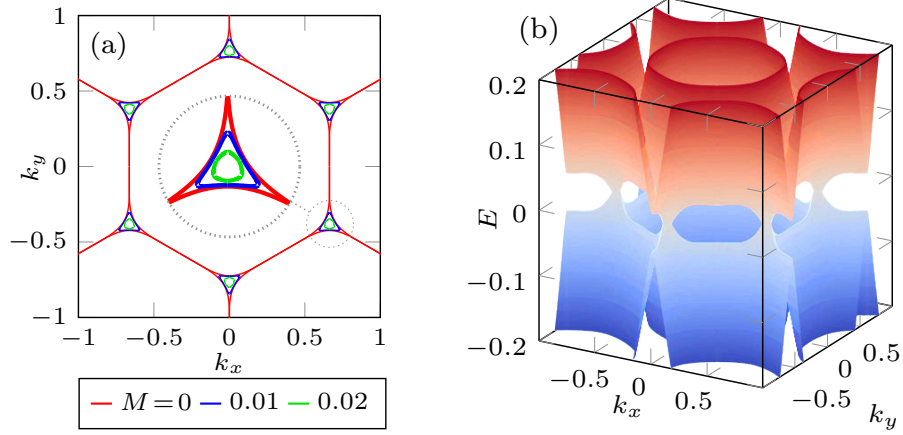


Figure 5.5: (a) Extended scheme of the Fermi surface for  $\mu = \mu_{\text{hex}}$  and  $\Delta = 0$  for different values of the magnetic gap  $M$ . (b) Partly gapped band structure for  $\Delta = 0$  and  $M = 0.02$ .

In this section we describe how the spatially dependent magnetic texture  $\mathbf{M}(\mathbf{r})$  induces a supercurrent  $\mathbf{J}(\mathbf{r})$  that can serve as signature of the magnetic order. The lowest order term which provides information about the skyrmion charge has the form

$$\mathcal{J}(\mathbf{r}) \equiv J_x(\mathbf{r})[J_x^2(\mathbf{r}) - 3J_y^2(\mathbf{r})]. \quad (5.39)$$

It corresponds to an octupolar supercurrent distribution. At lowest order in the magnetization one obtains  $\mathbf{J}(\mathbf{r}) \propto \hat{\mathbf{z}} \times \mathbf{M}(\mathbf{r})$ , which yields the supercurrent distribution

$$\mathcal{J}(\mathbf{r}) \propto M_y(\mathbf{r}) [M_y^2(\mathbf{r}) - 3M_x^2(\mathbf{r})]. \quad (5.40)$$

Interestingly, there is a direct connection between  $\mathcal{J}(\mathbf{r})$  and the skyrmion charge  $\mathcal{C}$ . The integral of the supercurrent distribution  $\mathcal{J}(\mathbf{r})$  over the unit cell  $\mathcal{J}_0 \equiv \int_{\text{UC}} d\mathbf{r} \mathcal{J}(\mathbf{r})$  yields non-zero only for the topologically non-trivial skyrmion phases. In particular it holds  $\mathcal{C} = \text{sign } \mathcal{J}_0$ . We plot the distribution  $\mathcal{J}(\mathbf{r})$  in Fig. 5.6, where the overall color illustrates that  $\mathcal{J}_0$  depends indeed on the charge of the skyrmions. This illustration does not take screening effects since the superconductor in proximity to the topological insulator is not treated in a self-consistent manner. Even if the distribution may deviate due to screening effects, the value  $\mathcal{J}_0$  is a topological invariant and will not change as long as the magnetic ground state is not modified significantly.

There exist also inverse effects. In the presence of an in-plane supercurrent, an effective in-plane Zeeman field  $\hat{\mathbf{z}} \times \mathbf{J}$  [34] is induced. Similarly the aforementioned octupolar supercurrent moment  $J_x(J_x^2 - 3J_y^2)$  produces a  $B_z$  component. These fields

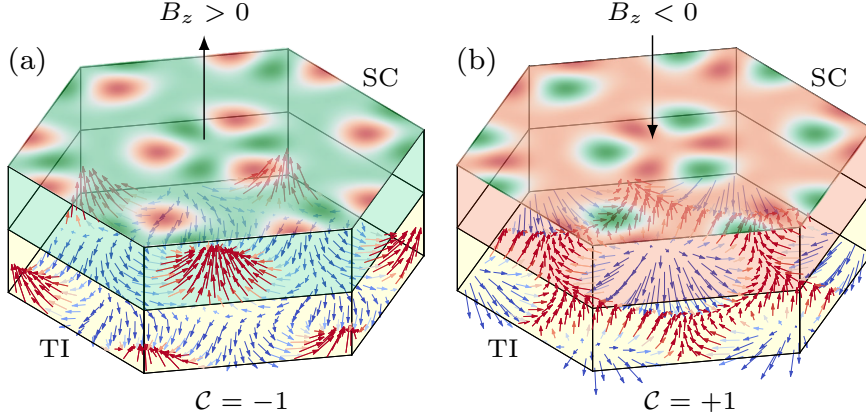


Figure 5.6: Supercurrent distribution of  $\mathcal{J}(\mathbf{r})$  induced by the magnetic skyrmion texture. The skyrmion charge  $C = -1$  ( $+1$ ) is selected by a weak perpendicular magnetic field  $B_z > 0$  ( $< 0$ ). The quantity  $\mathcal{J}_0 = \int_{\text{UC}} d\mathbf{r} \mathcal{J}(\mathbf{r})$  is proportional to the skyrmion charge  $C$  and acts as a signature of the magnetic state. Due to screening effects the pattern observed in experiments could deviate from the plotted distribution. Despite that, the topological invariant  $\mathcal{J}_0$  will not change under smooth modifications of the distribution.

follow from Eq. (4.2) when the replacement  $\mathbf{k} \mapsto \mathbf{k} + \mathbf{J}\tau_z/2$  is performed, one obtains

$$\mathbf{B}_{\text{eff}}(\mathbf{k}) = \frac{J_x}{2} \hat{\mathbf{y}} - \frac{J_y}{2} \hat{\mathbf{x}} + \left[ \frac{J_x}{8} (J_x^2 - 3J_y^2) + \frac{J_x}{2} (k_x^2 - 3k_y^2) + k_x (k_x J_x - 3k_y J_y) \right] \hat{\mathbf{z}}. \quad (5.41)$$

Since this effective magnetic field (induced by supercurrents) couples to the magnetic order parameters, it would be indirectly possible to control the magnetic phase as discussed in Section 4.4.

## 5.4 Topological superconductivity and Majorana flat bands

In this section we focus on the topological superconductivity present in a heterostructure consisting of a magnetic layer and a conventional superconductor. Gap closings in the bulk bandstructure at  $\mathbf{k} = \mathbf{0}$  are related to the occurrence of Majorana modes [65, 126, 135, 136].

In the system based on the topological insulator  $\text{Bi}_2\text{Te}_3$  we find a gap closing for  $\Delta = M|f_i(\mathbf{0})|$  since  $\delta_{i,0,\pm} = 0$ . For  $\Delta < M|f_i(\mathbf{0})|$  the block of the system is in the topologically non-trivial phase and the block can support a single zero-energy Majorana mode. Plugging in the approximate  $\widehat{\mathbf{M}}_i$  given in Eq. (4.28) yields  $|f_i(\mathbf{0})| \approx \sqrt{2}$ , i.e., the gap closes for  $\Delta \approx \sqrt{2}M$ . Given the numeric results shown in Fig. 5.4, we can

answer the question whether the system can become topologically non-trivial, i.e., whether the inequality  $|\Delta| < \sqrt{2}M(U, \Delta)$  can be satisfied. If the system is tuned to the point where  $\mu = \mu_{\text{hex}}$  with an induced superconducting gap  $\Delta = 2.5 \times 10^{-3}$  corresponding to 0.65 meV for  $\text{Bi}_2\text{Te}_3$  one finds that the interaction must be  $U \gtrsim 13$ . This value corresponds to  $U \gtrsim 3.38$  eV for  $\text{Bi}_2\text{Te}_3$  and a magnetic gap of  $M \approx 0.01$  (2.6 meV). Therefore the heterostructure forms an engineered  $C_3$ -symmetric topological superconductor [34, 138–142]. The remaining question is whether the interaction in  $\text{Bi}_2\text{Te}_3$  or similar materials is sufficiently strong to satisfy the above conditions.

At domain walls Majorana modes will appear. In particular chiral Majorana modes are expected for the given topological superconductor. Furthermore Majorana flat bands will occur due to the structure of the Hamiltonian at domain walls, where  $\sqrt{2}M - \Delta$  changes sign. Here we focus on the flat bands since they are a special feature of this system.

#### 5.4.1 Majorana flat bands

Here we consider in particular the Majorana flat bands, which occur at a domain wall of a topological superconductor with a local anisotropy. A prototype for a model yielding flat bands is an anisotropic p-wave superconductor, which we described in Section 2.3.2. For the discussion we return to the more general setting. The relevant Hamiltonian has the form

$$\mathcal{H} = \frac{1}{2} \int d\mathbf{r} \Psi^\dagger(\mathbf{r}) \left[ \mathbf{g}(\hat{\mathbf{k}}) \cdot \tau_z \tilde{\boldsymbol{\sigma}} - \mu \tau_z + \mathbf{M}(\mathbf{r}) \cdot \tilde{\boldsymbol{\sigma}} - \Delta \tau_y \sigma_y \right] \Psi(\mathbf{r}). \quad (5.42)$$

Since we are interested in the low energy solutions to the system we expand the field operators in the relevant Fourier components around the nested points

$$\Psi(\mathbf{r}) = \sum_{i=1,2,3} \left[ e^{i\mathbf{Q}_i \cdot \mathbf{r}/2} \Psi_{+\mathbf{Q}_i/2}(\mathbf{r}) + e^{-i\mathbf{Q}_i \cdot \mathbf{r}/2} \Psi_{-\mathbf{Q}_i/2}(\mathbf{r}) \right]. \quad (5.43)$$

The field operators  $\Psi_{+\mathbf{Q}_i/2}(\mathbf{r})$  vary slowly in space, which means that the corresponding wavevector is small  $|\mathbf{k}| \ll |\mathbf{Q}_i|$ .

Furthermore the low energy physics is determined by the upper helicity band projection of the Hamiltonian. The operators of the spin bands are determined by the upper helicity band

$$\psi_{\mathbf{k} \pm \mathbf{Q}_i \uparrow} \approx A_{k_w \hat{w} \pm \mathbf{Q}_i/2} \psi_{\mathbf{k} \pm \mathbf{Q}_i, +} \quad \text{and} \quad \psi_{\mathbf{k} \pm \mathbf{Q}_i \downarrow} \approx B_{k_w \hat{w} \pm \mathbf{Q}_i/2} \psi_{\mathbf{k} \pm \mathbf{Q}_i, +}. \quad (5.44)$$

The coefficients  $A_{k_w \hat{\mathbf{w}} \pm \mathbf{Q}_i/2}$  and  $B_{k_w \hat{\mathbf{w}} \pm \mathbf{Q}_i/2}$  are determined by the solutions to the bare Hamiltonian without superconductivity and magnetic term

$$|k_w \hat{\mathbf{w}} \pm \mathbf{Q}_i/2, +\rangle \approx \begin{pmatrix} A_{k_w \hat{\mathbf{w}} \pm \mathbf{Q}_i/2} \\ B_{k_w \hat{\mathbf{w}} \pm \mathbf{Q}_i/2} \end{pmatrix}. \quad (5.45)$$

In this basis the linearized Hamiltonian blocks for each  $\mathbf{Q}_i$  wavevector have the form

$$\hat{h}_i(\mathbf{k}) = v \mathbf{Q}_i \cdot \mathbf{k} \tau_z \rho_z + \Delta \tau_x - B \rho_y. \quad (5.46)$$

In the case of  $\text{Bi}_2\text{Te}_3$  with threefold symmetry the Dirac velocity is given by  $v = (k_0 + 3k_0^5)/\mu_{\text{hex}}$ . The Hamiltonian has the form of a nanowire Hamiltonian [66], in  $\mathbf{Q}_i$  direction, where the  $\rho$  matrices take the role of the spin matrices. However the nanowire Hamiltonian is defined in one dimension whereas the given Hamiltonian blocks are defined in two dimensions with a highly anisotropic  $\rho$ -orbit coupling.

To find Majorana modes one introduces a domain wall along  $\hat{\mathbf{w}} = \cos \omega \hat{\mathbf{x}} + \sin \omega \hat{\mathbf{y}}$ , where  $B - \Delta$  changes sign, with  $B = \sqrt{2}M$ . The domain wall is located at  $r_{\perp} = 0$  with  $B - \Delta = G > 0$  for  $r_{\perp} > 0$  and  $B - \Delta = -G < 0$  for  $r_{\perp} < 0$ .

We split the momentum in a component along the domain wall  $k_w$  and a momentum component orthogonal to the wall  $k_{\perp}$ . The momentum along the wall  $k_w$  is still a good quantum number since translational symmetry along the wall is unbroken. Then the Hamiltonian takes the form

$$\hat{h}_i(\mathbf{k}) = (v_{i,w} k_w + v_{i,\perp} k_{\perp}) \tau_z \rho_z + \Delta \tau_x - B \rho_y, \quad (5.47)$$

with  $v_{i,w} = v \mathbf{Q}_i \cdot \hat{\mathbf{w}}$  and  $v_{i,\perp} = v \mathbf{Q}_i \cdot \hat{\mathbf{w}}_{\perp}$ . The solutions to  $k_{\perp}$  are given by the Schrödinger equation  $v_{i,\perp} k_{\perp} = -v_{i,w} k_w - \imath(B \tau_z \rho_x + \Delta \tau_y \rho_z)$  as follows

$$k_{\perp} = -v_{i,w} k_w / v_{i,\perp} - \imath(B + \Delta) / v_{i,\perp}, \quad \phi = \frac{1}{2}(\imath, \imath, -1, 1)^{\text{T}}, \quad (5.48)$$

$$k_{\perp} = -v_{i,w} k_w / v_{i,\perp} + \imath(B + \Delta) / v_{i,\perp}, \quad \phi = \frac{1}{2}(\imath, -\imath, 1, 1)^{\text{T}}, \quad (5.49)$$

$$k_{\perp} = -v_{i,w} k_w / v_{i,\perp} - \imath(B - \Delta) / v_{i,\perp}, \quad \phi = \frac{1}{2}(\imath, \imath, 1, -1)^{\text{T}}, \quad (5.50)$$

$$k_{\perp} = -v_{i,w} k_w / v_{i,\perp} + \imath(B - \Delta) / v_{i,\perp}, \quad \phi = \frac{1}{2}(-\imath, \imath, 1, 1)^{\text{T}}. \quad (5.51)$$

The relevant solutions decay for  $r_{\perp} \rightarrow \pm\infty$ . For  $r_{\perp} < 0$  these solutions satisfy  $\text{Im } k_{\perp} < 0$  and for  $r_{\perp} > 0$  the solutions satisfy  $\text{Im } k_{\perp} > 0$ .

The full solution on either side of the domain wall takes the form

$$\Phi = \frac{1}{N} e^{ik_w(r_w - r_\perp v_{i,\perp}/v_{i,\perp})} e^{-G|r_\perp/v_{i,\perp}|} \frac{1}{2} (\imath \text{sign}(v_{i,\perp}), \imath, 1, -\text{sign}(v_{i,\perp}))^\top \quad (5.52)$$

with normalization constant  $N$ . Given those, the wavefunction of the electronic part on the left  $\phi_{e,k_w}^-$  ( $r_\perp < 0$ ) and on the right  $\phi_{e,k_w}^+$  ( $r_\perp > 0$ ) reads as

$$\begin{aligned} \phi_{e,k_w}^\pm(\mathbf{r}) = & \frac{1}{2N} \sum_i e^{ik_w(r_w - r_\perp v_{i,w}/v_{i,\perp})} e^{-G|r_\perp/v_{i,\perp}|} \\ & \times a_{i,k_w}^\pm \left\{ e^{\imath \mathbf{Q}_i \cdot \mathbf{r}/2} \begin{pmatrix} \imath \text{sign}(v_{i,\perp}) A_{k_w \hat{\mathbf{w}} + \mathbf{Q}_i/2} \\ \imath \text{sign}(v_{i,\perp}) B_{k_w \hat{\mathbf{w}} + \mathbf{Q}_i/2} \end{pmatrix} + e^{-\imath \mathbf{Q}_i \cdot \mathbf{r}/2} \begin{pmatrix} \imath A_{k_w \hat{\mathbf{w}} - \mathbf{Q}_i/2} \\ \imath B_{k_w \hat{\mathbf{w}} - \mathbf{Q}_i/2} \end{pmatrix} \right\}. \end{aligned} \quad (5.53)$$

The hole part of the wavefunction  $\phi_{h,k_w}^\pm$  can be recovered by charge-conjugation symmetry of the Bogoliubov-de Gennes Hamiltonian.

In the next step, the wavefunctions on the left and the right must be matched at  $r_\perp = 0$ , where we assume that the superconducting phase and the magnetic order do not change over the domain wall. Here the question is whether the wavefunctions for the different vectors  $\mathbf{Q}_i$  mix. One finds that for the domain wall angle  $\omega = n\pi/6$  two of the velocities  $|v_{i,w}|$  become equal leading to a mixing. For  $\omega = (2n+1)\pi/12$  the velocities become maximally different. Furthermore for  $\hat{\mathbf{w}} \parallel \mathbf{Q}_i$  the subsystem  $i$  does not support a Majorana mode.

In the case of maximally different velocities one finds the coefficient  $a_{i,k_w} = a_{i,k_w}^\pm$ . In the case of other angles the coefficients are determined by a system of coupled equations. However the determinant of this system of equations is zero such that the solutions can always be written in the decoupled form

$$\begin{aligned} \phi_{e,k_w,i}^\pm(\mathbf{r}) = & \frac{a_{i,k_w}}{2N} e^{ik_w(r_w - r_\perp v_{i,w}/v_{i,\perp})} e^{-G|r_\perp/v_{i,\perp}|} \\ & \times \left\{ e^{\imath \mathbf{Q}_i \cdot \mathbf{r}/2} \begin{pmatrix} \text{sign}(v_{i,\perp}) A_{k_w \hat{\mathbf{w}} + \mathbf{Q}_i/2} \\ \text{sign}(v_{i,\perp}) B_{k_w \hat{\mathbf{w}} + \mathbf{Q}_i/2} \end{pmatrix} + e^{-\imath \mathbf{Q}_i \cdot \mathbf{r}/2} \begin{pmatrix} A_{k_w \hat{\mathbf{w}} - \mathbf{Q}_i/2} \\ B_{k_w \hat{\mathbf{w}} - \mathbf{Q}_i/2} \end{pmatrix} \right\}. \end{aligned} \quad (5.54)$$

Since the flat bands are highly degenerate we proceed with a discussion of possible interaction effects.

### 5.4.2 Interaction effects on the flat bands

The arising flat bands are susceptible to interaction effects due to their high degeneracy. We proceed by considering the interaction present in the given system, which is a repulsive Hubbard interaction, also responsible for the stabilization of the magnetic

texture. The Hubbard interaction has the form

$$H = U \int d\mathbf{r} \psi_{\uparrow}^{\dagger}(\mathbf{r})\psi_{\uparrow}(\mathbf{r})\psi_{\downarrow}^{\dagger}(\mathbf{r})\psi_{\downarrow}(\mathbf{r}). \quad (5.55)$$

The goal is to replace the fermionic field operators with Majorana operators. For this purpose we project the fermionic operators onto the Majorana operators. The fermionic operators are decomposed in the relevant Fourier components as follows

$$\begin{aligned} \Psi(r_w, r_{\perp}) &= \sum_{i=1,2,3} \int \frac{dk_w}{2\pi} e^{ik_w r_w} \\ &\times \left[ e^{i\mathbf{Q}_i \cdot \mathbf{r}/2} \Psi_{k_w \hat{w} + \mathbf{Q}_i/2}(r_{\perp}) + e^{-i\mathbf{Q}_i \cdot \mathbf{r}/2} \Psi_{k_w \hat{w} - \mathbf{Q}_i/2}(r_{\perp}) \right], \end{aligned} \quad (5.56)$$

$$\Psi_{i,k_w}(r_{\perp}) = \int dr_w \left[ e^{i\mathbf{Q}_i \cdot \mathbf{r}/2} \Psi_{k_w \hat{w} + \mathbf{Q}_i/2}(r_{\perp}) + e^{-i\mathbf{Q}_i \cdot \mathbf{r}/2} \Psi_{k_w \hat{w} - \mathbf{Q}_i/2}(r_{\perp}) \right]. \quad (5.57)$$

Replacing the electronic operators  $\Psi_{i,k_w}(r_{\perp})$  with the Majorana operators  $\gamma_i(k_w)$  and mean-field decoupling the interaction in the most-relevant zero-momentum channel yields a Hamiltonian for three Majorana bands  $\gamma_i(k_w)$  of the general form

$$\mathcal{H}_{3\text{MF}} = \int_{-\Lambda}^{\Lambda} dk_w \begin{pmatrix} \gamma_1(-k_w) \\ \gamma_2(-k_w) \\ \gamma_3(-k_w) \end{pmatrix}^{\top} \begin{pmatrix} f_1(k_w) & m_{12}(k_w) & m_{13}(k_w) \\ m_{21}(k_w) & f_2(k_w) & m_{23}(k_w) \\ m_{31}(k_w) & m_{32}(k_w) & f_3(k_w) \end{pmatrix} \begin{pmatrix} \gamma_1(k_w) \\ \gamma_2(k_w) \\ \gamma_3(k_w) \end{pmatrix}. \quad (5.58)$$

The Majorana operators satisfy  $\{\gamma_i(-k_w), \gamma_j(k'_w)\} = \delta_{ij} \delta(k_w - k'_w)$  which implies the relations  $f_i(k_w) = -f_i(-k_w)$  and  $m_{ij}(k_w) = -m_{ji}(-k_w)$  on the matrix elements.

Given these relations the matrix elements can be approximated at first order to  $f_i(k_w) \approx \alpha_i k_w$  and  $m_{ij}(k_w) = -m_{ji}(-k_w) \approx \text{const.}$  This leads to two possible outcomes: Either the flat bands are tilted and transformed into chiral bands to the diagonal elements or a gap opens because of the off-diagonal matrix elements.

As an example, we present the case where only two subsystems give rise to Majorana flat bands. In this case the Hamiltonian reduces to

$$\mathcal{H}_{2\text{MF}} = \int_{-\Lambda}^{\Lambda} dk_w \begin{pmatrix} \gamma_1(-k_w) \\ \gamma_2(-k_w) \end{pmatrix}^{\top} \begin{pmatrix} (J + \delta)k_w & -im \\ im & (J - \delta)k_w \end{pmatrix} \begin{pmatrix} \gamma_1(k_w) \\ \gamma_2(k_w) \end{pmatrix}. \quad (5.59)$$

We introduce the eigenenergies of the bands  $\epsilon_{\pm, k_w} = Jk_w \pm \sqrt{\delta^2 k_w^2 + m^2}$ .

We illustrate the possible modifications of the dispersion in Fig. 5.7. The Majorana bands are tilted by  $J$ , acquiring a chiral character.  $\delta$  corresponds to a tilting of the bands relative to each other or a bending and  $m$  leads to a gap opening.

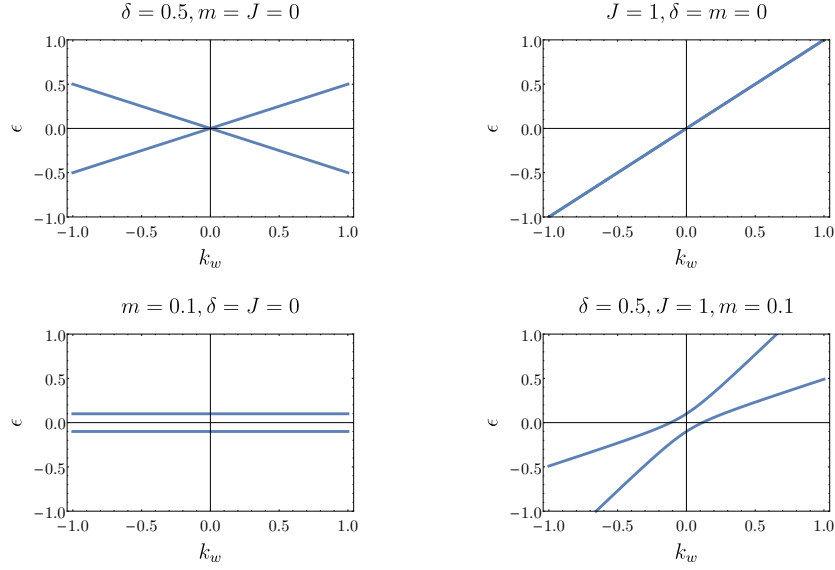


Figure 5.7: Modified dispersion of two Majorana flat bands

## 5.5 Summary and conclusion

In this chapter we discussed a heterostructure consisting of a magnetic layer with spin-orbit coupling and a conventional superconductor. We derived a free energy theory describing the coupled systems. Given this theory we introduced the various feedback effects between the systems.

Then we considered a more specific model, based on a Bi-based topological insulator. We derived the modified susceptibility and computed the magnetic gap in a self-consistent manner. Furthermore we considered a multipolar supercurrent distribution appearing in the superconductor due to the coupling. In particular, the skyrmion lattice may lead to a characteristic pattern of supercurrents.

After that we analyzed the topological properties of the given system. We demonstrated that a magnetic topological insulator in proximity to a conventional superconductor indeed allows to engineer a  $C_3$ -symmetric topological superconductor. We discussed Majorana flat bands which appear as low energy excitations at a domain wall where  $B - \Delta$  changes sign. Here  $\Delta$  is the proximity induced superconducting gap and  $B$  is the intrinsic magnetic field due to the magnetic texture. The number of Majorana flat bands depends on the orientation of the wall. Since flat bands are generally unstable in the presence of interactions we discussed interaction effects on the bands, which can lead a modification of the flat dispersion, resulting in tilted or gapped bands.

# 6

## Chapter 6

---

# Conclusion and outlook

In this thesis we studied heterostructures with interaction-driven magnetic ordering and superconductivity. We analyzed magnetic adatom chains and transport through Majorana bound states. Furthermore we considered topological insulator surface states with the tendency for magnetic ordering, which can provide a platform for Majorana setups. For this purpose the topological insulator must be combined with a conventional superconductor, resulting in a topological superconductor.

More precisely, in Chapter 3 we studied chains of magnetic adatoms, placed on a superconducting substrate. The adatoms order via a substrate-mediated RKKY interaction [2]. Within the topological phase diagram, there are topologically non-trivial regimes, which support either one or two Majorana bound states per end of the chain. The two Majorana bound states are protected by chiral symmetry which can be selectively broken by external fields. This feature provides an experimental knob in the detection of Majorana bound states in engineered topological superconductors.

In Ref. [3] we calculated the tunneling conductance, which is expected in a magnetic adatom chain in ferromagnetic ordering. In the phase with two Majorana bound states a tunneling conductance of  $4e^2/h$  is expected, which should reduce to  $2e^2/h$  for a single Majorana bound state. In particular, the breaking of chiral symmetry should be observable in the tunneling conductance experiments.

A more important aspect is, that the Majorana bound states, hosted in Yu-Shiba-Rusinov chains, show a spin character which can be revealed in spin-polarized tunneling conductance measurements, when a scanning tunneling microscope with spin-polarized tip is used. The analysis of the tunneling conductance using a spin-polarized tip was the main focus of our analysis. We found that tunneling conductance measurements

can show an asymmetry if the Majorana bound states at both ends of the chain are probed.

Experiments with magnetic adatom chains have been performed [6] and further experiments are planned, also with a focus on the spin polarization. Interestingly, the quantization  $2e^2/h$  was found just recently in a semiconductor based setup [7]. In our work, we included more complex setups involving multiple chains coupled via Josephson junctions. The discussed extensions are currently out of reach experimentally in the case of adatom chains, but we are optimistic that this will change in the future.

Potentially our work could be extended to networks of topological Yu-Shiba-Rusinov chains with braiding capabilities, to provide the ultimate Majorana signature by demonstrating non-abelian statistics [43]. This would at the same time demonstrate the feasibility of topological quantum computation using Majorana bound states.

In Chapter 4 we focused on topological insulator surface states with the tendency for magnetic ordering. Topological insulators are characterized by their surface states, which are a consequence of the bulk topology. On the other hand, the bulk of the material is insulating with a bulk gap. There are experiments, showing these characteristic properties of topological insulators [99, 121].

For the  $\text{Bi}_2\text{Te}_3$  compound, the Fermi surface shows hexagonal warping depending on the chemical potential, which is controlled by doping the material. In particular the chemical potential can be tuned to a special value  $\mu_{\text{hex}}$ , where the Fermi surface forms a nearly perfect hexagon. In this case, three dominant wavevectors  $\mathbf{Q}_{1,2,3}$  connect the nested flat sides of the Fermi surface. These wavevectors correspond to three magnetic order parameters  $\mathbf{M}_{1,2,3}$ .

In our work we analyzed the possible magnetic phases in a microscopically-derived Landau theory in the presence of a repulsive Hubbard interaction. The second order of the theory, corresponding to the susceptibility, fixes the direction of the magnetic order parameters. At fourth order the Landau theory determines whether a magnetic phase with one order parameter  $\mathbf{M}_i$  or all three order parameters  $\mathbf{M}_{1,2,3}$  dominates. As a result we showed that for a chemical potential in the vicinity of  $\mu_{\text{hex}}$  the phase with all three  $\mathbf{M}_{1,2,3}$  is favored [1].

At sixth order, one additional phase degree of freedom  $\Phi_z$  is fixed, while two massless Goldstone phasons remain unfixed, as expected by the spontaneous symmetry breaking of translational symmetry. The fixed phase  $\Phi_z$  leads to a topologically non-trivial skyrmion phase, which constitutes the dominant ground state for chemical potential  $\mu_{\text{hex}}$  [1]. The skyrmion texture is composed by the linear superposition of three helical spin density waves, rotated by  $2\pi/3$ .

---

The presence of helical magnetism is useful to build topological superconductors supporting Majorana fermions, by combining the magnetic material with a conventional superconductor. However for the material to transit to the magnetic phase a sufficiently strong interaction must be present. While currently no materials of this family are known providing such an interaction, the mechanism to generate a skyrmion texture is general. In experiment, it could be helpful to stabilize the skyrmion texture by coupling to external fields. In particular we found that a magnetic field  $B_z$ , orthogonal to the topological insulator surface, couples directly to the skyrmion charge. Possible extensions of our work include different types of skyrmion lattices for different point group symmetries and the study of the dynamics of the magnetic texture.

Chapter 5 extends our work on magnetic topological insulator surfaces. We considered a heterostructure formed from a magnetic layer and a conventional superconductor. At first we derived a general theory applying to heterostructures of this type to gain understanding of the feedback effects between the magnetic layer and the superconductor.

At first order, the superconductor induces a superconducting gap in the magnetic layer, the superconducting proximity effect. This superconducting gap competes with the magnetic order of the magnetic layer. There are higher order feedback effects, including possible staggered superconducting correlations due to the magnetic texture and multipolar supercurrent distributions occurring at the interface between the subsystems.

In the case of a heterostructure formed from a Bi-based topological insulator with hexagonal warping, we analyzed the phase diagram of the magnetic gap self-consistently in the presence of the superconducting gap. We derived a low energy model confirming the possibility of topological superconductivity in this heterostructure [1]. In this case the supercurrent distribution reflects the skyrmion charge of the underlying texture and could act as a probe. We analyzed the phenomenon of topological superconductivity in the given system in more detail. Additional to chiral edge modes, which occur in topological superconductors built from two dimensional surfaces of topological insulators, we found that due to the anisotropic structure of the low energy Hamiltonian, Majorana flat bands can occur. The bands appear at domain walls where  $B - \Delta$  changes the sign, with  $B$  the intrinsic magnetic field due to the magnetic layer and  $\Delta$  the proximity-induced superconducting gap. The domain wall breaks translational symmetry perpendicular to the wall, however along the wall Majorana flat bands disperse.

Since interactions are present in the system under consideration, the flat bands may acquire a chiral dispersion and gap openings. Even very weak interactions are of importance here, since flat bands are very susceptible to modification due to their high degeneracy. Similar effects on Majorana flat bands are expected in comparable topological systems with anisotropy, e.g., in an anisotropic p-wave superconductor. The effects of interactions in flat band systems require further studies. In particular strong interactions in topological systems pose many interesting research questions. While there exists an exhaustive topological classification of topological insulators and superconductors [89], for interacting systems such an exhaustive classification is still out of reach.

Concerning the combination of superconductors with materials with non-trivial magnetic texture, further work is needed to propose experiments based on existing materials. Especially the expected feedback effects are of interest and perhaps relevant for applications within spintronics or even ‘skyrmionics’. In particular the interplay of Majorana states and skyrmions, which are both topological structures or of topological origin, provides interesting perspectives for quantum information processing.

# A

## Appendix A

# Appendices

### A.1 Tunneling conductance for two coupled magnetic adatom chains

We present the conductance formula in the form

$$\frac{dI_i}{dV} = \frac{2e^2}{h} \frac{N(eV)}{D(eV)}. \quad (\text{A.1})$$

We introduced  $\mathcal{M} = \sqrt{m_{ad}^2 + M_{ab}^2 + M_{db}^2}$  and the denominator and nominator functions

$$\begin{aligned} D(\omega) = & \omega^6 + \omega^4 \left[ (\Gamma_{aa}^i)^2 + (\Gamma_{dd}^i)^2 + 2 \operatorname{Re}^2 \Gamma_{ad}^i - 2\mathcal{M}^2 \right] \\ & + \omega^2 \left\{ \left[ \Gamma_{aa}^i \Gamma_{dd}^i - \operatorname{Re}^2 \Gamma_{ad}^i + \mathcal{M}^2 \right]^2 \right. \\ & \quad \left. - 2(\Gamma_{aa}^i + \Gamma_{dd}^i) \left[ \Gamma_{aa}^i M_{db}^2 + \Gamma_{dd}^i M_{ab}^2 - 2(\operatorname{Re} \Gamma_{ad}^i) M_{ab} M_{db} \right] \right\} \\ & + \left[ \Gamma_{aa}^i M_{db}^2 + \Gamma_{dd}^i M_{ab}^2 - 2(\operatorname{Re} \Gamma_{ad}^i) M_{ab} M_{db} \right]^2, \end{aligned} \quad (\text{A.2})$$

$$\begin{aligned} N(\omega) = & \omega^4 \left\{ (\Gamma_{aa}^i)^2 + (\Gamma_{dd}^i)^2 + 2 \left[ \operatorname{Re}^2 \Gamma_{ad}^i - \operatorname{Im}^2 \Gamma_{ad}^i \right] \right\} \\ & + 2\omega^2 \left[ \Gamma_{aa}^i \Gamma_{dd}^i - \operatorname{Re}^2 \Gamma_{ad}^i + m_{ad}^2 \right] \left[ \Gamma_{aa}^i \Gamma_{dd}^i - |\Gamma_{ad}^i|^2 \right] \\ & - 2\omega^2 \left\{ \left[ (\Gamma_{aa}^i)^2 + \operatorname{Re}^2 \Gamma_{ad}^i - \operatorname{Im}^2 \Gamma_{ad}^i \right] M_{db}^2 + \left[ (\Gamma_{dd}^i)^2 + \operatorname{Re}^2 \Gamma_{ad}^i - \operatorname{Im}^2 \Gamma_{ad}^i \right] M_{ab}^2 \right. \\ & \quad \left. - 2(\Gamma_{aa}^i + \Gamma_{dd}^i) (\operatorname{Re} \Gamma_{ad}^i) M_{ab} M_{db} \right\} \\ & + \left[ \Gamma_{aa}^i M_{db}^2 + \Gamma_{dd}^i M_{ab}^2 - 2(\operatorname{Re} \Gamma_{ad}^i) M_{ab} M_{db} \right]^2. \end{aligned} \quad (\text{A.3})$$

## A.2 Magnetic order parameter classification of warped topological insulators

We consider the case of a hexagonal FS and three dominant nesting vectors  $\mathbf{Q}_{1,2,3}$ . Then we can classify linear combinations of the order parameters  $\mathbf{M}_{\mathbf{Q}_\lambda} = \mathbf{M}_{-\mathbf{Q}_\lambda}^* \equiv (M_{\lambda x}, M_{\lambda y}, M_{\lambda z})^\top$  for  $\lambda = 1, 2, 3$ , which transform under the point group representations  $A_1$ ,  $A_2$  and  $E$  of the point group  $C_{3v}$ . The axial vector  $\mathbf{M}_q$  transforms under a group operation  $\mathcal{G} \in C_{3v}$  as  $\mathcal{G}\mathbf{M}_q \equiv \hat{D}_{\mathcal{G}}^- \mathbf{M}_{\mathcal{G}^{-1}q}$ .

We define the following 18-dimensional basis in terms of the original order parameters

$$\begin{aligned} \mathbf{M}^\top &\equiv \left( \mathbf{M}_{\mathbf{Q}_1}^\top, \mathbf{M}_{-\mathbf{Q}_1}^\top, \mathbf{M}_{\mathbf{Q}_2}^\top, \mathbf{M}_{-\mathbf{Q}_2}^\top, \mathbf{M}_{\mathbf{Q}_3}^\top, \mathbf{M}_{-\mathbf{Q}_3}^\top \right) \\ &\equiv \left( M_{1x}, M_{1y}, M_{1z}, M_{1x}^*, M_{1y}^*, M_{1z}^*, \dots \right), \end{aligned} \quad (\text{A.4})$$

$$\mathbf{M}^\dagger = [\mathbf{1}_3 \otimes \rho_x \otimes \mathbf{1}_3] \cdot \mathbf{M}^\top = \left( M_{1x}^*, M_{1y}^*, M_{1z}^*, M_{1x}, M_{1y}, M_{1z}, \dots \right). \quad (\text{A.5})$$

The 18-dimensional space can be decomposed in the  $\lambda$ ,  $\rho$  and axial part. Rotations in the 3D  $\lambda$  space connect the different  $\mathbf{M}_{1,2,3}$ . Transformations in 2D  $\rho$  space connect the order parameters  $\pm\mathbf{Q}_i$ .

To perform the classification we have to consider the action of the point group operations  $\mathcal{G} \in C_{3v}$  on the magnetic order parameters. The representations  $\hat{D}_M(\mathcal{G})$  acting in the basis  $\mathbf{M}$  are given as

$$\hat{D}_M(C_3) = \hat{D}_\lambda(C_3) \otimes \mathbf{1}_2 \otimes \hat{D}_{C_3}^- \quad \text{and} \quad \hat{D}_M(\sigma_v) = \hat{D}_\lambda(\sigma_v) \otimes \rho_x \otimes \hat{D}_{\sigma_v}^-. \quad (\text{A.6})$$

The representations of the point group operations in  $\lambda$  space are given by the representations

$$\hat{D}_\lambda(C_3) = \begin{pmatrix} 0 & 0 & 1 \\ 1 & 0 & 0 \\ 0 & 1 & 0 \end{pmatrix} \quad \text{and} \quad \hat{D}_\lambda(\sigma_v) = \begin{pmatrix} 1 & 0 & 0 \\ 0 & 0 & 1 \\ 0 & 1 & 0 \end{pmatrix}. \quad (\text{A.7})$$

This form can be obtained by considering how the  $\mathbf{Q}$  vectors transform under the group operations. The rotation  $C_3$  rotates the wave vector  $\mathbf{Q}_1$  to  $\mathbf{Q}_2$ , etc.. The reflection at the  $yz$  plane reflects  $\mathbf{Q}_1 \rightarrow -\mathbf{Q}_1$  and  $\mathbf{Q}_{2,3} \rightarrow -\mathbf{Q}_{3,2}$ .

In order to connect the order parameters to the ones, which can appear in a Hamiltonian, we represent them in the real basis

$$\begin{pmatrix} \mathbf{M}_q^R \\ \mathbf{M}_q^I \end{pmatrix} \equiv \frac{1}{\sqrt{2}} \begin{pmatrix} 1 & 1 \\ -i & i \end{pmatrix} \cdot \begin{pmatrix} \mathbf{M}_q \\ \mathbf{M}_{-q} \end{pmatrix}. \quad (\text{A.8})$$

To complete the symmetry analysis, we write the linear combinations of the order parameters, which transform according to respective representations of the point group. The two-dimensional  $E$  representations are formed by  $(\mathcal{M}_{x,i}, \mathcal{M}_{y,i})$ . The representations  $i = 1, 2, 3$  are chosen in such a way that they transform like a  $(k_x, k_y)$  vector. The representations  $i = 4, 5, 6$  are chosen to transform like  $(-k_y, k_x)$ .

$$\mathcal{M}_{A_{1,1}} = 1/\sqrt{12} \left( -2M_{1x}^R + M_{2x}^R + M_{3x}^R - \sqrt{3}M_{2y}^R + \sqrt{3}M_{3y}^R \right), \quad (\text{A.9})$$

$$\mathcal{M}_{A_{1,2}} = 1/\sqrt{12} \left( -\sqrt{3}M_{2x}^I + \sqrt{3}M_{3x}^I + 2M_{1y}^I - M_{2y}^I - M_{3y}^I \right), \quad (\text{A.10})$$

$$\mathcal{M}_{A_{1,3}} = 1/\sqrt{3} \left( M_{1z}^I + M_{2z}^I + M_{3z}^I \right), \quad (\text{A.11})$$

$$\mathcal{M}_{A_{2,1}} = 1/\sqrt{12} \left( 2M_{1x}^I - M_{2x}^I - M_{3x}^I + \sqrt{3}M_{2y}^I - \sqrt{3}M_{3y}^I \right), \quad (\text{A.12})$$

$$\mathcal{M}_{A_{2,2}} = 1/\sqrt{12} \left( -\sqrt{3}M_{2x}^R + \sqrt{3}M_{3x}^R + 2M_{1y}^R - M_{2y}^R - M_{3y}^R \right), \quad (\text{A.13})$$

$$\mathcal{M}_{A_{2,3}} = 1/\sqrt{3} \left( M_{1z}^R + M_{2z}^R + M_{3z}^R \right), \quad (\text{A.14})$$

$$\mathcal{M}_{x,1} = 1/\sqrt{24} \left( -\sqrt{3}M_{2x}^R + \sqrt{3}M_{3x}^R + 3M_{2y}^R + 3M_{3y}^R \right), \quad (\text{A.15})$$

$$\mathcal{M}_{y,1} = 1/\sqrt{24} \left( -4M_{1x}^R - M_{2x}^R - M_{3x}^R + \sqrt{3}M_{2y}^R - \sqrt{3}M_{3y}^R \right), \quad (\text{A.16})$$

$$\mathcal{M}_{x,2} = 1/\sqrt{24} \left( 3M_{2x}^I + 3M_{3x}^I + \sqrt{3}M_{2y}^I - \sqrt{3}M_{3y}^I \right), \quad (\text{A.17})$$

$$\mathcal{M}_{y,2} = 1/\sqrt{24} \left( \sqrt{3}M_{2x}^I - \sqrt{3}M_{3x}^I + 4M_{1y}^I + M_{2y}^I + M_{3y}^I \right), \quad (\text{A.18})$$

$$\mathcal{M}_{x,3} = 1/\sqrt{2} \left( M_{3z}^I - M_{2z}^I \right), \quad (\text{A.19})$$

$$\mathcal{M}_{y,3} = 1/\sqrt{6} \left( 2M_{1z}^I - M_{2z}^I - M_{3z}^I \right), \quad (\text{A.20})$$

$$\mathcal{M}_{x,4} = 1/\sqrt{24} \left( \sqrt{3}M_{2x}^I - \sqrt{3}M_{3x}^I - 3M_{2y}^I - 3M_{3y}^I \right), \quad (\text{A.21})$$

$$\mathcal{M}_{y,4} = 1/\sqrt{24} \left( 4M_{1x}^I + M_{2x}^I + M_{3x}^I - \sqrt{3}M_{2y}^I + \sqrt{3}M_{3y}^I \right), \quad (\text{A.22})$$

$$\mathcal{M}_{x,5} = 1/\sqrt{24} \left( 3M_{2x}^R + 3M_{3x}^R + \sqrt{3}M_{2y}^R - \sqrt{3}M_{3y}^R \right), \quad (\text{A.23})$$

$$\mathcal{M}_{y,5} = 1/\sqrt{24} \left( \sqrt{3}M_{2x}^R - \sqrt{3}M_{3x}^R + 4M_{1y}^R + M_{2y}^R + M_{3y}^R \right), \quad (\text{A.24})$$

$$\mathcal{M}_{x,6} = 1/\sqrt{2} \left( M_{3z}^R - M_{2z}^R \right), \quad (\text{A.25})$$

$$\mathcal{M}_{y,6} = 1/\sqrt{6} \left( 2M_{1z}^R - M_{2z}^R - M_{3z}^R \right). \quad (\text{A.26})$$

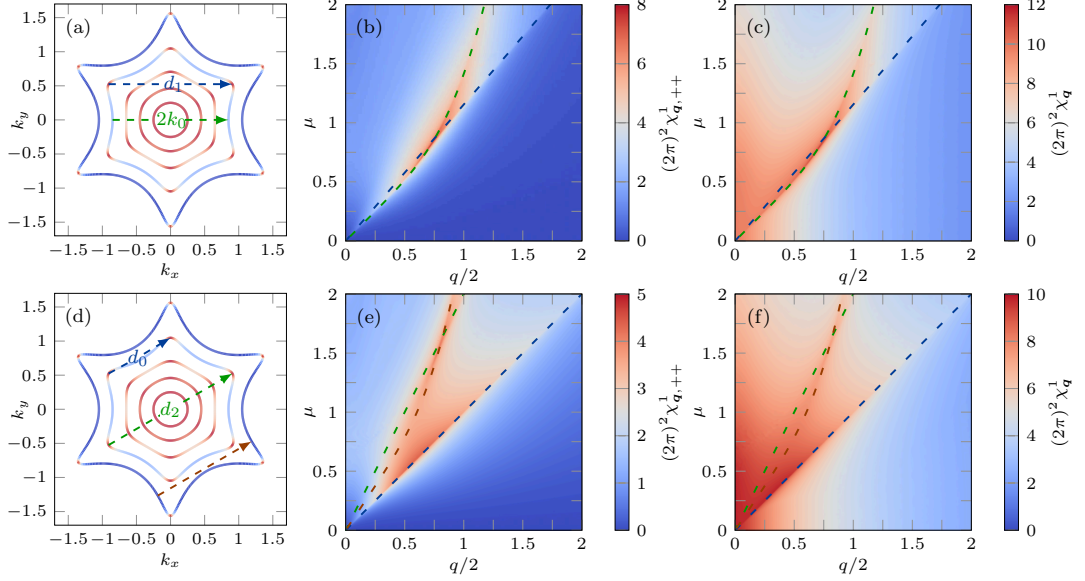


Figure A.1: Largest susceptibility eigenvalue for momentum transfers along two different high-symmetry lines shown in (a,d). Figures (b,c) show the susceptibility of the upper helicity band and figures (c,f) the full susceptibility of both bands.

### A.3 Magnetic susceptibility of warped topological insulators

We performed a scan of the parameter space for a wide range of the chemical potential and for different temperatures. We cover the regimes from circular via hexagonal to snowflake-like and focus on momentum transfers along high-symmetry lines, which yield the highest contributions to the susceptibility.

Two flat sides of the Fermi surface for a given chemical potential have the distance  $2k_0$ . Using the equation for the Fermi surface Eq. (4.8) we can find the connecting wavevectors and distances  $d_{0,1,2}$  between the corners of the Fermi surface. We illustrate the wavevectors in Fig. A.1(a,d). The distances are given by

$$d_0 = 2\mu \sin(\pi/6) = \mu, \quad (\text{A.27})$$

$$d_1 = 2\mu \sin(\pi/3) = \sqrt{3}\mu, \quad (\text{A.28})$$

$$d_2 = 2k(\pi/6, \mu) = 2\mu. \quad (\text{A.29})$$

Furthermore Fig. A.1(a,d) shows the spin susceptibility for  $T = 0$  as a function of  $\mu$  and the modulus of two vectors  $\mathbf{q} = q(1, 0)$  and  $\mathbf{q}' = q'(\sqrt{3}/2, 1/2)$ , both running along high-symmetry lines in momentum space and connecting sides or corners respectively.

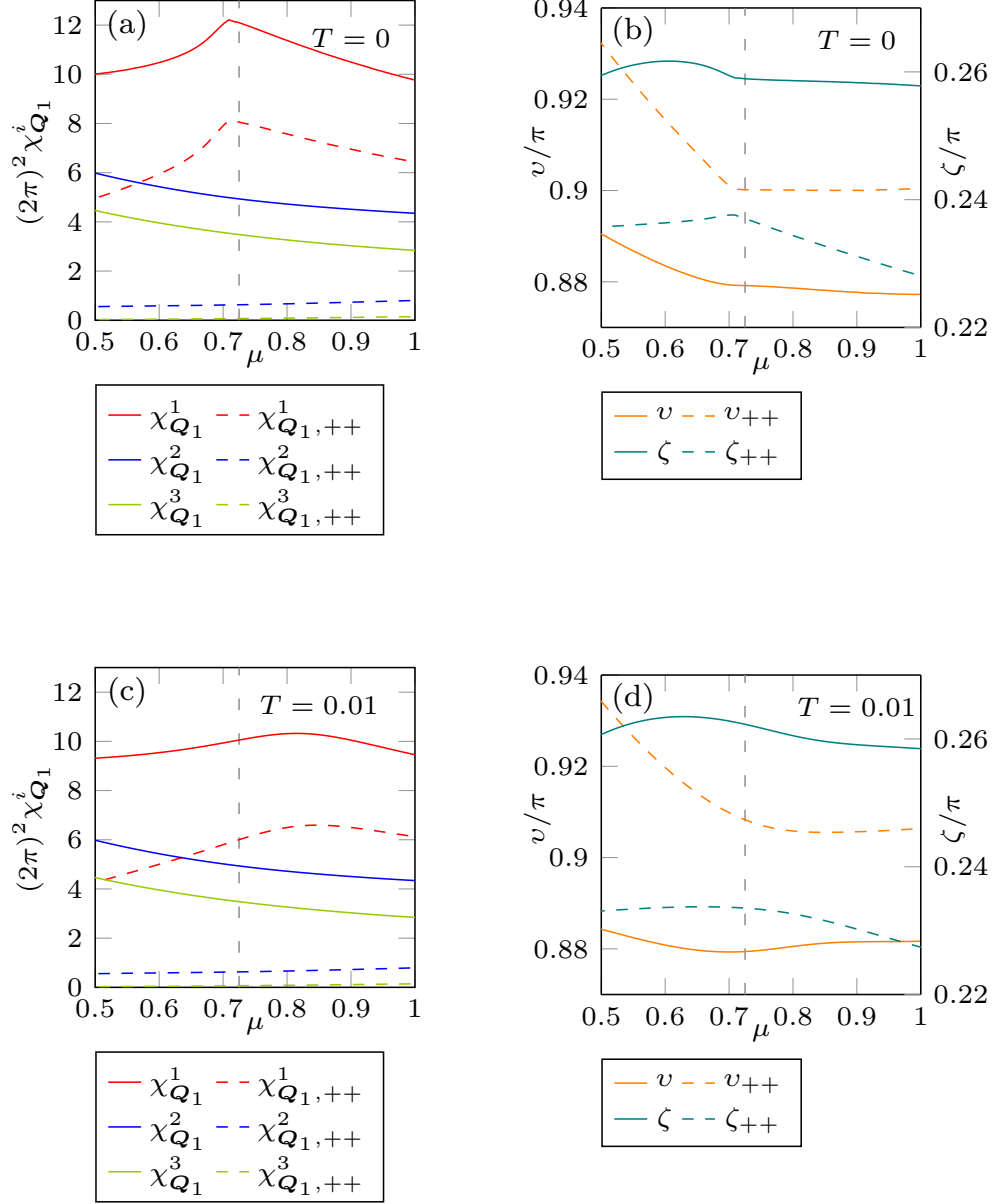


Figure A.2: All three susceptibility eigenvalues and spherical angles  $\nu$  and  $\zeta$  of the magnetization direction depending on chemical potentials at temperature  $T = 0$  and  $T = 0.01$ . The vertical dashed line shows the value of chemical potential  $\mu_{\text{hex}}$ , where the Fermi surface is hexagonal.

Scanning the parameters simultaneously allows to determine the optimal relations for  $\mu(q)$  and  $\mu(q')$ , which maximize the spin susceptibility. In the plots of Fig. A.1(b,c,e,f) the dominant features are the two ridges where the susceptibility is higher than at other parts of the parameter space. These ridges can be attributed to scattering processes between sides of the Fermi surface and corners with high density of states.

For instance in Fig. A.1(b,c) the dominant ridge in the susceptibility is along the quartic curve  $\mu = (q/2)\sqrt{1 + (q/2)^4}$  with  $q = 2k_0$  which is due to the scattering process along the nesting vector connecting the approximately flat parts of the Fermi surface. The subdominant ridge which goes along the line  $\mu = q/\sqrt{3} = d_1/\sqrt{3}$  and arises due to the nesting of the high density of states corners of the Fermi surface connected by the mirror symmetries  $(x, y) \mapsto (x, -y)$ .

In Fig. A.1(e,f) there is one ridge along the line  $\mu = q' = d_0$ , originating from nested neighboring corners of the Fermi surface. The subleading linear ridge along the line  $\mu = q'/2 = d_2/2$  is due to nesting between opposite corners connected by the reflection  $(x, y) \mapsto (-x, -y)$ . The arising nonlinear ridge is related to the nesting of Fermi surface edges in the snowflake like regime which bend outwards for higher values of  $\mu$ .

In Fig. A.2(a,c) we show the three spin susceptibility eigenvalues for the most dominant ridge  $\mu = k_0\sqrt{1 + k_0^4}$  and the dominant nesting vector  $\mathbf{Q}_1 = 2k_0(1, 0)$ . The plots of (a) and (c) correspond to the temperatures  $T = 0$  and  $T = 0.01$ , respectively. Rescaling with the energy scale yields the temperature in Kelvin. For  $\text{Bi}_2\text{Te}_3$  the temperature value  $T = 0.01$  corresponds to 30 K.

The solid curves in the plot show the susceptibility due to all bands and the dashed lines correspond to the upper helicity intraband contribution. The lower helicity intraband contribution is negligible. The largest spin susceptibility eigenvalue is two or three times larger than the remaining two, which justifies to consider only the dominant magnetic order.

The dashed vertical line is at the chemical potential  $\mu = \mu_{\text{hex}}$  which corresponds to the relevant scenario of hexagonal Fermi surface. We also analyzed the stability of the magnetization direction as can be seen in Fig. A.2(d). In spite of the fact that the susceptibility decreases with temperature, the magnetization direction stays more or less stable.

## A.4 Free energy coefficients of warped topological insulators

In this appendix we present the details on how to compute the coefficients of the Landau expansion. The coefficients obtained here are computed numerically. The free

energy up to fourth order has the form

$$\mathcal{F}^{(4)} = \alpha \sum_{i=1}^3 |M_i|^2 + \frac{\beta_1}{2} \sum_{i=1}^3 |M_i|^4 + \beta_2 \sum_{i<j} |M_i|^2 |M_j|^2. \quad (\text{A.30})$$

Furthermore we consider the decisive sixth order parameter of the form

$$\mathcal{F}_{\Phi_z}^{(6)} = \eta(M_1 M_2 M_3)^2 + \eta(M_1^* M_2^* M_3^*)^2 = 2\eta |M_1 M_2 M_3|^2 \cos(2\Phi_z). \quad (\text{A.31})$$

By deriving these free energy terms with respect to the order parameters  $M_{1,2,3}$  we obtain the coefficients

$$\alpha(U=0) = \left. \frac{\partial^2 \mathcal{F}}{\partial M_1 \partial M_1^*} \right|_{M_{1,2,3}=0} = \Pi^{(2)}(\mathbf{Q}_1, -\mathbf{Q}_1), \quad (\text{A.32})$$

$$2\beta_1 = \left. \frac{\partial^4 \mathcal{F}}{(\partial M_1 \partial M_1^*)^2} \right|_{M_{1,2,3}=0} = \frac{1}{4} \sum_{\sigma \in S_4} \Pi^{(4)}(\sigma(\mathbf{Q}_1, -\mathbf{Q}_1, \mathbf{Q}_1, -\mathbf{Q}_1)), \quad (\text{A.33})$$

$$\beta_2 = \left. \frac{\partial^4 \mathcal{F}}{\partial M_1 \partial M_1^* \partial M_2 \partial M_2^*} \right|_{M_{1,2,3}=0} = \frac{1}{4} \sum_{\sigma \in S_4} \Pi^{(4)}(\sigma(\mathbf{Q}_1, -\mathbf{Q}_1, \mathbf{Q}_2, -\mathbf{Q}_2)), \quad (\text{A.34})$$

$$8\eta = \left. \frac{\partial^6 \mathcal{F}}{(\partial M_1 \partial M_2 \partial M_3)^2} \right|_{M_{1,2,3}=0} = \frac{1}{6} \sum_{\sigma \in S_6} \Pi^{(6)}(\sigma(\mathbf{Q}_1, \mathbf{Q}_2, \mathbf{Q}_3, \mathbf{Q}_1, \mathbf{Q}_2, \mathbf{Q}_3)). \quad (\text{A.35})$$

Here  $\Pi^{(n)}$  are correlation functions of order  $n$ .  $\sigma \in S_n$  denotes permutations of the arguments to this function. The correlation functions are given by

$$\Pi^{(2)}(\mathbf{q}_1, \mathbf{q}_2) = \sum_{s_{1,2}} \int \frac{d\mathbf{k}}{(2\pi)^2} S^{(2)}(\epsilon) \text{tr} \left\{ P_{s_1}(\mathbf{k}) \sigma_{\mathbf{q}_1} P_{s_2}(\mathbf{k} + \mathbf{q}_2) \sigma_{\mathbf{q}_2} \right\}, \quad (\text{A.36})$$

$$\begin{aligned} \Pi^{(4)}(\mathbf{q}_1, \dots, \mathbf{q}_4) &= \sum_{s_{1,2,3,4}} \int \frac{d\mathbf{k}}{(2\pi)^2} S^{(4)}(\epsilon) \text{tr} \left\{ P_{s_1}(\mathbf{k}) \sigma_{\mathbf{q}_1} P_{s_2}(\mathbf{k} - \mathbf{q}_1) \sigma_{\mathbf{q}_2} P_{s_3}(\mathbf{k} - \mathbf{q}_1 - \mathbf{q}_2) \right. \\ &\quad \left. \sigma_{\mathbf{q}_3} P_{s_4}(\mathbf{k} + \mathbf{q}_4) \sigma_{\mathbf{q}_4} \right\}, \end{aligned} \quad (\text{A.37})$$

$$\begin{aligned} \Pi^{(6)}(\mathbf{q}_1, \dots, \mathbf{q}_6) &= \sum_{s_{1,\dots,6}} \int \frac{d\mathbf{k}}{(2\pi)^2} S^{(6)}(\epsilon) \text{tr} \left\{ P_{s_1}(\mathbf{k}) \sigma_{\mathbf{q}_1} P_{s_2}(\mathbf{k} - \mathbf{q}_1) \sigma_{\mathbf{q}_2} P_{s_3}(\mathbf{k} - \mathbf{q}_1 - \mathbf{q}_2) \right. \\ &\quad \left. \sigma_{\mathbf{q}_3} P_{s_4}(\mathbf{k} + \mathbf{q}_4 + \mathbf{q}_5 + \mathbf{q}_6) \sigma_{\mathbf{q}_4} P_{s_5}(\mathbf{k} + \mathbf{q}_5 + \mathbf{q}_6) \sigma_{\mathbf{q}_5} P_{s_6}(\mathbf{k} + \mathbf{q}_6) \sigma_{\mathbf{q}_6} \right\}, \end{aligned} \quad (\text{A.38})$$

where we used the shorthand notation  $\sigma_{\mathbf{q}} \equiv \widehat{\mathbf{M}}_{\mathbf{q}} \cdot \boldsymbol{\sigma}$  and introduced the Matsubara summation as separate functions  $S^{(2,4,6)}(\epsilon)$  with the pole structure.

The Matsubara sums take the general form

$$\begin{aligned}
 S(m_1 \times \epsilon_1, \dots, m_\mu \times \epsilon_\mu) &= \frac{1}{\beta} \sum_{k_n} \prod_{\nu=1}^{\mu} \frac{1}{(ik_n - \epsilon_\nu)^{m_\nu}} \\
 &= \sum_{\nu=1}^{\mu} \frac{1}{(m_\nu - 1)!} \frac{\partial^{m_\nu-1}}{\partial \epsilon_\nu^{m_\nu-1}} \left[ n_F(\epsilon_\nu) \prod_{\rho \neq \nu} \frac{1}{(\epsilon_\nu - \epsilon_\rho)^{m_\rho}} \right], \quad (\text{A.39})
 \end{aligned}$$

where  $\epsilon_i \neq \epsilon_j$  are pairwise different energies and  $m_\nu$  denotes the multiplicities of the arguments and the poles. In the simplest case of single poles ( $m_\nu = 1$  for all  $\nu$ ), the sum reduces to

$$S(\epsilon_1, \dots, \epsilon_\mu) = \sum_{\nu=1}^{\mu} n_F(\epsilon_\nu) \prod_{\rho \neq \nu} \frac{1}{\epsilon_\nu - \epsilon_\rho}. \quad (\text{A.40})$$

The second order correlation function  $\alpha$  corresponds to the susceptibility. The explicit form is given by

$$\begin{aligned}
 \chi_{\mathbf{q},s,s'}^{ab} &= - \int \frac{d\mathbf{k}}{(2\pi)^2} \frac{n_F(\epsilon_{\mathbf{k},s}) - n_F(\epsilon_{\mathbf{k}+\mathbf{q},s'})}{\epsilon_{\mathbf{k},s} - \epsilon_{\mathbf{k}+\mathbf{q},s'}} \langle \mathbf{k}, s | \sigma^a | \mathbf{k} + \mathbf{q}, s' \rangle \langle \mathbf{k} + \mathbf{q}, s' | \sigma^b | \mathbf{k}, s \rangle \\
 &= - \frac{1}{2} \int \frac{d\mathbf{k}}{(2\pi)^2} \frac{n_F(\epsilon_{\mathbf{k},s}) - n_F(\epsilon_{\mathbf{k}+\mathbf{q},s'})}{\epsilon_{\mathbf{k},s} - \epsilon_{\mathbf{k}+\mathbf{q},s'}} \\
 &\quad \times \left\{ \delta^{ab} [1 - ss' \hat{g}^m(\mathbf{k}) \hat{g}^m(\mathbf{k} + \mathbf{q})] + i\varepsilon^{abm} [s \hat{g}^m(\mathbf{k}) - s' \hat{g}^m(\mathbf{k} + \mathbf{q})] \right. \\
 &\quad \left. + ss' [\hat{g}^a(\mathbf{k}) \hat{g}^b(\mathbf{k} + \mathbf{q}) + \hat{g}^a(\mathbf{k} + \mathbf{q}) \hat{g}^b(\mathbf{k})] \right\}. \quad (\text{A.41})
 \end{aligned}$$

## Bibliography

1. Mendler, D., Kotetes, P. & Schön, G. Magnetic order on a topological insulator surface with warping and proximity-induced superconductivity. *Phys. Rev. B* **91**, 155405 (2015).
2. Heimes, A., Mendler, D. & Kotetes, P. Interplay of topological phases in magnetic adatom-chains on top of a Rashba superconducting surface. *New J. Phys.* **17**, 023051 (2015).
3. Kotetes, P., Mendler, D., Heimes, A. & Schön, G. Majorana fermion fingerprints in spin-polarised scanning tunnelling microscopy. *Physica E* **74**, 614 (2015).
4. Mendler, D. *Topological phases in systems with coexisting density waves and superconductivity* Diploma thesis (Karlsruhe Institute of Technology, 2013).
5. Mourik, V., Zuo, K., Frolov, S. M., Plissard, S. R., Bakkers, E. P. A. M. & Kouwenhoven, L. P. Signatures of Majorana Fermions in Hybrid Superconductor-Semiconductor Nanowire Devices. *Science* **336**, 1003 (2012).
6. Nadj-Perge, S., Drozdov, I. K., Li, J., Chen, H., Jeon, S., Seo, J., MacDonald, A. H., Bernevig, B. A. & Yazdani, A. Observation of Majorana fermions in ferromagnetic atomic chains on a superconductor. *Science* **346**, 602 (2014).
7. Nichele, F., Drachmann, A. C. C., Whiticar, A. M., O'Farrell, E. C. T., Suominen, H. J., Fornieri, A., Wang, T., Gardner, G. C., Thomas, C., Hatke, A. T., Krogstrup, P., Manfra, M. J., Flensberg, K. & Marcus, C. M. Scaling of Majorana Zero-Bias Conductance Peaks. arXiv: 1706.07033 (2017).
8. Kitaev, A. Y. Unpaired Majorana fermions in quantum wires. *Physics-Uspekhi* **44**, 131 (2001).
9. Thouless, D., Kohmoto, M., Nightingale, M. & den Nijs, M. Quantized Hall Conductance in a Two-Dimensional Periodic Potential. *Phys. Rev. Lett.* **49**, 405 (1982).
10. Kohmoto, M. Topological invariant and the quantization of the Hall conductance. *Annals of Physics* **160**, 343 (1985).

11. Altland, A. & Zirnbauer, M. R. Nonstandard symmetry classes in mesoscopic normal-superconducting hybrid structures. *Phys. Rev. B* **55**, 1142 (1997).
12. Kitaev, A. Periodic table for topological insulators and superconductors. *AIP Conf. Proc.* **1134**, 22 (2009).
13. Hasan, M. Z. & Kane, C. L. Colloquium: Topological insulators. *Rev. Mod. Phys.* **82**, 3045 (2010).
14. Qi, X.-L. & Zhang, S.-C. Topological insulators and superconductors. *Rev. Mod. Phys.* **83**, 1057 (2011).
15. Sato, M. & Ando, Y. Topological superconductors: a review. *Rep. Prog. Phys.* **80**, 076501 (2017).
16. Klitzing, K., Dorda, G. & Pepper, M. New Method for High-Accuracy Determination of the Fine-Structure Constant Based on Quantized Hall Resistance. *Phys. Rev. Lett.* **45**, 494 (1980).
17. Tsui, D. C., Stormer, H. L. & Gossard, A. C. Two-Dimensional Magnetotransport in the Extreme Quantum Limit. *Phys. Rev. Lett.* **48**, 1559 (22 1982).
18. Tong, D. Lectures on the Quantum Hall Effect. arXiv: 1606.06687 (2016).
19. Haldane, F. D. M. Model for a Quantum Hall Effect without Landau Levels: Condensed-Matter Realization of the “Parity Anomaly”. *Phys. Rev. Lett.* **61**, 2015 (1988).
20. Skyrme, T. H. R. A Non-Linear Theory of Strong Interactions. *Proc. Royal Soc. A* **247**, 260 (1958).
21. Qi, X., Hughes, T., Raghu, S. & Zhang, S. Topological Superconductivity and Superfluidity. *Phys. Rev. Lett.* **102**, 187001 (2009).
22. Kane, C. L. & Mele, E. J.  $Z_2$  Topological Order and the Quantum Spin Hall Effect. *Phys. Rev. Lett.* **95**, 146802 (2005).
23. Kane, C. L. & Mele, E. J. Quantum Spin Hall Effect in Graphene. *Phys. Rev. Lett.* **95**, 226801 (2005).
24. Bernevig, B. A. & Zhang, S.-C. Quantum Spin Hall Effect. *Phys. Rev. Lett.* **96**, 106802 (2006).
25. Bernevig, B. A., Hughes, T. L. & Zhang, S.-C. Quantum Spin Hall Effect and Topological Phase Transition in HgTe Quantum Wells. *Science* **314**, 1757 (2006).

- 
26. König, M., Wiedmann, S., Brune, C., Roth, A., Buhmann, H., Molenkamp, L. W., Qi, X.-L. & Zhang, S.-C. Quantum Spin Hall Insulator State in HgTe Quantum Wells. *Science* **318**, 766 (2007).
  27. Volovik, G. The Superfluid Universe. arXiv: 1004.0597v2 (2012).
  28. Kallin, C. Chiral p-wave order in Sr<sub>2</sub>RuO<sub>4</sub>. *Rep. Prog. Phys.* **75**, 042501 (2012).
  29. Penrose, R. Role of aesthetics in pure and applied research. *Bull. Inst. Math. Appl.* **10**, 266 (1974).
  30. De Bruijn, N. G. Algebraic theory of Penrose's non-periodic tilings of the plane, I, II. *Indag. Math.* **84**, 39 (1981).
  31. Cotton, F. *Chemical applications of group theory* (Wiley, 1990).
  32. Wigner, E. P. & Dirac, P. A. M. On the statistical distribution of the widths and spacings of nuclear resonance levels. *Math. Proc. Camb. Philos. Soc.* **47**, 790 (1951).
  33. Dyson, F. J. Statistical Theory of the Energy Levels of Complex Systems. I. *J. Math. Phys.* **3**, 140 (1962).
  34. Kotetes, P. Classification of engineered topological superconductors. *New J. Phys.* **15**, 105027 (2013).
  35. Karoubi, M. *K-theory: An introduction* (Springer, 2008).
  36. Hatcher, A. *Algebraic Topology* **5259** (Cambridge University Press, 2002).
  37. Melrose, R. B. *The Atiyah-Patodi-singer index theorem* (AK Peters Wellesley, 1993).
  38. Kaufmann, R. M., Li, D. & Wehefritz-Kaufmann, B. Notes on topological insulators. *Rev. Math. Phys.* **28**, 1630003 (2016).
  39. Schechter, J. & Valle, J. W. F. Neutrinoless double- $\beta$  decay in SU(2) $\times$ U(1) theories. *Phys. Rev. D* **25**, 2951 (11 1982).
  40. Sarma, S. D., Freedman, M. & Nayak, C. Majorana zero modes and topological quantum computation. *npj Quantum Information* (2015).
  41. Rao, S. An anyon primer. arXiv: hep-th/9209066 (1992).
  42. Rainis, D. & Loss, D. Majorana qubit decoherence by quasiparticle poisoning. *Phys. Rev. B* **85**, 174533 (2012).
  43. Alicea, J., Oreg, Y., Refael, G., Von Oppen, F. & Fisher, M. P. Non-Abelian statistics and topological quantum information processing in 1D wire networks. *Nat. Phys.* **7**, 412 (2011).

44. Dawson, C. M. & Nielsen, M. A. The Solovay-Kitaev Algorithm. *Quantum Info. Comput.* **6**, 81 (2006).
45. Trebst, S., Troyer, M., Wang, Z. & Ludwig, A. W. W. A Short Introduction to Fibonacci Anyon Models. *Prog. Theor. Phys.* **176**, 384 (2008).
46. Aasen, D., Hell, M., Mishmash, R. V., Higginbotham, A., Danon, J., Leijnse, M., Jespersen, T. S., Folk, J. A., Marcus, C. M., Flensberg, K. & Alicea, J. Milestones Toward Majorana-Based Quantum Computing. *Phys. Rev. X* **6**, 031016 (2016).
47. Sato, M., Tanaka, Y., Yada, K. & Yokoyama, T. Topology of Andreev bound states with flat dispersion. *Phys. Rev. B* **83**, 224511 (2011).
48. Li, Y., Wang, D. & Wu, C. Spontaneous breaking of time-reversal symmetry in the orbital channel for the boundary Majorana flat bands. *New J. Phys.* **15**, 085002 (2013).
49. Sedlmayr, N., Aguiar-Hualde, J. & Bena, C. Flat Majorana bands in two-dimensional lattices with inhomogeneous magnetic fields: Topology and stability. *Phys. Rev. B* **91**, 115415 (2015).
50. Volovik, G. E. Flat band in the core of topological defects: bulk-vortex correspondence in topological superfluids with Fermi points. *JETP letters* **93**, 66 (2011).
51. Heikkilä, T. T., Kopnin, N. B. & Volovik, G. E. Flat bands in topological media. *JETP letters* **94**, 233 (2011).
52. Wong, C. L. M., Liu, J., Law, K. T. & Lee, P. A. Majorana flat bands and unidirectional Majorana edge states in gapless topological superconductors. *Phys. Rev. B* **88**, 060504 (2013).
53. Deng, S., Ortiz, G., Poudel, A. & Viola, L. Majorana flat bands in s-wave gapless topological superconductors. *Phys. Rev. B* **89**, 140507 (2014).
54. Yuan, N., Wong, C. & Law, K. Probing Majorana flat bands in nodal d-wave superconductors with Rashba spin-orbit coupling. *Physica E* **55**, 30 (2014).
55. Brydon, P. M. R., Schnyder, A. P. & Timm, C. Topologically protected flat zero-energy surface bands in noncentrosymmetric superconductors. *Phys. Rev. B* **84**, 020501 (2011).
56. Brydon, P., Timm, C. & Schnyder, A. P. Interface currents in topological superconductor–ferromagnet heterostructures. *New J. Phys.* **15**, 045019 (2013).

- 
57. Schnyder, A. P. & Ryu, S. Topological phases and surface flat bands in superconductors without inversion symmetry. *Phys. Rev. B* **84**, 060504 (2011).
  58. Schnyder, A. P., Brydon, P. M. R. & Timm, C. Types of topological surface states in nodal noncentrosymmetric superconductors. *Phys. Rev. B* **85**, 024522 (2012).
  59. Schnyder, A. P., Timm, C. & Brydon, P. M. R. Edge Currents as a Signature of Flatbands in Topological Superconductors. *Phys. Rev. Lett.* **111**, 077001 (2013).
  60. Chang, P.-Y., Matsuura, S., Schnyder, A. P. & Ryu, S. Majorana vortex-bound states in three-dimensional nodal noncentrosymmetric superconductors. *Phys. Rev. B* **90**, 174504 (2014).
  61. Nakosai, S., Tanaka, Y. & Nagaosa, N. Two-dimensional p-wave superconducting states with magnetic moments on a conventional s-wave superconductor. *Phys. Rev. B* **88**, 180503 (2013).
  62. Lababidi, M. & Zhao, E. Nearly flat Andreev bound states in superconductor-topological insulator hybrid structures. *Phys. Rev. B* **86**, 161108 (2012).
  63. Potter, A. C. & Lee, P. A. Edge Ferromagnetism from Majorana Flat Bands: Application to Split Tunneling-Conductance Peaks in High- $T_c$  Cuprate Superconductors. *Phys. Rev. Lett.* **112**, 117002 (2014).
  64. Read, N. & Green, D. Paired states of fermions in two dimensions with breaking of parity and time-reversal symmetries and the fractional quantum Hall effect. *Phys. Rev. B* **61**, 10267 (2000).
  65. Fu, L. & Kane, C. Superconducting Proximity Effect and Majorana Fermions at the Surface of a Topological Insulator. *Phys. Rev. Lett.* **100**, 096407 (2008).
  66. Lutchyn, R. M., Sau, J. D. & Sarma, S. D. Majorana fermions and a topological phase transition in semiconductor-superconductor heterostructures. *Phys. Rev. Lett.* **105**, 077001 (2010).
  67. Lutchyn, R. M., Sau, J. D. & Sarma, S. D. Majorana Bound States in Quantum Wires. *Phys. Rev. Lett.* **105**, 177002 (2010).
  68. Heimes, A., Kotetes, P. & Schön, G. Majorana fermions from Shiba states in an antiferromagnetic chain on top of a superconductor. *Phys. Rev. B* **90**, 060507 (2014).
  69. Kjaergaard, M., Wölms, K. & Flensberg, K. Majorana fermions in superconducting nanowires without spin-orbit coupling. *Phys. Rev. B* **85**, 020503 (2012).

70. Martin, I. & Morpurgo, A. F. Majorana fermions in superconducting helical magnets. *Phys. Rev. B* **85**, 144505 (2012).
71. Choy, T.-P., Edge, J. M., Akhmerov, A. R. & Beenakker, C. W. J. Majorana fermions emerging from magnetic nanoparticles on a superconductor without spin-orbit coupling. *Phys. Rev. B* **84**, 195442 (2011).
72. Flensberg, K. Tunneling characteristics of a chain of Majorana bound states. *Phys. Rev. B* **82**, 180516 (2010).
73. Jiang, L., Pekker, D., Alicea, J., Refael, G., Oreg, Y. & von Oppen, F. Unconventional Josephson signatures of Majorana bound states. *Phys. Rev. Lett.* **107**, 236401 (2011).
74. Pawlak, R., Kisiel, M., Klinovaja, J., Meier, T., Kawai, S., Glatzel, T., Loss, D. & Meyer, E. Probing atomic structure and Majorana wavefunctions in mono-atomic Fe chains on superconducting Pb surface. *npj Quantum Information* **2**, 16035 (2016).
75. Law, K. T., Lee, P. A. & Ng, T. K. Majorana Fermion Induced Resonant Andreev Reflection. *Phys. Rev. Lett.* **103**, 237001 (2009).
76. Liu, J., Potter, A. C., Law, K. T. & Lee, P. A. Zero-Bias Peaks in the Tunneling Conductance of Spin-Orbit-Coupled Superconducting Wires with and without Majorana End-States. *Phys. Rev. Lett.* **109**, 267002 (2012).
77. Lee, E. J. H., Jiang, X., Houzet, M., Aguado, R., Lieber, C. M. & de Franceschi, S. Spin-resolved Andreev levels and parity crossings in hybrid superconductor-semiconductor nanostructures. *Nat. Nanotechnol.* **9**, 79 (2014).
78. Kjaergaard, M., Wölms, K. & Flensberg, K. Majorana fermions in superconducting nanowires without spin-orbit coupling. *Phys. Rev. B* **85**, 020503 (2012).
79. Pöyhönen, K., Westström, A., Röntynen, J. & Ojanen, T. Majorana states in helical Shiba chains and ladders. *Phys. Rev. B* **89**, 115109 (2014).
80. Brydon, P. M. R., Das Sarma, S., Hui, H.-Y. & Sau, J. D. Topological Yu-Shiba-Rusinov chain from spin-orbit coupling. *Phys. Rev. B* **91**, 064505 (2015).
81. Li, J., Chen, H., Drozdov, I. K., Yazdani, A., Bernevig, B. A. & MacDonald, A. H. Topological superconductivity induced by ferromagnetic metal chains. *Phys. Rev. B* **90**, 235433 (2014).
82. Ebisu, H., Yada, K., Kasai, H. & Tanaka, Y. Odd-frequency pairing in topological superconductivity in a one-dimensional magnetic chain. *Phys. Rev. B* **91**, 054518 (2015).

- 
83. Peng, Y., Pientka, F., Glazman, L. I. & von Oppen, F. Strong Localization of Majorana End States in Chains of Magnetic Adatoms. *Phys. Rev. Lett.* **114**, 106801 (2015).
  84. Hui, H.-Y., Brydon, P. M. R., Sau, J. D., Tewari, S. & Sarma, S. D. Majorana fermions in ferromagnetic chains on the surface of bulk spin-orbit coupled s-wave superconductors. *Sci. Rep.* **5**, 8880 (2015).
  85. Zhang, J., Kim, Y., Rossi, E. & Lutchyn, R. M. Topological superconductivity in a multichannel Yu-Shiba-Rusinov chain. *Phys. Rev. B* **93**, 024507 (2016).
  86. Čadež, T. & Sacramento, P. D. Zero energy modes in a superconductor with ferromagnetic adatom chains and quantum phase transitions. *J. Phys. Condens. Matter* **28**, 495703 (2016).
  87. He, J. J., Ng, T. K., Lee, P. A. & Law, K. T. Selective Equal-Spin Andreev Reflections Induced by Majorana Fermions. *Phys. Rev. Lett.* **112**, 037001 (2014).
  88. Yao, N. Y., Glazman, L. I., Demler, E. A., Lukin, M. D. & Sau, J. D. Enhanced Antiferromagnetic Exchange between Magnetic Impurities in a Superconducting Host. *Phys. Rev. Lett.* **113**, 087202 (2014).
  89. Ryu, S., Schnyder, A. P., Furusaki, A. & Ludwig, A. W. W. Topological insulators and superconductors: tenfold way and dimensional hierarchy. *New J. Phys.* **12**, 065010 (2010).
  90. Tewari, S. & Sau, J. D. Topological Invariants for Spin-Orbit Coupled Superconductor Nanowires. *Phys. Rev. Lett.* **109**, 150408 (2012).
  91. Röntynen, J. & Ojanen, T. Topological Superconductivity and High Chern Numbers in 2D Ferromagnetic Shiba Lattices. *Phys. Rev. Lett.* **114**, 236803 (2015).
  92. Romming, N., Hanneken, C., Menzel, M., Bickel, J. E., Wolter, B., von Bergmann, K., Kubetzka, A. & Wiesendanger, R. Writing and Deleting Single Magnetic Skyrmions. *Science* **341**, 636 (2013).
  93. Sticlet, D., Bena, C. & Simon, P. Spin and Majorana Polarization in Topological Superconducting Wires. *Phys. Rev. Lett.* **108**, 096802 (2012).
  94. Romito, A., Alicea, J., Refael, G. & von Oppen, F. Manipulating Majorana fermions using supercurrents. *Phys. Rev. B* **85**, 020502 (2012).
  95. Fu, L. & Kane, C. Topological insulators with inversion symmetry. *Phys. Rev. B* **76**, 045302 (2007).

96. Zhang, H., Liu, C.-X., Qi, X.-L., Dai, X., Fang, Z. & Zhang, S.-C. Topological insulators in  $\text{Bi}_2\text{Se}_3$ ,  $\text{Bi}_2\text{Te}_3$  and  $\text{Sb}_2\text{Te}_3$  with a single Dirac cone on the surface. *Nat. Phys.* **5**, 438 (2009).
97. Hsieh, D., Qian, D., Wray, L., Xia, Y., Hor, Y. S., Cava, R. J. & Hasan, M. Z. A topological Dirac insulator in a quantum spin Hall phase. *Nature* **452**, 970 (2008).
98. Hsieh, D., Xia, Y., Wray, L., Qian, D., Pal, A., Dil, J. H., Osterwalder, J., Meier, F., Bihlmayer, G., Kane, C. L., Hor, Y. S., Cava, R. J. & Hasan, M. Z. Observation of Unconventional Quantum Spin Textures in Topological Insulators. *Science* **323**, 919 (2009).
99. Chen, Y. L., Analytis, J. G., Chu, J.-H., Liu, Z. K., Mo, S.-K., Qi, X. L., Zhang, H. J., Lu, D. H., Dai, X., Fang, Z., Zhang, S. C., Fisher, I. R., Hussain, Z. & Shen, Z.-X. Experimental Realization of a Three-Dimensional Topological Insulator,  $\text{Bi}_2\text{Te}_3$ . *Science* **325**, 178 (2009).
100. Xia, Y., Qian, D., Hsieh, D., Wray, L., Pal, A., Lin, H., Bansil, A., Grauer, D., Hor, Y. S., Cava, R. J. & Hasan, M. Z. Observation of a large-gap topological-insulator class with a single Dirac cone on the surface. *Nat. Phys.* **5**, 398 (2009).
101. Brüne, C., Liu, C. X., Novik, E. G., Hankiewicz, E. M., Buhmann, H., Chen, Y. L., Qi, X. L., Shen, Z. X., Zhang, S. C. & Molenkamp, L. W. Quantum Hall Effect from the Topological Surface States of Strained Bulk HgTe. *Phys. Rev. Lett.* **106**, 126803 (2011).
102. Souma, S., Kosaka, K., Sato, T., Komatsu, M., Takayama, A., Takahashi, T., Kriener, M., Segawa, K. & Ando, Y. Direct Measurement of the Out-of-Plane Spin Texture in the Dirac-Cone Surface State of a Topological Insulator. *Phys. Rev. Lett.* **106**, 216803 (2011).
103. Moore, J. & Balents, L. Topological invariants of time-reversal-invariant band structures. *Phys. Rev. B* **75**, 121306 (2007).
104. Qi, X.-L., Hughes, T. L. & Zhang, S.-C. Topological field theory of time-reversal invariant insulators. *Phys. Rev. B* **78**, 195424 (2008).
105. Roy, R.  $\mathbb{Z}_2$  classification of quantum spin Hall systems: An approach using time-reversal invariance. *Phys. Rev. B* **79**, 195321 (2009).
106. Ando, Y. Topological Insulator Materials. *J. Phys. Soc. Jpn.* **82**, 102001 (2013).
107. Fu, L. Hexagonal Warping Effects in the Surface States of the Topological Insulator  $\text{Bi}_2\text{Te}_3$ . *Phys. Rev. Lett.* **103**, 266801 (2009).

- 
108. Liu, C.-X., Qi, X.-L., Zhang, H., Dai, X., Fang, Z. & Zhang, S.-C. Model Hamiltonian for topological insulators. *Phys. Rev. B* **82**, 045122 (2010).
  109. Alpichshev, Z., Analytis, J. G., Chu, J.-H., Fisher, I. R., Chen, Y. L., Shen, Z. X., Fang, A. & Kapitulnik, A. STM Imaging of Electronic Waves on the Surface of  $\text{Bi}_2\text{Te}_3$ : Topologically Protected Surface States and Hexagonal Warping Effects. *Phys. Rev. Lett.* **104**, 016401 (2010).
  110. Wang, Y. H., Hsieh, D., Pilon, D., Fu, L., Gardner, D. R., Lee, Y. S. & Gedik, N. Observation of a Warped Helical Spin Texture in  $\text{Bi}_2\text{Se}_3$  from Circular Dichroism Angle-Resolved Photoemission Spectroscopy. *Phys. Rev. Lett.* **107**, 207602 (2011).
  111. Henk, J., Flieger, M., Maznichenko, I. V., Mertig, I., Ernst, A., Ereameev, S. V. & Chulkov, E. V. Topological Character and Magnetism of the Dirac State in Mn-Doped  $\text{Bi}_2\text{Te}_3$ . *Phys. Rev. Lett.* **109**, 076801 (2012).
  112. Kuroda, K., Arita, M., Miyamoto, K., Ye, M., Jiang, J., Kimura, A., Krasovskii, E. E., Chulkov, E. V., Iwasawa, H., Okuda, T., Shimada, K., Ueda, Y., Namatame, H. & Taniguchi, M. Hexagonally Deformed Fermi Surface of the 3D Topological Insulator  $\text{Bi}_2\text{Se}_3$ . *Phys. Rev. Lett.* **105**, 076802 (2010).
  113. Jiang, J.-H. & Wu, S. Spin susceptibility and helical magnetic order at the edges/surfaces of topological insulators due to Fermi surface nesting. *Phys. Rev. B* **83**, 205124 (2011).
  114. Baum, Y. & Stern, A. Magnetic instability on the surface of topological insulators. *Phys. Rev. B* **85**, 121105 (2012).
  115. Baum, Y. & Stern, A. Density-waves instability and a skyrmion lattice on the surface of strong topological insulators. *Phys. Rev. B* **86**, 195116 (2012).
  116. Li, Z. & Carbotte, J. Hexagonal warping on optical conductivity of surface states in topological insulator  $\text{Bi}_2\text{Te}_3$ . *Phys. Rev. B* **87**, 155416 (2013).
  117. Li, Z. & Carbotte, J. Magneto-optical conductivity in a topological insulator. *Phys. Rev. B* **88**, 045414 (2013).
  118. Xiao, X. & Wen, W. Optical conductivities and signatures of topological insulators with hexagonal warping. *Phys. Rev. B* **88**, 045442 (2013).
  119. Zhang, Y., He, K., Chang, C.-Z., Song, C.-L., Wang, L.-L., Chen, X., Jia, J.-F., Fang, Z., Dai, X., Shan, W.-Y., Shen, S.-Q., Niu, Q., Qi, X.-L., Zhang, S.-C., Ma, X.-C. & Xue, Q.-K. Crossover of the three-dimensional topological insulator  $\text{Bi}_2\text{Se}_3$  to the two-dimensional limit. *Nat. Phys.* **6**, 584 (2010).

120. Pan, Z.-H., Vescovo, E., Fedorov, A. V., Gardner, D., Lee, Y. S., Chu, S., Gu, G. D. & Valla, T. Electronic Structure of the Topological Insulator  $\text{Bi}_2\text{Se}_3$  Using Angle-Resolved Photoemission Spectroscopy: Evidence for a Nearly Full Surface Spin Polarization. *Phys. Rev. Lett.* **106**, 257004 (2011).
121. Hsieh, D., Xia, Y., Qian, D., Wray, L., Dil, J., Meier, F., Osterwalder, J., Patthey, L., Checkelsky, J., Ong, N., Fedorov, A., Lin, H., Bansil, A., Grauer, D., Hor, Y., Cava, R. & Hasan, M. A tunable topological insulator in the spin helical Dirac transport regime. *Nature* **460**, 1101 (2009).
122. Grüner, G. The dynamics of spin-density waves. *Rev. Mod. Phys.* **66**, 1 (1994).
123. Schulz, H. Incommensurate antiferromagnetism in the two-dimensional Hubbard model. *Phys. Rev. Lett.* **64**, 1445 (1990).
124. Akhmerov, A., Nilsson, J. & Beenakker, C. Electrically Detected Interferometry of Majorana Fermions in a Topological Insulator. *Phys. Rev. Lett.* **102**, 216404 (2009).
125. Linder, J., Tanaka, Y., Yokoyama, T., Sudbø, A. & Nagaosa, N. Interplay between superconductivity and ferromagnetism on a topological insulator. *Phys. Rev. B* **81**, 184525 (2010).
126. Alicea, J. New directions in the pursuit of Majorana fermions in solid state systems. *Rep. Prog. Phys.* **75**, 076501 (2012).
127. Beenakker, C. Search for Majorana Fermions in Superconductors. *Annu. Rev. Con. Mat. Phys.* **4**, 113 (2013).
128. Sacépé, B., Oostinga, J. B., Li, J., Ubaldini, A., Couto, N. J., Giannini, E. & Morpurgo, A. F. Gate-tuned normal and superconducting transport at the surface of a topological insulator. *Nat. Comm.* **2**, 575 (2011).
129. Williams, J. R., Bestwick, A. J., Gallagher, P., Hong, S. S., Cui, Y., Bleich, A. S., Analytis, J. G., Fisher, I. R. & Goldhaber-Gordon, D. Unconventional Josephson Effect in Hybrid Superconductor-Topological Insulator Devices. *Phys. Rev. Lett.* **109**, 056803 (2012).
130. Veldhorst, M., Snelder, M., Hoek, M., Gang, T., Guduru, V. K., Wang, X. L., Zeitler, U., van der Wiel, W. G., Golubov, A. A., Hilgenkamp, H. & Brinkman, A. Josephson supercurrent through a topological insulator surface state. *Nat. Mat.* **11**, 417 (2012).

- 
131. Qu, F., Yang, F., Shen, J., Ding, Y., Chen, J., Ji, Z., Liu, G., Fan, J., Jing, X., Yang, C. & Lu, L. Strong Superconducting Proximity Effect in Pb-Bi<sub>2</sub>Te<sub>3</sub> Hybrid Structures. *Sci. Rep.* **2**, 339 (2012).
  132. Knez, I., Du, R.-R. & Sullivan, G. Andreev Reflection of Helical Edge Modes in InAs/GaSb Quantum Spin Hall Insulator. *Phys. Rev. Lett.* **109**, 186603 (2012).
  133. Oostinga, J. B., Maier, L., Schüffelgen, P., Knott, D., Ames, C., Brüne, C., Tkachov, G., Buhmann, H. & Molenkamp, L. W. Josephson Supercurrent through the Topological Surface States of Strained Bulk HgTe. *Phys. Rev. X* **3**, 021007 (2013).
  134. Hart, S., Ren, H., Wagner, T., Leubner, P., Mühlbauer, M., Brüne, C., Buhmann, H., Molenkamp, L. W. & Yacoby, A. Induced superconductivity in the quantum spin Hall edge. *Nat. Phys.* **10**, 638 (2014).
  135. Kotetes, P., Schön, G. & Shnirman, A. Engineering and manipulating topological qubits in 1D quantum wires. *J. Korean Phys. Soc.* **62**, 1558 (2013).
  136. Jiang, L., Pekker, D., Alicea, J., Refael, G., Oreg, Y., Brataas, A. & von Oppen, F. Magneto-Josephson effects in junctions with Majorana bound states. *Phys. Rev. B* **87**, 075438 (2013).
  137. Aperis, A., Varelogiannis, G. & Littlewood, P. B. Magnetic-Field-Induced Pattern of Coexisting Condensates in the Superconducting State of CeCoIn<sub>5</sub>. *Phys. Rev. Lett.* **104**, 216403 (2010).
  138. Zhang, F., Kane, C. L. & Mele, E. J. Topological Mirror Superconductivity. *Phys. Rev. Lett.* **111**, 056403 (2013).
  139. Chiu, C.-K., Yao, H. & Ryu, S. Classification of topological insulators and superconductors in the presence of reflection symmetry. *Phys. Rev. B* **88**, 075142 (2013).
  140. Ueno, Y., Yamakage, A., Tanaka, Y. & Sato, M. Symmetry-Protected Majorana Fermions in Topological Crystalline Superconductors: Theory and Application to Sr<sub>2</sub>RuO<sub>4</sub>. *Phys. Rev. Lett.* **111**, 087002 (2013).
  141. Shiozaki, K. & Sato, M. Topology of crystalline insulators and superconductors. *Phys. Rev. B* **90**, 165114 (2014).
  142. Fang, C., Bernevig, B. A. & Gilbert, M. J. Tri-Dirac surface modes in topological superconductors. *Phys. Rev. B* **91**, 165421 (2015).